GUIDEBOOK 12

5th International Conference of IGCP 588 and Fieldtrip Guide

SEISMIC AND NON-SEISMIC INFLUENCES ON COASTAL CHANGE IN ALASKA

May 3–10, 2014, South-Central Alaska, USA

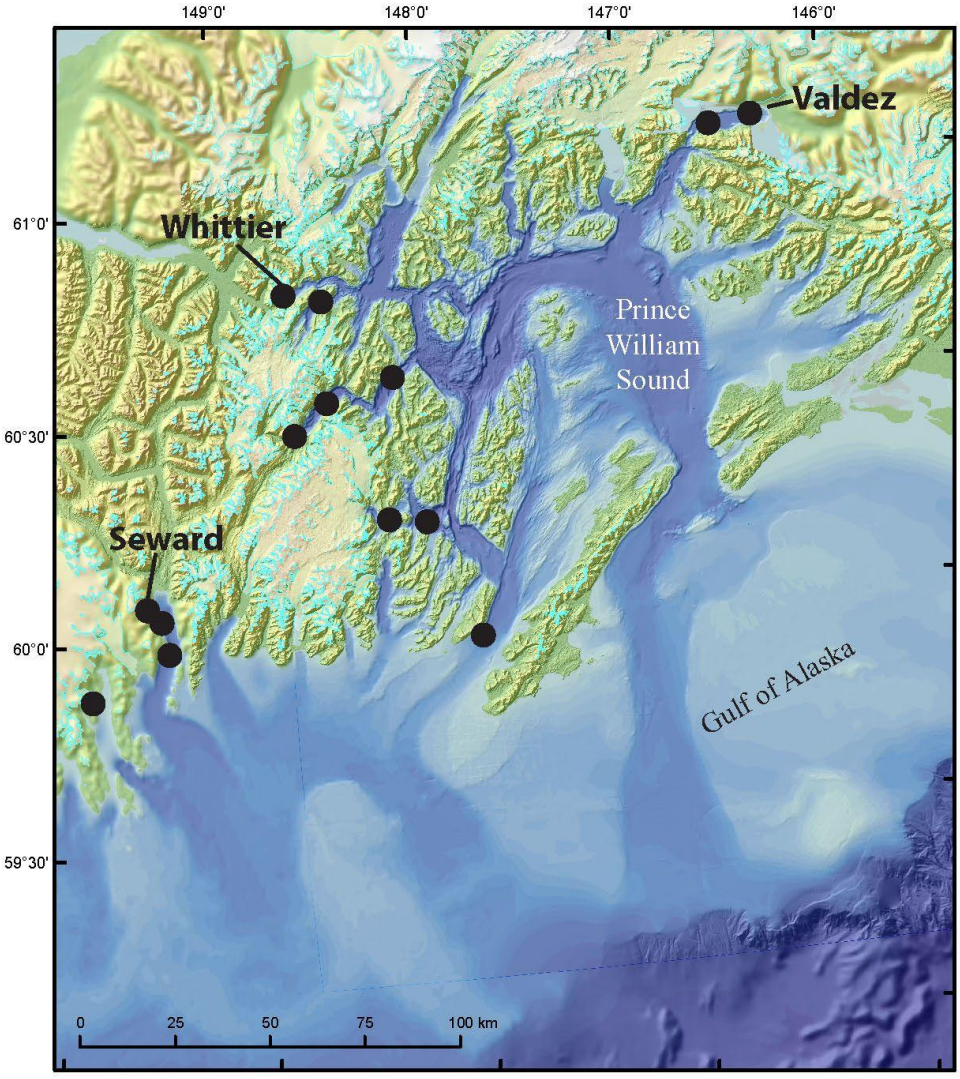

Published by

STATE OF ALASKA
DEPARTMENT OF NATURAL RESOURCES
DIVISION OF GEOLOGICAL & GEOPHYSICAL SURVEYS

2015

SEISMIC AND NON-SEISMIC INFLUENCES ON COASTAL CHANGE IN ALASKA

A Fieldtrip Guide and Conference Abstracts
5th International Conference of IGCP 588

COMPILED BY:

Natasha Barlow
Sea Level Research Unit
Department of Geography
Durham University
South Road, Durham, DH1 3LE, UK
n.l.m.barlow@durham.ac.uk

Rich Koehler
Neotectonics Group
State of Alaska, Department of Natural Resources
Division of Geological & Geophysical Surveys
3354 College Road, Fairbanks, Alaska 99709-3707
907-451-5006
richard.koehler@alaska.gov
www.dggs.alaska.gov

This guidebook was made possible with the publications support of
State of Alaska
Department of Natural Resources
Division of Geological & Geophysical Surveys
3354 College Road, Fairbanks, AK 99709-3707
907-451-5010
dggspubs@alaska.gov
www.dggs.alaska.gov

WELCOME

Welcome to the fifth, and final, IGCP 588 meeting, and welcome to coastal south-central Alaska. During this weeklong combined conference–fieldtrip in the 50th anniversary year of the 1964 M_w 9.2 Good Friday earthquake we will visit sites that experienced coseismic deformation during 1964, but also record late Holocene paleoseismicity and add to an increasing knowledge of seismic and tsunami hazard along the Aleutian megathrust. During the week, we travel west to east from Anchorage to the Copper River Delta, taking in key seismic, tsunami, glacial, and geologic sites. In the middle of the week, at Orca Lodge, we will hold the paper and poster session while overlooking the east side of Prince William Sound in an area impacted by the Exxon-Valdez disaster, now regularly frequented by sea otters that play outside the lodge. We hope that this trip will not only include excellent science, but will also be a once-in–a-lifetime opportunity to take in many of the natural and scientific highlights of southern Alaska. We are very pleased you are able to join us in this wonderful part of the world and hope that you enjoy Alaska as much as we do.

Ian, Rob, Natasha, and Peter
Conference Organizers

TIMETABLE

The timetable for the week is as follows. Please note that the Alaska weather can be both wonderful and awful and therefore there will be a degree of flexibility in the order of sites. In particular we will need to be flexible regarding the poster and paper days and may reorder them with the field day in the Copper River Delta to make the best use of the weather. We therefore ask you to please be ready to present on any one of the three days in Cordova.

Day		Activity
Sunday	4 May	**DAY 1: 1964 earthquake and late Holocene paleoseismology of upper Cook Inlet** • Anchorage: 4th Street 1964 landslide site; Earthquake Park; Glenn Alps; Ocean View • Girdwood marsh and ghost forest Conference dinner at Jack Sprats, Girdwood (8:00 pm) *Overnight at Girdwood*
Monday	5 May	**DAY 2: Seward and the outer coast (tsunami hazards and drowned glacial landscapes; calving glaciers)** • Summit Lake • Seward, charter boat through Resurrection Bay to outer coast of Kenai Peninsula and Harding Icefield glaciers *Overnight at Girdwood*
Tuesday	6 May	**DAY 3: Field day en route to Whittier for 12:15 pm ferry to Cordova** • Portage garage (iconic site of the 1964 earthquake) • Portage valley Little Ice Age moraines and current glacier retreat • Ferry: Crossing Prince William Sound—Recent science (arrive Cordova 3:30 pm) Evening speaker: Jeff Freymueller *Overnight at Orca Lodge, Cordova*
DAYS 4–6 may be switched to use the use the best combination of weather and river levels for the field program. IGCP Business Meeting to be held at the Orca—time to be confirmed to fit with the flexible schedule.		
Wednesday	7 May	**DAY 4: Full-day paper session** 8:50– 9:00 Welcome 9:00–10:30 Long-term uplift and exhumation (1) 11:00–12:30 Long term uplift and exhumation (2) 12:30– 2:00 Lunch 2:00– 3:30 Methods in reconstructing sea level change 4:00– 6:30 Posters *Overnight at Orca Lodge, Cordova*
Thursday	8 May	**DAY 5: Half-day paper session, half-day optional program** 8:30–10:00 Hazards 10:30–12:00 Segmentation of the Aleutian–Alaska megathrust 12:00– 1:30 Lunch **Free afternoon:** Additional costs not included in conference fee. Options include Hiking, flightseeing to Bering Glacier, boat trip, kayaking, walk about town *Overnight at Orca Lodge, Cordova*

Friday	9 May	**DAY 6: Long-term and short-term uplift, building mountains** • Hartney Bay • Whitshed Bay • Copper River Delta and jet boat trip to Alaganik Slough • Sheridan Glacier (if the road is snow free) *Overnight at Orca Lodge, Cordova*
Saturday	10 May	**DAY 7: Ferry from Cordova 7:15 am, arriving Whittier 10:30 am, travel to Anchorage** • Portage garage (iconic site of the 1964 earthquake) and area of maximum coseismic submergence *Overnight in Anchorage*
Sunday	11 May	**DAY 8: Fly out**

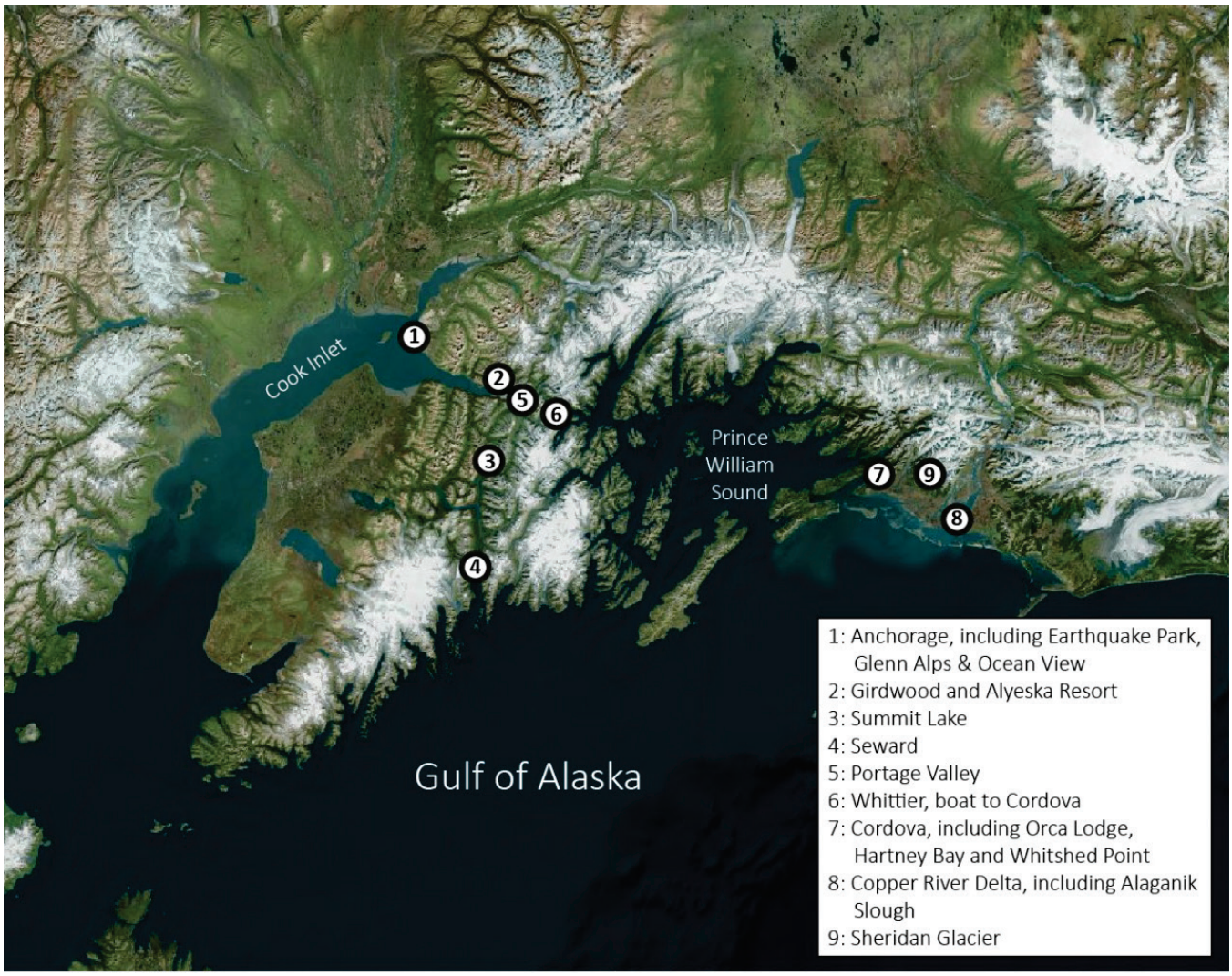

Map of south-central Alaska with key conference locations, numbered in the approximate order they will be visited during the meeting. Base map from www.maps.bing.com.

A BRIEF OVERVIEW OF ALASKA — *Natasha Barlow*

Alaska is the largest state of the United States of America, covering more than 1.4 million km^2. To the east it borders Canada, with the rest of state surrounded by the Pacific and Arctic oceans and Bering Sea. The conference visits three main regions: upper Cook Inlet, Prince William Sound, and the Copper River Delta—all environments of extremes. Cook Inlet stretches 350 km from Barren Islands, Gulf of Alaska, to Anchorage where it divides into Turnagain Arm and Knik Arm. The Cook Inlet watershed covers 120,000 km^2, draining water from the surrounding Chugach and Kenai Mountains and Aleutian Range. Prince William Sound encompasses 10,000 mi^2 of protected waterways, islands, fjords, and more than 10,000 glaciers of the Chugach Mountains, and was the epicentre of the 1964 Good Friday earthquake. The Copper River drains more than 27,000 mi^2 of interior Alaska and its delta extends over 700,000 acres, making it the largest contiguous wetland along the Pacific coast of North America, and is used annually by 16 million shorebirds.

The Cook Inlet region of Alaska marks the transition between the maritime climate of the southern coastal area and the continental climate of the interior. Girdwood is the western limit of the southern Alaska rainforest. Precipitation varies greatly due to the maritime influence of the Gulf of Alaska and local mountainous relief. At Cordova average annual precipitation is 3,769 mm/yr, at Tutka Bay at the southernmost point of the Kenai Mountains precipitation is 1,683 mm/yr, while Mirror Lake, northeast Knik Arm, only experiences 352 mm/yr. The average July maximum temperature for Cook Inlet is 19°C and the average January minimum -14°C (Shulski and Wendler, 2007), with an average annual temperature at Cordova of 6°C.

Upper Cook Inlet and Turnagain Arm are macrotidal, with semidiurnal tides and a mean tidal range of 7.98 m at Anchorage and a diurnal range of 8.89 m (NOAA), exposing up to 90 percent of the Turnagain Arm mudflats at low tide. A 1.2–1.8 m tidal bore forms in inner Turnagain Arm and travels inland from Bird Point at up to 4 m/sec (Bartsch-Winkler and Ovenshine, 1984; Greb and Archer, 2007). In comparison the mean tidal range at Cordova is 3.01 m (NOAA).

The present-day tectonics of south-central Alaska are affected by the oblique collision of the Yakutat terrane into Alaska and subduction along the Aleutian megathrust of the Pacific plate beneath the Alaskan plate (Plafker and Berg, 1994). The Pacific plate moves northward at ~55 mm/yr. The Yakutat microplate, a fragment of the North American plate that is partially subducted beneath and partially accreted to the continental margin of North America, moves northwest at 40–50 mm/yr, 10–20° counter-clockwise to the direction of the Pacific–Alaska convergence (Bruhn *et al.*, 2004; Fletcher and Freymueller, 1999).

Sudden deformation of any part the active tectonic boundaries results in large-magnitude earthquakes. The largest historical earthquake in upper Cook Inlet (M_w = 9.2) occurred in AD 1964 at 6:36 pm. A 600–800 km rupture of the eastern segment of the Aleutian megathrust produced surface deformation over 170,000–200,000 km^2 of south-central Alaska (Plafker, 1969) with upper Cook Inlet experiencing up to 2.5 m of subsidence and a zone uplift seaward of the subsidence region through Prince William Sound and Copper River Delta. One hundred thirty-one people died (115 in Alaska and 16 in Oregon and California), primarily due to local and regional tsunami waves. Alaska also experiences intraplate earthquakes with ruptures along interior faults, including the M_w = 7.9 AD 2002 Denali fault earthquake.

The anthropogenic history of Alaska is relatively short, with rapid population expansion only occurring in the last 130 years. Prior to the expeditions of Bering (AD 1725–1730 and AD 1733–1745) and Cook (AD 1776–1779), occupation of Alaska was solely by Native Peoples with the Tanaina and Dena'ina Indians (Athabaskan tribe) living in the Cook Inlet–Susitna River basin and Kenai Peninsula, respectively (Gibson, 1976). From c. AD 1750, Russian fur hunters began to explore the southern and western coasts for sea-otter pelts, setting up permanent establishments in Cook Inlet from AD 1787 (Naske and Slotnick, 1987). In AD 1867, Russia sold Alaska to the USA and rapid development and population growth occurred as a consequence of gold discovery, initially in southeast Alaska from AD 1870 (Naske and Slotnick, 1987). Gold mining in Turnagain Arm started in AD 1888 at Sunrise, resulting in 3,000 people in Hope (Turnagain Arm) by AD 1896. In AD 1897, due to the Klondike gold rush in Canada's Yukon, the population at Sunrise fell to 150. However, the easier conditions of Turnagain Arm, compared to interior Alaska–Canada, attracted around 10,000 people to the area in a second gold rush in AD 1898 (Hope and Sunrise Historical and Mining Museum, 2005). Mining continued around Turnagain Arm until c. AD 1940, when activity dramatically reduced due to World War II, though some mining continues to the present day (Lampright, 2008).

Population growth led to the building of railways to connect the coast to interior Alaska. In AD 1903, railroad construction was begun at Seward, reaching the head of Turnagain Arm in AD 1910. Rail building started again from Ship Creek (now part of Anchorage) in AD 1915, and in AD 1923, Seward and Fairbanks were connected. The establishment of Ship Creek as the headquarters of the Alaska Railroad resulted in the expansion (of what was initially a tent city) of Anchorage; population and infrastructure in upper Cook Inlet rapidly developed from AD 1915 (Naske and Slotnick, 1987). In AD 1950, the Anchorage–Seward Highway opened. Many communities in Alaska today are only accessible by boat or plane. The Alaska Marine Highway (part of which we will use to cross Prince William Sound) has been designated a National Scenic Byway and an All American Road, the only marine route with this designation.

TABLE OF CONTENTS

CHAPTER 1

CHAPTER 1.1

THE TURNAGAIN HEIGHTS AND FOURTH AVENUE LANDSLIDES

by Ed Garrett[1]

Seismically triggered landslides posed perhaps the greatest geological hazard to the Anchorage area in 1964. The earthquake initiated large translational block landslides at Turnagain Heights, Fourth Avenue, Government Hill, L Street, and Native Hospital, devastating large areas of downtown and surrounding residential neighborhoods. The Fourth Avenue landslide involved 14 city blocks on the north side of downtown Anchorage, immediately east of our starting point at the Hilton Hotel. The largest landslide occurred at Turnagain Heights, a residential area approximately 4 km to the southwest. Here, two main lobes together extended for 2.6 km along the Knik Arm coastline. In the more developed eastern lobe, 75 houses were destroyed and four lives lost; the largely undeveloped western lobe is preserved as Earthquake Park. Our stop here provides an opportunity to discuss a hazard intricately linked to Alaska's geological, glacial, and tectonic history. The descriptions below are based on Hansen's comprehensive account (Hansen, 1965).

The Fourth Avenue Landslide

Incorporating a volume of more than 1.5 million m^3 of material, the Fourth Avenue landslide devastated blocks north of Fourth Avenue between E Street and Barrow Street (fig. 1.1.1). The landslide moved as a single large block, sliding on a subhorizontal basal shear surface (fig. 1.1.2). The north side of Fourth Avenue descended into the graben, which subsided 3 m in response to 5 m of horizontal movement (fig. 1.1.3). The translational sliding mechanism created zones of extensional ground cracking landward of the scarp, with fissures occurring up to 150 m to the south. The movement also created pressure ridges around Second Avenue at the toe of the slide.

The Turnagain Heights Landslide

Mobilization of material at Turnagain Heights began approximately two minutes after shaking started and continued for one or two minutes after noticeable shaking ceased. The failure was retrogressive, progressing south from the 20–30-m-high coastal bluff. The maximum headward retrogression exceeded 350 m in the western lobe and 150 m in the eastern lobe, with a combined total of 12 million m^3 of material moved (fig. 1.1.4). Sub-horizontal basal shear surfaces caused blocks to rotate out from the bluff face, with the toe of the slide eventually extending more than 600 m offshore from the original bluff face. Subsequent erosion has restored the coastline of Bootlegger Cove to close to its pre-landslide position and subdued the chaotic topography of jagged rotated blocks and grabens in the area of Earthquake Park. Extensional fissures occurred more than 100 m behind the western lobe and 600 m behind the eastern lobe.

Failure Mechanism

A layer of glacioestuarine sediments, the Bootlegger Cove Formation, underlies the center and west of Anchorage. Debate in the years following 1964 revolved around whether landsliding could be attributed to liquefaction of noncohesive sands and silts (e.g. Shannon and Wilson, Inc., 1964; Seed and Wilson, 1967) or sensitive clay failure within the Bootlegger Cove Formation (e.g. Hansen, 1965). This debate was not resolved until the 1980s, with the publication of comprehensive geotechnical investigations by Updike *et al.* (1988) supporting the latter hypothesis. The formation, incorporating silty clay and clayey sit, with thin beds of sand, diamicton, and occasional pebbles

[1] *Ed Garrett, Department of Geography, Durham University, Lower Mountjoy, South Road, Durham, DH1 3LE, United Kingdom. Now at: Geological Survey of Belgium, Royal Belgian Institute for Natural Sciences, Jennerstraat 13, 1000 Brussels, Belgium. egarrett@naturalsciences.be*

and cobbles, consists of three layers: stiff upper and lower facies, separated by a sensitive intervening units. Sensitivity is a measure of the reduction in shear strength of a clay when remolded; samples from the middle unit of the Bootlegger Cove Formation exhibit very low strengths and high sensitivity ratios. During long-duration shaking, the flocculated sedimentary fabric collapsed, allowing platy clay particles to reorient, releasing pore fluid and enabling failure (Updike *et al.*, 1988). With the shear resistance of the sensitive clays reduced by shaking during the earthquake, gravity provided the propelling mechanism and the landslides continued until resistance from the toe or shear resistance of the clay exceeded the gravitational component on the shear surface.

The Bootlegger Cove Formation is 40–65 m thick in the vicinity of Anchorage, with the upper part dated at 15,870 cal yr BP (Schmoll *et al.*, 1972; Reger *et al.*, 1995). The high sensitivity ratios may derive in part from the leaching of salts following the postglacial uplift of clays deposited in marine settings (Kerr and Drew, 1968).

Stability and Future Landslide Susceptibility

The landslides at Turnagain Heights, Fourth Avenue, Government Hill, L Street, and Native Hospital demonstrated that seismically-triggered landslides are a major geohazard in the Anchorage area. Quantifying and mapping the potential for further large translational landslides is consequently of strategic importance for planning, zoning, and emergency response preparation. Such activities rely on hazard maps produced by Harding-Lawson Associates (1979), recently updated by Jibson and Michael (2009).

The failure mechanism responsible for the larger Anchorage-area landslides requires long-duration shaking, implying that large translational block slides generally occur only during large subduction earthquakes. Shallow crustal earthquakes, such as those generated along the Castle Mountain and Border Ranges faults, are unlikely to trigger failures of this kind (Jibson and Michael, 2009). Barnhardt and Kayen (2000), however, suggest the substantial drop in shear resistance resulting from straining during megathrust earthquakes persists for decades to centuries, leaving soils vulnerable to further failures.

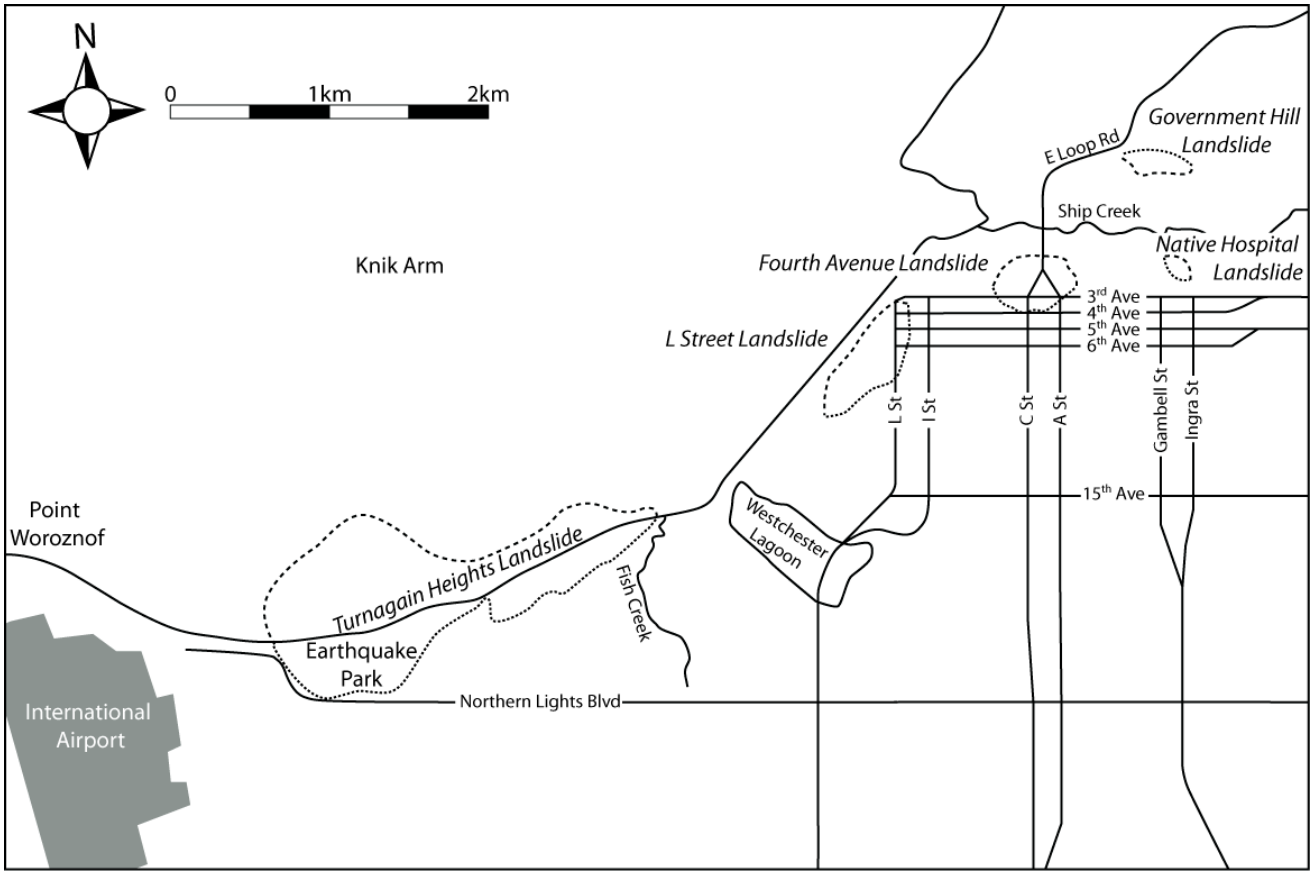

Figure 1.1.1. *Map showing locations of the main seismically-triggered translational landslides around Anchorage.*

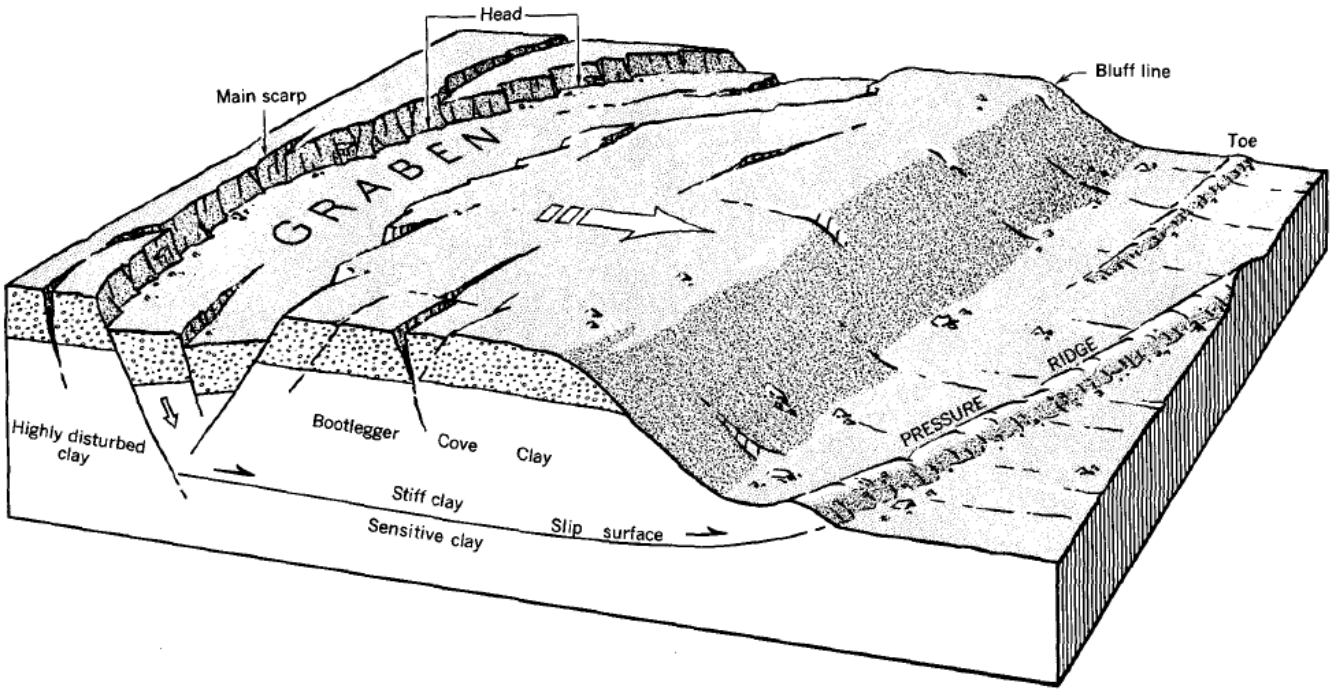

Figure 1.1.2. *Generalized cross section of a translational block landslide (reproduced from Hansen, 1965).*

Figure 1.1.3. *The 4th Avenue landslide. Photos* ***a****,* ***b****, and* ***c.*** *The scarp and graben along 4th Avenue;* ***d.*** *Warehouses destroyed by compression buckling and foreshortening at the toe of the landslide. All photos from the U.S. Geological Survey Photographic Library.*

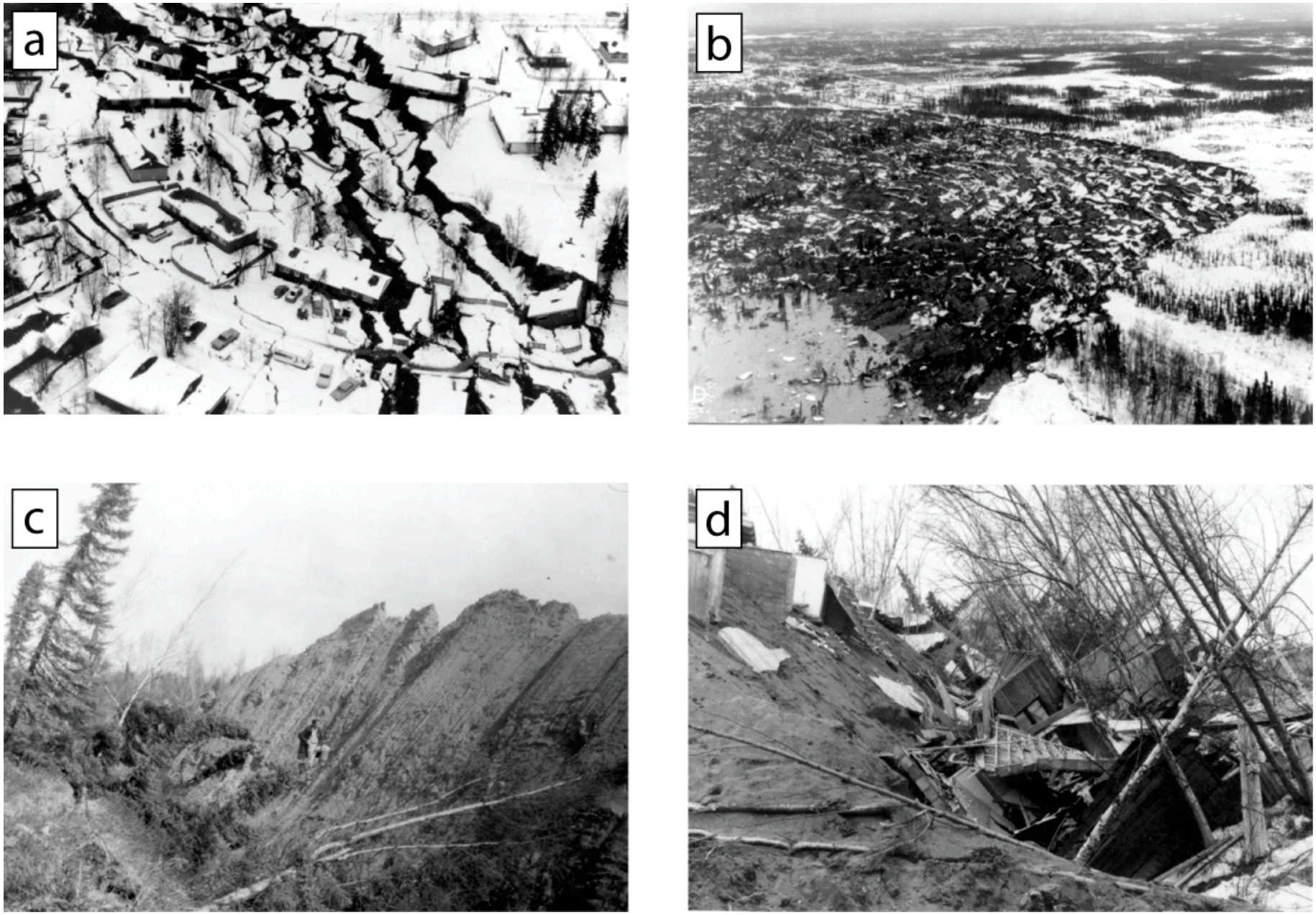

Figure 1.1.4. *The Turnagain Heights landslide.* ***a.*** *Part of the eastern lobe;* ***b.*** *The western lobe;* ***c.*** *Rotated blocks and 20-ft-high clay ridge; and* ***d.*** *Homes devastated by the landslide. All photos from the U.S. Geological Survey Photographic Library.*

CHAPTER 1.2

THIS CHAPTER EXCERPTED FROM:

Karl, S.M., Bradley, D.C., Combellick, R.A., and Miller, M.L., 2011, Field Guide to the Accretionary Complex and Neotectonics of South-Central Alaska, Anchorage to Seward: AAPG data pages; Alaska Geological Society, 45 p., http://www.alaskageology.org/publications.htm

INTRODUCTION AT GLENN ALPS

The Glenn Alps overlook in Anchorage provides a spectacular overview of the three main components of a long-lived convergent margin. These are the accretionary complex, the arc volcanoes, and the forearc basin. With a little imagination, you can also envision the subducting slab about 50 km beneath your feet, and bending downward beneath the arc volcanoes at a depth of about 100 km. If it is a very clear day, you can also see the arc of the Alaska Range and Denali (also known as Mt. McKinley) about 225 km (140 miles) to the north.

In brief, the Chugach accretionary complex is the remnants of 200 million years of subduction history beneath the southern Alaska margin. Looking to the northwest, you can see the northeasternmost active volcanoes of the Alaska–Aleutian arc. This modern arc is built on the Wrangellia–Peninsular composite terrane, which had their origins as intraoceanic arcs, and accreted to North America in mid-Cretaceous time. In between you can see the Cook Inlet forearc basin, which has a history extending back to early Mesozoic time, but has seen significant Miocene and younger sedimentation, and Pliocene or younger deformation.

This fieldtrip will not be stopping at bedrock exposures along Turnagain Arm. However, there are excellent boulders lining the parking lot that show superb examples of mélange textures formed by deformation of unconsolidated sediment in the accretionary prism. It is worth sticking your nose to the boulders, noting the many rock types, and the swirly textures indicating deformation before lithification.

As the Anchorage area has about half the population of Alaska, and there is an extensive road network, considerable work has been completed on the rocks in this area. Moreover, there have been numerous geology field trips in this region and a number of field guides produced that explain these rocks in great detail. The most recent and complete of these was by Karl *et al.* (2011), which was produced for an Alaska Geological Society field trip, and covered much of the same ground that we are covering on this field trip. Instead of re-inventing the wheel, it is worth quoting much of that guide's introductory text verbatim. The following is from that guide, with minor deletions of sections that are likely of little interest to this audience. Note the text or figure captions sometimes refer to field trip stops that were for the 2011 field trip, not this one. We may see some of these stops during our boat trip in Resurrection Bay.

—Peter Haeussler[2]

The remainder of this chapter is excerpted from the Karl et al. (2011) field guide.

Tectonic Setting

South-central Alaska's Pacific margin is underlain by two parallel composite terranes (Plafker *et al.*, 1994). On the inboard side is the Wrangellia–Peninsular composite terrane. The Peninsular terrane has been the site of episodic arc magmatism since the latest Triassic (Hacker and others, 2008; 2011). Farther outboard and paired with it is the Chugach–Prince William composite terrane, an accretionary complex that formed in the same time interval. These terranes were juxtaposed before they approached the North American margin in latest Jurassic to Cretaceous time (e.g., Trop *et al.*, 2002; Pavlis and Roeske, 2007). The Border Ranges fault forms the boundary between the Wrangellia–Peninsular and Chugach terranes; it began as a subduction thrust but has been reactivated in various places as strike-slip or normal faults (e.g., Little and Naeser, 1989; Pavlis and Roeske, 2007). The Mesozoic

[2] *Peter Haeussler, U.S. Geological Survey, 4210 University Drive, Anchorage, AK, U.S.A., 99508. pheuslr@usgs.gov*

part of the accretionary wedge is referred to as the Chugach terrane, the Cenozoic part as the Prince William terrane. The distinction between Chugach and Prince William terranes appears artificial (Dumoulin, 1987; 1988) but the names are entrenched and are retained for now.

McHugh Complex

The McHugh Complex constitutes the older, inboard part of the Chugach terrane in south-central Alaska. On Kodiak Island, equivalent rocks are called the Uyak Complex (Connelly, 1978). Along Turnagain Arm (fig. 1.2.2), the northwestern, more inboard part of the McHugh Complex is a mélange composed of fragments and disrupted bands of mafic volcanic rocks, bedded chert, graywacke, and rare limestone in a phacoidally cleaved matrix of dominantly argillite and subordinate tuff. The southeastern part is mainly composed of siliciclastic rocks, including boulder and cobble conglomerate, massive graywacke, and graywacke–argillite turbidites. Southwest of Turnagain Arm, on Kodiak Island and near Seldovia, and northeast of Turnagain Arm, near the Tazlina Glacier and the Copper River, a discontinuous band of high pressure(high-P)/low temperature (low-T) schist blocks that have Early Jurassic metamorphic mineral ages (Sisson and Onstott, 1986; Roeske *et al.*, 1989) marks the inboard contact of the McHugh Complex. Next outboard, best exposed near Seldovia, is a discontinuous band of kilometer-scale basalt-ribbon chert blocks encased in thin bands of scaly argillite mélange. Faulted against the basalt-chert band is a discontinuous band of graywacke turbidites that include beds of Early Jurassic chert, and outboard of the turbidites are argillite-matrix mélange and more turbidites. In Turnagain Arm, the more inboard, high-P metamorphic rocks, basalt-chert, and graywacke turbidite facies are absent; argillite-matrix mélange lies along the Knik Fault that locally marks the inner contact of the McHugh Complex.

The McHugh Complex is characterized by moderate to intense stratal disruption, which resulted in tectonic juxtaposition of a variety of rock types. Where mapped in the Valdez (Winkler *et al.*, 1981) and Seldovia (Bradley *et al.*, 1999) quadrangles, fault slices of chert, basalt, and graywacke have been traced for tens of kilometers along strike. The Anchorage and Seward quadrangles have not yet been mapped in equivalent detail, but the map pattern is probably comparable. At all scales, from thin section to outcrop, chert, basalt, and graywacke occur as more competent rock types in scaly argillite matrix. The predominant mode of early deformation was layer-parallel fragmentation; breakup of relatively competent beds, such as chert and graywacke, was accompanied by flowage of argillite (± tuff) matrix into gaps. The resulting fragment foliation is the most conspicuous fabric element in the McHugh Complex; along Turnagain Arm, it strikes north–northeast and in most places dips steeply northwest. The foliation is commonly displaced across narrow (up to a few centimeters wide), early ductile shear zones. When the dominant foliation is restored to horizontal, the ductile shear zones show a very consistent sense of slip, seaward side down (Bradley and Kusky, 1992; Kusky and Bradley, 1999). Clark (1973) reported prehnite-pumpellyite metamorphic facies mineral assemblages in the McHugh Complex along Turnagain Arm. The primary mélange foliation, ductile shear zones, and prehnite-pumpellyite grade metamorphism are all believed to have formed during subduction–accretion processes. Ductile shear zones slice through penetrative foliations and impose successive generations of strain fabrics on blocks and matrix in the mélange (fig. 1.2.3A). The deformation is pervasive but inhomogenous; strain is partitioned along zones of localized intense shear and is also focused into less competent rock types such as argillite. Extensive translation in high strain zones is indicated by isolation of discrete lithologies such as limestone, chert, and pillow basalt in centimeter- to meter-scale blocks in scaly argillite, far from any stratigraphic horizon or even blocks of similar lithology. Exposures of basalt are common in the more inboard parts of the Chugach accretionary complex and they are only found in the argillite matrix mélange facies of the McHugh Complex in Turnagain Arm. Mafic rocks include pillow lava, pillow breccia, massive flows, diabase dikes, and gabbro in meter-scale fault-bounded bodies. There are also common syndeformational mafic dikes and rare pepperites intruding blocks and matrix. On trace-element discriminant diagrams, various McHugh Complex basalts plot in the N-MORB, E-MORB, and “within-plate” fields (Nelson and Blome, 1991). Trace-element ratios suggest some of the basalts of the McHugh Complex in Kachemak Bay may represent seamounts (Luchetti *et al.*, 1984; Nelson and Blome, 1991). Some of the ocean floor that was offscraped and incorporated into the McHugh Complex may date back to Paleozoic time. Age control for the basalt is provided by overlying cherts (fig. 1.2.3B) that contain radiolarians that have yielded mid-Triassic to mid-Cretaceous ages (discussed below) (Winkler *et al.*, 1981; Karl *et al.*, 1979; Nelson *et. al.*, 1986; Nelson, Blome, and Karl, 1987; Bradley *et al.*, 1999). A fault-bounded

gabbro block in the McHugh Complex in the Seldovia Quadrangle yielded an earliest Carnian (Late Triassic) concordant $^{206}Pb/^{238}U$ zircon age of 227.7 ± 0.6 Ma (R. Tucker, written commun., 2000).

Rhythmically bedded chert forms one of the most distinctive components of the McHugh Complex. The chert is typically gray or green, less commonly black or red, in centimeter-scale beds that may or may not have interbedded argillite. Large chert sections are intensely faulted and disharmonically folded, such as are exposed along the shoreline of Kachemak Bay in Seldovia Quadrangle. Late Triassic, Early and Late Jurassic, and Early Cretaceous radiolarians have been reported from exposures of chert interbedded with argillite, and chert depositionally overlying basalt in western Turnagain Arm (Karl *et al.*, 1979; Nelson *et al.*, 1986; Nelson, Blome, and Karl, 1987). Equivalent rocks in the Seldovia Quadrangle have more complete age control and some indication of stratigraphic horizons in the McHugh Complex. At several places in that area, radiolarian age data for basal ages of chert that depositionally overlies basalt vary from Ladinian (middle Triassic) to Albian–Aptian (middle Cretaceous) (Bradley *et al.*, 1999; Bradley *et al.*, 2000). North of Prince William Sound, radiolarian age distributions in the McHugh Complex define three belts: An older northern, inboard belt of chert blocks that contain radiolarians of Late Triassic to Early Jurassic(?) age, a central belt of chert blocks that contain radiolarians of Jurassic to Early Cretaceous age, and a southern belt of chert blocks that contain radiolarians of Late Jurassic or Early Cretaceous to mid-Cretaceous age (Winkler *et al.*, 1981).

Argillite dominates the inboard mélange facies of the McHugh Complex. The argillite is dark gray and locally massive, but commonly includes meter-scale beds of graywacke, volcaniclastic detritus, and centimeter- to meter-scale lenses of bedded gray chert, one of which yielded radiolarians of Carnian (Late Triassic) age at a locality in Turnagain Arm (Nelson, Blome, and Karl, 1987; fig. 1.2.2). The ubiquitous graywacke and volcaniclastic material reflect proximity to an arc source, and the dark gray color reflects a low oxygen environment such as the lower slope or trench. Argillite interbedded with thin layers of dark gray sandstone and chert is inferred to represent slope and slope basin deposition in a low-sediment environment. Triassic and Jurassic detrital zircon ages for interbedded sandstones provide maximum depositional ages for some argillites; Late Triassic to Early Cretaceous radiolarian ages from interbedded chert layers provide the depositional ages for other argillites. This range of ages suggests argillites of Late Triassic to Early Cretaceous age are tectonically mixed along Turnagain Arm. The incompetent argillite absorbed the bulk of the strain during subduction and accretion of the McHugh Complex, and flowed around boudins and phacoids of extremely extended layers of interbedded graywacke, volcaniclastic rock, chert, and around incorporated blocks of ocean-plate basalt, chert, and limestone that also show a range of ages. In Turnagain Arm, syndeformational mafic dikes that feather into argillite, sandstone, and chert beds, and also cut intercalated blocks of basalt and chert no younger than Valanginian (Early Cretaceous), reflect magmatic activity in the lower slope and trench. This syndeformational magmatic activity may be related to the 120- to 130-Ma syntectonic plutonism and high-T metamorphism in the McHugh Complex to the north of Turnagain Arm that is interpreted to record an episode of Early Cretaceous ridge subduction and also corresponds to the end of the argillite-dominant phase of accretion (Clift *et al.*, 2005; Pavlis and Roeske, 2007; Amato and Pavlis, 2010).

Graywacke and associated conglomerate are dominant components of the most outboard and youngest phase of the McHugh Complex along Turnagain Arm. The graywacke and conglomerate typically occur as massive, structureless bodies. Bedding is seldom observed and even where visible, it generally cannot be traced far (as will be seen at Stop 3). Graywacke and conglomerate are matrix-supported and poorly sorted; the clast population consists of predominant chert and volcanic rock fragments, and subordinate quartz and feldspar. Quartz generally constitutes less than 5 percent, and feldspar less than 15 percent, of clasts in the graywacke (Karl, unpublished data). McHugh Complex conglomerates, such as will be seen at Stop 3 (fig. 1.2.3C), contain a broad mix of clast types, including granitic and metamorphic rocks, volcanic rocks, limestone, sandstone, argillite, and chert.

Regionally, the graywacke in the McHugh Complex as a whole ranges in age from Early Jurassic (Pliensbachian) through early Late Cretaceous (Turonian). At one location in the Seldovia Quadrangle, graywacke conformably overlies ribbon chert that yielded Pliensbachian radiolarians (Bradley *et al.*, 1999). Along Turnagain Arm, two samples of graywacke interbedded with the argillite matrix in the mélange facies of the McHugh Complex contain detrital zircons that have U-Pb ages ranging older than 146 Ma and 157 Ma, respectively (Amato and Pavlis, 2010). Three samples from the massive graywacke facies to the southeast (outboard direction) contain detrital zircons

that have U-Pb ages ranging older than 89 Ma, 89 Ma, and 84 Ma, respectively (Amato and Pavlis, 2010), and graywacke from Beluga Point contains detrital zircons that have U-Pb ages that are 91 Ma and older (Bradley *et al.*, 2009). The inboard mélange facies of the McHugh Complex includes chert blocks with radiolarians as young as Barremian (Nelson, Blome, and Karl, 1987), and near the Matanuska River is intruded by a trondjhemitic pluton dated at 120 Ma (Amato and Pavlis, 2010). This age information allows discrimination of an Early Jurassic graywacke turbidite facies along the inboard margin of the clastic rocks in the McHugh Complex in the Kachemak Bay area, and two discrete facies of graywacke in the McHugh Complex in the Knik Arm–Turnagain Arm area; an inner facies of Early Cretaceous age, and an outer facies of Late Cretaceous age. The ages, compositions, and structural features of these facies help to constrain the timing for three episodes of accretion of the McHugh Complex regionally, including (1) accretion associated with Early Jurassic high pressure (blueschist grade) metamorphism of rocks in tectonic panels along the farthest inboard margin (Roeske *et al.*, 1989; Clift *et al.*, 2005), (2) accretion of a central mélange facies constrained by the ages of late Early Cretaceous 125 to 120 Ma intrusions (Amato and Pavlis, 2010), and (3) accretion of a massive graywacke and conglomerate facies later than early Late Cretaceous, constrained by youngest detrital zircon ages of 84 to 91 Ma (Amato and Pavlis, 2010).

Detrital zircon ages also provide some information about provenance and the timing of juxtaposition of various sources that contributed to the McHugh Complex. Sandstones from the Early Cretaceous melange facies of the McHugh Complex do not have ages older than Mesozoic, supporting their association with the oceanic Talkeetna and Chitina arcs of the Peninsular–Wrangellia terrane; detrital zircons from the early Late Cretaceous graywacke facies of the McHugh Complex include zircons that have Paleozoic and Precambrian ages, suggesting that a connection with an inferred North American Coast Mountains orogen source was established by the Late Cretaceous (Amato and Pavlis, 2010).

Limestone in the McHugh Complex typically occurs as tectonic blocks or severely extended strings of boudins. In the Seldovia Quadrangle, Permian fusulinids and conodonts have been recovered from several blocks (Stevens *et al.*, 1997; B. Wardlaw and A. Harris, written commun., 1994). The fusulinids and conodonts are of shallow-water, tropical, Tethyan affinity; the fusulinids are quite distinct from those found in the Wrangellia terrane. Along Turnagain Arm, limestone occurs as centimeter- to meter-scale lenses and blocks in the argillite matrix mélange; one limestone lens in argillite contained radiolarians of 'probably Early Cretaceous' age (C.D. Blome, USGS, written commun. 1988). A limestone clast in conglomerate of the younger graywacke and conglomerate facies contained conodonts of Late Mississippian to Early Pennsylvanian age (Nelson et. al., 1986).

A depositional model (fig. 1.2.4) developed by Connelly (1978) for the Uyak Complex, an equivalent of the McHugh Complex on Kodiak Island, shows inferred depositional relationships of the various rock types before they were chaotically deformed in the mélange. According to this model, the McHugh basalts were formed at seafloor spreading centers, the overlying cherts were deposited on the flanks of spreading centers and on seamounts on oceanic crust that was conveyed toward a trench, and the argillite and graywacke record deposition on the downgoing plate in and near the trench, just prior to subduction-accretion. The range of ages of chert that depositionally overlies basalt in the McHugh Complex, and the NMORB and EMORB chemistry of much of the basalt (Nelson and Blome, 1991), supports the model of production of basalt over time at an oceanic spreading center. In addition to the oceanic-plate component, it is likely that parts of the McHugh Complex were deposited on the overriding plate, for example, on the inner trench slope, at the toe of the accretionary wedge. In the accretionary wedge, slope facies rocks are tectonically mixed with fault slivers of oceanic-plate rocks, some of which may have been faulted away from the downgoing plate in the trench, and some of which may have been partly or deeply subducted and brought back up into the accretionary wedge along thrust faults. The timing of subduction-accretion is not well known, but accumulated age data suggest it apparently spanned Late Triassic to early Late Cretaceous time, and was punctuated by at least three episodes of change in tectonic style (Clift *et al.*, 2005; Hacker *et al.* 2008; 2011; Amato and Pavlis, 2010). The initiation of subduction is inferred from latest Triassic to Early Jurassic magmatic ages of the Talkeetna arc in the upper plate (Hacker *et al.*, 2008; 2011), and Early Jurassic ages for a discontinuous belt of high-pressure metamorphic rocks lies along the inboard margin of the McHugh Complex (Roeske *et al.*, 1989; Bradley *et al.*, 1999; Pavlis and Roeske, 2007). In terms of the Connelly (1978) model, basalt-ribbon chert blocks in the McHugh Complex might represent spreading center or seamount deposits, and some

of the limestone blocks associated with the greenstone might represent the tops of seamounts that were decapitated at the subduction zone. Argillite interbedded with graywacke or chert, and graywacke interbedded with chert might represent trench and slope deposits that were tectonically interleaved with ocean floor deposits by accretionary processes.

Valdez Group

The outboard, or seaward part of the Chugach terrane is underlain by the Valdez Group of latest Late Cretaceous (Campanian? to Maastrichtian) age. Age control is based on the ages of inoceramid bivalves, which constitute monospecific assemblages of *Inoceramus kusiroensis* of Late Maastrichtian age at 15 localities in the Chugach Mountains (Jones and Clark, 1973). The Valdez Group includes medium- and thin-bedded graywacke turbidites (fig. 1.2.3D), black argillite, and minor pebble to cobble conglomerate. Sandstones of the Valdez Group are moderately well sorted, and consist mostly of angular grains of quartz and feldspar, volcanic rock fragments, and rare chert. Microcline, mica and coarse monocrystalline quartz indicate a component of plutonic provenance (Dumoulin, 1987; 1988). Point counts of sandstones from the Valdez Group yielded QFL ratios of 15.5-35-49.5 for the western Prince William Sound area, and 26.5-38.5-35 for the central Prince William Sound area, which plot in the arc-orogen field on the provenance discrimination diagram of Dickinson and Suczek (1979) (Dumoulin 1987; 1988). Graywacke of the Valdez Group contains abundant quartz and feldspar relative to lithic (volcanic, chert, and argillite) clasts, in contrast to graywacke in the McHugh Complex. Detrital zircons from a Valdez Group sandstone collected at a locality west of Indian on the north side of Turnagain Arm yielded seven U-Pb ages between 69 and 80 Ma, indicating a maximum latest Cretaceous depositional age (Bradley *et al.*, 2009). A sample collected on the south shore of Turnagain Arm east of Hope contains detrital zircons that yielded a dozen U-Pb ages between 65 and 68 Ma (S.M. Karl and Paul O'Sullivan, unpub. data), at a locality that also has inoceramid bivalves, and adjacent to a new fossil locality that contains a bed of "*Inoceramus" kusiroensis* (W.P. Elder, USGS, retired, written commun., 2009), also indicating a latest Cretaceous age of deposition. In the Seldovia quadrangle, one conglomerate clast of an intermediate plutonic rock yielded a U-Pb SHRIMP zircon age of about 223 Ma (Bradley et. al., 2009), an age that contributes information for inferences about provenance. Detrital zircons from sandstones of the Valdez Group include zircons that have Paleozoic and Precambrian ages, suggesting North American sources (Bradley *et al.*, 2009; Amato and Pavlis, 2010). Most of the Valdez Group consists of relatively coherent strata that were deformed into regional-scale tight to isoclinal folds, and cut by a slaty cleavage. The Valdez Group was probably deposited on the outer forearc slope and deep-sea trench (Nilsen and Zuffa, 1982), and accreted prior to the intrusion of the Crow Pass and similar age granitic stocks around 55 Ma in age that cut penetrative regional fabrics in rocks of the Valdez Group.

The McHugh Complex and Valdez Group are juxtaposed across a regional-scale thrust fault, which in the area of Turnagain Arm is called the Eagle River Fault. Beneath the fault is a mélange of partially to thoroughly disrupted Valdez Group turbidites. This mélange of slate and graywacke, which is quite distinct from the lithologically diverse mélanges of the McHugh Complex, can be traced for hundreds of kilometers in the footwall of the Eagle River fault and its along-strike equivalents (Kusky, Bradley, Haeussler, and Karl, 1997).

Resurrection Peninsula Ophiolite

A nearly complete ophiolite section is exposed on the Resurrection Peninsula (fig. 1.2.5). From east to west, base to top, the igneous sequence consists of: (1) gabbro, minor plagiogranite, and local pods of ultramafic rock, (2) sheeted dikes, and (3) pillow basalt (fig. 1.2.5); original stratigraphic tops are to the west. Siliciclastic sedimentary rocks interbedded with the pillow lavas suggests the spreading center was relatively near a continental source (e.g., Bol *et al.*, 1992). The age of the ophiolite is interpreted to be 57 Ma based on a U-Pb zircon age from plagiogranite (Nelson *et al.*, 1989). Serpentinized peridotite and pyroxenite occur as pods in the gabbro and, on the east side of the peninsula, as fault-bounded slices in Valdez Group flysch. Dikes and small plugs of plagiogranite intrude the upper parts of the gabbro. The Resurrection Peninsula ophiolite lacks a tectonized peridotite basal section, which would complete the classic ophiolite sequence (Coleman, 1977). Rocks of this mafic–ultramafic complex have undergone ocean floor metamorphism, which is typical of ophiolite sequences (Coleman, 1977), and is

marked by low greenschist facies minerals and the absence of penetrative fabric. The contact between the Resurrection Peninsula ophiolite and the surrounding sedimentary rocks is demonstrably a thrust fault on the northeast (Miller, 1984; Nelson, Miller, and Dumoulin, 1987; Nelson *et al.*, 1989), but the western contact with sedimentary rock is problematic (see below).

The ultramafic rock of the Resurrection Peninsula ophiolite is almost entirely serpentinized. It occurs as pods and small bodies in the gabbro, and as fault-bounded slices in the Valdez Group (figs. 1.2.5; 1.2.6A). In most places enough relict texture and mineralogy remains to recognize original clinopyroxenite, dunite, and harzburgite in thin sections (Miller, 1984). The irregular pods within the gabbro range from a few meters to a few tens of meters across. In the Valdez Group, the serpentinized rock occurs along more linear trends, and has slickensides and fractures that are locally filled with calcite (Miller, 1984). As pointed out by Tysdal *et al.* (1977), the exposure is poor in the northeastern part of the mafic sequence, and the ultramafic rock may be more abundant than shown on the map.

The gabbro occurs as two distinct bodies (herein referred to as the eastern gabbro and the western gabbro) that are separated by a fault-bounded block of interbedded volcanic and sedimentary rocks of the Valdez Group. Locally, well developed, west-dipping magmatic mineral layering occurs in the structurally lowest part of the western gabbro (Miller, 1984). The alternating light- and dark-gray layers reflect different proportions of pyroxene and feldspar. The layered gabbro grades westward into massive gabbro containing an increasing percentage of mafic dikes which then grades westward into the sheeted dike unit. Typical exposures consist of medium- to coarse-grained, subophitic clinopyroxene gabbro; plagioclase ranges from about An_{60-70} (optically determined). The clinopyroxene is always at least in part altered to actinolite plus chlorite (uralitized); the plagioclase is sericitized, and secondary epidote is common (Miller, 1984). Stratigraphically higher in the succession, primary hornblende gabbro (plagioclase composition of about An_{55}) crops out, and pods and dikes of hornblende-bearing plagiogranite are present. The largest exposure of plagiogranite is near the north entrance to Killer Bay (fig. 1.2.5, Stop 15; fig. 1.2.6B). At this location, a 20-m-wide stockwork zone of light-gray hornblende plagiogranite intruded gabbro. In a zone extending at least 3 km to the north, other small dikes and pods of plagiogranite intrude the gabbro unit. The plagiogranite is fine- to medium-grained and contains about 15 percent green hornblende that is slightly altered to actinolite and chlorite. Other constituents include sodic plagioclase, quartz, and intergrain alteration minerals such as epidote and prehnite (Miller, 1984). In a few places, prehnite occurs in veins 1–2 mm wide, cutting both the plagiogranite and the country rock. Also, mafic dikes become more numerous stratigraphically higher in the gabbro. They range from 10–50 cm in width and consist chiefly of fine-grained diabase containing primary hornblende altered to actinolite plus chlorite, plagioclase microlites with brown cryptocrystalline alteration, and interstitial very-fine-grained epidote or sphene (Miller, 1984).

Petrographic characteristics indicate that the eastern gabbro body was originally part of the same sequence as the western gabbro, but was stratigraphically lower. The eastern clinopyroxene gabbro does not show mineral layering in outcrop (perhaps due to poor exposure), but it has a cumulate texture. In addition, more pods of ultramafic rock are found in the eastern gabbro than in the western gabbro. These aspects, along with the lack of a trend of increasing basaltic dikes and the lack of plagiogranite, would place the eastern gabbro lower in an idealized ophiolite section than the western gabbro (Miller, 1984). Therefore, the sense of displacement between the two gabbro bodies is inferred to be up to the east.

The gabbro complex grades westward into sheeted dikes that form the rugged crest of the central part of the peninsula (fig. 1.2.6C). The dikes generally trend north–northwest to north–northeast and generally dip steeply to the east, although at the southern end of the peninsula, the dikes trend west–northwest. Cross-cutting dikes locally intrude pre-existing dikes at low angles. Most dikes range in thickness from 30 cm to 1 m, and one-sided chilled margins indicate sheeted intrusion. Aphanitic, porphyritic, and diabasic textures are common. Low-grade metamorphic assemblages are displayed and include actinolized clinopyroxene, brown-altered plagioclase, interstitial chlorite and epidote, and occasional veins of prehnite (Miller, 1984). The sheeted dikes grade westward to pillow basalt through a mixed zone of increasing pillow screens and volcanic breccia.

Pillow basalt and subordinate massive basalt and broken-pillow breccia make up most of the western flank of the Resurrection Peninsula. The pillow basalt forms a west-dipping sequence and contains minor interbedded siltstone; strike is approximately north and dips are 30–45° to the west. Discrete pillows average 0.5 m in diameter; beautifully preserved forms include long, thin pillows, tubes, and stubby and budded pillows (fig. 1.2.5, Stop 9; figs. 1.2.6D; 1.2.6E). Interpillow spaces are locally filled with red and green chert (lacking radiolarians). In thin section the pillows show axiolitic and glassy textures indicating rapid cooling. Amygdules are filled with secondary chlorite, zeolites, and in some places epidote; prehnite veins are sparse (Miller, 1984). Siliceous siltstone is locally interbedded with the pillow lavas and shows clay alteration of detrital grains, consistent with the low pressure, hydrothermal, ocean floor metamorphism of the ophiolite sequence (Miller, 1984). Trace-element abundances from basalts of the Resurrection Peninsula ophiolite and related ophiolites in Prince William Sound are broadly MORB-like but show some enrichment in incompatible elements (Lytwyn *et al.*, 1997; Nelson and Nelson, 1993; Crowe *et al.*, 1992). These trends can be explained in terms of contamination of normal MORB with sediment in a near-trench setting. A paleomagnetic study suggested that when it formed (1) the ophiolite was 13 ± 9° south of its present position with respect to cratonic North America, and (2) the strike of the ridge was about 026 ± 12° (Bol *et al.*, 1992, but see Haeussler, Bradley, Wells, and Miller, 2003).

We now turn to the contact relationships between the ophiolite and adjacent largely sedimentary rocks. As stated previously, the northern and northeastern contact (fig. 1.2.5) is clearly a thrust fault separating the 57 Ma ophiolite from the 70–65 Ma Valdez Group (Miller, 1984; Nelson *et al.*, 1989). The western contact is problematic and interpreted as either depositional or faulted. Tysdal and Case (1979) thought the contact was depositional and that both the ophiolite and a purportedly capping sedimentary section were Cretaceous in age and part of the Valdez Group. Kusky and Young (1999) also interpreted a depositional contact on the west side, but given the 57 Ma age of the ophiolite, they regarded the sedimentary section as late Paleocene to early Eocene and named these rocks the "Humpy Cove Formation" of the Orca Group[3]. Noting a significant difference in metamorphic grade across this boundary, Miller (1984), Nelson, Miller, and Dumoulin, (1987), and Nelson *et al.* (1989) interpreted this same contact as likely a fault separating Valdez Group from the ophiolite. The contact itself can be most closely approached in Humpy Cove (fig. 1.2.5, Stop 10). Here, Kusky and Young (1999) reported that turbidites overlie the pillow basalts; however, cleavage along this contact obliterates bedding and leaves open a fault interpretation (Miller, 1984). All workers agree that some siliciclastic rocks are demonstrably interbedded with the pillow lavas; the question is how much original sedimentary section is preserved above the pillow lavas—a minor amount, or ~2.5 km as suggested by Kusky and Young (1999)?

Fox Island[4], which lies a few kilometers west of Resurrection Peninsula (fig. 1.2.5, Stop 11), is a key area for interpreting the purportedly capping sedimentary rocks. On the east side of the island a cliff exposure shows varicolored units of interbedded tuff and siltstone (fig. 1.2.6F). These rocks are metamorphosed to biotite zone of greenschist facies, or approximately middle greenschist facies (Miller, 1984). Although metamorphosed and locally semischistose, original protoliths are easily identified as silty argillite, sandy siltstone, tuff, and rare flows or sills. On the west side of the island metasandstone and metavolcanic rocks are strongly semischistose and of even higher metamorphic grade. The metasandstones show abundant syndeformational secondary biotite, lesser muscovite, and minor chlorite, indicating metamorphic grade well into the upper greenschist facies (Miller, 1984). The metavolcanic rocks have secondary mineral assemblages consisting of hornblende, plagioclase, and minor biotite, indicative of amphibolite facies metamorphism (Miller, 1984). The metamorphic grade displayed in the rocks of Fox Island is distinctly higher than that of the ophiolite and its demonstrably interbedded sedimentary rock, but is completely consistent with that displayed by Valdez Group rocks on trend to the north of the Peninsula.

---

[3] *As further support of their conclusion that the rocks on the west are not Valdez Group, Kusky and Young (1999) cited the work of Dumoulin (1988), who reported that the Valdez Group sandstones of the "Resurrection Peninsula area" differed from most Valdez Group samples in that they were finer grained, better sorted, and had higher feldspar content. The "Resurrection Peninsula area" samples cited by Dumoulin (1988) were from northeast of the mafic complex, not from the problematic strata, hence have no bearing on Kusky and Young's argument.*

[4] *The island is variously known as Fox Island and Renard Island, the French name for fox. The U.S. Geological Survey uses the latter name on its topographic maps.*

Fox Island may also provide evidence bearing on the emplacement of the ophiolite, but this too is controversial. Kusky and Young (1999) mapped a shear zone on the west side of Fox Island (fig. 1.2.5), which in their view separates Cretaceous Valdez Group on the west from the purported ophiolite cover rocks on the east. They documented a west-over-east shear sense and argued that the ophiolite was emplaced into the accretionary prism along this structure. This interpretation rests on two others: (1) that the rocks to the west of the shear zone are Cretaceous Valdez Group, and (2) that rocks to the east depositionally overlie the ophiolite. Extrapolating offshore to the south, they interpreted this shear zone to be intruded by the 53.4 Ma (Bradley, Parrish, *et al.*, 2000) granodiorite of Hive Island (Kusky and Young, 1999)—something that is not self-evident from the map pattern (fig. 1.2.5). Thus they bracketed the emplacement of the ophiolite into the accretionary prism between 57 Ma and 53.4 Ma. These numbers fed, in turn, into conjectures about the travel distance of the ophiolite from an original location well to the south in the northern Pacific. All this rests, however, on the interpretation that the rocks of eastern Fox Island are the sedimentary cap of the ophiolite section, a concept that we question. Attempts to determine the age of these problematic strata by dating the tuffs have failed. We plan to next try U-Pb geochronology on detrital zircons from Fox Island sandstone, hoping to solve the dilemma; Paleocene zircons would support the Kusky and Young (1999) interpretation.

Near-Trench Intrusive Rocks

Early Cretaceous (~125–120 Ma) and Paleocene to early Eocene (~61–50 Ma) near-trench intrusive rocks are a key part of the tectonic history of the Chugach–Prince William composite terrane. Early Cretaceous plutons intrude mélange facies rocks of the McHugh Complex , are similar in age to high-T cooling ages in the metamorphic rocks, and are interpreted to represent near-trench plutonism derived from subduction of a spreading center in the Early Cretaceous (Clift *et al.*, 2005; Pavlis and Roeske, 2007; Amato and Pavlis, 2010; Hacker *et al.*, 2011). They do not form a well-defined belt because they are not widely dated and they have been dislocated by several generations of faults. The Paleogene Sanak–Baranof belt of intrusive rocks was recognized and named by Hudson *et al.* (1979). Intrusive bodies in the Sanak–Baranof belt range from narrow dikes to granitic batholiths as large as 10 by 100 km (figs. 1.2.7A, B). The plutons intrude turbidites and argillite that only a few million years earlier were being deposited along the trench axis. The Sanak–Baranof plutons show a remarkably smooth time-transgressive age pattern: from 61 Ma in the west to 51–50 Ma in the east, for some 2,200 km along strike (Marshak and Karig, 1977; Bradley *et al.*, 2003 and older references therein). For these and other reasons, the Sanak–Baranof plutonic belt is regarded as marking the site of a trench–ridge–trench triple junction, which migrated from west to east (e.g., Bradley *et al.*, 2003).

Metamorphism

A high-P, low-T metamorphic belt is the most landward part of the Chugach terrane. This metamorphism in Seldovia quadrangle to the southwest of Turnagain Arm has been dated at 191-192 Ma ($^{40}Ar/^{39}Ar$ white mica and amphibole, Bradley, Parrish, *et al.*, 2000), and 189 Ma ($^{40}Ar/^{39}Ar$ white mica, Sisson and Onstott, 1986) in the Chugach Mountains north of Turnagain Arm. The high-pressure belt is discontinuous and does not crop out on the field-trip transect. The McHugh Complex was regionally metamorphosed, presumably during subduction-accretion, to prehnite-pumpellyite facies. This metamorphism has not been directly dated, and may have occurred over a long period of time. The Valdez Group was regionally metamorphosed to low greenschist facies during the latest Cretaceous to early Paleocene, prior to emplacement of intrusive rocks of the Sanak–Baranof belt. As described above, the inferred Valdez Group units on Fox Island exhibit mid and upper greenschist facies conditions. The 61–50 Ma near-trench intrusive pulse was accompanied by contact metamorphism to cordierite grade, and by development of a few regional-scale, low-P, high-T metamorphic zones. The largest of these is the Chugach Metamorphic Complex east of Cordova (fig. 1.2.1; Pavlis and Sisson, 1995), but others are known as well (Roeske *et al.*, 1989; Bradley *et al.*, 2003; Hacker *et al.*, 2008; 2011).

Gold Mineralization

The Chugach terrane hosts hundreds of early Tertiary lode gold occurrences, prospects, and a few small mines (fig. 1.2.7C). The Kenai Peninsula has had a long history of mineral activity. The first report of gold was in 1848

when a Russian surveyor discovered gold in the Russian River area. Placer gold was mined by the Russians near Kenai Lake in the early 1850s (Jansons *et al.*, 1984). By the late 1800s placer gold miners were active in the Kenai Peninsula area and lode gold was subsequently discovered on the Kenai Peninsula, near Girdwood, in northern Prince William Sound, and near Valdez (Nelson and Miller, 2000). The first notable production came in 1911 from mines in the Falls Creek area (Jansons *et al.*, 1984). The most recent significant lode gold production from the region was in the 1930s and 1940s. Little or no production from lode gold deposits has taken place since 1956, but small-scale placer mining continues today. Over the nearly 100 years of mining, the northern Kenai Peninsula has produced ~133,800 oz. of placer gold and an additional 30,000 oz. of lode gold (Huber and Kurtak, 2001).

The gold-bearing veins occur along brittle faults that truncate accretion-related structures, mostly in the Valdez Group, but also rarely in the McHugh Complex (Haeussler, Bradley, and Goldfarb, 2003). Quartz, calcite, and ankerite are the typical gangue minerals, arsenopyrite is the most abundant sulfide, and tiny grains of native gold can still be found on many mine dumps. Goldfarb *et al.* (1986) invoked a regional-scale ore-forming process because the vein mineralogy, isotopic data, and fluid inclusion composition, salinities, and homogenization temperatures are consistent over a very wide area. The mineralizing fluids were most likely metamorphic in origin (Goldfarb *et al.*, 1986). The forearc setting of these gold occurrences is unusual, as forearcs are normally relatively "cold" places not noted for hydrothermal activity. $^{40}Ar/^{39}Ar$ dating of sericite from a number of gold mines has shown that mineralization took place at 57–53 Ma in the Kenai Peninsula area, continuing from 52–49 Ma in southeastern Alaska (Haeussler *et al.*, 1995). Near-trench gold mineralization thus was essentially coeval with the diachronous pulse of near-trench magmatism, and by implication, the two processes occurred in the same tectonic setting.

Ductile and Brittle Deformation

In the Knik Arm area, the age of an early phase of ductile deformation in high-P/low-T metamorphic rocks and syndeformational plutons at the base of the Talkeetna arc and structurally beneath it is thought to be Middle Jurassic based on isotopic ages of metamorphic minerals (Sisson and Onstott, 1986; Roeske *et al.*, 1989; Hacker *et al.*, 2011). Ductile deformation of the Early Cretaceous mélange of the Chugach accretionary complex, manifested by foliations warped around asymmetric and rotated phacoids and boudins in scaly argillite in the McHugh Complex, must be older than crosscutting late Early Cretaceous plutons (Pavlis and Roeske, 2007; Amato and Pavlis, 2010).

Later episodes of ductile deformation are recorded along the Border Ranges fault zone, which underlies the lowlands along the Kenai–Chugach mountain front. Initially a subduction-zone thrust separating the Talkeetna arc basement from the Chugach accretionary complex, the Border Ranges Fault was subsequently reactivated in multiple tectonic events (Pavlis and Roeske, 2007). The age of a major episode of ductile–brittle dextral faulting along the trace of the Border Ranges Fault is constrained by the age of Paleocene–Eocene strata of the Chickaloon Formation that are involved in the deformation (Little and Naser, 1989). The Border Ranges fault zone is currently occupied by a complex system of brittle faults locally superimposed on older ductile structures, with zones of hydrothermal alteration and intense cataclasis as much as 1,500 m in structural thickness, zones of intense faulting 3–5 km thick, and broad zones of faulting as wide as 30 km (Pavlis and Roeske, 2007).

Throughout southern Alaska, rocks of the Chugach terrane are pervasively cut by late brittle faults (Bradley and Kusky, 1990; Kusky, Bradley, and Haeussler, 1997) (fig. 1.2.7D). Along Turnagain Arm, these late faults include sets of: (1) dextral and sinistral strike-slip faults, (2) synthetic and antithetic thrust faults, and (3) synthetic and antithetic normal faults. The faults are typically spaced every few meters to tens of meters, and can be seen at most of the outcrops visited on this trip. The thrust faults shortened the wedge subhorizontally nearly perpendicular to strike; then, the somewhat younger normal and strike-slip faults extended the wedge nearly parallel to orogenic strike. The three fault sets are characterized by quartz + calcite + chlorite slickensides; curved slickenlines on some faults of each set reveal that displacement directions changed over time. We believe that this resulted from progressive changes (relative to the rocks, at least) in the orientation or magnitude of principal stresses during exhumation of the accretionary wedge, while the faults were active (Kusky, Bradley, and Haeussler, 1997). Although none of the brittle faults along Turnagain Arm have been dated, the similarity in their character with the gold–quartz veins suggests that they were active at the time of near-trench magmatism, at about 53–57 Ma (Haeussler,

Bradley, and Goldfarb, 2003). As noted above, most of the gold–quartz veins in the Chugach terrane—including those that have been dated—occupy strike-slip and normal faults that resemble the ones along Turnagain Arm.

Triassic to Cretaceous Tectonic Interpretations

The oldest fossil ages that are considered to represent depositional ages of sedimentary rocks in the forearc deposits of the McHugh Complex and the oldest magmatic ages in the overlying oceanic arc are Late Triassic (Nelson, Blome, and Karl, 1987; Hacker *et al.*, 2008; 2011), suggesting that subduction beneath an oceanic arc was initiated at that time. Blocks of Permian limestone in the accretionary complex are inferred to reflect the possibility of subduction of oceanic crust as old as Permian (Bradley *et al.*, 1999), but could also have been derived from the arc. A clast of Mississippian to Pennsylvanian limestone in Late Cretaceous conglomerate of the McHugh Complex (Nelson *et al.*, 1986) may have been derived from the arc, or may have been from another source, such as that represented by Paleozoic and Precambrian detrital zircons in the conglomerate (Amato and Pavlis, 2010). Most of the intrusive underpinnings of the Talkeetna oceanic arc have an Early Jurassic age coeval with high P/low T metamorphic rocks in the oldest dated panels of the McHugh accretionary complex, reflecting subduction zone processes (Pavlis and Roeske, 2007). The lack of younger ages for high-P metamorphism, subduction erosion of the forearc, and a lack of evidence for post-Middle Jurassic ductile deformation led Clift *et al.* (2005) and Pavlis and Roeske (2007) to infer a transition to a strike-slip-dominant tectonic setting during Middle Jurassic to Early Cretaceous deposition and deformation of the argillite-dominant mélange of the McHugh Complex. Cooling ages for high temperature metamorphic rocks, ductile deformation in the base of the arc, sinistral–oblique faults, and near-trench syntectonic plutons reflect a transition to Early Cretaceous subduction of a spreading center (Clift *et al.*, 2005; Pavlis and Roeske, 2007). A hiatus in arc plutonism and trench deposition in the mid-Cretaceous may reflect a strike-slip-dominated tectonic setting following Early Cretaceous ridge subduction. Late Cretaceous plutons in the arc indicate resumption of subduction (Clift *et al.*, 2005). Rejuvenation of uplift and voluminous sediment influx into the forearc and trench, represented by the massive early Late Cretaceous graywacke and conglomerate facies of the McHugh Complex (Amato and Pavlis, 2010) reflects a different tectonic setting than the sediment-starved Early Cretaceous argillite matrix mélange facies of the McHugh Complex. The transition may have been due in part to a collision with a backstop such as Wrangellia or North America (Clift *et al.*, 2005; Pavlis and Roeske, 2007). This interpretation is supported by the presence of a few Paleozoic and Precambrian detrital zircons recovered from Late Cretaceous graywacke of the McHugh Complex; pre-Mesozoic zircons are absent in the Early Cretaceous graywacke (Amato and Pavlis, 2010). Latest Cretaceous graywacke turbidites of the Valdez Group contain a more robust population of Precambrian detrital zircons, which are inferred to reflect proximity of the arc and accretionary complex to North American sources (Bradley *et al.*, 2009; Amato and Pavlis, 2010).

Cenozoic Tectonic Interpretations

The Paleocene and early Eocene history of the Gulf of Alaska margin can be best explained as the consequence of ridge–trench interaction, in which a spreading center between oceanic plates is subducted. The oceanic crustal "slabs" on either side of the subducted spreading center continue to spread beneath the overriding plate, forming an expanding "slab window" beneath the subduction complex. The Sanak–Baranof plutons were diachronously intruded along the entire ~2,100-km length of the accretionary complex, from ~61 Ma in the west to ~50 Ma in the east. Marshak and Karig (1977) postulated that it is difficult to envision a plausible mechanism, other than ridge subduction, for generating intrusions in a near-trench setting with such a large-scale trend in ages; alternative ideas have been discussed at length by Bradley *et al.* (2003). Other geologic effects of ridge subduction are shown in figure 1.2.8.

Global plate reconstructions imply that a spreading center was subducted somewhere along the western margin of North America during the early Tertiary (Atwater, 1989). Most of what is known about the ancient seafloor of the northwestern Pacific is from the mirror-image magnetic anomaly pattern embedded in surviving parts of the Pacific Plate. The magnetic stripes require that three oceanic plates existed (Pacific, Kula, and Farallon), that the Kula–Farallon Plate boundary was a ridge, and that this ridge must have trended toward the western margin of North America. The Sanak–Baranof near-trench plutonic belt thus might have marked the place where the Kula–

Farallon Ridge met the margin (e.g. Marshak and Karig, 1977; Bradley *et al.*, 1993) (fig. 1.2.9A). However, evidence for simultaneous ridge subduction in Alaska and Washington (fig. 1.2.9B) suggests a more complex plate geometry involving an additional ridge and thus a fourth oceanic plate (fig. 9C). We have called this the Resurrection Plate (Haeussler, Bradley, Wells, and Miller, 2003; Miller *et al.*, 2002) after the Resurrection Peninsula, possibly its largest surviving piece. The post-50-Ma history of ridge subduction has recently been discussed by Madsen *et al.*, (2006).

Cenozoic tectonic activity in the forearc region of the Aleutian arc commonly exploits older structures. The Cook Inlet forearc basin, between the volcanic arc and the accretionary complex, has a long, discontinuous history of sedimentation since Triassic time. Drilling and seismic reflection data indicate that high-angle normal faults define much of the northwest and southeast margins of Cook Inlet (Boss *et al.*, 1976). Faults on the southeast margin of Cook Inlet parallel the margin of crystalline basement that underlies the Aleutian arc, inferred from a pronounced, deep magnetic high and gravity low that underlie Cook Inlet (Grantz *et al.*, 1963; Burns, 1982; Pavlis and Bruhn, 1983; Saltus *et al.*, 2001; Bruhn and Haeussler, 2006). The steep front of the Kenai and Chugach Mountains on the southeast side of Cook Inlet is a forearc ridge bounded by down-to-the-northwest normal faults, locally including the Knik fault that follows the trace of the Border Ranges fault. The forearc ridge is postulated to result from uplift above the back of the accretionary wedge, where the accreted material is deeper than the brittle–ductile transition and can flow upwards against the backstop of the leading edge of arc basement (Pavlis and Bruhn, 1983). Uplift of the Kenai and Chugach Mountains is recorded by an unconformity beneath voluminous detritus of the Middle Miocene to Pliocene Sterling Formation on the Kenai Peninsula (Boss *et al.*, 1976; Flores and Stricker, 1993; Swenson, 1997). A sample of Early Cretaceous graywacke of the McHugh Complex on Turnagain Arm and a sample of latest Cretaceous graywacke from the Valdez Group on the Kenai River yielded apatite U-Th/He (AHe) ages of 22.0 ± 1.7 Ma and 19.9 ± 7.6 Ma, respectively (Buscher *et al.*, 2008), which supports a hypothesis of Early Miocene uplift of the Kenai–Chugach forearc ridge. These ages document the time that apatite in these rocks passed through a closure temperature of 50° to 90°C, or about 2–3 km depth at the local geothermal gradient (Buscher *et al.*, 2008). Farther outboard, a granite sample at Whittier and a graywacke sample at Seward yielded AHe ages of 14.9 ± 1.2 Ma and 13.5 ± 0.8 Ma, respectively, suggesting low long-term uplift rates of ~0.2 mm/a in this sector of the Aleutian forearc (Buscher *et al.*, 2008). The few data points do not elucidate whether uplift was steady or in pulses, but indicate very slow rates of uplift for the forearc region, about 0.1mm/year since the Miocene. On the north side of Cook Inlet, Haeussler *et al.* (2008) recorded three main pulses of uplift at about 35, 23, and 6 Ma, using apatite fission track (AFT) and apatite AHe dating in the Tordrillo Mountains; they attribute this uplift and folding of the Pliocene Sterling Formation to far-field effects of Yakutat microplate collision and flat-slab subduction beneath south-central Alaska.

Tertiary and Quaternary strata in Cook Inlet have been deformed into open, assymetric, and fault-cored folds that Haeussler *et al.* (2000) attributed to transpression. The folds are important structural traps of oil and gas in the Cook Inlet basin—the first petroleum province extensively developed in Alaska. Haeussler *et al.* (2000) also noted that in addition to the fault cored folds, tilted stratified glacial deposits on the northwest shore of Cook Inlet signify neotectonic activity. Although some of the tilted beds are chaotically deformed and now interpreted to represent submarine mass flow deposits that alternate with diamict layers (Reger, 2009), this section is disconformably overlain by peat that has a calibrated age of 14,304 ^{14}C yr B.P. Deformation of Pleistocene diamicts can be tied to folded Quaternary deposits in seismic sections that cross a structure on the floor of Cook Inlet near Granite Point (Haeussler *et al.*, 2000). Young structures in Cook Inlet oriented at a high angle to the Aleutian megathrust are interpreted by Haeussler *et al.* (2000) to result from forces pushing the forearc to the west, driven by the collision of the Yakutat block, which caused uplift at Denali and in south-central Alaska for the last 5 million years (Plafker *et al.*, 1992).

Glacial History

Several major glacial advances during the Pleistocene profoundly affected the landscape and Quaternary geology of the Cook Inlet trough. The earliest known glaciation in the Cook Inlet area is the only one to have deposited erratics on top of 4,396-foot-high Mount Susitna and was named the Mount Susitna glaciation, inferred to be as

old as early Pleistocene or late Pliocene (Karlstrom, 1964; Hamilton, 1994). The later Knik glaciation is considered to be middle Pleistocene in age based on the age of the Goose Bay tephra in the Goose Bay peat that overlies Knik till. Goose Bay tephras yielded a composite isochron $^{40}Ar/^{39}Ar$ age of 378 ± 0.67 ka (Reger *et al.*, 1996). Features formerly assigned to the Knik glaciation by Karlstrom (1964, pl. 6) are now known to be of Naptowne age (Reger *et al.*, 1996; 2007). Deposits correlating with the type Knik till at Goose Bay are not identified elsewhere in the upper Cook Inlet trough, so their extent is unknown.

Landforms in the southern Kenai lowlands and Caribou Hills show evidence of another extensive pre-late-Wisconsin advance, the Caribou Hills glaciation of Karlstrom (1964), which completely filled the Cook Inlet trough. Although the Caribou Hills glaciation was previously thought to precede the Knik glaciation (Karlstrom, 1964), evidence now shows that the Caribou Hills glaciation occurred later, probably in early Wisconsin time (approximately 80–50 ka; Reger *et al.*, 2007). The last major glaciation, locally referred to as the Naptowne (Karlstrom, 1964), occurred between about 30,000 and 11,000 years ago in the Cook Inlet region (Reger *et al.*, 2007). The maximum advance during the Naptowne glaciation was the oldest one, the Moosehorn stade, during which ice flowed southeastward from the Alaska Range across Cook Inlet and onto the Kenai lowlands, merging with ice flowing westward from the Matanuska Valley and Turnagain Arm to form a backstop to smaller glaciers flowing northwestward across the lowlands occupied by Skilak and Tustumena lakes (Reger *et al.*, 2007). The Moosehorn stade reached its maximum about 23 cal ka, blanketing most of the Cook Inlet trough with glacial ice, and retreated gradually by about 19 cal ka, based on the radiocarbon age of calcareous barnacle plates in the coastal bluff at Kenai (Reger *et al.*, 2007). The less extensive Killey stade began around 18.5 cal ka, based on radiocarbon ages of barnacle plates from the Bootlegger Cove Formation (Reger *et al.*, 1996), and ended around 17.5 cal ka (Reger *et al.*, 2007). Around that time, the glacier dam formed by Killey-age ice in the Nikiski area breached, allowing glacioestuarine waters to invade upper Cook Inlet, providing the environment for deposition of the Bootlegger Cove Formation there. Shortly thereafter, glaciers again advanced during the smaller, poorly dated Skilak stade, which ended before about 16 cal ka based on the age of peat at the bottom of a core from the Hidden Lake basin, which is dammed on the west end by three small end moraines of Skilak age (Reger *et al.*, 1996; Reger *et al.*, 2007). Skilak-age ice retreated up Turnagain Arm at least as far as Hope before 16.7 ka, dated by mollusks from the Bootlegger Cove Formation near Hope (Reger *et al.*, 1995).

The final Naptowne advance, the Elmendorf stade, began after about 16 cal ka, based on ages of shells from the Bootlegger Cove Formation below the Elmendorf moraine (Reger *et al.*, 1995). During the Elmendorf advance, ice extended down Knik Arm as far as the type Elmendorf moraine north of Anchorage, overriding Bootlegger Cove Formation and shedding outwash gravels over what is now downtown Anchorage. Elmendorf-age ice also extended down Turnagain Arm as far as the Hope area. The Elmendorf stade ended about 11 cal ka, based on the age of peat deposited against an end moraine that formed during a small advance in Turnagain Pass (Reger *et al.*, 1995; Reger *et al.*, 2007). Smaller glacial advances continued during the Holocene, culminating with the Little Ice Age advance in the late 18th to 19th centuries.

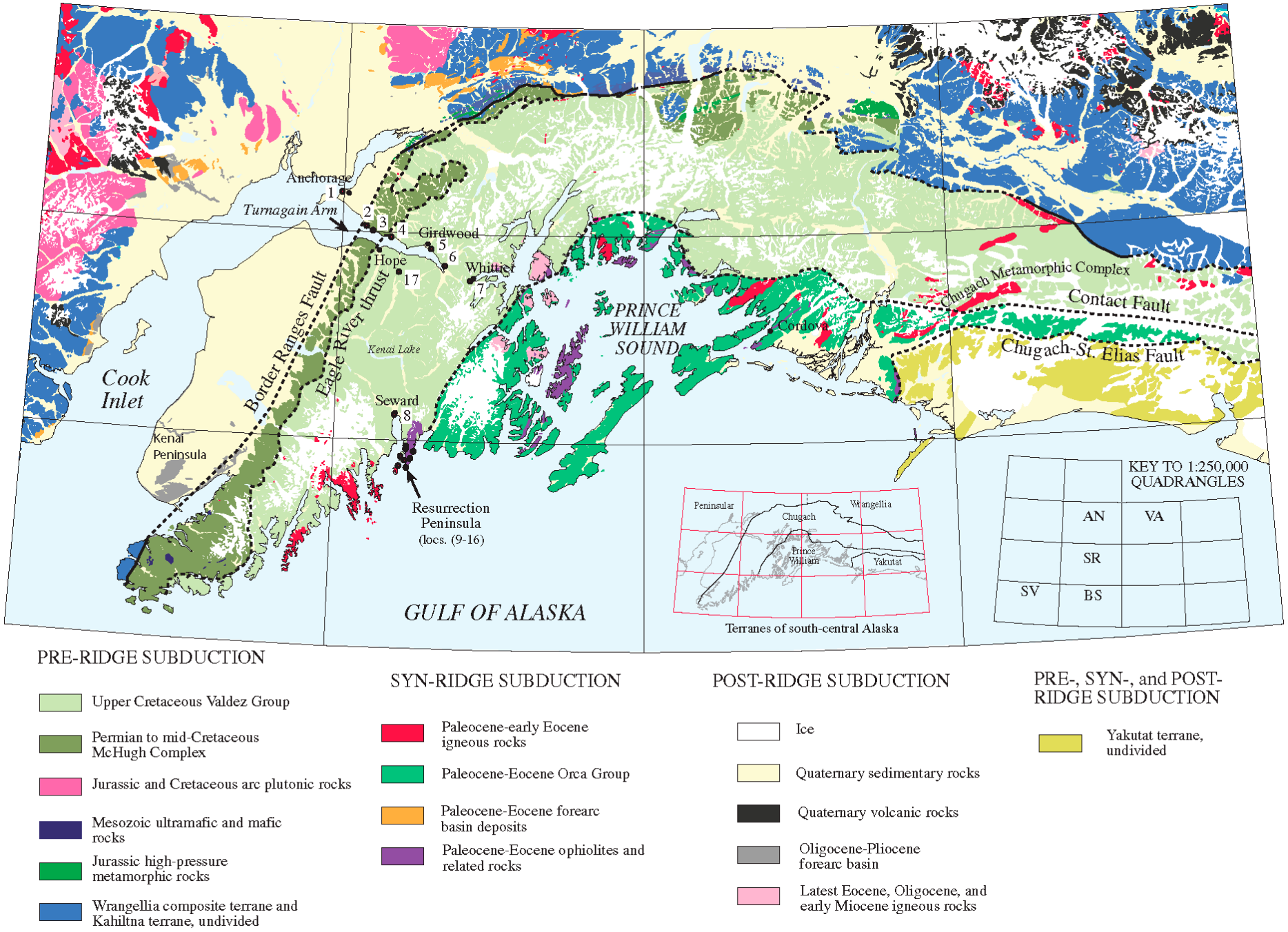

Figure 1.2.1. *Generalized geologic map of south-central Alaska, from Bradley et al. (2003) and sources cited therein. Numbers 1–17 are field trip stops. Abbreviations for 1:250,000-scale quadrangles: AN, Anchorage; BS, Blying Sound; SR, Seward; SV, Seldovia; VA, Valdez.*

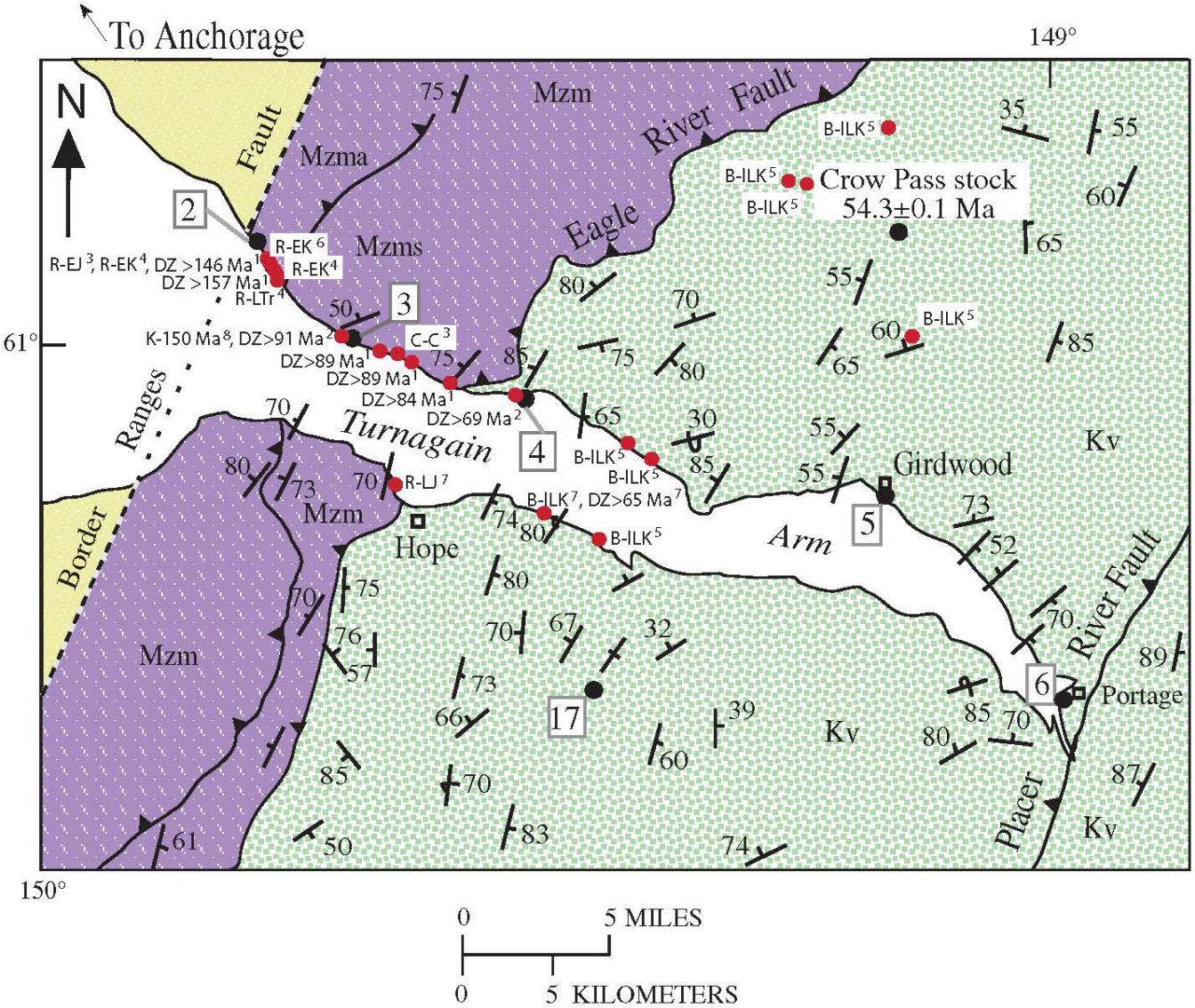

Figure 1.2.2. *Generalized geologic map of Turnagain Arm, south-central Alaska.*

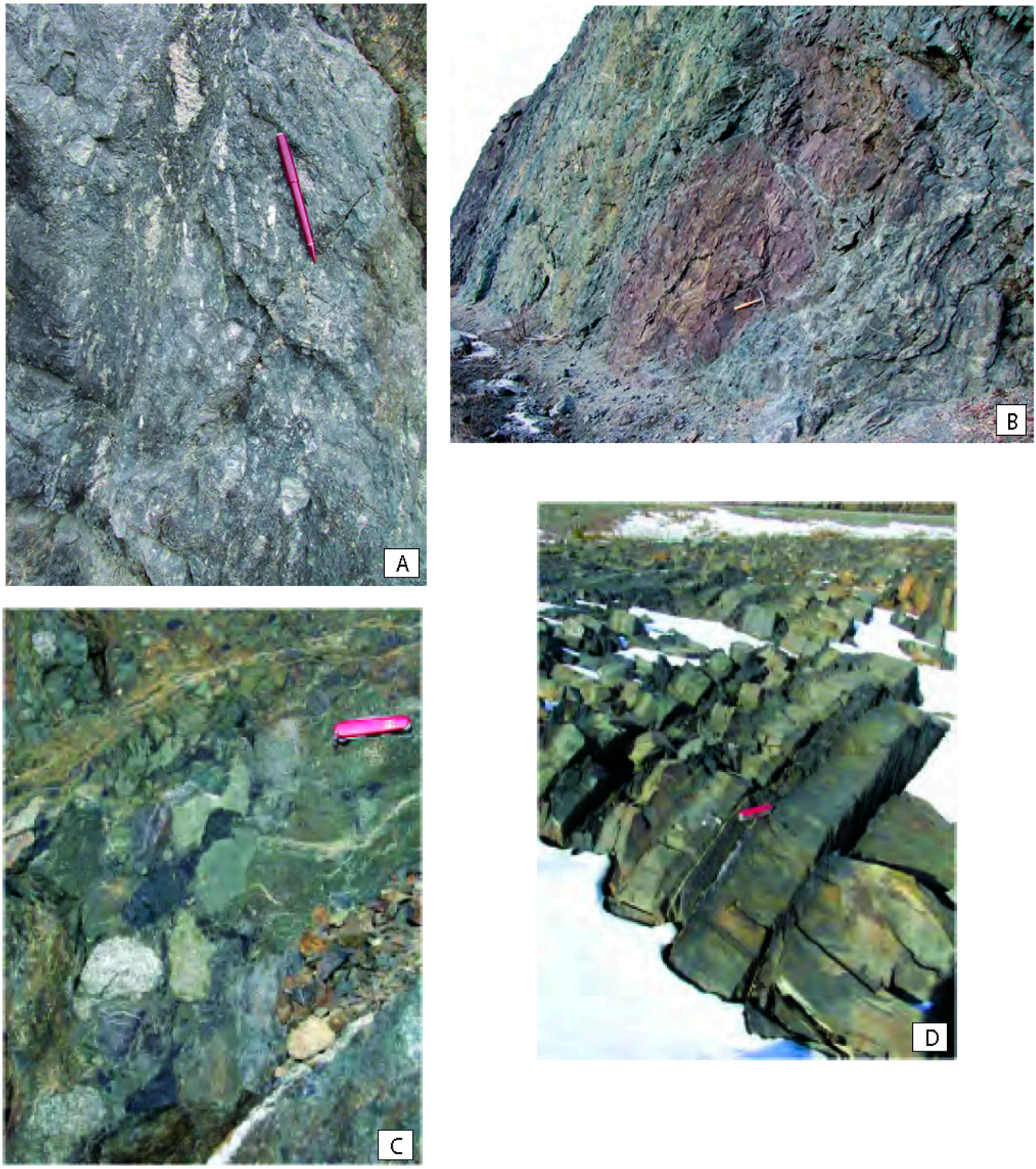

Figure 1.2.3. *Photographs of rocks in the McHugh Complex and the Valdez Group along Turnagain Arm.* ***A.*** *Rotated block of sheared mélange matrix in the McHugh Complex on the beach below the weigh station, Stop 2.* ***B.*** *Early Jurassic red and green radiolarioan ribbon chert on pillow basalt in the McHugh Complex 0.7 mile south of the weigh station.* ***C.*** *Assorted clasts in the conblomerate of the McHugh Complex at Beluga Point, Stop 3.* ***D.*** *Turbidites of the Valdez Group west of Indian, Stop 4.*

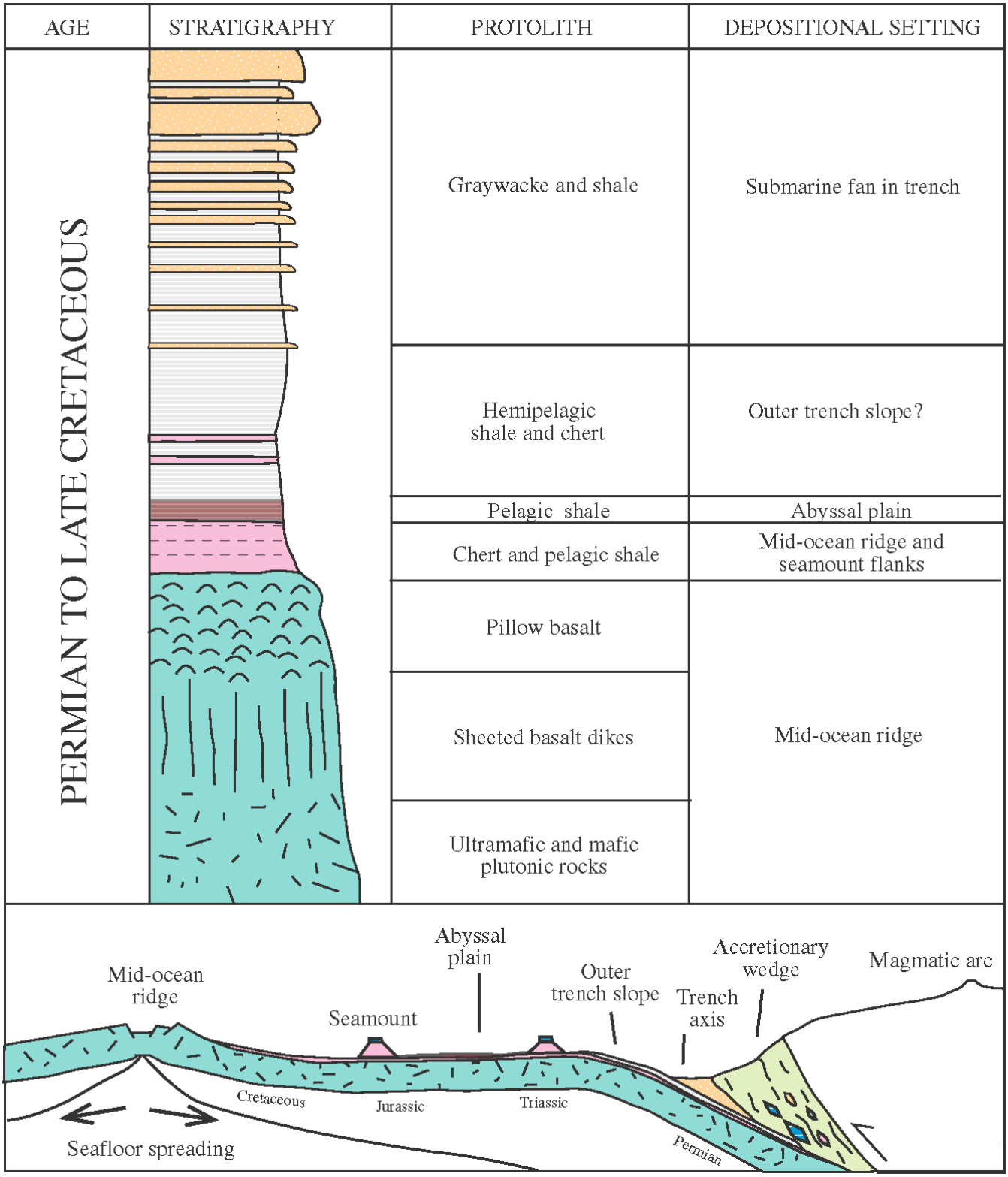

Figure 1.2.4. *Conceptual model for genesis of the diachronous igneous and sedimentary components of the McHugh Complex, modified from Connelly (1978). The presence of Permian limestones, interpreted as decapitated seamounts, requires that some of the subducted oceanic crust was Permian or older.*

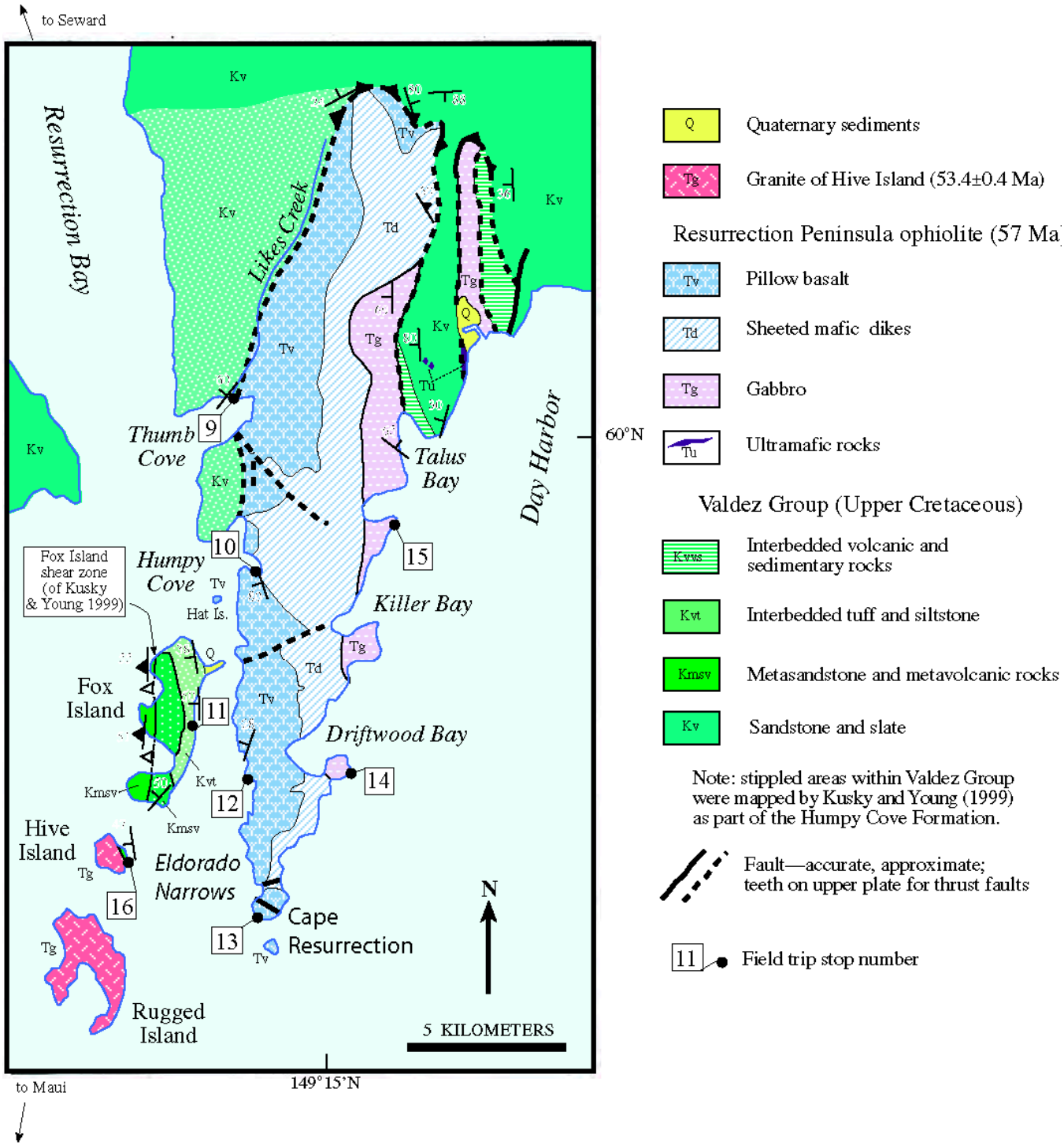

Figure 1.2.5. *Geologic map of the Resurrection Peninsula, from Miller (1984) and Nelson et al. (1989), including the Fox Island shear zone of Kusky and Young (1999).*

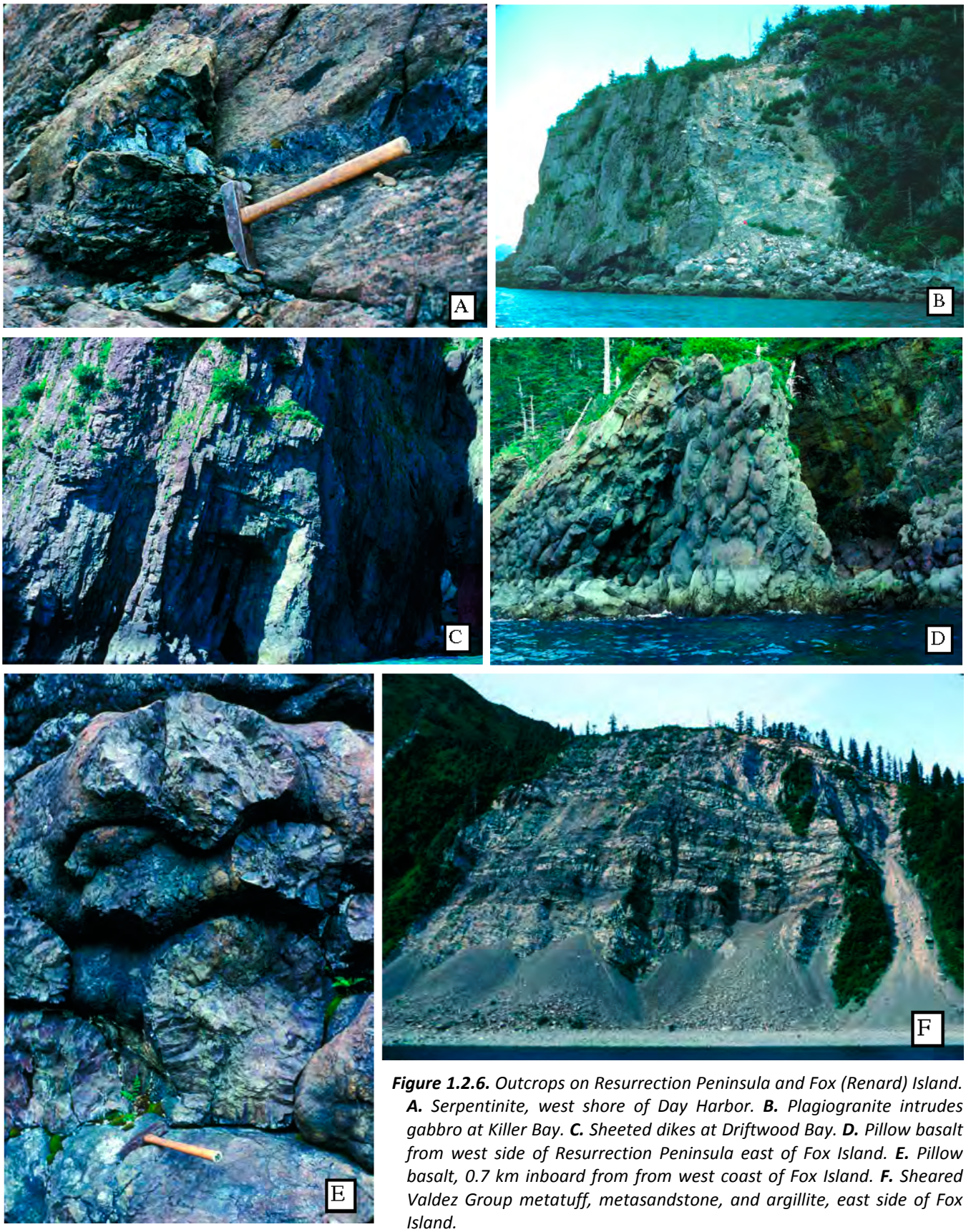

Figure 1.2.6. *Outcrops on Resurrection Peninsula and Fox (Renard) Island.* ***A.*** *Serpentinite, west shore of Day Harbor.* ***B.*** *Plagiogranite intrudes gabbro at Killer Bay.* ***C.*** *Sheeted dikes at Driftwood Bay.* ***D.*** *Pillow basalt from west side of Resurrection Peninsula east of Fox Island.* ***E.*** *Pillow basalt, 0.7 km inboard from from west coast of Fox Island.* ***F.*** *Sheared Valdez Group metatuff, metasandstone, and argillite, east side of Fox Island.*

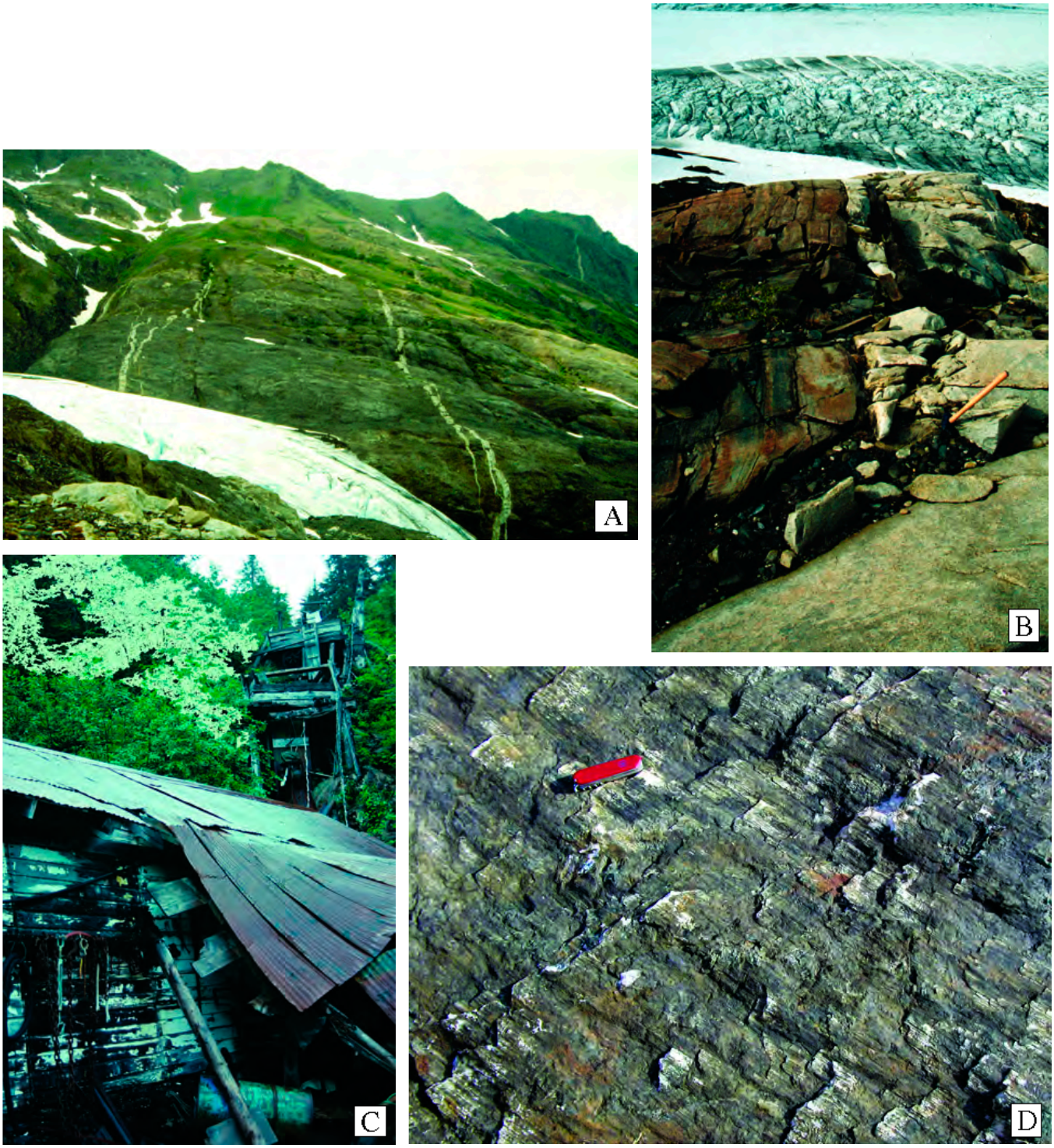

Figure 1.2.7. *Photographs of features attributed to early Tertiary ridge subduction.* ***A.*** *Dike swarm cutting McHugh Complex, Seldovia quadrangle.* ***B.*** *Chernof pluton, Seldovia Quadrangle.* ***C.*** *Beauty Bay gold mine, Seldovia Quadrangle. Mineralization is thought to be associated with near-trench magmatism; see text for discussion.* ***D.*** *Slickensided fault surface at Beluga Point, Stop 3, Turnagain Arm.*

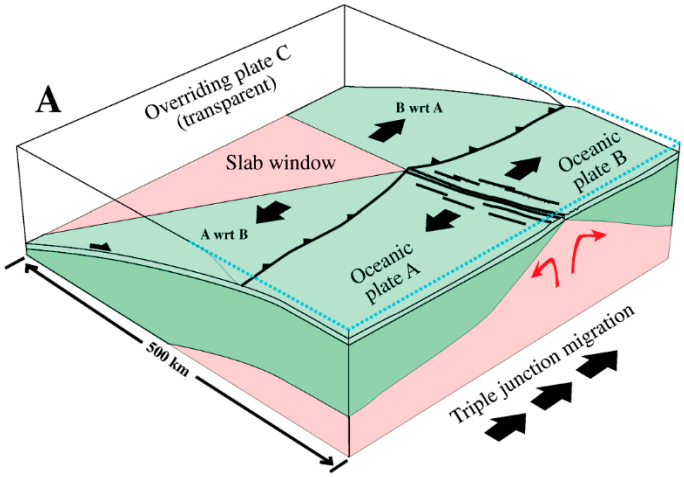

Figure 1.2.8. *Block diagrams illustrating the geologic effects of ridge subduction in south-central Alaska.* ***A.*** *The overriding plate has been rendered transparent to schematically show the opening of a slab window downdip of the spreading center. The gap between subducting, diverging slabs allows hot asthenosphere to come into contact with the normally cold base of the forearc. Beneath the arc axis, where dehydration reactions would ordinarily give rise to arc magmas, there is no plate to dehydrate and hence a gap in arc magmatism over the slab window, as shown in* ***B.***

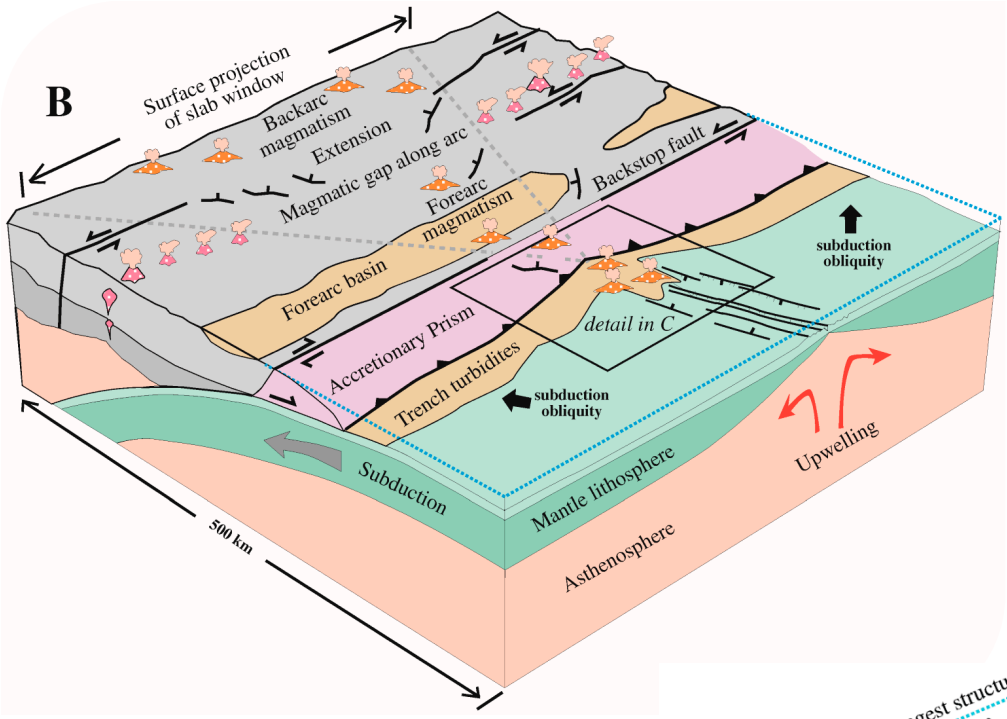

Figure 1.2.8.B. *Igneous activity along the arc just prior to the magmatic lull might perhaps be related to the thin, hot, trailing edge of the subducted plate or to the first interactions between slab-window asthenosphere and the base of the arc. Margin-parallel strike-slip faults are a response to oblique convergence that affects the upper plate differently on either side of the triple junction. Transtension drives subsidence of the forearc basin.*

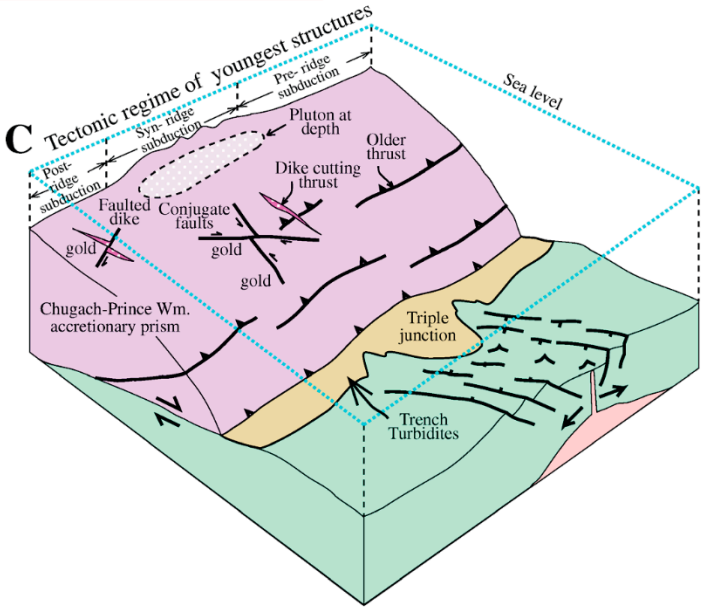

Figure 1.2.8.C. *In the triple junction area, ocean-floor basalts formed by seafloor spreading are interbedded with trench turbidites. Depending on bathymetric details, turbidity flows might either be funneled into or blocked from the axial valley of the ridge, and accordingly, both Besshi- and Kuroko-type massive sulfide mineralization are possible in the triple junction area. The presence of near-trench, forearc volcanoes is inferred by analogy with the Woodlark triple junction; only near-trench plutons and dikes remain at the crustal levels now exposed in Alaska. Brittle faults, some of them mineralized by gold-quartz veins, facilitate orogen-normal shortening (i.e. the narrowing of the prism) and orogeny-parallel extension.*

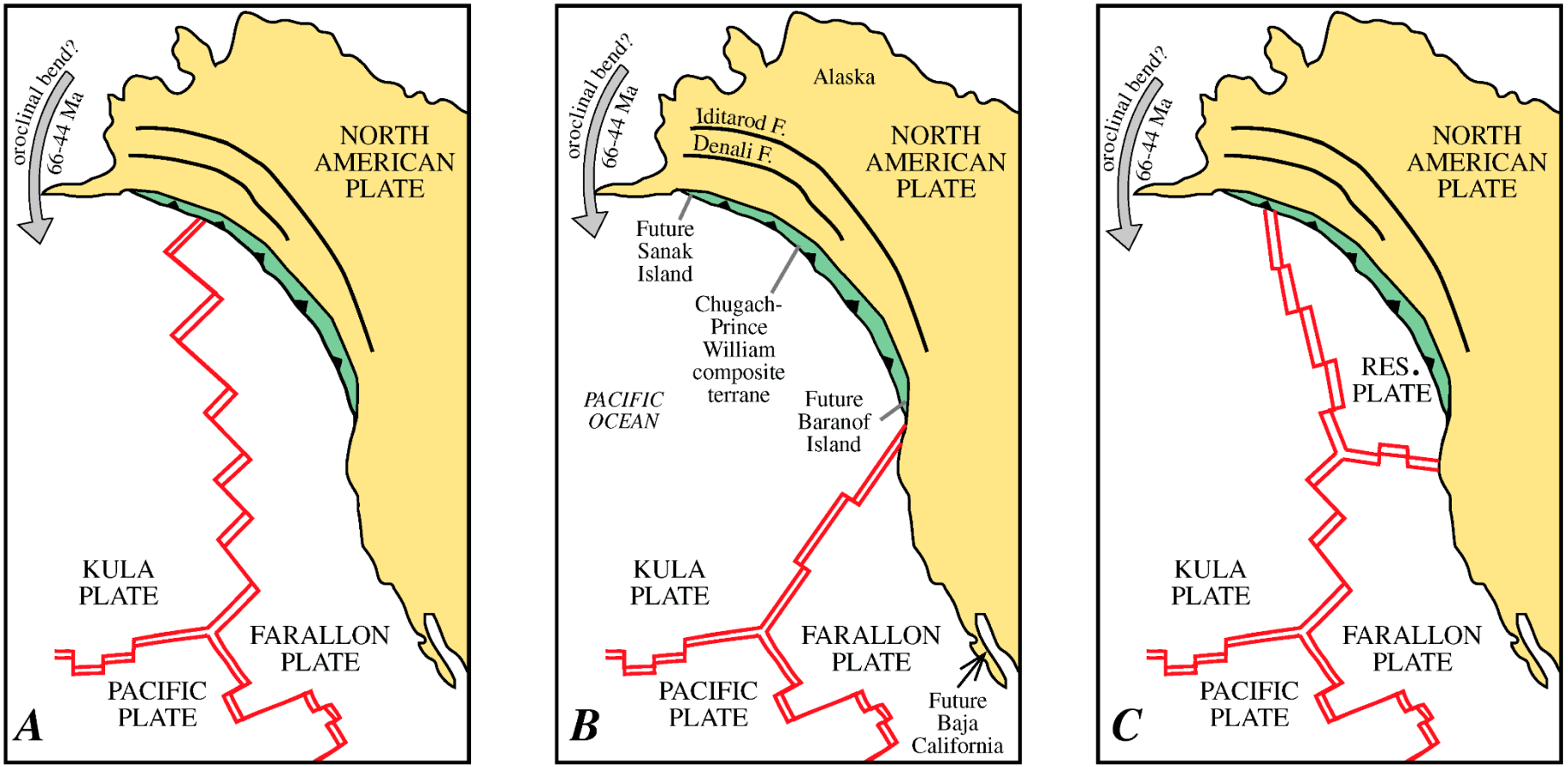

Figure 1.2.9. *Alternative plate models for 57 Ma.* ***A.*** *Kula–Farallon ridge subducted beneath Chugach terrane.* ***B.*** *Kula–Farallon ridge subducted beneath Washington.* ***C.*** *Preferred model: Kula–Resurrection was ridge subducted beneath the Chugach terrane while the Resurrection–Farallon ridge was subducted beneath Washington.*

CHAPTER 1.3

OCEAN VIEW

by Ian Shennan[5]

Ocean View is the name given to a large expanse of marsh to the south of Anchorage. It forms part of the Anchorage Coastal Wildlife Refuge that extends from Point Woronzof, near the airport, to Potter Creek, on the road south along Turnagain Arm. Estimates for land surface deformation in 1964 around Anchorage are in the order of 0.7 to 1.5 m co-seismic subsidence (Plafker, 1969). The range of coastal wetland environments make it a valuable site for the study of modern sedimentary processes and biota to aid interpretation of past environmental changes recorded in the sediment sequences.

The aims for this stop are:

❶ Introduce the "Nelson *et al.* (1996) criteria" for distinguishing between coseismic and nonseismic relative sea-level change.
❷ Outline the principles of using modern and fossil biological indicators to reconstruct elevation change.
❸ Introduce aspects of winter sedimentation processes.
❹ Summarize the paleoseismological evidence of great earthquakes recorded in the marsh sequences.

❶ In analyzing coastal sediment sequences, four critical criteria help determine a coseismic signal and discriminate from nonseismic processes that might cause abrupt wetland submergence or emergence: lateral extent of peat-mud couplets (subsidence) or mud-peat couplets (uplift) with sharp contacts; suddenness of subsidence or emergence; amount of vertical motion; and synchroneity with other sites (Nelson *et al.*, 1996). Presence of tsunami sediments may also help in certain geographic settings.

❷ Transfer functions use statistical regression methods to quantify the relationship between surface biological data collected from modern tidal flats, salt marshes, and acidic bogs and their associated elevation (m) relative to Mean Higher High Water (Hamilton and Shennan, 2005). In south-central Alaska we find that diatoms are the most ubiquitous microfossils preserved in sediments (fig. 1.3.1). Having established quantitative models to summarize the relationships between modern diatom assemblages and elevation we can apply the same models to reconstruct past elevation and elevation change from fossil diatom assemblages, also giving sample-specific error terms.

❸ In most winters, large volumes of ice cover the tidal flats at Ocean View and most marshes along Turnagain Arm (Hamilton *et al.*, 2005). For example, in 2002 we observed a 3-m-high ice dam 1,500 m out on the tidal flat at Ocean View that restricted tidal inundation landward (fig 1.3.2). Some high tides carry ice blocks onto the tidal marsh and, once melted, leave accumulations of melt-out sediment on the marsh surface. Silt cover on leaves and melt-out accumulations disperse quickly by rain and tides and seem to be part of the annual transport of sediment. We also observed slabs of sediment rafted by ice, transported onto the marsh, and colonized by marsh plants the following summer.

Diatom analysis of ice, melt-out sediment, and frozen surface sediment show that winter processes contribute to movement of diatoms from lower elevations in the intertidal zone to higher elevations, on both tidal flat and tidal marsh. There is no evidence in our analyses to suggest frozen sea ice brings in a distinct marine planktonic assemblage. All assemblages have good modern analogues with marsh or tidal flat samples. While our results clearly demonstrate the process of diatom (and sediment) movement, they do not reveal the relative magnitude compared to other processes contributing to a diatom assemblage, whether allochthonous or in situ. Widespread

[5] *Ian Shennan, Department of Geography, Durham University, Lower Mountjoy, South Road, Durham, DH1 3LE, United Kingdom.* *Ian.shennan@durham.ac.uk*

freezing and heaving of tidal flat sediment may just be one additional factor to tidal mixing over the rest of the year that together determine the resolution of diatom assemblages for reconstructing elevation.

Two particular processes may be important. Large blocks (fig. 1.3.2) of clastic tidal flat sediment can be transported onto the marsh by ice, become colonized by marsh vegetation, and incorporated into predominantly organic sediment. If these sediments were preserved then sampled in an investigation employing only a single core, they could be misinterpreted as indicating rapid relative sea-level change or coseismic subsidence during an earthquake. A systematic stratigraphic survey, as outlined in the criteria of Nelson *et al.* (1996) will prevent such a misinterpretation.

Although the majority of melt-out sediment is dispersed by rain and tides the ice transport process is important in transporting other allochthonous components onto marsh areas where ice blocks are particularly concentrated. In addition to tidal silt and clay fractions we observed transport of gravel, small cobbles, and organic elements ranging from large pieces of wood to degraded and decomposed herbaceous fragments, and also peat. This has important implications for radiocarbon dating different fractions of a sediment unit.

❹ Coring along three transects at Ocean View (Hamilton *et al.*, 2005) reveal up to five buried peat-silt couplets, labeled A through E (see fig. 1.3.3). A maximum of three buried peat layers are found at Shore Drive and up to five at Coral Lane. "Ghost forests" of dead spruce trees are most extensive in the Coral Lane area and extend west to transect 2 at Shore Drive. Exposures in creeks and shallow pits show that these trees are rooted in peat E. The upper herbaceous peat layer (peat E) is characteristically ~0.3 to 1.5 m thick and is typically found 0.2 to 0.6 m below present marsh surface. In contrast to most other studies, where a peat-silt couplet records coseismic subsidence, the upper contact of peat E along much of the Shore Drive transect is not sharp, but transitional over 5 cm. At OV-15 detectable levels of ^{137}Cs commence approximately 12 cm below the top of peat E and peak at the contact with the silt, indicating that burial coincided with the AD 1964 earthquake.

In summary, the marsh stratigraphy records (Shennan and Hamilton, 2006):

- The 1964 earthquake, with coseismic subsidence estimated as 0.67 ± 0.43 m at core 4 and -0.71 ± 0.31 at core 15;
- The penultimate earthquake ~850–900 cal yr BP with coseismic subsidence estimated at 0.23 ± 0.32 m, core 15;
- Earthquake ~1,500 cal yr BP, coseismic subsidence 0.99 ± 0.32 m at core 2 and 0.43 ± 0.30 m at core 23;
- Older sediments, peat A and peat B, do not indicate abrupt changes in elevation.

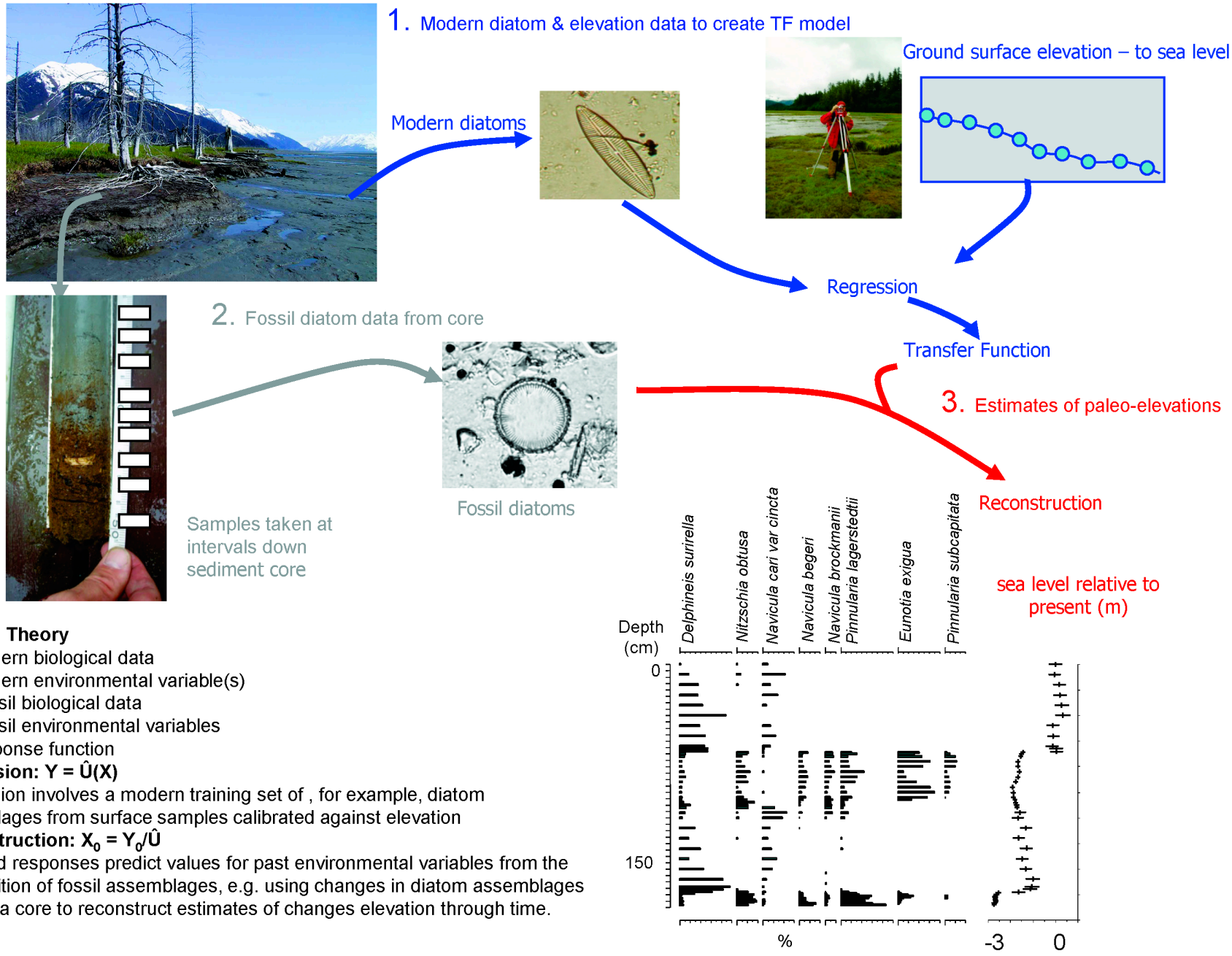

General Theory
Y = Modern biological data
X = Modern environmental variable(s)
Y_0= Fossil biological data
X_0= Fossil environmental variables
Û = response function
Regression: Y = Û(X)
Regression involves a modern training set of , for example, diatom assemblages from surface samples calibrated against elevation
Reconstruction: $X_0 = Y_0/Û$
Modelled responses predict values for past environmental variables from the composition of fossil assemblages, e.g. using changes in diatom assemblages through a core to reconstruct estimates of changes elevation through time.

Figure 1.3.1


A. Ocean View, April 5, 2002, from the public access point at the junction of Victor Road and Shore Drive
B. Ocean View looking SE towards the ghost forest and Turnagain Arm
C. Ocean View, ice heaves on tidal flat
D. Ocean View, ice dam, 1,500 m out on the tidal flat
E. Girdwood, April 10, 2002
F. Girdwood, ice block and rising tide
G. Girdwood; note gravel in silt melt-out
H. Girdwood, sediment block still intact in September, staff ~1.3 m.

Figure 1.3.2

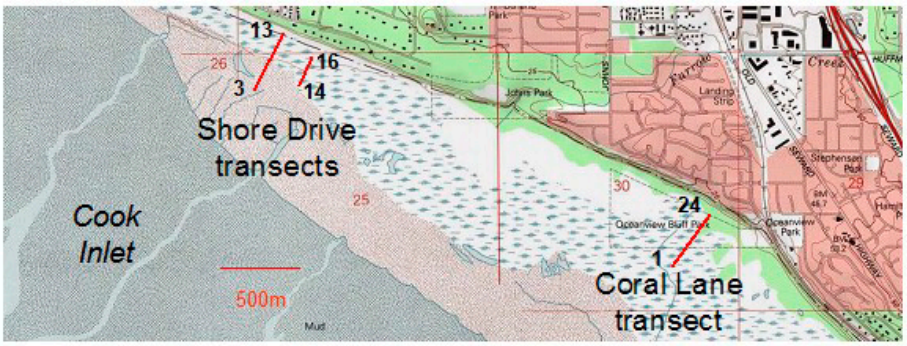

Map created with TOPO!™ ©2002 National Geographic Holdings (www.topo.com)

Peat
Silty peat
Silt
Diatoms counted
Diatoms prepared, none present

95% age ranges cal yr BP

Reconstructed elevation change, mean ± 2σ

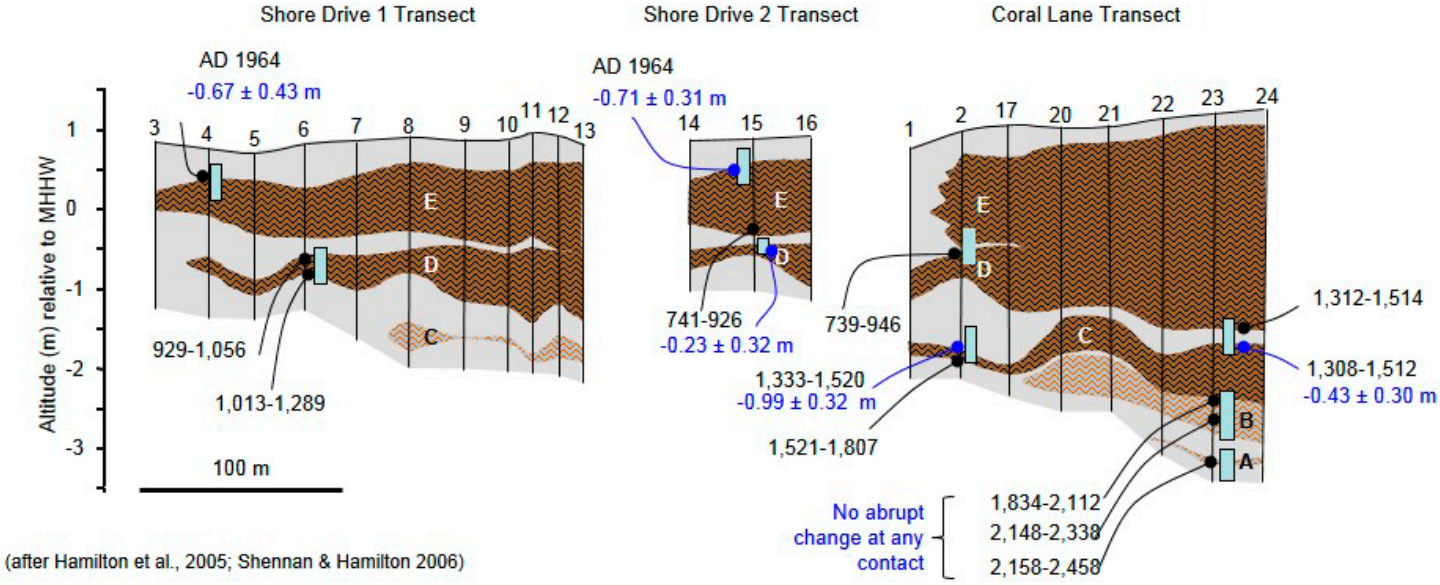

(after Hamilton et al., 2005; Shennan & Hamilton 2006)

Figure 1.3.3

CHAPTER 1.4

GIRDWOOD MARSH AND GHOST FOREST

by Ian Shennan[6] and Natasha Barlow[6]

Girdwood is probably the classic site in Alaska for recording multiple cycles of coseismic subsidence. Karlstrom (1964) provides one of the earliest descriptions and radiocarbon dates of the upper part of the sequence, but this was written before the 1964 earthquake during which there was ~1.5 m regional subsidence and up to ~0.9 m additional local subsidence of unconsolidated sediment (Plafker *et al.*, 1969). Combellick (1991) provided much of the impetus for later research, providing a key analogue used by Atwater (1987) in his seminal paper on the seismic hazard to the northwest coast of the Lower 48. Full details on discussion of the topics summarized can be found in recent publications (Barlow *et al.*, 2012; Hamilton and Shennan, 2005; Shennan *et al.*, 2008; Shennan and Hamilton, 2006).

The aims for this stop are:

1. Field stratigraphy that records marsh subsidence in 1964
2. Previous earthquakes and the concept of an earthquake deformation cycle model
3. Evidence for preseismic sea-level change
4. Glacial isostatic adjustment due to the Little Ice Age

This guide complements the description of the lithostratigraphic and chronostratigraphic evidence of late Holocene great earthquakes in the Cook Inlet region by Combellick and Reger (Combellick 1991, 1994; Combellick and Reger, 1994) and presents the biostratigraphy from one exposure at Girdwood. Full details and discussion can be found in recent publications (Hamilton and Shennan, 2005a,b; Hamilton *et al.*, 2005; Shennan *et al.*, 1999; Shennan and Hamilton, 2006; Zong *et al.*, 2003).

Late Holocene diatom stratigraphy at Girdwood

Sediment sequences beneath the present tidal marsh contain a record of potential earthquake cycles (fig. 1.4.1), with up to ten peat-mud couplets. Diatom analyses indicate no elevation change associated with couplets Z, B and C, and we do not attribute these to be the result of coseismic subsidence (fig. 1.4.2). For all couplets, the upper stratigraphic boundary of each peat is sharp, usually < 2 mm. Relative land-level changes through the last two peat-mud couplets are similar (fig. 1.4.3).

Accumulation of peat G, ~1,100 cal yr BP, reflects interseismic strain accumulation at the plate boundary causing gradual relative land uplift. In the upper 3 cm of peat G, diatom assemblages show land subsidence. The boundary between peat G and overlying silt represents coseismic subsidence during the penultimate great earthquake. Evidence of rapid marsh submergence following subsidence includes a buried peat layer with a sharp upper boundary that can be traced widely across the marsh and intertidal diatoms dominant in the overlying silt.

Interseismic recovery followed, with relative land uplift allowing development of peat H ~450 BP. Within peat H, a temporary increase in silt between 82 and 91 cm coincides with a temporary decrease in salt-intolerant diatoms and an increase in intertidal diatoms. A similar oscillation in diatom stratigraphy at Kenai indicates a regional rather than local-scale process. We suggest this is probably Little Ice Age expansion of ice fields, causing glacio-isostatic loading and deformation of the Earth's crust. Diatom assemblages indicate relative land subsidence in the upper few centimeters of peat H followed by rapid subsidence in AD 1964. The diatom estimate is close to that observed (Plafker *et al.*, 1969).

[6] *Ian Shennan, Natasha Barlow, Department of Geography, Durham University, Lower Mountjoy, South Road, Durham, DH1 3LE, United Kingdom.* Ian.shennan@durham.ac.uk, n.l.m.barlow@durham.ac.uk

Earthquake deformation cycle model

Similarities between each earthquake cycle leads to a model for the Girdwood area with coseismic subsidence, followed by rapid postseismic uplift in the decades after the earthquake. This merges into centuries of slower interseismic uplift before a period of preseismic subsidence.

Evidence for preseismic sea-level change

Almost all the peat-mud couplets that record great earthquakes at Girwood have a precursor: Diatom or pollen evidence of preseismic land subsidence in contrast to relative sea-level fall through the preceding interseismic period of each earthquake cycle. Of 24 couplets analysed, from Girdwood, Ocean View, Kenai and Kasilof only 4 appear to be influenced by mixing of sediment and diatoms from overlying silt into the peat. Many couplets show preseismic elevation change smaller than the error term but the evidence suggests that changes are not random. Trends indicating subsidence appear in lithostratigraphy, and in biostratigraphy and all the quantitative estimates are negative (indicating land subsidence), rather than a mixture of positive and negative values.

Independent observations of relative land-level changes before 1964 offer limited support for preseismic subsidence. Storm tides that first flooded the marsh surface at Girdwood after AD 1953 deposited thin surface layers of silt that became progressively thicker each year thereafter (Karlstrom, 1964). This date agrees with ^{137}Cs profiles and the start of the preseismic subsidence identified from the microfossil data at both Girdwood and Kenai.

Glacial isostatic adjustment (GIA) due to the Little Ice Age

Diatom-based reconstructions of sea-level change coupled with detailed age models, from AD 1400 to the AD 1964 great earthquake, show deviations from a purely tectonically driven model of regional sea-level change. Glacial isostatic modeling, constrained by GPS data, predicts up to 70 cm sea-level change due to mountain glacier mass balance changes during the Little Ice Age (Barlow *et al.*, 2012). Misfits between the GIA model predictions and RSL (relative sea level) reconstructions in the 19th and 20th century highlight that the tidal marshes of upper Cook Inlet potentially record a hemispheric-wide acceleration in sea level and that other more complex Earth process combinations may contribute to regional RSL change.

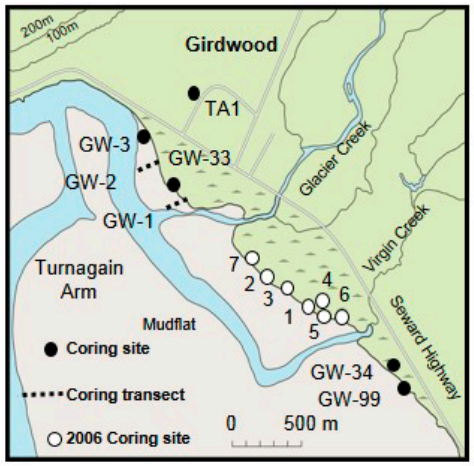
200m
100m
Girdwood
TA1
GW-3
GW-33
GW-2
GW-1
Glacier Creek
Virgin Creek
Turnagain Arm
Mudflat
Coring site
Coring transect
2006 Coring site
7
2
3
1
4
6
5
GW-34
GW-99
Seward Highway
0
500 m

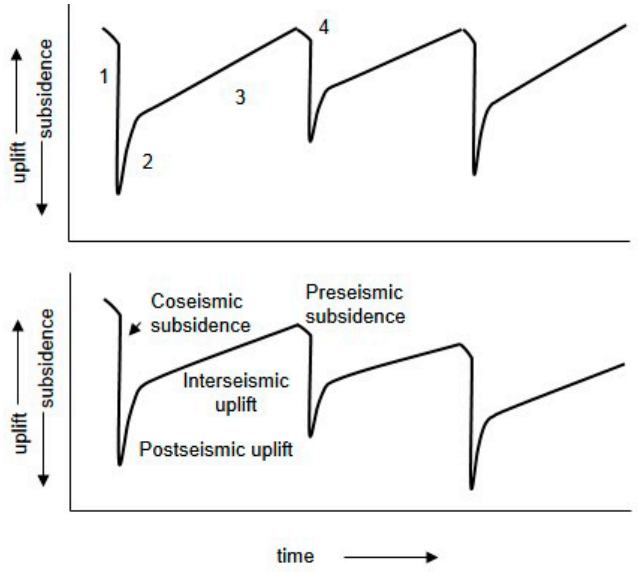
uplift
subsidence
1
2
3
4
Coseismic subsidence
Preseismic subsidence
Interseismic uplift
Postseismic uplift
time

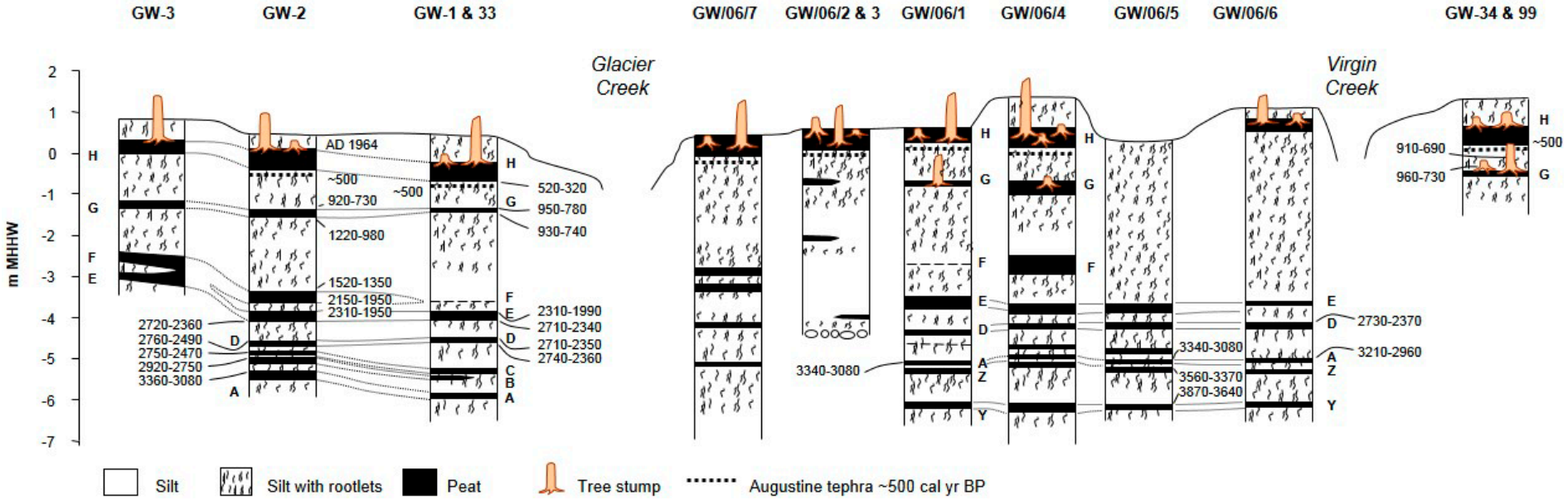
GW-3
GW-2
GW-1 & 33
GW/06/7
GW/06/2 & 3
GW/06/1
GW/06/4
GW/06/5
GW/06/6
GW-34 & 99
Glacier Creek
Virgin Creek
m MHHW
AD 1964
~500
920-730
1220-980
1520-1350
2150-1950
2310-1950
2720-2360
2760-2490
2750-2470
2920-2750
3360-3080
520-320
950-780
930-740
2310-1990
2710-2340
2710-2350
2740-2360
3340-3080
3560-3370
3870-3640
2730-2370
3210-2960
910-690
960-730
Silt
Silt with rootlets
Peat
Tree stump
Augustine tephra ~500 cal yr BP

Figure 1.4.1

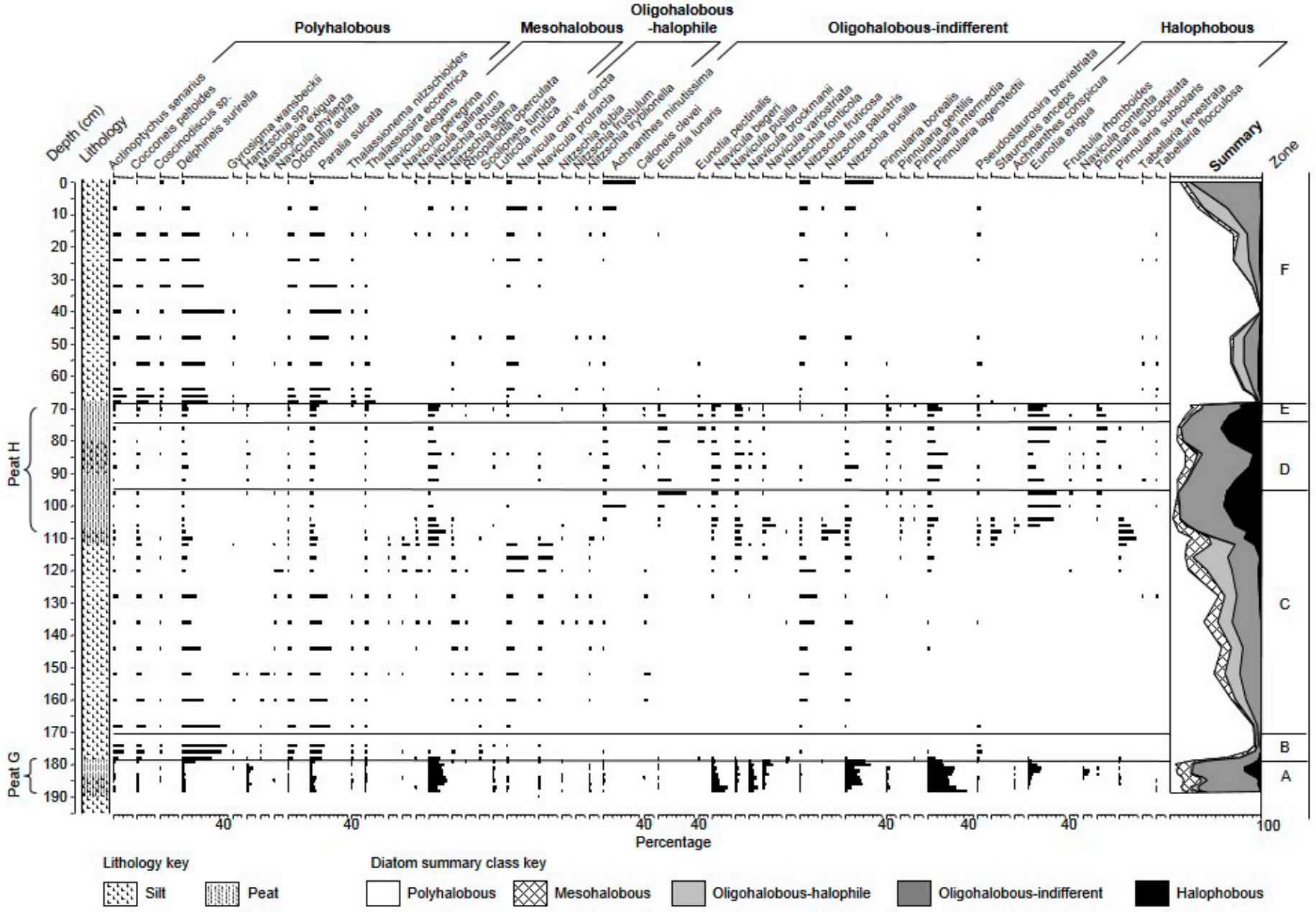
Polyhalobous
Mesohalobous
Oligohalobous -halophile
Oligohalobous-indifferent
Halophobous
Depth (cm)
Lithology
Summary
Zone
Actinoptychus senarius
Cocconeis peltoides
Coscinodiscus sp.
Delphineis surirella
Gyrosigma wansbeckii
Hantzschia spp
Mastogloia exigua
Navicula phyllepta
Odontella aurita
Paralia sulcata
Thalassionema nitzschioides
Thalassiosira eccentrica
Navicula elegans
Navicula peregrina
Navicula salinarum
Nitzschia obtusa
Nitzschia sigma
Rhopalodia operculata
Scoliopleura tumida
Luticola mutica
Navicula cari var cincta
Navicula protracta
Nitzschia dubia
Nitzschia frustulum
Nitzschia tryblionella
Achnanthes minutissima
Caloneis clevei
Eunotia lunaris
Eunotia pectinalis
Navicula bergeri
Navicula pusilla
Navicula brockmanii
Navicula vanostriata
Nitzschia fonticola
Nitzschia fruticosa
Nitzschia palustris
Nitzschia pusilla
Pinnularia borealis
Pinnularia gentilis
Pinnularia intermedia
Pinnularia lagerstedtii
Pseudostaurosira brevistriata
Stauroneis anceps
Achnanthes conspicua
Eunotia exigua
Frustulia rhomboides
Navicula contenta
Pinnularia subcapitata
Pinnularia subsolaris
Tabellaria fenestrata
Tabellaria flocculosa
Peat H
Peat G
F
E
D
C
B
A
Percentage
Lithology key
Silt
Peat
Diatom summary class key
Polyhalobous
Mesohalobous
Oligohalobous-halophile
Oligohalobous-indifferent
Halophobous

Figure 1.4.2

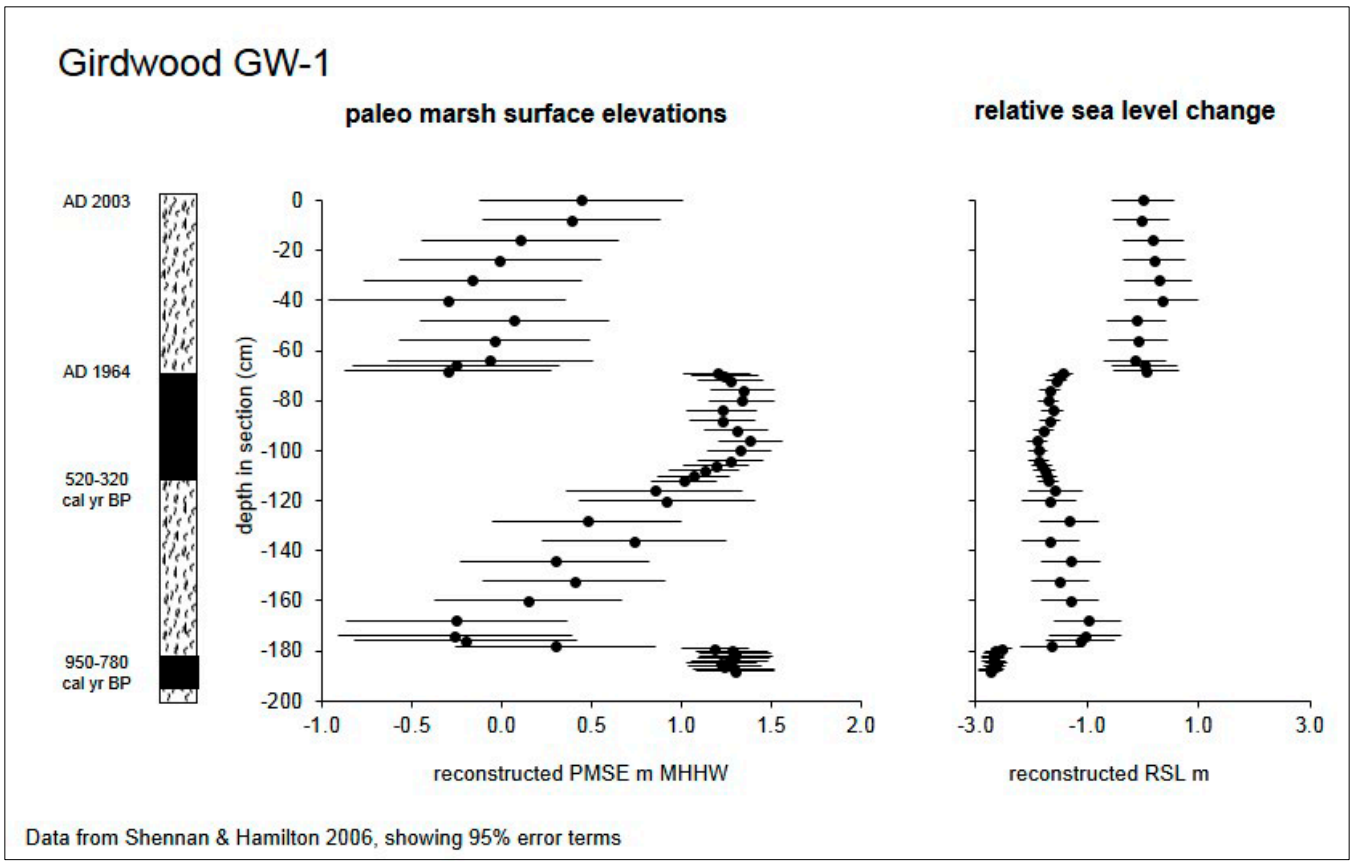
Girdwood GW-1
paleo marsh surface elevations
relative sea level change
AD 2003
AD 1964
520-320
cal yr BP
950-780
cal yr BP
depth in section (cm)
0
-20
-40
-60
-80
-100
-120
-140
-160
-180
-200
-1.0
-0.5
0.0
0.5
1.0
1.5
2.0
reconstructed PMSE m MHHW
-3.0
-1.0
1.0
3.0
reconstructed RSL m
Data from Shennan & Hamilton 2006, showing 95% error terms

Figure 1.4.3

CHAPTER 2

Chapter 2.1

CRUSTAL DEFORMATION STUDIES WITHIN THE 1964 ALASKA EARTHQUAKE RUPTURE ZONE

By Jeff Freymueller[7]

Field Trip Stops

Stop A. PBO GPS site. There are two Plate Boundary Observatory (PBO) GPS sites along our path. The preferred stop will be at site AC20 at Bird Point. Access to the site should be OK, but it may be excessively muddy and sloppy depending on the weather. If AC20 is not easily accessible then we will fall back to stopping at site AC15 in Cooper Landing. If we can go to AC20, then Max Enders of UNAVCO will join us and open up the enclosures so we can see how everything is constructed. At AC15, we can view only the outside of the enclosures. Either way, we will see a modern continuous GPS site, discuss how the GPS measurements are made, and discuss the important features evident in the GPS time series.

Stop B. At a convenient scenic location on the Kenai Peninsula. The important scientific results from GPS studies come from combining data from all the sites in the area, not from a single location, so we can stop and discuss these results in any convenient location. Here we will discuss an overview of the major findings from GPS studies within the 1864 rupture zone. Some of these will be amplified further in the Tuesday evening talk.

Background

The subduction zone earthquake cycle is now a familiar concept to most geoscientists. During the long interseismic phase between large earthquakes, the shallow part of the megathrust remains locked by friction while the deeper part creeps at the long-term plate motion rate. This change in the slip behavior along the megathrust results in the accumulation of elastic strain energy in the surrounding material, and eventually the stresses driving fault slip exceed the force of friction and cause the fault to move abruptly. In the simplest (elastic) earthquake cycle models, the interseismic phase begins immediately after the earthquake is done, and elastic strain begins to accumulate again. Deformation of the Earth's surface (and strain within the body) also results from the variations in slip along the megathrust, and these deformations can be measured at the surface using GPS (fig. 2.1.1). Another characteristic of this deformation signal is that the motion of sites on the overriding plate will be in the direction of the relative plate motion vector (small variations in direction occur in cases of significant subduction obliquity).

Following Savage (1983), we describe the slip distribution on the megathrust as a superposition of two components: Uniform slip on the entire interface, and backwards slip or *slip deficit* on the parts of the interface that are locked and thus not slipping. The *slip deficit* is defined as the difference between the slip occurring on a part of the fault and the slip expected based on the long-term slip rate. If a part of a fault has been creeping steadily at the long-term slip rate, it will have a slip deficit of zero. Slip deficit changes with time, accumulating between earthquakes and being reduced by earthquakes. For a fully locked fault, slip deficit accumulates at the long-term slip rate. The total deformation is computed by summing the deformation caused by each component of the superposition. Savage (1983) proposed that the deformation of the overriding plate from a freely slipping subduction zone would be zero or nearly so, so the deformation due to the locked subduction zone can be computed from the deformation associated with the slip deficit. This is computed by imposing backwards slip on the appropriate parts of the megathrust, using elastic dislocation theory (Okada, 1985).

[7] *Jeff Freymueller, Geophysical Institute and Department of Geology and Geophysics, University of Alaska Fairbanks, 505 South Chandalar Drive, Fairbanks, AK, U.S.A., 99775.* Jeff.freymueller@gi.alaska.edu

We also know that the slip rate on the megathrust is not constant in time, and that the response of the Earth to tectonics and earthquakes is not purely elastic. Variations in slip rate result from slow-slip events, and from afterslip that follows large earthquakes. Large earthquakes also trigger a viscoelastic flow response from the mantle (and potentially the lower crust), which also contributes to the observed surface deformation. The best available models for these contributions for the area of the 1964 earthquake are given by Suito and Freymueller (2009).

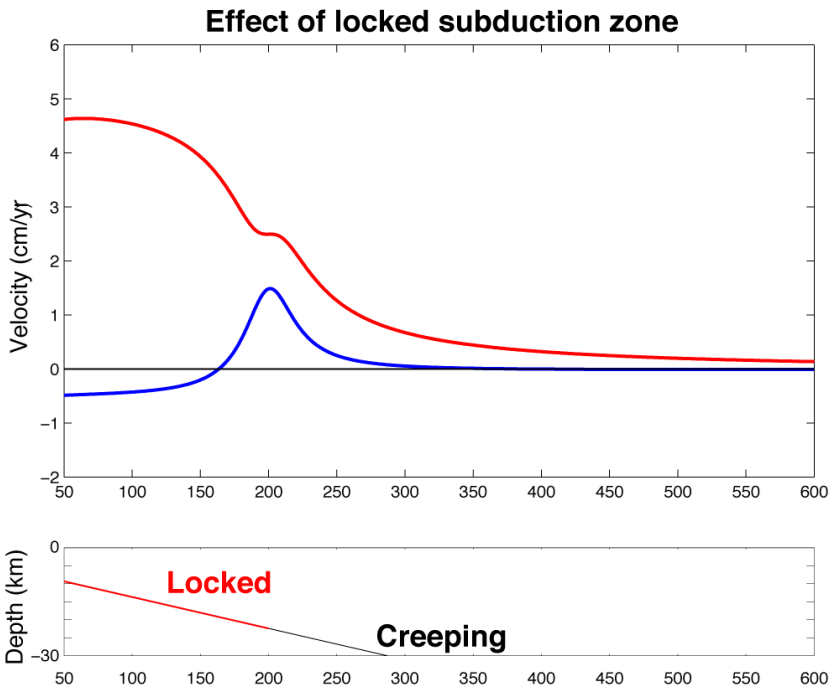

Figure 2.1.1. *Cross-section of deformation across a locked subduction zone, with distance from the trench on the horizontal axis. The bottom panel shows the extent of locked and creeping sections of the megathrust. The top panel shows the horizontal (red) and vertical (blue) velocities observed at the surface as a result of the variations in slip rate. The geometry and rate of plate motion here are modeled after southern Alaska. The deformation is computed using elastic dislocation theory, following Savage (1983) and Okada (1985).*

Geodetic studies were an important part of the study of the 1964 earthquake. Cohen and Freymueller (2004) summarized the historical observations. Horizontal and vertical displacements for the earthquake were computed from repeated terrestrial surveying techniques by the National Geodetic Survey (NGS). The horizontal displacements computed by Parkin (1969) settled any remaining doubts about the megathrust model for the earthquake. Postseismic uplift over the first decade after the earthquake was estimated by Brown *et al.* (1977) based on repeated leveling surveys by the NGS along Turnagain Arm. Unfortunately, there was a nearly two decade hiatus in observations after the mid-1970s, aside from the permanent tide gauge sites.

Geodetic work in the region began again in the early 1990s, mainly supported by NASA and showcasing the newly mature technology of GPS. The USGS, led by Jim Savage, Will Prescott, and Wayne Thatcher, surveyed two profiles of sites across Prince William Sound and Kodiak Island to measure the present-day elastic deformation due to the locked subduction zone (Savage *et al.*, 1998). Jeanne Sauber of Goddard Space Flight Center surveyed a network to the east in the St. Elias Range, with similar goals for the St. Elias collision and Yakataga gap. Finally, Steve Cohen of Goddard Space Flight Center surveyed a set of leveling benchmarks across the Kenai Peninsula with the aim of measuring longer-term postseismic uplift by comparing height changes between 1960s leveling and 1990s GPS, to determine whether the postseismic deformation had been due to afterslip, viscoelastic relaxation of the mantle, or a combination of both. My involvement began in 1995, when I arrived in Alaska and began to collaborate with Steve Cohen on this effort. (Max Wyss deserves special credit for being the "matchmaker" who put us together.)

In 1995, Cohen and I surveyed a much more extensive set of leveling marks across the area, and repeated the six sites he had originally surveyed in 1993. When we compared the 1993 and 1995 surveys, we found an unexpected surprise: The sites on the western part of the Kenai Peninsula were moving trenchward (Cohen and Freymueller, 1997). This turned out to be a signature of ongoing rapid postseismic deformation, combined with a dramatic along-strike variation in the pattern of locked vs creeping behavior of the megathrust. Both of these were unexpected surprises. Once we had confirmed the measurement, we devoted more time and effort to repeat surveys to better define the present-day deformation field, which led to the later postseismic studies of Zweck *et al.* (2002)

and Suito and Freymueller (2009). These studies refined models for the mechanisms of postseismic deformation and estimates of the present-day distribution of locked and creeping patches on the megathrust. One key conclusion based on the latter finding is that the present-day locked region on the megathrust closely matches the region of large coseismic slip in the 1964 earthquake. This suggests that the large seismic asperities on the megathrust persist from cycle to cycle, and thus are likely to result from changes in physical properties on the interface rather than random variations in the slip patterns from event to event. Further work along the Aleutian arc suggests that this is true for all of the great subduction earthquakes of the 20th century along this margin (fig. 2.1.2).

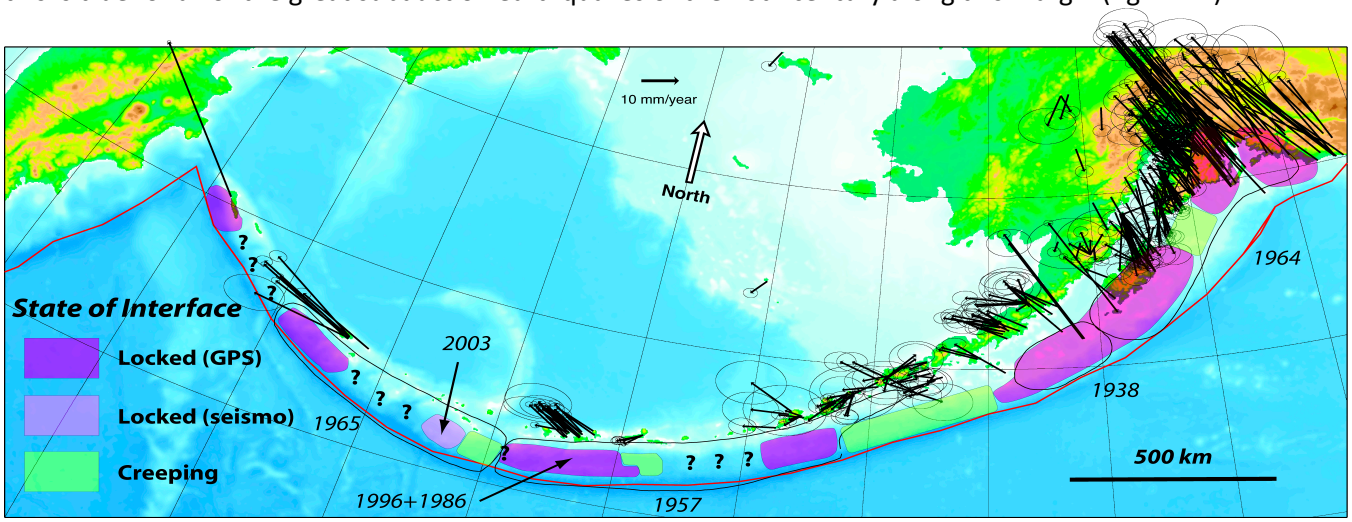

Figure 2.1.2. *Inferred locked and creeping segments along the Aleutian arc, from Freymueller et al. (2008).*

Overview of Contributions to the GPS Steady Velocity Field

Horizontal GPS velocities from Freymueller *et al.* (2008) are shown in figure 2.1.3. These velocities were derived mainly from repeated surveys of marks across southern Alaska from 1992 through 2007, and combine all of the data collected by UAF and many other groups. A small number of continuous sites are incorporated into this velocity field, but at the time it was derived the PBO sites were still quite new and their velocities were not yet so precise.

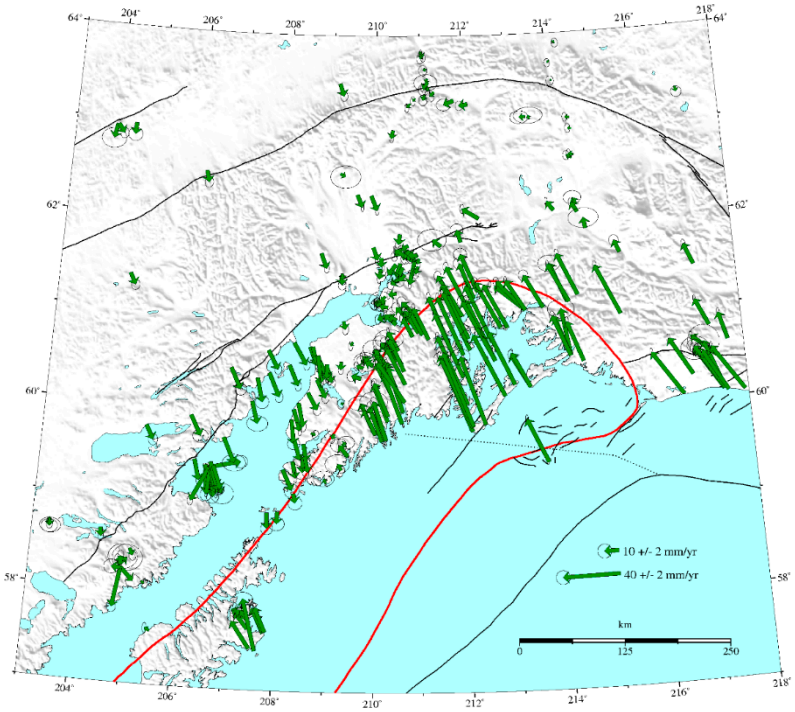

Figure 2.1.3. *Present-day horizontal velocity field relative to the North American plate, from Freymueller et al. (2008). Available online at http://www.gps.alaska.edu/jeff/Chapman_GPS_velocities.html.*

Several important features are evident in this velocity field. First, sites near the southern coast mostly move to the north–northwest, which is primarily due to the elastic strain from the locked subduction zone. Second, sites in the Cook Inlet and Kenai Peninsula region move in roughly the opposite direction, southeastward or toward the trench. This is a signature of the ongoing postseismic deformation due to the 1964 earthquake. The postseismic signal is actually present along the entire 1964 rupture zone, but we see it most prominently in this area because there is only a small component of motion due to the elastic deformation from the locked subduction zone here; this is an indication of the along-strike variations in the pattern of locked regions along the megathrust. Sites to the north, near the Denali fault, display a counter-clockwise rotational pattern, which results mainly from the permanent deformation of the overriding plate and reflects the active slip along the Denali fault. Finally, the trenchward motion pattern extends far away from trench, north of the Denali fault. Those sites move slowly toward the south, resulting from far-field postseismic deformation (Suito and Freymueller, 2009).

Slip Patterns on the Megathrust

Suito and Freymueller (2009) estimated the coseismic and postseismic slip distributions for the 1964 earthquake, and the present-day slip deficit distribution on the megathrust (fig. 2.1.4). The coseismic slip distribution was derived through forward modeling, perturbing the slip distribution estimated by Johnson *et al.* (1996) to better explain what we considered the most robust features of the coseismic slip observations. The spatial distribution of postseismic afterslip was estimated from the cumulative postseismic uplift data of Cohen and Freymueller (2004) for the Kenai Peninsula and Gilpin (1995) for Kodiak Island, plus the tide gauge data. The time history of afterslip (not shown here) was estimated from the tide gauge data. The present-day slip deficit distribution was estimated from the present-day velocity field, after removing a model for the postseismic deformation (fig. 2.1.5) and a simple upper plate deformation model based on Lahr and Plafker (1980) and Fletcher (2002).

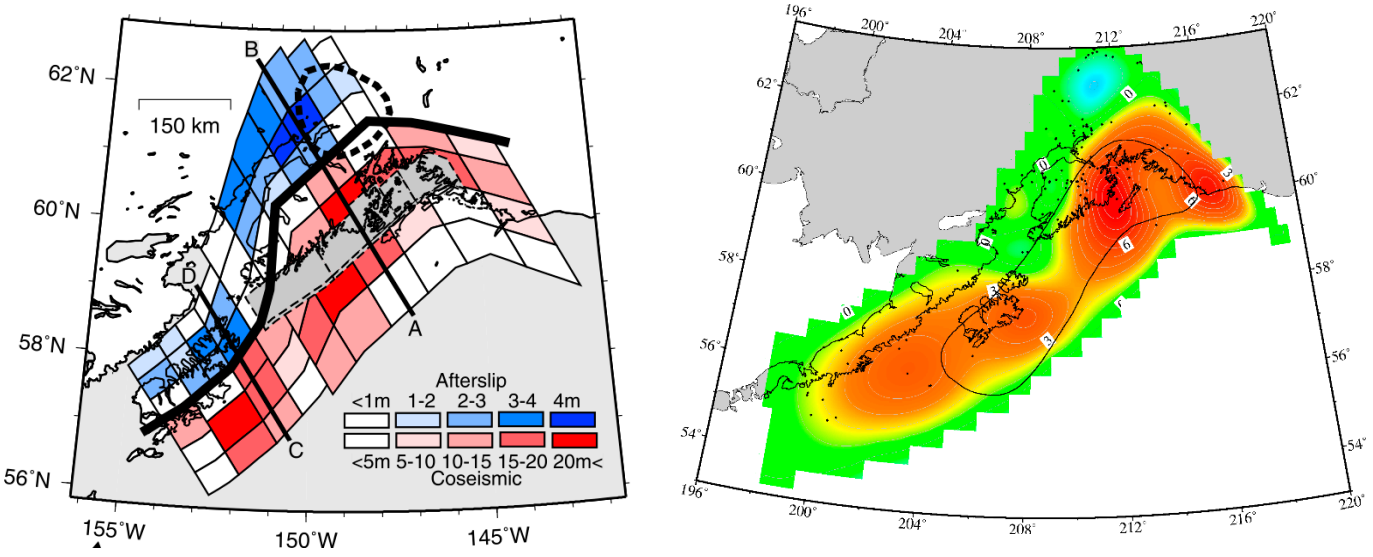

Figure 2.1.4. *(Left) Coseismic and postseismic slip distributions for the 1964 earthquake. Note the different scales for the two components, as postseismic afterslip was 10–20 percent as large as the largest coseismic slip. (Right) Present-day slip deficit distribution. Both figures from Suito and Freymueller (2009).*

Figure 2.1.5 shows the postseismic velocities from the combined afterslip and viscoelastic model of Suito and Freymueller (2009), and the residual velocities after removal of the postseismic model. The postseismic velocities were computed using a finite element model with a realistic 3-D geometry (the inclusion of an elastic slab is the most important 3-D element). Coseismic slip was imposed at the time of the earthquake, and afterslip was imposed based on the estimated afterslip time history. The model includes an elastic upper plate and slab, and a viscoelastic asthenosphere. The afterslip had largely died away by the 1990s, so the present-day postseismic veloc-

ities are dominated by the viscoelastic response to the combined coseismic and postseismic slip. The asthenospheric viscosity was estimated by Suito and Freymueller (2009), and corresponds to a viscoelastic relaxation time of 15–25 years (20 years was chosen for the optimal model.

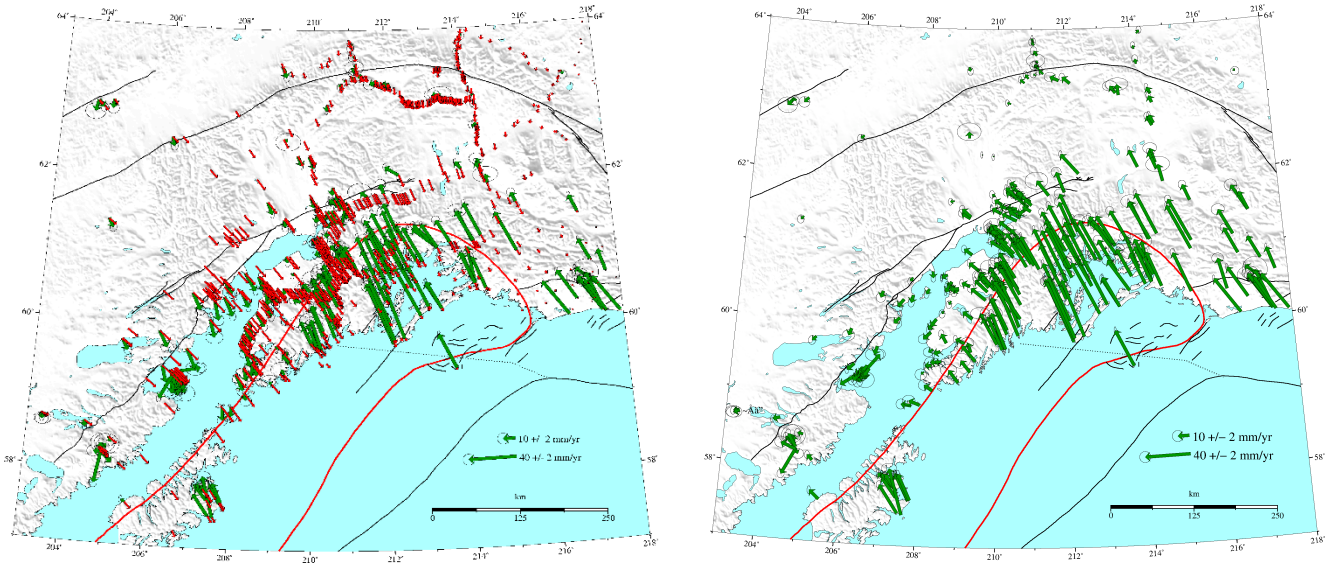

Figure 2.1.5. *Removal of the postseismic deformation. (Left) Present-day velocities (green) and predictions (red) of the postseismic model of Suito and Freymueller (2009). (Right) Velocities after removal of the postseismic model.*

A close-up view of the residual velocities is shown in figure 2.1.6. The removal of the postseismic model removes the trenchward motion in the Cook Inlet area, although a trench-parallel motion remains. This must be due to permanent motion of the overriding plate relative to the North American plate, because neither the elastic nor postseismic components have such a significant trench-normal component.

The along-strike variations in the elastic signal are clearly visible in figure 2.1.6. In the Prince William Sound area, you can clearly see the shortening of the upper plate that results from the locked megathrust. The amount of shortening observed over a similar trench-normal distance is much less for the western Kenai Peninsula. The velocity relative to North America of a point at a given distance from the trench is also smaller for the western Kenai Peninsula compared to Prince William Sound. Both of these are exactly what one would expect from changing the width of the locked region (fig. 2.1.1), from a wider region under Prince William Sound to a narrower region offshore of the Kenai Peninsula. This is reflected in the inversion result of figure 2.1.4.

Also, with the exception of a few sites with large uncertainties, the direction of motion for almost all of the sites is very close to the direction of relative plate motion. This indicates that the postseismic model has successfully removed most of the remaining signals in the trench-normal direction. Deviations from this are seen for sites that have a small elastic signal. These deviations are a result of the superposition of a small trench-parallel motion relative to North America with a much larger motion in the plate motion direction.

Vertical Velocity Field

Vertical velocities have not been studied as completely for most of Alaska as the horizontal velocities, mainly because they are intrinsically less precise and because there are large non-tectonic contributions to the vertical velocity field. In particular, most of southern Alaska experiences rapid uplift due to post-Little Ice Age (LIA) glacier retreat and loss of ice. In southeast Alaska this is the dominant signal (Larsen *et al.*, 2005; Elliott *et al.,* 2010). However, in the greater Cook Inlet and Kenai Peninsula area, more work on the recent glacial history needs to be integrated into glacial isostatic adjustment (GIA) models.

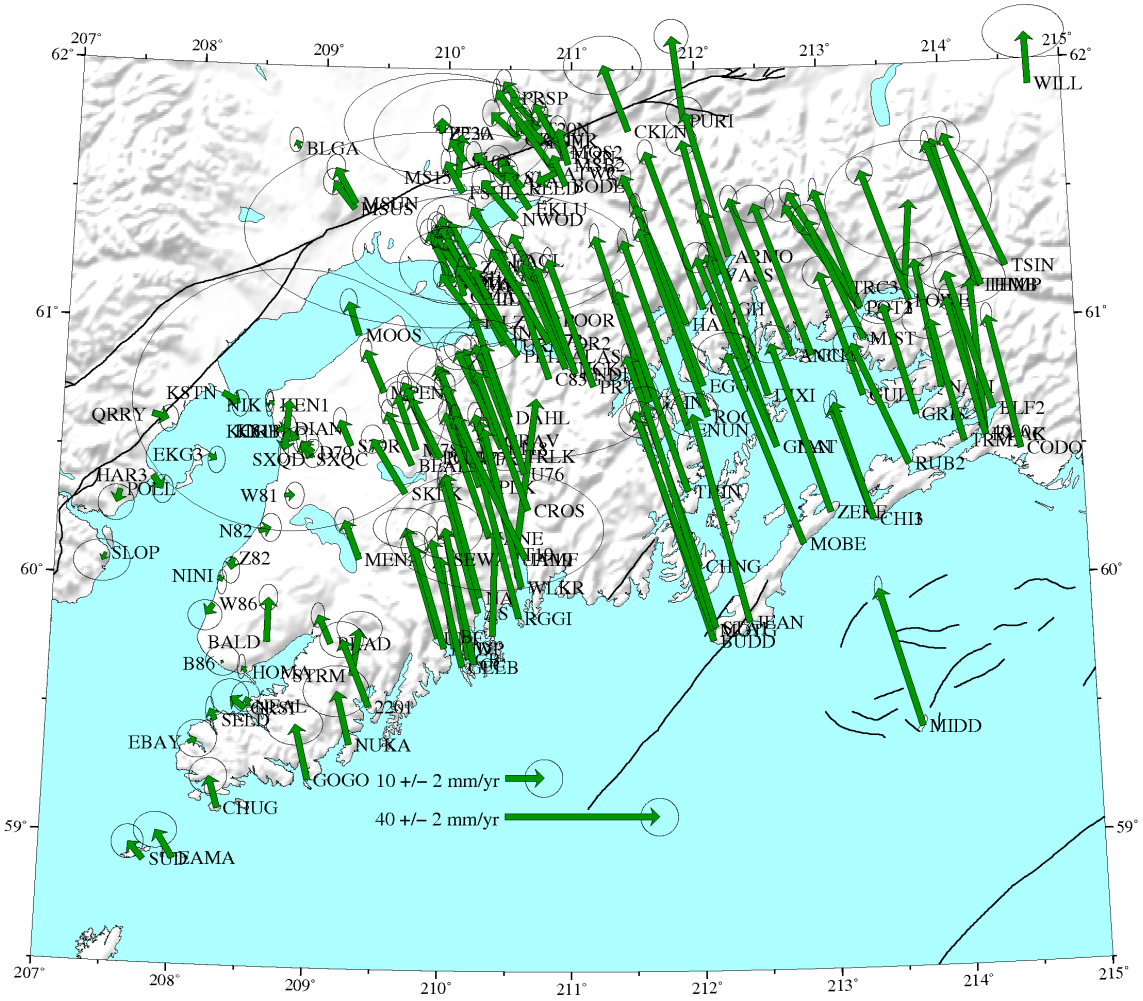

Figure 2.1.6. *Close-up of the velocities after removal of the postseismic model, for the Kenai Peninsula, Cook Inlet, and Prince William Sound. Data from Suito and Freymueller (2009).*

There is also considerable geodetic data on vertical velocities over a decadal time scale after the 1964 earthquake. Due to postseismic afterslip, some parts of the region experienced rapid postseismic uplift after the earthquake, totaling several decimeters or more. Along Turnagain Arm, uplift relative to the Anchorage tide gauge in the first year after 1964 exceeded 10 cm (Brown *et al.*, 1977), and they estimated that ~50 cm of postseismic uplift occurred within the first decade after the earthquake. This section begins with these decadal scale data.

Decadal scale vertical velocity field

Vertical motions during the 1964 earthquake were large, and most of southern Alaska has experienced significant vertical movements since that time. Relative sea level change data from permanent tide gauges provided one of the first clear estimates of these motions (fig. 2.1.7). Other decadal scale vertical motion data came from GPS surveys of leveling benchmarks, which were carried out in the 1990s.

The most recent analysis of the tide gauge data for measurements of uplift was done by Larson *et al.* (2003). They used monthly mean tide levels and applied a series of corrections and filters to remove atmospheric pressure effects, seasonal variations, and regionally correlated oceanographic variations from the records. They then converted the tide gauge records into estimates of crustal uplift assuming the model of Tamisiea *et al.* (2001). That model predicts sea surface rise over the globe that incorporates the effects of the changing gravity field as mass moves from glaciers and ice sheets into the ocean, including mantle mass variations due to viscoelastic flow. The model predicts an average sea surface rise rate of 1 mm/yr for the Gulf of Alaska. Within the area of the 1964

rupture, most tide gauge records show non-linear vertical motion with time (fig. 2.1.7), which is characteristic of postseismic deformation. The exception is Seldovia, located across Kachemak Bay from Homer, which shows nearly constant uplift with time at a rate of 9.6 ± 1.0 mm/yr. In most cases, the tide gauge data show that the uplift rate was very rapid after the earthquake, and decreased over time. Valdez and Cordova showed initial subsidence after the earthquake, which transitioned to uplift or near-zero vertical rates late in the time span (1990s).

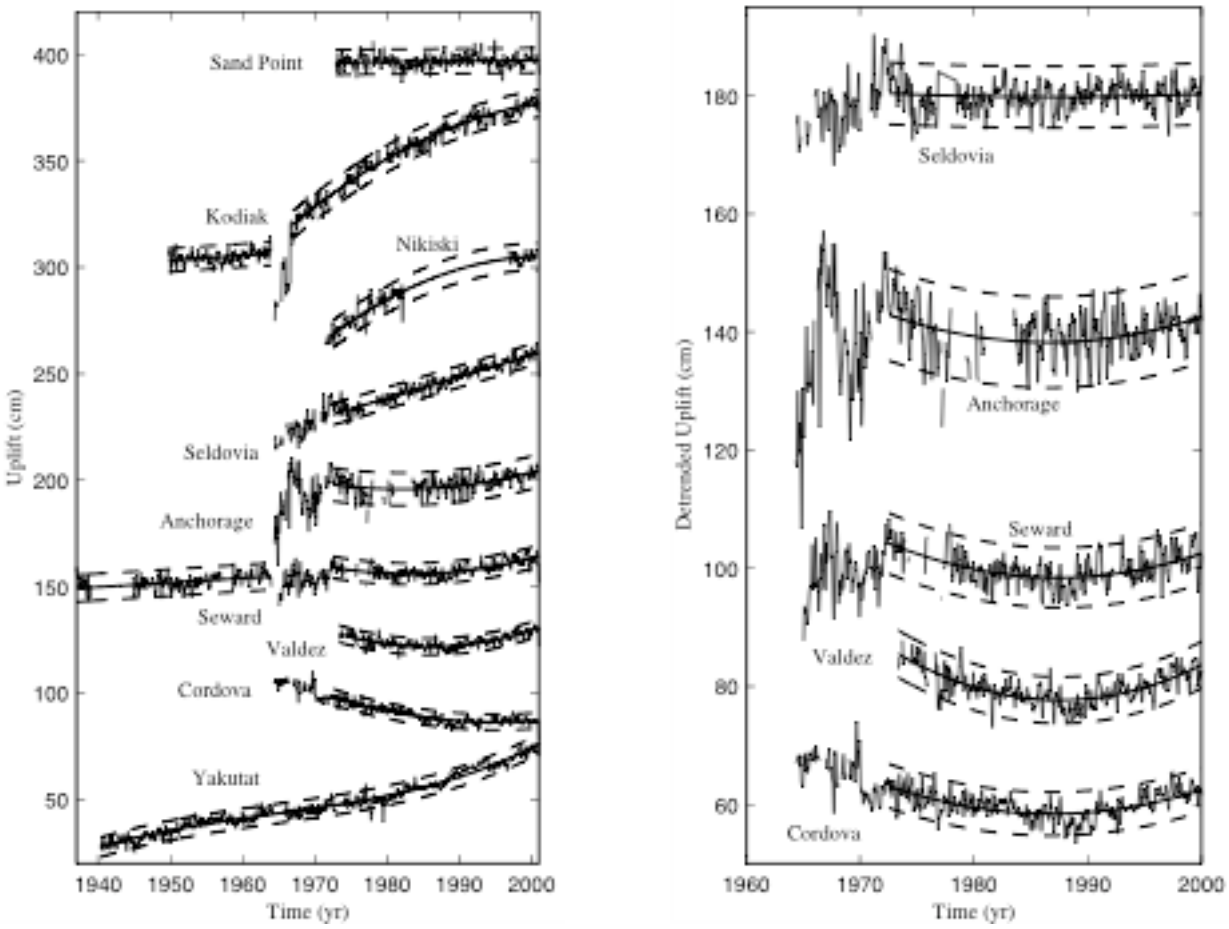

Figure 2.1.7. *Uplift rates inferred from tide gauge data by Larsen et al. (2003), assuming that the ocean surface in the study area rises by a rate of 1 mm/yr, which is based on a model that incorporates non-eustatic variations due to changes in the gravity field (Tamisiea et al., 2001). The left panel shows gauges from Yakutat to Sand Point, and the right panel shows detrended records for the gauges in the Kenai to Prince William Sound area.*

One other intriguing feature is seen in these data. Anchorage shows an initial periodic variation in relative sea level (RSL) and thus uplift in the first decade after the earthquake, before the record stabilizes by the mid-1970s. A similar but smaller signal can be seen in the detrended Seward record, and there is perhaps a hint of the same thing in the Seldovia record (fig. 2.1.7, right panel). Evidence for this feature was noted as early as Brown *et al.* (1977), but a definitive explanation has not been proposed. As Larsen *et al.* (2003) noted, it is possible to explain this feature in terms of propagating slip pulses on the megathrust, although any such model would be very poorly constrained. The magnitude of the oscillation at Anchorage was 34 ± 5 cm, over a period of ~5 years. The idea of multiple propagating slip pulses is also not easy to reconcile with the leveling data from Turnagain Arm, which are sparsely sampled in time but suggest that the updip edge of the postseismic afterslip got steadily deeper with time. No comparable signal has been observed from more recent M9+ earthquakes.

Suito and Freymueller (2009) used the tide gauge records in two ways. They based the time history of the afterslip on the shape of the tide gauge record at Kodiak. They also used the cumulative uplift measurements (1964 to 1990s) at all of the regional tide gauges along with measurements of cumulative postseismic uplift determined by

Cohen and Freymueller (2004) from repeated surveys of leveling benchmarks (fig. 2.1.8). The 1990s surveys of the benchmarks were done using GPS, which measures heights relative to the ellipsoid, a theoretical figure of the Earth, rather than relative to the geoid as is done with leveling. We needed to apply a geoid model to correct for the difference between the two height systems, and the uncertainty in the geoid model is by far the dominant error. Uncertainty in the geoid slope limited the spatial scope of their data set to the Kenai Peninsula. Uplift measurements for 1964–1990s were also available for Kodiak Island from repeated occupations of temporary tide gauges (Gilpin *et al.*, 1994; Gilpin, 1995).

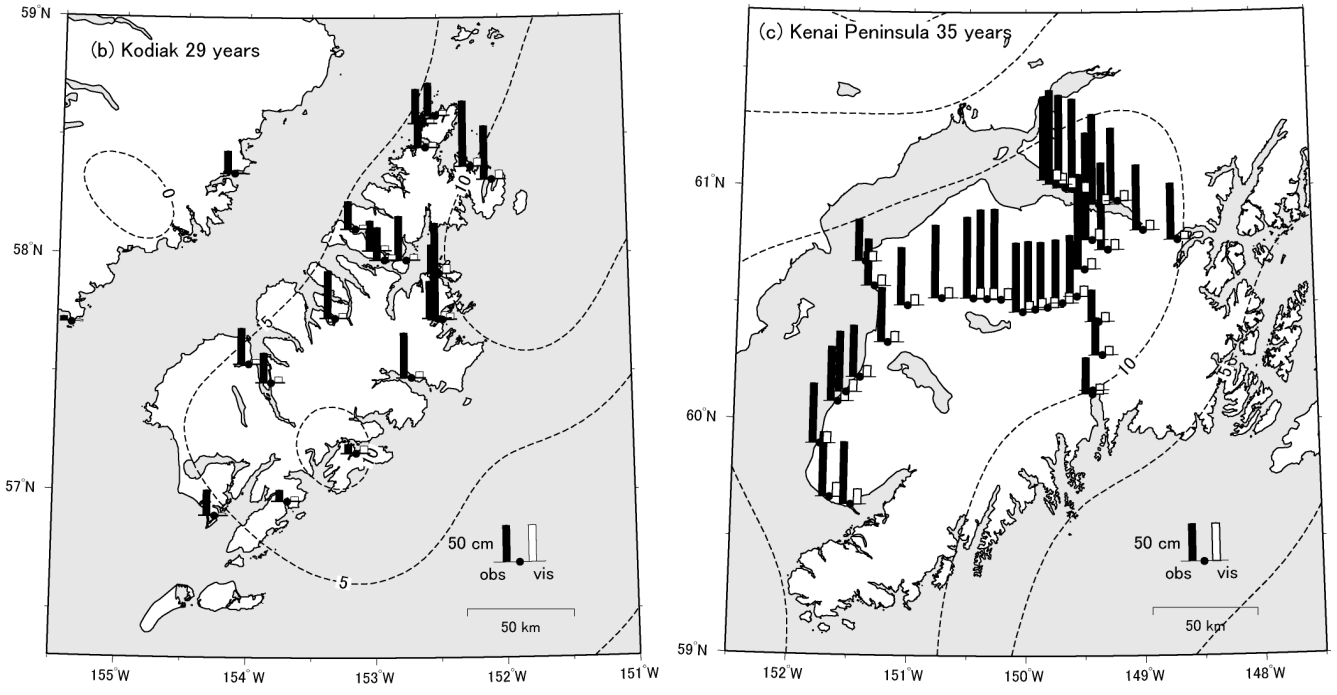

Figure 2.1.8. (a) *Computed postseismic uplift caused by viscoelastic response for 35 years across the entire region. Dashed black line indicates trace of inland faults. White circles with station name indicate the tide gauge stations.* ***(b)*** *Time span for 29 years in Kodiak Island, as compared with the observation (black bar).* ***(c)*** *Time span for 35 years in Kenai Peninsula, as compared with the observation (black bar). Figure from Suito and Freymueller (2009).*

Cumulative uplift on the Kenai Peninsula over 1964–1990s reached values as large as 1.2 meters, with the peak uplift observed along Turnagain Arm. There is some chance that errors in the geoid model might contribute 2 decimeters or perhaps more to this estimate. A more accurate calculation should be possible within a few years once NGS has completed work on a new purely gravimetric geoid for Alaska based on airborne gravity measurements. Suito and Freymueller (2009) corrected these data for an estimate for the GIA contribution and the uplift due to elastic strain, and these corrected values are shown in figure 2.1.8. They then computed the uplift due to viscoelastic relaxation and found that this contribution was very small over the entire region, due to the shallow dip of the slab. This meant that a reasonable correction for this component of the postseismic relaxation could be removed from the data. The residual uplift measurements were then inverted to determine the afterslip distribution (fig. 2.1.4). It was fortunate that the cumulative postseismic uplift was nearly insensitive to the viscoelastic model, because this allowed us to separate the two postseismic processes without significant tradeoffs between viscoelastic and afterslip models.

Present-day GPS vertical velocity field

The noise level on vertical GPS positions/velocities is roughly three times larger than that of the horizontal data, and vertical tectonic signals are generally smaller than horizontal motions. In addition, the vertical is more prone to systematic biases that result from aliasing of atmospheric path delays into the vertical component, and is also more sensitive to any errors in antenna calibration models. Thus, vertical accuracy in earlier generations of GPS processing was considerably worse than in the horizontal, and most studies have used mainly the horizontal. In addition, vertical positions often have significant seasonal periodic variations, which further complicates the interpretation of the vertical. However, for the last few years it has been clear that reliable results can be obtained.

The present-day vertical velocity field for southern Alaska is shown in figure 2.1.9 in the form of a contour map. This figure is based on an updated velocity solution compared to all the others in this chapter; it includes all data through late 2013 and includes all PBO sites. All sites with vertical velocity uncertainties smaller than 2.5 mm/yr are used in the contouring. Some anomalies in this data set reflect individual sites, which may not be representative of the surrounding area, although obvious measurement blunders have been removed. Uplift rates range from 6 to 10 mm/yr over most of the Kenai Peninsula. There is a clear region of subsidence in Prince William Sound, with separate subsidence maxima near Montague Island and Valdez. The Cordova area shows nearly zero uplift rate. In general, the GPS uplift rates show good agreement with those estimated from the tide gauges (a quantitative assessment using this velocity field is in progress).

The present-day vertical velocities are mainly due to a sum of three effects: glacial isostatic adjustment (GIA), postseismic deformation from the 1964 earthquake, and elastic deformation from the locked subduction zone. These components will be discussed individually in the remainder of this section.

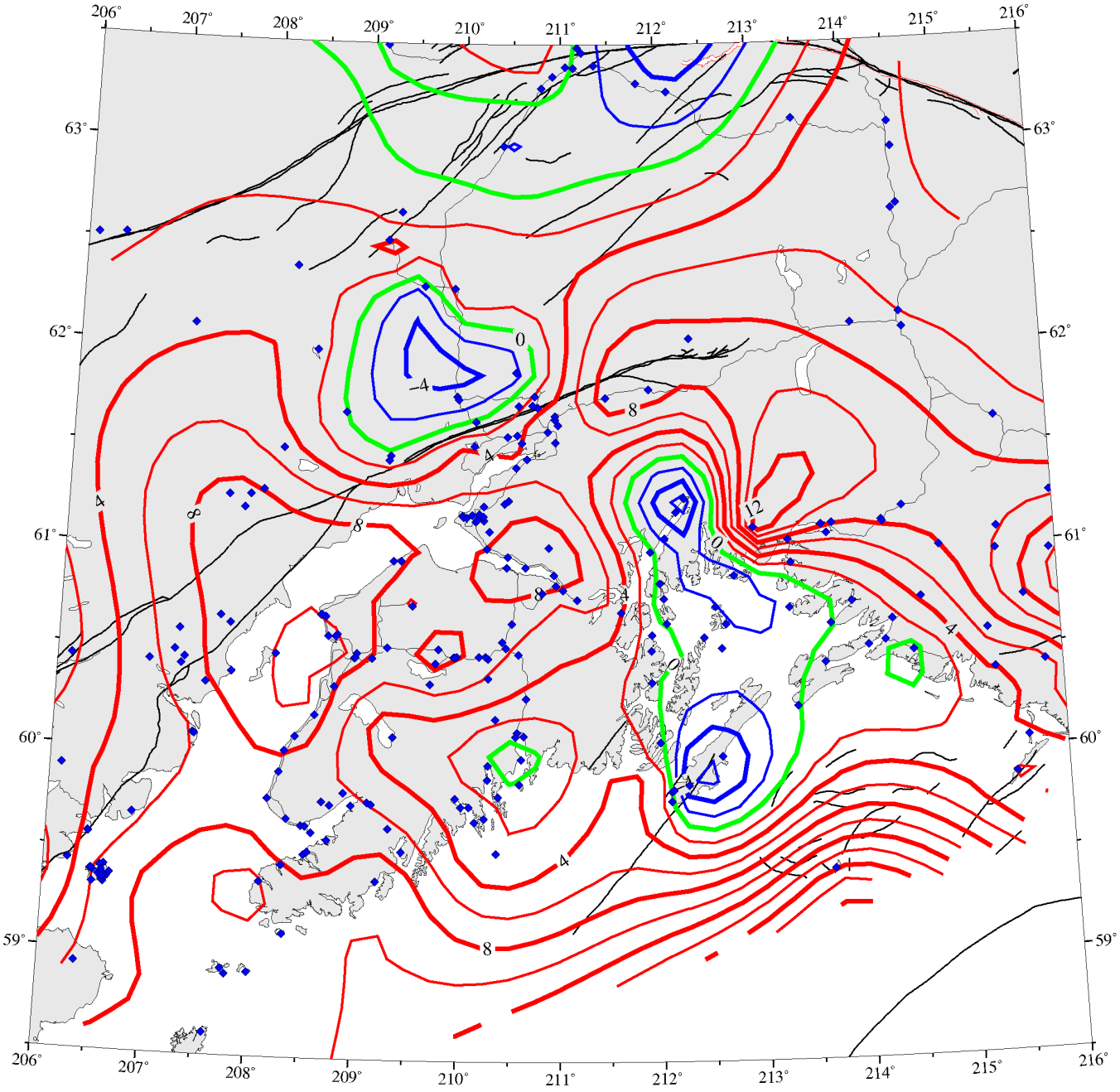

Figure 2.1.9. *Contoured uplift rates inferred from GPS data. This uses an updated data set relative to the other figures in this guide, and includes the PBO data. Red contours indicate uplift and blue contours represent subsidence, and the green contour is zero. Small diamonds indicate locations of sites.*

The GIA signal for Alaska is dominated by the ice loss following the LIA (Larsen *et al.*, 2003; Larsen *et al.*, 2005). The main reason for this is the low asthenospheric viscosity characteristic of southern Alaska. Viscosity estimates from postseismic studies (Suito and Freymueller, 2009) and GIA modeling studies (Larsen *et al.*, 2005; Elliott *et al.*, 2010) agree that the upper mantle viscosity beneath Alaska is ~10^{19} Pa-s, far lower than that beneath the main ice sheets. As a result of the low upper mantle viscosity, the effects of deglaciation in Alaska post-LGM have decayed away to nearly zero, and the effect of the Laurentide ice sheet or post-LGM deglaciation of the Alaska/British Columbia coast is also very small, less than 1 mm/yr. On the other hand, uplift rates from the post-LIA deglaciation exceed 30 mm/yr in parts of Southeast Alaska, and exceed 10 mm/yr over a large area of southern and southeastern Alaska (Larsen *et al.,* 2005).

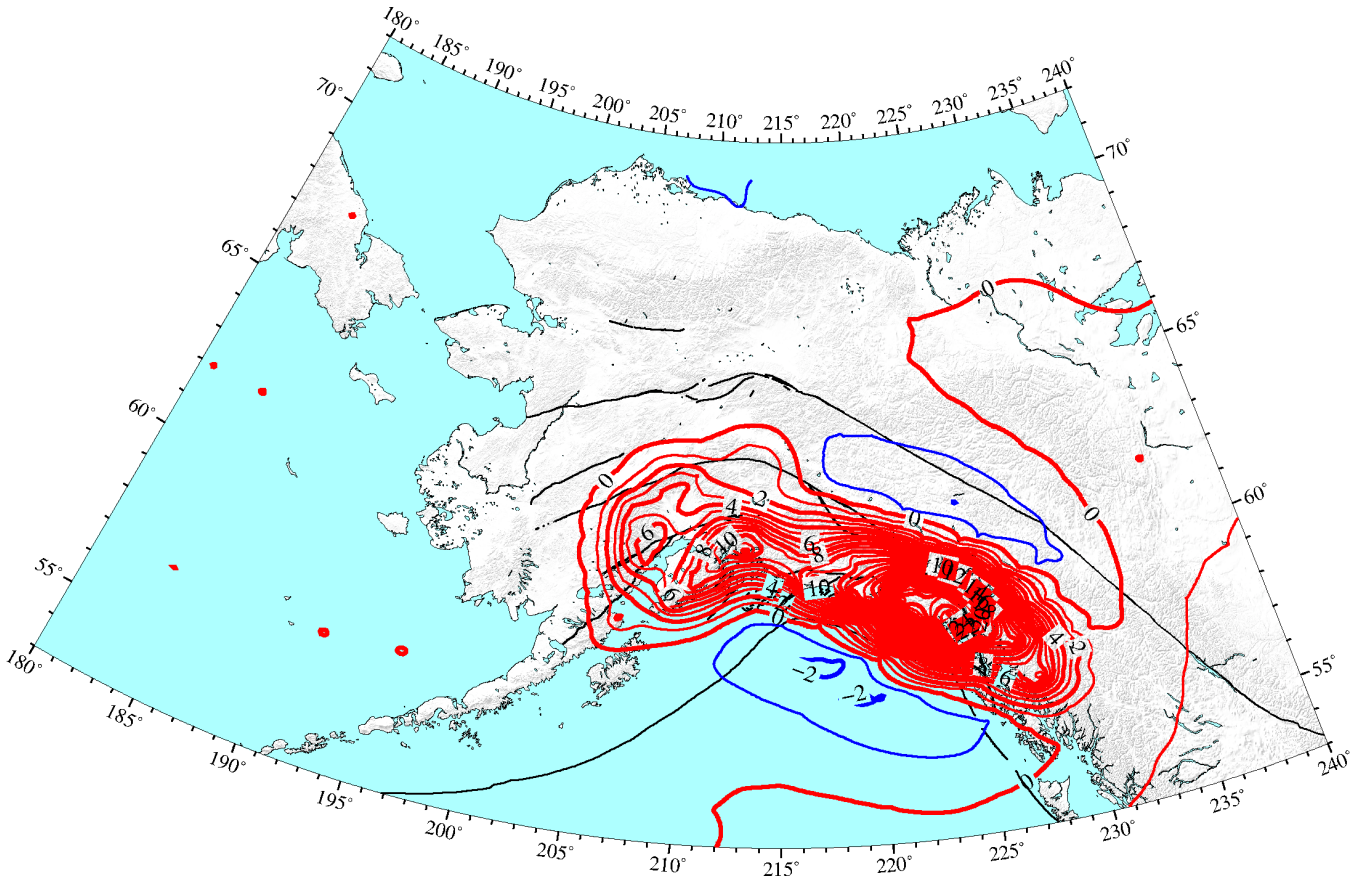

Figure 2.1.10. *Uplift and subsidence rates caused by GIA, including both post-LIA and post-LGM effects. The latter are small, although they do contribute ~1 mm/yr in NW Alaska (less than one contour interval). Contours are drawn at 2 mm/yr intervals, with red contours for uplift and blue contours for subsidence.*

Recently we have developed a new GIA model for all of Alaska (Hu and Freymueller, manuscript in preparation). This new model is based on a more complete model of late 20th century glacier change across the region, compared to the version used by Larsen *et al.* (2005) and Elliott *et al.* (2010). We found that for Southeast Alaska the rate of mass loss accelerated in the 1990s and then again around 2002. Applying this recent time history as a scale factor for the entirety of Alaska, and using the glacial history compiled by Larsen *et al.* (2005), we then computed the GIA deformation rate for all of Alaska (fig. 2.1.10). In Southeast Alaska, this model explains the data to within a typical misfit of 2–3 mm/yr, or about 10 percent of the maximum signal. I suspect that the model over-predicts the uplift rate in the Cook Inlet area, as the GIA model alone can nearly explain the observed uplift rates (fig. 2.1.9), and uplift should also be produced by elastic deformation from the locked subduction zone.

The second major component of the present-day vertical velocity field is due to continuing viscoelastic relaxation. The predictions of the preferred model of Suito and Freymueller (2009) are shown in figure 2.1.11 in contoured form. Peak uplift rates from this mechanism are slightly more than 4 mm/yr, located in a triangular region centered on Cook Inlet. Comparison to figure 2.1.9 shows a striking similarity in shape to a peak of uplift in the same location. Elsewhere, the signal from this mechanism is quite small.

The Kenai Peninsula also experiences uplift due to the elastic deformation from the locked subduction zone. The gradient in the horizontal deformation shows that the transition from locked to creeping behavior on the megathrust is located beneath this region, which will also correspond to a peak in the uplift rate (see fig. 2.1.1 for example). In the case shown in figure 2.1.1, there is an abrupt transition from locked to creeping behavior, and this produces a sharp and high amplitude uplift peak. If the transition from locked to creeping is gradual, then the uplift peak decreases in amplitude and broadens. The current models fit to horizontal velocities do not predict the vertical well at all (they predict too much uplift), and work is underway toward improving the models. The simplest

solution to this problem would be to use the vertical velocities in the inversion for the slip deficit distribution, but this cannot be done until the models for the GIA component are verified for this region.

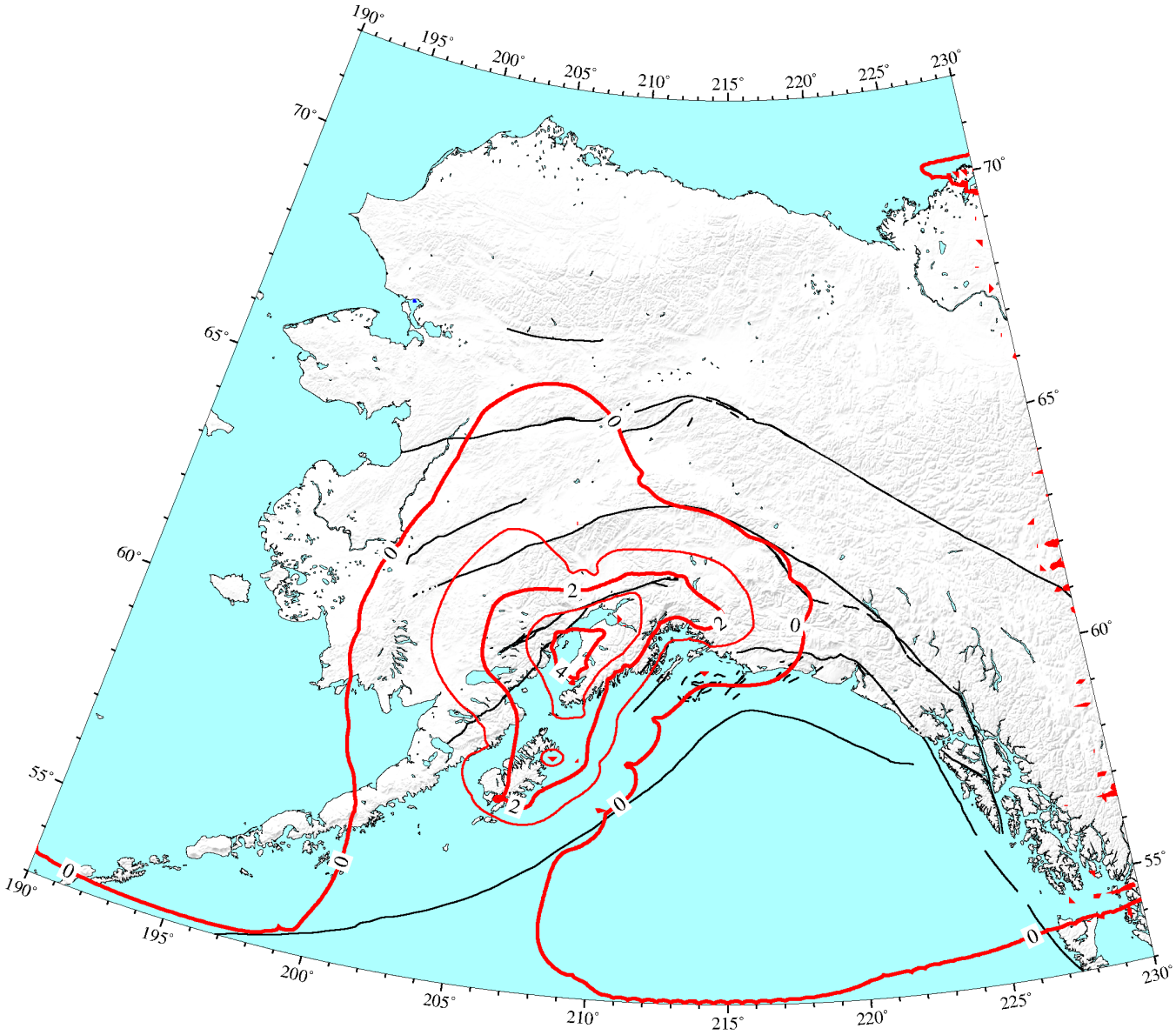

Figure 2.1.11. *Vertical motions predicted by the preferred model of Suito and Freymueller (2009), with contour interval of 1 mm/yr. Viscoelastic relaxation produces only a small signal, with a peak of slightly more than 4 mm/yr in a triangular region centered on Cook Inlet.*

One final vertical motion observation is worth discussion. The Upper Cook Inlet region is now known to have experienced multiple slow-slip events, essentially very slow earthquakes (Ohta *et al.*, 2006; Wei *et al.*, 2012; Fu and Freymueller, 2013). Unlike the small events observed in the Cascadia subduction zone, the Upper Cook Inlet events are very large, corresponding in slip and area to magnitude 7.3–7.5 earthquakes.

Figure 2.1.12 shows a combined time series for a pair of sites (ATWC and ATW2) located at the Tsunami Warning Center in Palmer. The ATWC site was destroyed in June 2001 by construction, but the site ATW2 was built nine months earlier and the offset between the site was estimated from the nine months of overlapping measurements. Elastic strain from the locked subduction zone causes a northward motion, which explains the general trend from 2001 through 2009. The northward trend is interrupted by the 2002 Denali fault earthquake and by small southward deviations that are probably small slow-slip events. The site is located just trenchward of the slip

patch during the slow-slip events, which means that slip causes a component of southward motion and uplift. The site uplifted nearly 5 cm during the 2009–2013 event, and a similar amount during the part of the 1998–2001 event that was recorded here (the 1998–2001 event is estimated from other data to have begun in May 2001, 5–6 months before the installation of this site). Although the slip model of Fu and Freymueller (2013), which did not use the vertical data, underestimates the amount of uplift, it is clear that large, slow-slip events can cause significant uplift. Future work will try to make full use of the vertical as well as horizontal displacements.

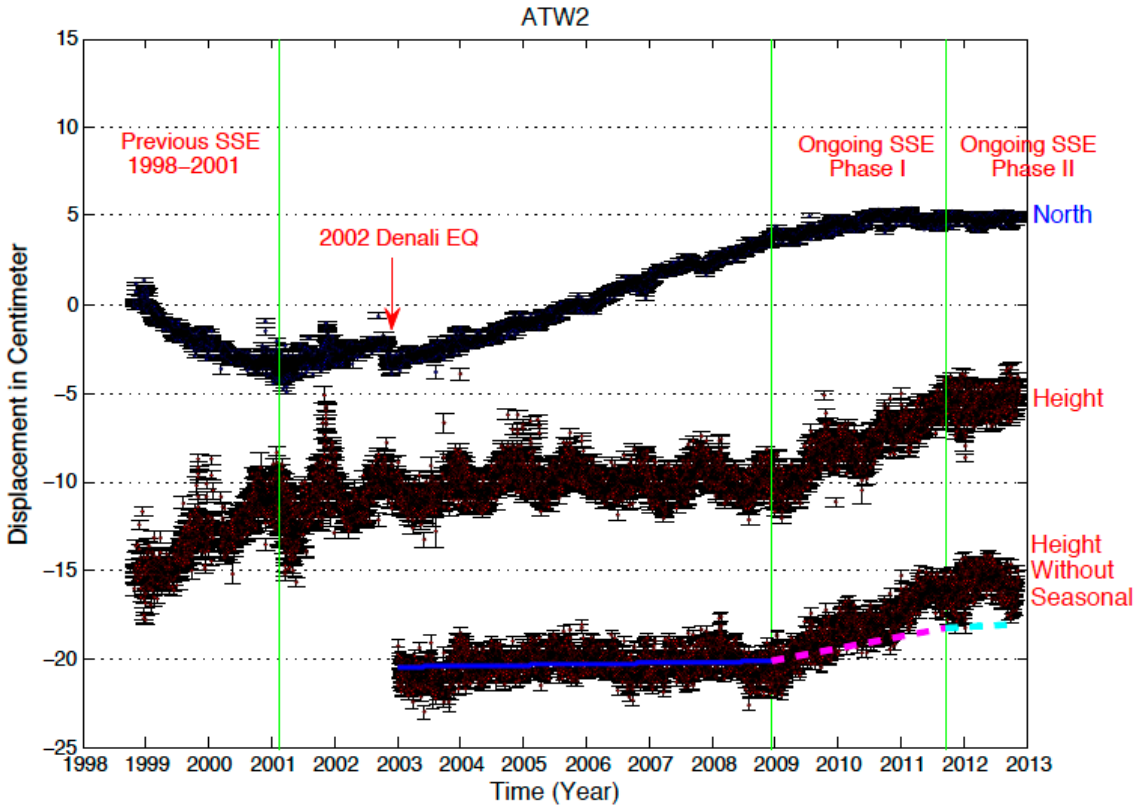

Figure 2.1.12. *Horizontal north–south (top) and vertical motion (middle) time series for site ATWC + ATW2 in Palmer, showing the effect of two slow-slip events, from Fu and Freymueller (2013). The bottom panel shows the vertical with a seasonal model based on GRACE (Fu et al., 2012) removed for 2003–2012. The three green bars show the end of the 1998–2001 slow-slip event, the beginning of the 2009–2013 event, and the boundary between Phase I and Phase II of the second event as defined by Fu and Freymueller (2013). This site, located slightly trenchward of the area of slow slip, uplifts during slow-slip events. The slip model fit to the horizontal data underestimates the uplift observed at the site.*

Plate Boundary Observatory (PBO) and present instrumentation

The National Science Foundation's EarthScope project began 10 years ago to study the structure and deformation of the North American continent. The geodetic part of EarthScope is called the Plate Boundary Observatory (PBO), and includes a network of 1,100 continuous GPS stations spread across the western United States, with a few in the central and eastern part of the continent, to improve the definition of the North American plate (fig. 2.1.13). PBO GPS receivers continuously record data available from UNAVCO, the U.S. university consortium for geodesy (http://www.unavco.org). When properly analyzed, daily position solutions from these data have a nominal precision of ~1 mm horizontal, ~3 mm vertical in a global reference system.

The GPS site consists of a receiver and a separate antenna, plus power and communications equipment. A number of the PBO GPS sites also have some additional equipment, such as meteorological sensors. These are used not for the primary analysis of the GPS data, but for the generation of additional products, such as estimates of atmospheric water vapor. One key element of the PBO site design is the construction of an ultra-stable mount for the

antenna. Because we are able to measure the position of the antenna daily at the millimeter level, we desire the antenna to be fixed to the crust as stably as possible. Most PBO sites used a braced structure, with several steel rods mounted in drill holes and welded together.

Most people think of a GPS receiver as a device that measures position, but in reality the receiver estimates positions using its actual measurements and satellite orbit information broadcast by the satellites. GPS receivers measure two types of observations from each GPS satellite, each of which is related to the distance between the satellite and receiver. The receiver measures a *pseudorange*, which is a measure of the distance (the *range*) plus the effects of satellite and receiver clock synchronization errors, for each satellite on two frequencies. Your handheld GPS or smartphone GPS makes the same measurement on one frequency only, although the high-precision GPS does this somewhat more precisely. These are measured by correlating timing codes broadcast by the satellites. The *carrier phase* data are the critical data recorded by the high-precision receiver, and allow its data to be used for millimeter-level positioning. These measurements are the phases of the underlying carrier signals on which the timing codes are multiplexed. The carrier phase data are about 100 times more precise than the pseudorange data, although they are biased by an unknown number of cycles; this means that to determine a precise position from the phase data we must have continuous measurements of the change in phase over an extended period of time. It is also possible to use the change in phase over time to measure motions of the receiver, for example displacements during an earthquake. The use of data from two frequencies makes it possible to remove the effects of the path delay through the ionosphere, which is frequency dependent.

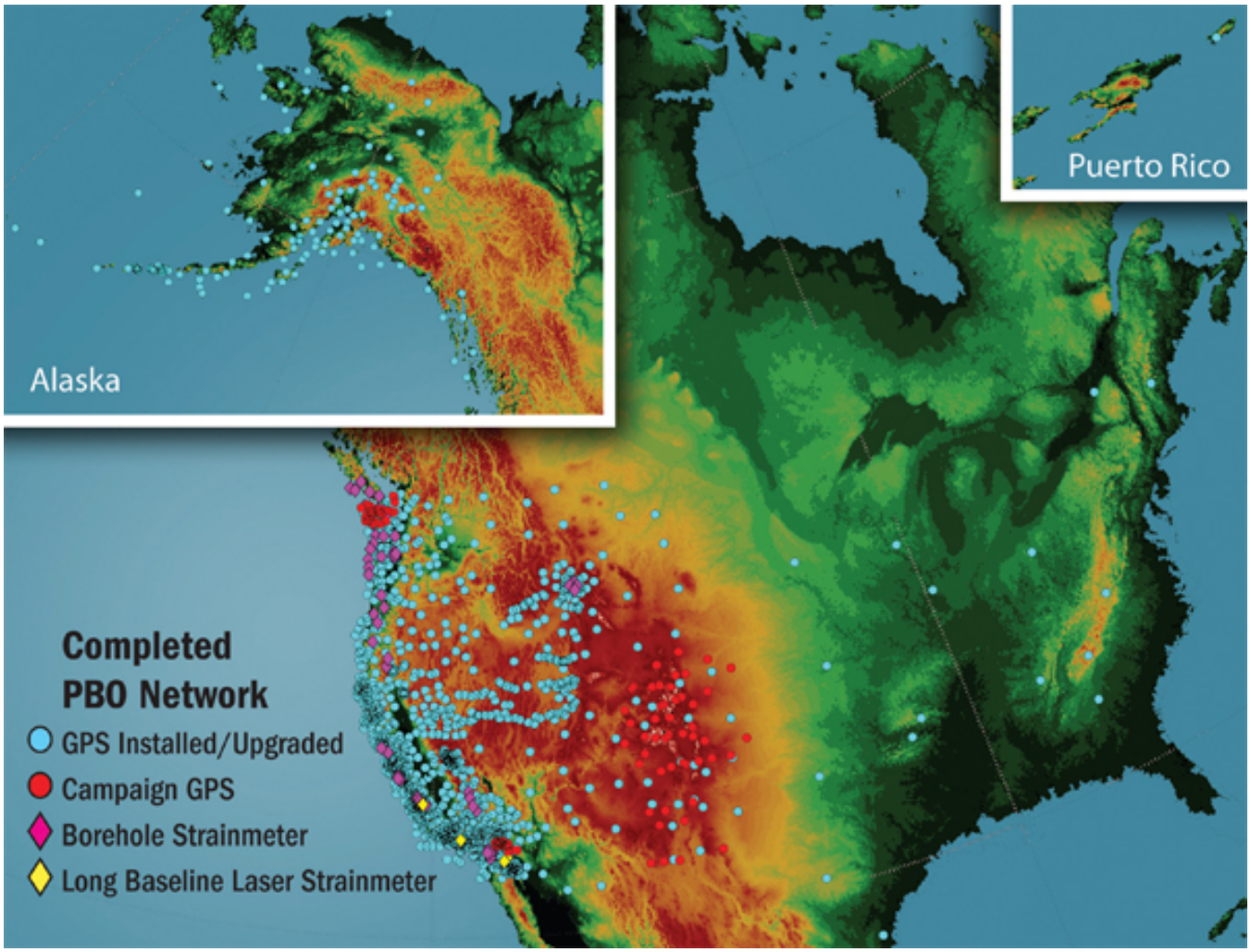

Figure 2.1.13. *Map of the Plate Boundary Observatory (PBO), from UNAVCO web page.*

Precise positions can be obtained in one of two ways. One way is to combine the data from many receivers to simultaneously estimate all station positions, receiver and satellite clock errors, and potentially the orbits of the satellites. The second way is to use satellite orbits and clock estimates from the first kind of solution and hold them fixed. In this case, single stations can be processed individually (point positioning), and the solutions from many stations concatenated together. Either way, we must also estimate propagation delays for the signal, mainly through the troposphere; these delays are dependent on atmospheric pressure and water vapor content. There are also a few other nuisance parameters like the phase ambiguities (phase biases). Today, extremely precise measurements of satellite orbits and satellite clock errors are available through the International GNSS Service (IGS), which allow easy analysis of GPS data from large numbers of sites.

At UAF, we use point positioning, using orbit and clock products from JPL. A large number of effects that contribute to the satellite-receiver distance are modeled and removed in the processing, including general relativistic corrections on the signal path, atmospheric path delays, solid earth tides, loading deformation due to ocean tides, azimuthal- and elevation-dependent variations in the phase center of the GPS antenna, and many other smaller effects. We combine solutions for hundreds of continuous GPS sites available on the internet (including some of ours), plus any sites we measure in the field ourselves, and produce a solution for the position of every site in the network. One key to the efficiency and consistency of our approach is that raw data from all sites are handled automatically and in the same manner, regardless of who collected the data. All site metadata (approximate position, antenna type, etc) are stored in a central database. This ensures that all solutions for the entire timespan of our solutions (1991 to present) are done as consistently as possible. This solution is then aligned with the ITRF2008 reference frame (a model for the position and velocity of a set of global sites that provides access to a stable global coordinate system). Individual station time series like those shown below can then be extracted from the daily network solutions.

ITRF2008 is the best approximation currently available to a geocentric coordinate system. Thus, ideally height changes in ITRF can be interpreted readily in terms of vertical movements relative to the geocenter. In practice, there is almost certainly some small error in the frame origin of ITRF. Current estimates of this error range from 0.2–1 mm/yr, primarily along the Earth's spin axes. For sites in Alaska, correcting for this error causes the northward and upward components of motion to increase slightly, in roughly equal proportions. The cause of the bias is probably related to weakness in the observation geometry of the global Satellite Laser Ranging network, which provides the accurate geocentric tie for the ITRF, or possibly from small inconsistencies between the datum constraints applied in the frame and long-wavelength vertical deformation such as GIA. The time series plots shown below have the motion of the North American plate removed, so that they show motion relative to North America. The linear trends plotted are based on a simple analysis and are not the final estimates.

PBO Site AC20 (Bird Point)

The Bird Point site AC20 (fig. 2.1.14) was built in summer 2005 and has operated without any significant data gaps. The equipment is standard for the PBO, using a Trimble Net-RS receiver and Trimble choke ring antenna (TRM29659.00) with a SCIGN radome. The exact antenna model and radome type must be known to make proper calibrations for the antenna response. Communication is via a VSAT terminal.

The AC20 position time series (fig. 2.1.15) shows northwestward motion of the site relative to the North American plate. The main cause of the northwestward trend is the elastic deformation from the locked subduction zone. There are a couple of notable deviations from a linear trend. One was at the very beginning of the time series and overlaps in time with a small slow-slip event on the plate interface (Ohta and Freymueller, AGU). The other is a southward deflection of the site's motion visible roughly over 2010–2013, after which the pre-event trend resumed. During 2010–2013 the site moved northward a little bit slower than usual. This was due to a long-lived slow-slip event beneath the Upper Cook Inlet region over that time (Fu and Freymueller, 2013); slip on the megathrust at depth there added a trenchward component to the motion over that time. Variations in the east component are not visible to the eye.

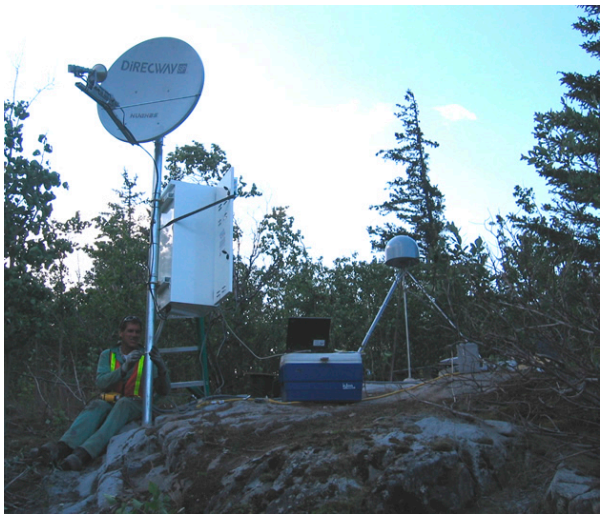

Figure 2.1.14. *Photos of PBO site AC20, all from the UNAVCO website.*

The vertical component shows uplift (at a rate of 5.8 mm/yr in ITRF2008), plus a sinusoidal signal on an annual timescale. The site uplifts faster from about April–May until October, and then subsides during the winter. This sinusoidal seasonal variation is dominantly due to snow loading, and the amplitude and phase of the signal are explained well by surface mass variation models derived from the GRACE mission data (Fu *et al.*, 2012). The vertical trend is a combination of uplift from GIA, elastic deformation from the locked subduction zone, and postseismic deformation from the 1964 earthquake.

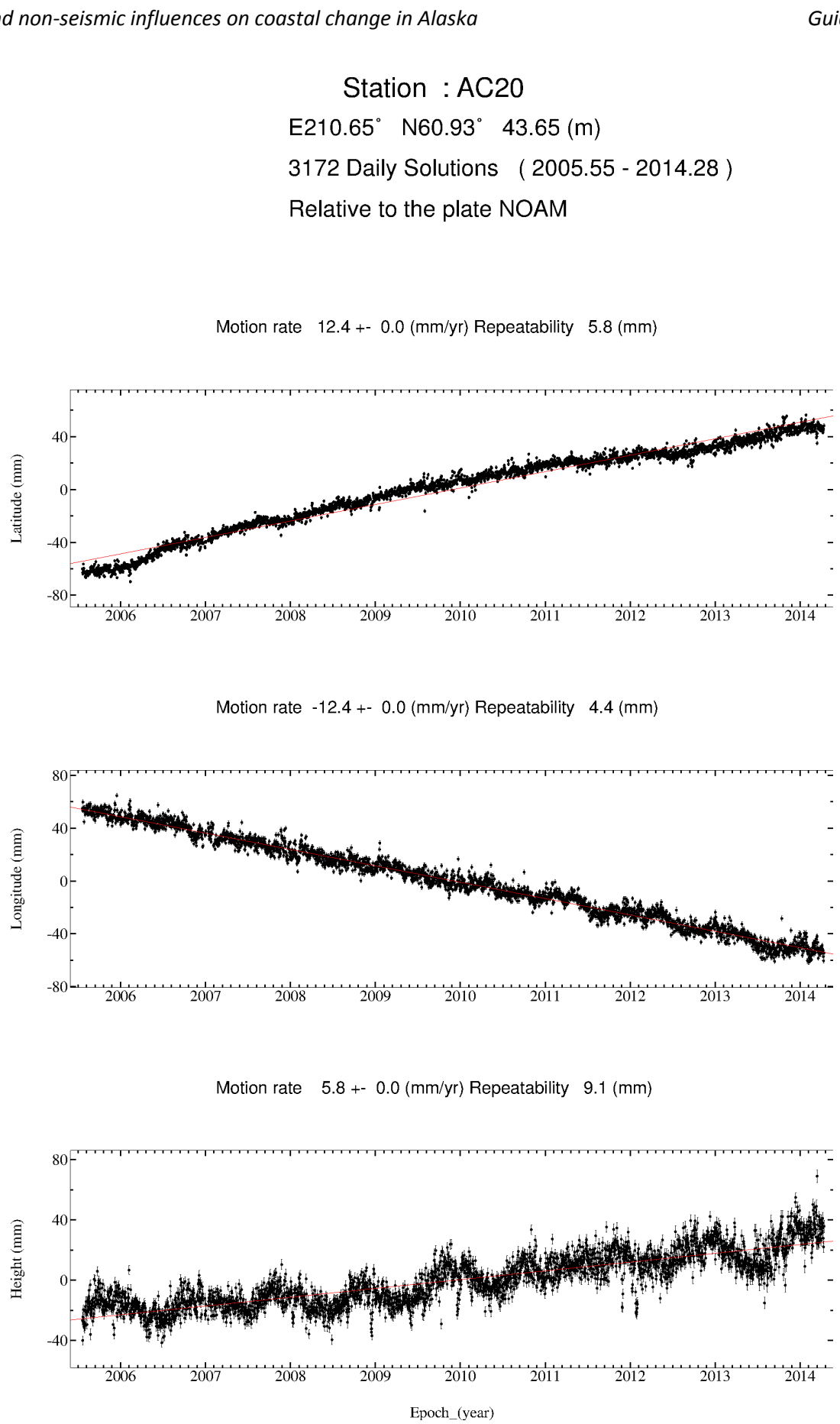

Figure 2.1.15. *Position time series for PBO site AC20, from the UAF analysis.*

PBO Site AC15 (Cooper Landing)

The Cooper Landing site AC15 (fig. 2.1.16) was built in late 2005 and has operated without any significant data gaps. The equipment is the same as for AC20.

Figure 2.1.16. *Photos of PBO site AC15, all by the author. The upper right photo shows a close-up of one leg of the drilled-braced monument.*

The contributions to the observed time series (fig. 2.1.17) are similar to those for AC20 at Bird Point, with the same causes. The average rate of motion is slightly faster than AC20 because AC15 is closer to the trench, and thus the elastic strain from the locked subduction zone is larger. The displacements from the slow-slip event are smaller at AC15 than at AC20, because AC20 is located farther from the slow-slip event. The seasonal sinusoidal signal is a little bit smaller amplitude and less consistent year to year, which indicates that AC15 is a bit farther from the main seasonal snow loading centers than is AC20.

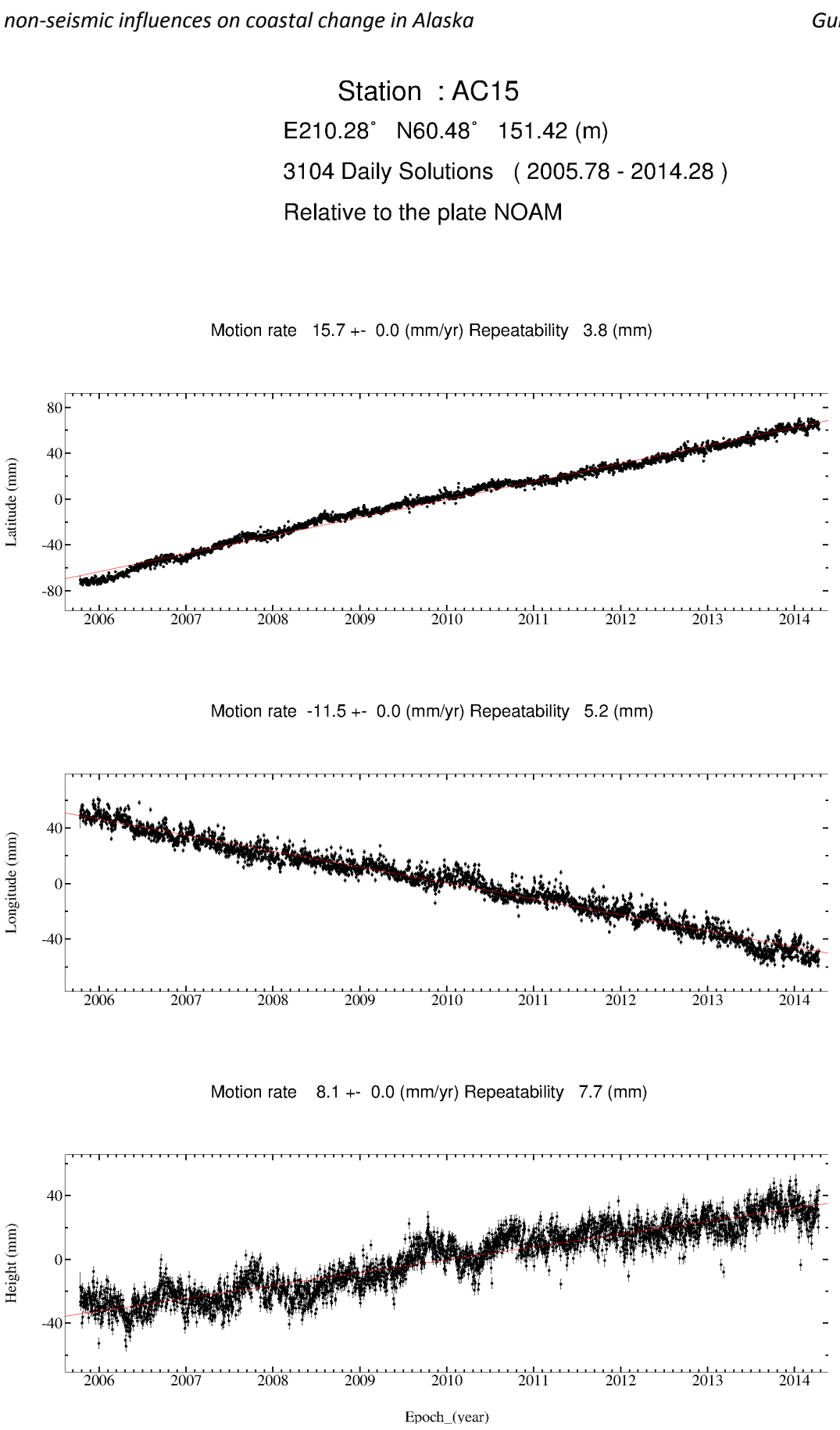

Figure 2.1.17. *Position time series for PBO site AC15, from the UAF analysis.*

CHAPTER 2.2

COASTAL PALEOSEISMOLOGY OF KENAI FJORDS NATIONAL PARK: QUICKSAND COVE AND VERDANT COVE, AIALIK BAY

Contributors: Rob Witter[8], Harvey Kelsey, Rich Briggs, Simon Engelhart, Alan Nelson, and Peter Haeussler

Introduction

In 1964 an 800-km-long rupture of the eastern Aleutian megathrust involved along-strike variations in coseismic slip that define separate segments of the megathrust. (e.g., Christensen and Beck, 1994). Megathrust slip was highest (up to 20 m) on the Prince William Sound (PWS) and Kodiak segments, and less on the Kenai segment (Suito and Freymueller, 2009). These segments also show along-strike variability in interplate coupling derived from GPS velocities in the region of the 1964 rupture (Freymueller *et al.*, 2008). GPS observations indicate that the PWS and Kodiak segments of the megathrust are locked and the Kenai segment is creeping.

In 2012, we conducted reconnaissance investigations at six sites along the southeastern coast of the Kenai Peninsula. Our investigations sought evidence for Aleutian megathrust earthquakes and tsunamis, including the 1964 event, across the boundary between the Kenai and PWS segments, which appear to accommodate plate convergence differently (Freymueller *et al.*, 2008). The aim of the research was to compare the record of prehistoric earthquakes and tsunamis along the Kenai segment to paleoseismic records from the PWS and Kodiak segments. Here we present preliminary observations from investigations at two sites in Aialik Bay.

Objectives

During our tour of Resurrection Bay, we will pass by Bear Glacier and Bulldog Cove. With this landscape as a backdrop, we will:

1. Reflect on the effects of the 1964 earthquake and tsunami along the outer coast of the Kenai Peninsula.
2. Present evidence for great earthquakes and tsunamis at Quicksand Cove.
3. Describe shoreline response to coseismic subsidence at Verdant Cove.
4. Summarize findings within the context of regional paleoseismic history.

Effects of the 1964 earthquake and tsunami on the outer Kenai coast

Few observations of the effects of the 1964 great Alaska earthquake and tsunami were documented on the remote, southeastern coast of the Kenai Peninsula. Plafker (1969) in 1964 used the upper growth limits of barnacles (*Balanus*) and marine algae (*Fucus*), the lower growth limit of terrestrial vegetation, and temporary tide gages to estimate subsidence along the outer Kenai coast, which ranged from 3.5 to 4 ft (~1.2 m) near Resurrection Bay to more than 7 ft (~2.1 m) near Nuka Island. Ghost forests along many shorelines in Kenai Fjords National Park provide visual signs of subsidence in 1964. Outside of Seward, where local tsunami impacts devastated the community, observations of tsunami inundation were few. Plafker *et al.* (1969) mapped shorelines showing 'slight damage from seismic sea waves' at Bulldog Cove, and near Calisto Head and Caines Head, where runup was estimated at 27 ft (8.2 m) and 33 ft (10.0 m), respectively. In Aialik Bay, local tsunami waves generated by submarine slumping near Pedersen Glacier reached elevations as high as 95 ft (~29 m, Plafker *et al.*, 1969).

Quicksand Cove

Quicksand Cove is at the downstream end of a drowned, glacially-cut valley on the west side of Aialik Bay. A 700-m-long, north-trending beach separates the cove from the Quicksand lowland to the west. The modern beach at Quicksand Cove is east of two forested ridges that climb in elevation seaward; each ridge has a local relief of 1.6

[8] *Rob C. Witter, U.S. Geological Survey, 4210 University Drive, Anchorage, AK, U.S.A., 99508. rwitter@usgs.gov*

m. In the wetland landward of the two beach ridges, buried organic soils evidence two episodes of submergence of the landscape followed by deposition of sand or silt.

The most obvious evidence for submergence is the fringe of dead trees (ghost forest) along the wetlands' western margin. A shallow-buried soil evident in cores and outcrops may correlate with soil in which the dead trees are rooted, but confirming this relationship in the field was difficult. In many cores, sand overlies the youngest buried soil. The youngest submergence event probably reflects coseismic subsidence along the outer Kenai coast as a consequence of the 1964 earthquake (Plafker, 1969). Therefore, we infer that the 3–15-cm-thick sand overlying the youngest buried soil on the seaward-most beach ridge is likely a deposit from the 1964 tsunami.

An older, weaker buried soil can be traced stratigraphically throughout the beach ridges and marsh. The older buried soil is recorded in cores along profile Y–Y' and also in riverbank exposures at a depth of ~50 cm. The cutbank buried soil is older than the 1964 soil because trees killed by coseismic subsidence in 1964 were rooted about 35 cm higher than the buried soil exposed in the cutbank. The older soil often is buried by sand or silty sand. We infer that the older buried soil records coseismic subsidence during the penultimate earthquake recorded at sites in PWS. Unfortunately, insufficient material for radiocarbon age analyses makes testing this hypothesis difficult.

Verdant Cove

A cobble spit in Verdant Cove has two sets of beach ridges that are distinctly different in trend and geomorphic character. One beach ridge set, most evident on the southwestern, seaward side of the spit, consists of closely spaced, north-trending, low-relief, (< 1 m high) ridges that are oriented obliquely to the shoreline. These oblique ridges reflect westward progradation of the coastal plain. The other set of beach ridges consists of three 1–3-m-high ridges that parallel the modern coastline and have a prominent escarpment on the seaward side. The coastward-most escarpment forms the seaward side of the active beach ridge and the two landward escarpments separate the composite strand plain into three surfaces.

Mann and Crowell (1996) reported the burial of a conifer forest by high-energy beach deposits in Verdant Cove about 800 years ago. Evidence included stumps of mountain hemlock, a salt-intolerant tree, buried below tide level exposed in a tidal pond on Verdant Cove spit. They concluded the evidence reflected 1–3.5 m of rapid subsidence that suddenly shifted the environment from upland forest to intertidal cobble beach. They likened the event to the observed subsidence at Verdant Cove in 1964 that dropped the area by 1.4 m.

We interpret the steep, seaward-facing escarpments and high beach ridges together as the signature of shoreline response to repeated episodes of coseismic subsidence during great earthquakes on the eastern Aleutian megathrust. Three earthquakes interrupted progradation of the strandplain on the Verdant Cove spit: The 1964 earthquake and two earlier events. In the time period between earthquakes, the Verdant Cove strand plain prograded westward, leaving behind beach ridges oriented obliquely to the shoreline. Infrequently, on the scale of once every several hundred years, the coastline suddenly subsided 1–2 m as a consequence of rupture on the eastern Aleutian megathrust. As a result of the corresponding sudden rise in relative sea level, the shoreline shifted landward and a new, higher active beach ridge formed. The beach ridges formed in response to coseismic subsidence are higher than beach ridges immediately to the interior. The steep seaward escarpments and high ridges were abandoned during interseismic periods when the strand plain prograded eastward.

Summary of Findings

Reconnaissance investigations at six sites along the southeastern coast of the Kenai Peninsula identified two types of environments that record evidence for the 1964 earthquake and tsunami as well as potential evidence for prehistoric great earthquakes. The two kinds of environments include: (1) stream deltas impounded behind barrier beaches in fjord embayments; and (2) prograding strandplains formed of a series of beach ridges that increase in elevation seaward.

The wetland at Quicksand Cove represents the first type of environment that shows promise for paleoseismic evidence. Stands of dead trees drowned by submergence provide evidence for coseismic subsidence in 1964. The

1964 tsunami deposited sand that buried a forest soil on the seaward-most beach ridge. Buried organic sediment (soil?) in cores from the back-barrier wetland suggests that one earlier earthquake also subsided the site.

Three beach-parallel scarps in the cobble spit of Verdant Cove exemplify an environment holding additional paleo-seismic evidence. Here, building on the original study of Mann and Crowell (1996), we infer that scarps on the spit record the shoreline response to coseismic subsidence during the 1964 earthquake and two earlier events.

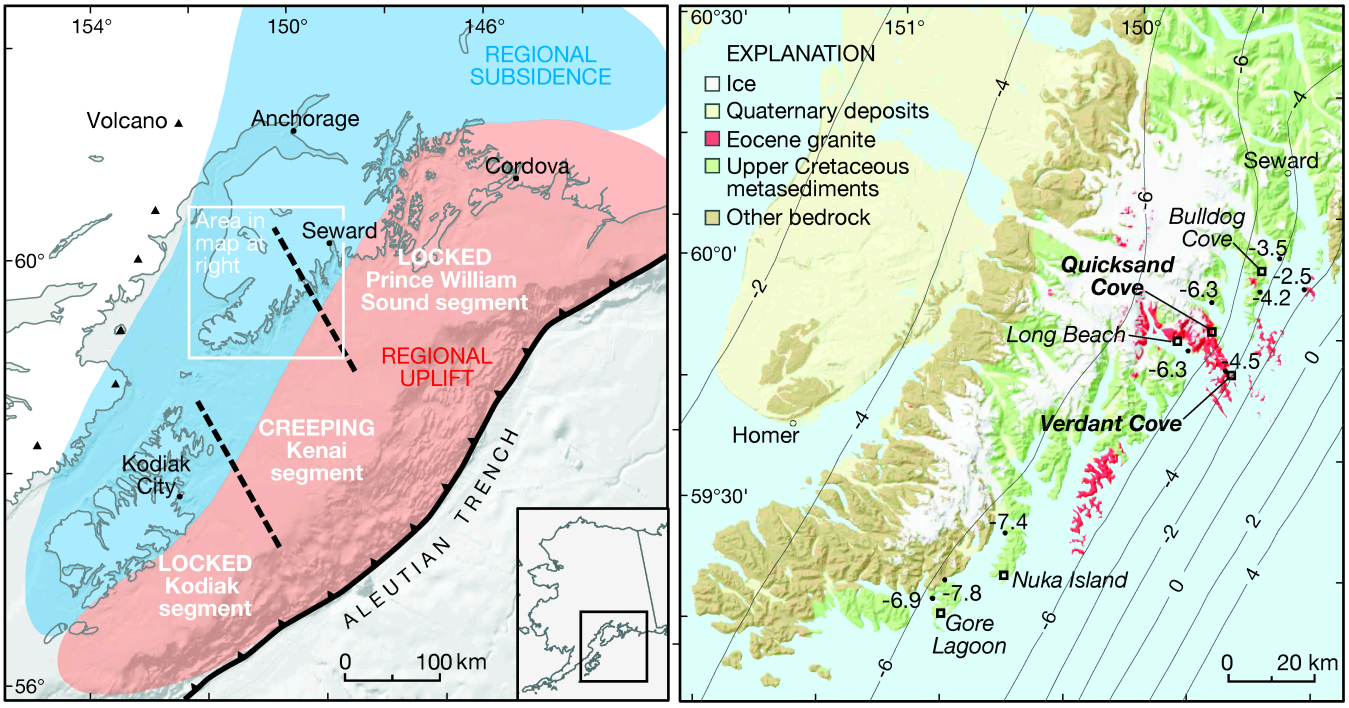

Figure 2.2.1. a. *Tectonic setting of the eastern Aleutian megathrust. Vertical deformation during the 1964 great Alaska earthquake included two margin-parallel belts of landward subsidence (blue) and seaward uplift (red). Areas of highest slip occurred below the Prince William Sound and Kodiak segments, which are thought to be locked currently (see fig. 2.2.2). The intervening Kenai segment is creeping presently.* ***b.*** *Geologic map of the Kenai Peninsula. We visited six sites along the outer coast of the Kenai Peninsula in August 2012. Two sites yielded the most promising evidence for prehistoric great earthquakes: Quicksand Cove and Verdant Cove. Contours and black circles depict vertical displacement (in feet) in 1964 (Plafker, 1969). Geology from Wilson and Hults (2007).*

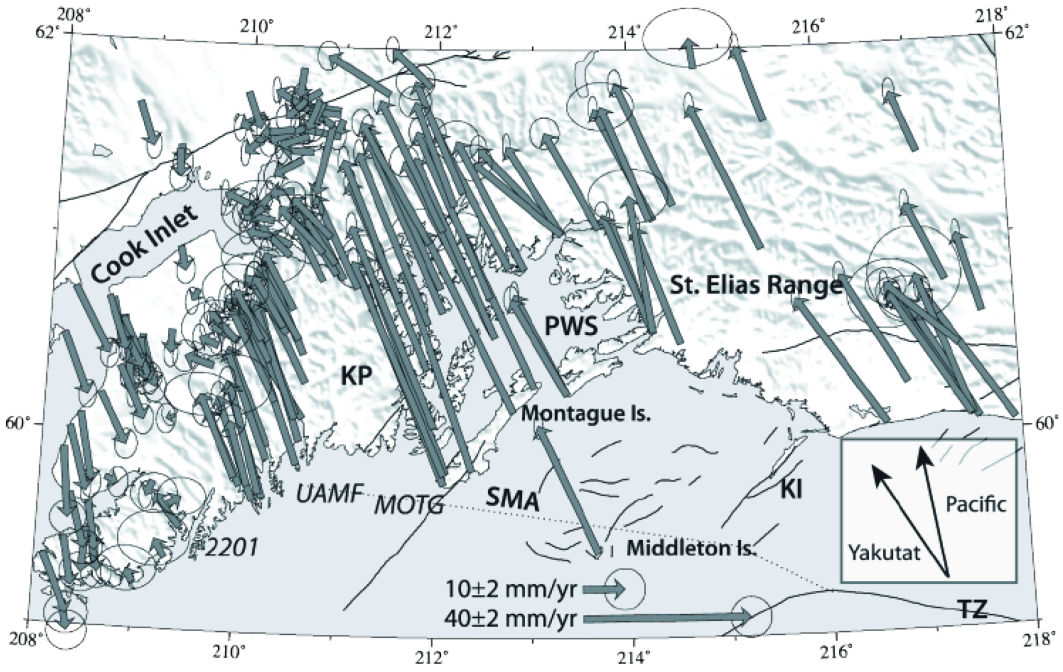

Figure 2.2.2. *Horizontal GPS velocities. The map by Freymueller et al., 2008, shows horizontal velocities from Prince William Sound (PWS), the Kenai Peninsula, and Upper Cook Inlet. South- to southeastward-directed velocities on the western Kenai Peninsula have been interpreted as evidence for creep on the megathrust between the locked PWS and Kodiak segments.*

Figure 2.2.3. *Fieldwork at Quicksand Cove. We collected and described cores and outcrops of wetland sediment. Core site elevations and a topographic profile of the site were collected with a GPS real-time kinematic survey.*

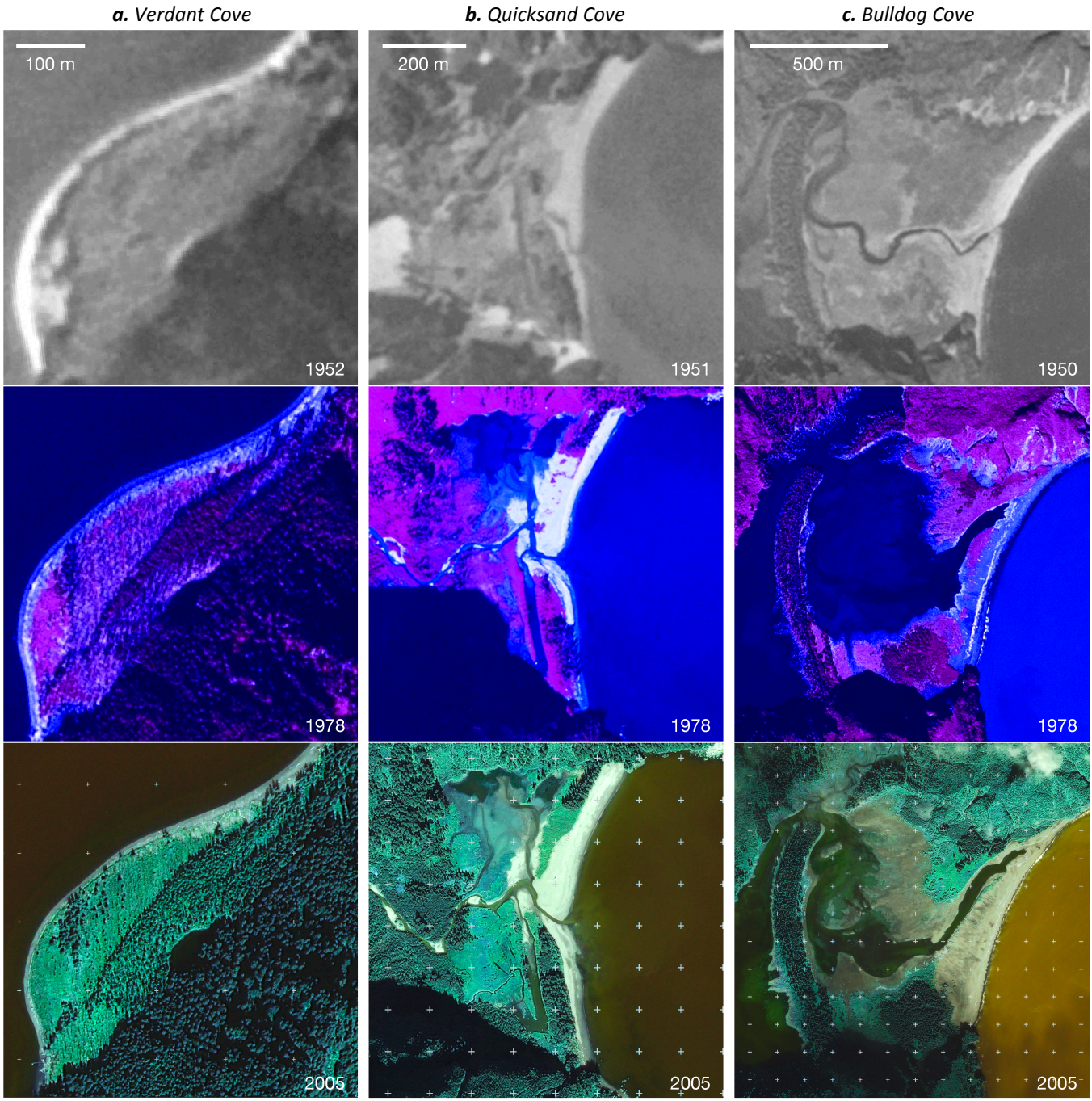

Figure 2.2.4. a. *Aerial images of Verdant Cove spit before (top) and after (middle) the 1964 earthquake. Post-earthquake observations by Plafker (1969) documented 4.5 ft (~1.4 m) of subsidence at Verdant Island, 2 km north of the spit. Lower image from 2005 shows a series of beach scarps oriented subparallel to the shoreline and obliquely oriented constructional beach ridges.* ***b.*** *Aerial images of Quicksand Cove before (top) and after (middle) the 1964 earthquake and in 2005 (lower image). Plafker (1969) documented 6.3 ft (~1.9 m) of subsidence at sites nearby.* ***c.*** *Aerial images of Bulldog Cove before (top) and after (middle) the 1964 earthquake and in 2005 (lower image). Plafker (1969) documented 6.3 ft (~1.9 m) of subsidence at sites nearby.*

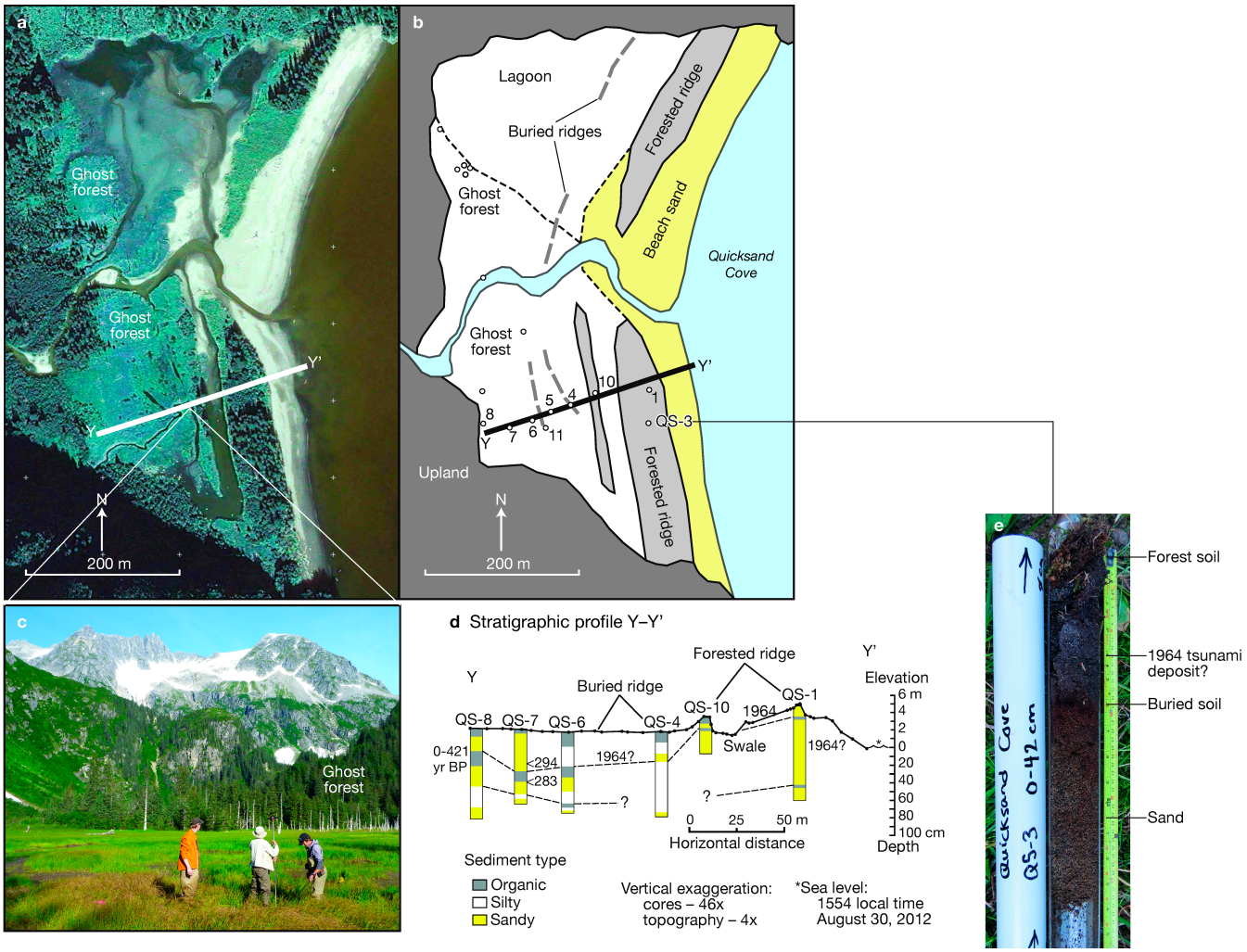

Figure 2.2.5. *Evidence for the 1964 earthquake and tsunami at Quicksand Cove.* ***a.*** *Aerial image of Quicksand Cove in 2005 showing the prominent forested ridge backing the active beach and ghost forests of standing dead trees.* ***b.*** *Geomorphic map of depositional environments at Quicksand Cove. Sediment cores are marked by open circles. Bold dashed lines mark buried beach ridges.* ***c.*** *Photograph looking west from the middle of profile Y–Y', showing standing dead trees of the ghost forest.* ***d.*** *Stratigraphic profile across the southern part of Quicksand Cove wetland.* ***e.*** *Core QS-3 (location in 5b), showing buried soil and overlying sand deposit probably deposited by the 1964 tsunami.*

CHAPTER 3

CHAPTER 3.1

PORTAGE VALLEY: LITTLE ICE AGE MORAINES AND CURRENT GLACIER RETREAT

by Bruce Molnia[9]

Introduction

We will visit several glaciers in the Chugach and Kenai mountains. Those who flightsee to Bering Glacier may also see some of the glaciers of the western St. Elias Mountains. Glaciers that all participants will 'visit' include Portage Glacier, Bear Glacier, and Sheridan Glacier. We may see Aialik and Pedersen glaciers as we travel along the Kenai Mountains coastline. We may also catch a glimpse of Tebenkof Glacier on our ferry ride to Cordova. Additionally, we will see many small cirque and hanging glaciers on the valley walls in Turnagain Arm, on the slopes above the Seward Highway, on the mountains surrounding Resurrection Bay, on mountains throughout Prince William Sound, and on the mountains in the Cordova area. This summary presents information about recent Alaskan glacier behavior and descriptions of some of the glaciers that we will 'visit.'

Recent Glacier Behavior

Glaciers cover ~75,000 km^2 of Alaska, or more than 5 percent of the State. They are present on 11 different mountain ranges and on three island areas. The exact number of Alaskan glaciers is unknown, only now being systematically mapped and counted by the Randolph Glacier Inventory (Arendt and others, 2012). The number probably exceeds 25,000. About 2,000 are valley glaciers that descend to elevations below 1,500 m. Since the 1890s, fewer than 800 of these glaciers have been officially named by the U.S. Board on Geographic Names. Alaska's glaciers range in size from tiny cirque glaciers to massive piedmont glaciers such as Bering Glacier and Malaspina Glacier, each larger than the State of Rhode Island. According to Grinsted (2013), if melted, Alaska's glaciers would cause the global ocean to rise 44.6 mm.

Alaska's climate is changing and one of the most significant indications of this change has been the late 19th to early 21st century behavior of Alaska's glaciers. First-order, standardized, weather station temperature data collection began in Alaska in the late 1940s. These temperature data document that since about 1950, average annual air temperatures have increased ~2.0°C statewide, with a dramatic warming trend beginning in the mid-1970s. Aside from instrument temperature records, perhaps the most significant other indication that southern Alaska regional climate has changed during the late 19th to early 21st century has been the change in glaciers. Photographic documentation of changes in the health of the region's glaciers began during the last quarter of the 19th century and by 1920, photographs had been made of more than 350 southern Alaskan glaciers. This visual record shows that long before an instrument record was started nearly every glacier photographed was retreating. This response, with retreat beginning in some regions a century or more before the beginning of the photographic record, suggests that a significant increase in temperature began to impact glacier area, length, and volume much earlier than the mid 20th century, perhaps in places as early as the mid 18th century.

To determine the magnitude and pattern of response of glaciers to this regional warming trend, a comprehensive analysis (Molnia, 2007, 2008) was made of the recent behavior of hundreds of glaciers located in the 11 Alaska mountain ranges and three island areas that currently support glaciers. Since very few Alaskan glaciers have systematic mass balance observations, and not all have adequate photographic records, determination of recent glacier behavior had to be based on the analysis of proxy data, including: maps; historical observations beginning in the late 18th century; dendrochronology and vegetation proxy data; and the thousands of ground- and aerial-

[9] *Bruce Molnia, U.S. Geological Survey, 12201 Sunrise Valley Drive, Reston, VA, U.S.A., 20192. bmolnia@usgs.gov*

photographs and satellite images. Results of these analyses were synthesized to provide an understanding of changes in the length, area, and thickness of as many individual glaciers as possible, for as long as possible.

In Alaska, ground photography began in 1883; aerial photography began in 1926, with the first statewide coverage completed by the early 1960s; and satellite imagery collection began in the early 1960s, with systematic Landsat imaging beginning in 1972. Therefore, determinations for about 2,000 glaciers could be produced based on the empirical observation of combinations of glacier extent, thickness, area, and volume data. In most areas analyzed, every glacier that descends below an elevation of ~1,500 m is currently thinning and/or retreating. Many glaciers have an uninterrupted history of continuous post-Little-Ice-Age retreat that spans more than 250 years. Others are characterized by multiple late 19th to early 21st century fluctuations.

Today, thinning and/or retreating glaciers represent more than 98 percent of the glaciers examined. In Alaska, only about a dozen lower-elevation glaciers are currently advancing and thickening. All are located less than 100 km from the Gulf of Alaska, in the Coast Mountains, St. Elias Mountains, Chugach Mountains, and the Aleutian Range. Many of the currently advancing glaciers are or were formerly tidewater glaciers. Several of these glaciers have been expanding for more than two centuries. Statewide, the present extent of Alaskan glaciers is reduced perhaps as much as 20 percent from the Little Ice Age maximum extent.

The area of Alaska's glaciers is:

- ~1/3 the glacier area of Canada
- ~1/2 the glacier area of Asia
- ~the same glacier area as Russia
- ~2.5 times the glacier area of China and Tibet
- ~3 times the glacier area of South America
- ~6 times the glacier area of Iceland
- ~12 times the glacier area of Europe
- ~75 times the glacier area of New Zealand
- ~100 times the glacier area of the rest of the U.S.
- ~1,000 times the glacier area of Africa

Chugach Mountains

Anchorage is bounded on the east by the Chugach Mountains. The Chugach Mountains are a 400-km-long by 95-km-wide mountain range that extends from Turnagain Arm and Knik Arm on the west to the eastern tributaries of Bering Glacier, Tana Glacier, and Tana River on the east. On the north, the Chugach Mountains are bounded by the Chitina, Copper, and Matanuska Rivers. On the south, they are bounded by the northern Gulf of Alaska and Prince William Sound. According to Post and Meier (1980), the Chugach Mountains contain about one-third of the present glacierized area of Alaska, ~21,500 km^2, and include one of the largest glaciers in continental North America, Bering Glacier. The Bering Glacier system, which includes the Bering's piedmont outlet lobe and the Steller Glacier, has an area of ~5,200 km^2 (Viens, 1995; Molnia, 2001). The eastern part of the Chugach Mountains is covered by a continuous series of connected glaciers and accumulation areas (Field, 1975). With a few exceptions, this region has experienced a significant 20th century retreat of its glaciers (Meier, 1984; Molnia and Post, 1995; Arendt and others, 2002; Meier and Dyurgerov, 2002).

A study by Sauber and others (2000) examined the effect of this regional ice loss on crustal deformation in the eastern Chugach Mountains. Recognizing that the annual thinning of glaciers in this region ranges from 1–6 m, they calculated that uplift in ablation regions of these glaciers ranges from 1–12 mm/yr, the greatest uplift located just east of the Chugach Mountains, in the Icy Bay region. Sauber and Molnia (2000, 2004) hypothesized that continuing loss of glacier ice volume could lead to a future increase in very-low-magnitude earthquakes. For a more complete discussion of this rapid viscoelastic uplift in southeastern Alaska caused by post-Little Ice Age glacial retreat, see Larsen and others (2005).

Kenai Mountains

The Kenai Mountains, with maximum elevations approaching 2,000 m, are a 195-km-long by 35-km-wide mountain range that extends southwest from Turnagain Arm, Portage Pass, and Passage Canal to the southern end of the Kenai Peninsula. Most of the Kenai Mountain glaciers are located in two large icefields, the Sargent and the Harding Icefields, and two smaller unnamed icefields, here informally called the Blackstone–Spencer and the Grewingk–Yalik. A number of other, generally smaller, glaciers descend from other isolated accumulation areas along the crests of many ridges and mountains.

Wiles, Barclay, and Calkin (1999), and Barclay, Calkin, and Wiles (1999), performed dendrochronological studies at a number of Kenai Mountain tidewater and former tidewater glacier locations, including Tebenkof, Cotterell, Taylor, Wolverine, Langdon, Kings, Nellie Juan, Ultramarine, Princeton, Excelsior, and Ellsworth glaciers. Their work involved both living trees, some more than 680 years old, and a 1,119-year tree-ring-width chronology derived from more than 100 logs, recovered from about a dozen glaciers in the western Prince William Sound area. Each of these logs had been sheared or uprooted by a past glacial advance. Their work showed that glacier fluctuations during the Little Ice Age were strongly synchronous on decadal time scales at many glaciers. Studies at eight locations indicated that advances occurred during the late 12th through 13th centuries and from the middle 17th to early 18th centuries. Nine glaciers showed evidence of a late 19th century advance.

The Harding Icefield has a maximum length of 80 km, a maximum width of about 50 km, and an area of about 1,800 km^2. It is the largest of the icefields in the Kenai Mountains and the largest single icefield located completely in the United States. The icefield has nearly 40 glaciers, 16 of which are outlet glaciers with lengths greater than 8 km. These glaciers have an area of about 1,380 km^2. Four of these glaciers (Bear, with a length of 26 km; Nameless Glacier, with a length of 29 km; Tustumena Glacier, with a length of 32 km; and Skilak Glacier, with a length of 34 km) exceed 25 km in length. Meier and Post (1962) estimated the icefield's ELA to be about 600 m and determined that the AAR was 0.68. Most of the northward-draining glaciers are unnamed and drain into the Resurrection River or Skilak Lake. Southward-draining glaciers generally reach sea level or near to it. Many others, including Aialik Glacier at the head of Aialik Bay, and Holgate Glacier in Holgate Arm of Aialik Bay, Northwestern, Anchor, and Ogive glaciers in Northwestern Fiord, and McCarty Glacier in McCarty Fiord have, or recently had, tidewater termini. Little Holgate Glacier had a tidewater terminus in the late 1990s but retreated from tidewater by 2001. In 1994 and 1996, Aðalgeirsdóttir, Echelmeyer, and Harrison (1998), obtained airborne surface elevation profiles of 13 Harding Icefield glaciers and the icefield's upper accumulation area. These were compared to 1:63,360-scale topographic maps and the aerial photographs, dating from 2 August 1950 and 15 August 1952. They conclude that the icefield has been thinning and shrinking since the 1950s, with a loss of about 34 km^3 of ice in the ~43-year period between being mapped and profiled. This corresponds to an icefield-wide lowering of about 21 m, the equivalent of an average mass balance of -0.4 m/yr of water. They also conclude that the rate of surface elevation change between 1994 and 1996 is significantly greater than the long-term average. The glaciers that they profiled were Aialik, Bear, Exit, Holgate, Skilak, Tustumena, Chernof, Dinglestadt, Kachemak, Little Dinglestadt, McCarty, Northeastern, and Northwestern Glaciers.

Portage Glacier

In the mid 1990s, Portage Glacier, a small lacustrine calving valley glacier with a 1914 length of ~4.25 km, retreated around a bend in its valley and disappeared from view from the Begich, Boggs Visitor Center, a U.S. Forest Service facility constructed on the position of a late 19th to early 20th century Little Ice Age (LIA) moraine. Prior to the late 18th century, the glacier was significantly shorter and its terminus was located several kilometers to the southeast of its LIA maximum location. This permitted an ice-free passage, a portage, between Turnagain Arm and Prince William Sound.

At the beginning of the 19th century, Portage Glacier was advancing. According to Tarr and Martin (1914), it reached its most recent maximum position about 1880. Crossen (2007) describes this LIA advance, and states that from 1799 to 1911 Portage Glacier completely filled the present Portage Lake basin and deposited three large moraines downvalley (west) of the modern lake shoreline. Viereck (1967) dates this maximum, based on botanical

evidence, at about 1895. A portage was still possible, but it required an over-ice journey of more than 7 km (Mendenhall, 1900). During this period, Portage Glacier's terminus bifurcated and a limb of the then-much-thicker glacier, the Passage Canal Arm of Portage Glacier, extended about 1.5 km into a side valley, flowing toward the head of Passage Canal.

The current Portage Lake, which is ~5 km long and 2 km wide, began to form in 1914 after the glacier retreated from the location of the 1852 AD moraine (Crossen, 2007). Schmidt (reported in Field, 1975), determined that the basin had a maximum depth of 181 m at a location about 300 m in front of the 1964 terminus position. When photographed in 1914, the presence of a small ice-marginal lake indicated that the terminus had retreated several hundreds of meters on its southwest side. When described in 1939 by Barnes (1943), Portage Glacier had a length of ~10 km and its terminus was located ~500 m behind the 1914 position of the glacier. By 1950, the date of the first USGS map of the area, the terminus retreated about 2.5 km from the 1914 position, an average retreat rate of ~70 m/yr. By the end of the 20th century, the glacier retreated nearly another 2 km, exposing about 4 km of the lake basin. The deep water of the lake caused calving to become the dominant ablation process. Crossen (2007) reports that from 1799 to 1914, the retreat rate averaged 3.8 m/yr when the ablation regime was dominated by melting. From 1914 to 1994, with calving as the dominant process, the rate increased to 56.3 m/yr. Since 1994, the terminus of Portage Glacier has become stabilized where it rests on bedrock at the east end of the lake. According to Crossen (2007), the glacier's mass balance is such that ice still flows to the terminus and calves into the lake, while the terminus remains in approximately the same location.

Figure 3.1.1. *Four photographs of Portage Glacier.* ***A.*** *Early 20th century (unknown photographer, "L.E.S.").* ***B.*** *1958 photo (provided by National Oceanic and Atmospheric Administration [NOAA]).* ***C.*** *Early 1980s (photo by B. Molnia).* ***D.*** *Taken in 2007 from near the location of the Begich, Boggs Visitor Center, adjacent to the 1914 moraine (photo by B. Molnia).*

Much of the ice that flowed toward Passage Canal was contributed by Burns Glacier, then a Portage Glacier tributary that entered it from the east. With retreat and thinning, this limb disappeared early in the 20th century. Burns Glacier maintained contact with Portage Glacier until the early 1980s, when its continued thinning caused it to lose contact. Its terminus is now more than a kilometer from the closest lake shoreline.

The Begich, Boggs Visitor Center was opened to the public in 1986 and rededicated with new exhibits in 2001. It offers a unique opportunity to learn about the Chugach National Forest, America's second largest national forest. The Visitor Center contains exhibits, educational presentations, the film "Retreat and Renewal: Stories from Alaska's Chugach National Forest," information services, and an Alaska Natural History Association bookstore.

Figure 3.1.2. *Two photographs of Portage Glacier, both taken with about the same perspective, showing changes in the terminus and Portage Lake between 1914 and 2004.* ***A.*** *1914 photograph of Portage Glacier taken from near the summit of Maynard Mountain. The glacier is about 4 km longer than present and fills much of today's Portage Lake (NOAA photo archive).* ***B.*** *2004 oblique aerial photograph of Portage Lake taken from above the summit of Maynard Mountain. The glacier is barely visible at the upper right end of the lake. It has retreated about 4 km since 1914 (photo by Gary Braasch).*

Figure 3.1.3. *Three oblique aerial photographs of Portage Glacier, taken by Bruce Molnia, showing changes in the terminus and Portage Lake between 1978 and 2011.*

Figure 3.1.4. *July 28, 2011, oblique aerial photograph of Explorer Glacier, a small retreating hanging glacier, located at the mouth of Portage Valley (photo by B. Molnia). Large, well-preserved lateral moraines indicate the Little Ice Age extent of the glacier.*

Bear Glacier

Bear Glacier was first mapped by Grant and Higgins (1913) on July 20–21, 1909. Then, 26-km-long Bear Glacier sat at the head of an outwash plain-sand flat, a maximum of about 300 m from the shore of Resurrection Bay The central part of the terminus was much closer to the Bay. Grant and Higgins stated, "Along the center of the ice front, high tides reach the glacier." An earlier trimline, seaward of the 1909 position, was dated by Viereck (1967), as having formed between 1835 and 1845. Trees beyond it were as much as 350 years old. By 1950, the glacier retreated an additional 400 m and a small ice-marginal lake developed along its east margin.

During the second half of the 20th century, the glacier retreated about 1.5 km. Aðalgeirsdóttir, Echelmeyer, and Harrison (1998), using only two temporal reference points, report that between the 1950s and the middle 1990s, Bear Glacier with a 1950 s area of 228.5 km^2, had its terminus retreat 1,550 m, its area decrease by 8.75 km^2, its volume decrease by 9.7 km^3, and its average elevation decrease by 38.4 m. They report that its mean annual mass balance was -0.7 m. For the same period, on an annual basis, Bear Glacier thinned by 0.872 m, had its volume decrease by 0.195 km^3, and shortened by 36 m/yr (personal commun., March 2001, K.A. Echelmeyer, W.D. Harrison, V.B. Valentine, and S.I. Zirnheld, University of Alaska Fairbanks). Since about 2000, parts of the terminus, which had been thinning rapidly, decreased in thickness to the point where terminus flotation began and calving by disarticulation (rapid retreat through passive calving) began and became the dominant retreat mechanism. This retreat was characterized by the shedding of large numbers of tabular icebergs, some up to 600 m in maximum dimension. It continues today. Between 2001 and 2005, the terminus retreat was a maximum of ~3.0 km.

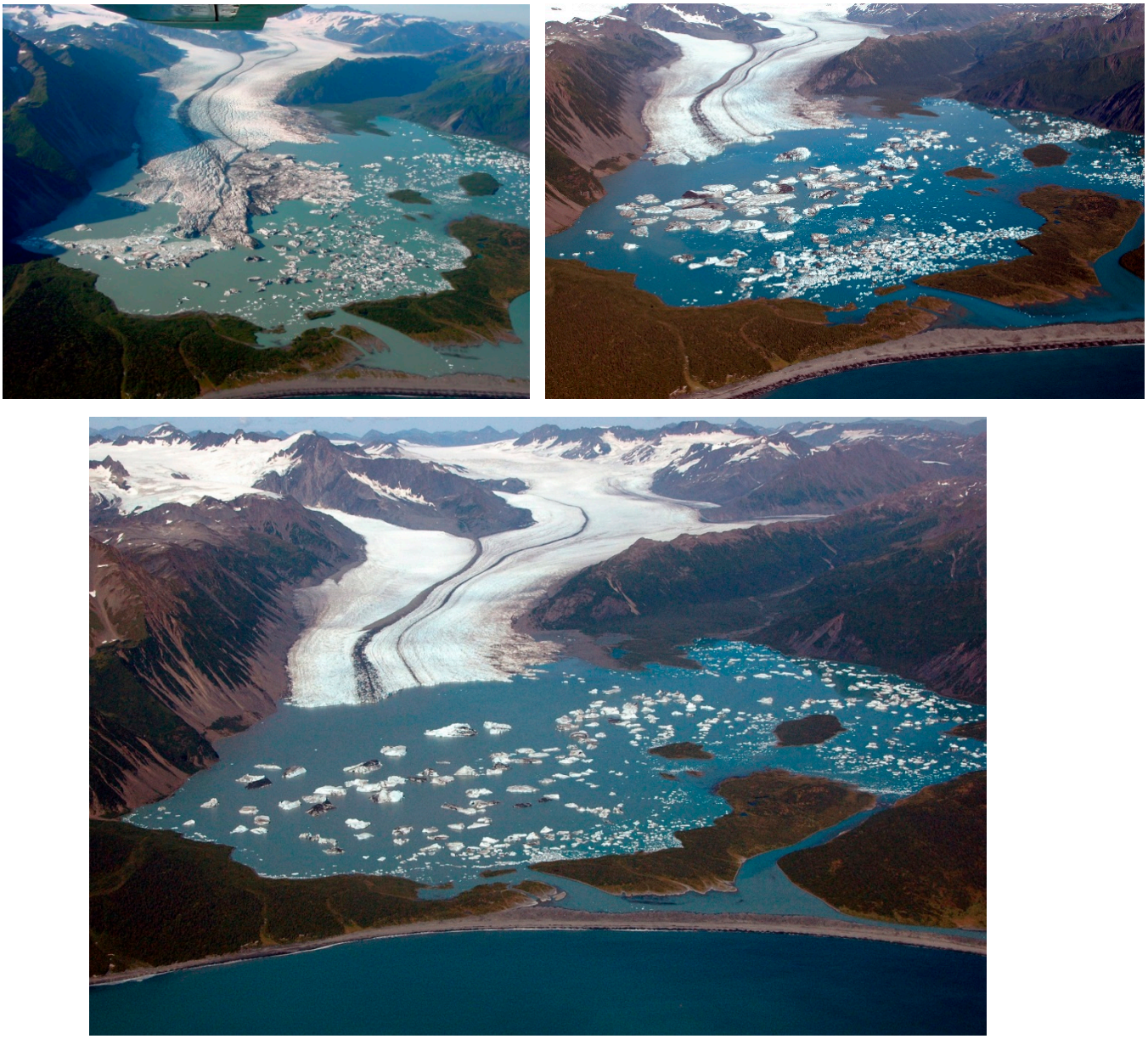

Figure 3.1.5. *First three of four oblique aerial photographs by Bruce Molnia, showing changes in the terminus of Bear Glacier, Kenai Mountains, Kenai Fjords National Park, Alaska, during the nine-year period between 2002 and 2011.* ***A.*** *The September 2, 2002, oblique aerial photograph is taken toward the north and shows the retreating, calving terminus of the glacier, located at the head of a large ice-marginal lake, informally named Bear Lake. Prior to 1950, the entire basin of Bear Lake was filled by Bear Glacier's piedmont lobe. By 1961, a small lake occupying less than 10 percent of the basin had developed adjacent to the southeast margin of the glacier. By 1984, the lake nearly doubled in size. In the 18 years between 1984 and September 2002, the lake quadrupled in size. The triangular-shaped terminus of the glacier depicted here has retreated at least 2 km from its 1984 maximum position. The large tabular icebergs and the low relief, low-gradient terminus suggest that the terminus has thinned so much that much of its lower reaches are afloat. Floating glacier termini typically retreat rapidly and calve large, tabular icebergs.* ***B.*** *August 6, 2005 photo. During the 35 months between photographs A and B, the triangular-shaped terminus of the glacier retreated more than 3 km with the large triangular lobe disappearing, the result of intensive passive calving. The glacier has also thinned by about 10 m. The large, tabular icebergs that are present are evidence of the continued rapid disarticulation of the glacier's terminus.* ***C.*** *August 13, 2007 photo. From 2005 through 2007, the terminus continued to retreat through passive calving, although at a slower rate than prior to 2005. A few of the large, tabular icebergs are remnants of even larger icebergs present in 2005; others are the result of continuing disarticulation of the glacier's western terminus. In the 24 months between images, the western margin of the glacier retreated more than 0.4 km.*

Figure 3.1.5. *Fourth of four oblique aerial photographs by Bruce Molnia, showing changes in the terminus of Bear Glacier, Kenai Mountains, Kenai Fjords National Park, Alaska, during the nine-year period between 2002 and 2011.* ***D.*** *July 28, 2011 photo. From 2007 through 2011, the terminus continued to slowly retreat through passive calving. In the 47 months between images; the western margin of the glacier retreated less than 0.1 km.*

Tebenkof Glacier

Named for the last Governor-General of Russian America, Tebenkof Glacier is 12.5 km long with an area of about 28 km^2. It drains into Blackstone Bay near its mouth. Until the 19th century, it had a small piedmont lobe and probably a tidewater terminus. Today, it is fronted by several ice-marginal lakes and a large outwash plain that separate it from the bay. During the 20th century, Tebenkof Glacier retreated more than 4.0 km and thinned by several hundred meters. Like all of the other glaciers in Blackstone Bay, it continues to retreat and thin. Wiles, Barclay, and Calkin (1999), found evidence of several advances of Tebenkof Glacier during the past 1,500 years. Seven logs, found ~1.5 km in front of the 1992 ice margin, that grew between 328 AD and 695 AD suggest an early glacial advance, dating at ~700 AD (~1,300 years BP). Twelve logs, found between 0.7 km and ~1.5 km in front of the 1992 ice margin, and which grew between 960 AD and 1300 AD, suggest a second glacial advance, beginning between 1289 AD and 1300 AD (~700 years BP). Another group of 11 logs killed between 1633 AD and 1653 AD, suggest a third advance ~350 years BP. Their analysis of recent moraines suggests that ice retreat from this ~350-year-old maximum position began prior to 1891. They state that "…the 1891 maximum was the greatest extent of Tebenkof Glacier since at least AD 1189." They also document an 1891 to 1992 retreat of 2.7 km, with an additional kilometer of retreat between 1983 and 1992.

Aialik Glacier and the glaciers of Aialik Bay

Named glaciers in Aialik Bay include Aialik, Addison, Pedersen, and Holgate glaciers. Depending on how far to the west our Day 2 boat trip to the outer coast of the Kenai Peninsula goes, we may see some of these glaciers. Aialik Glacier, with a length of 11 km, is a tidewater glacier at the head of Aialik Bay. Since July 1909, when first investigated and mapped by Grant and Higgins (1913), and the present, the terminus position has fluctuated more than 0.5 km. However it is currently very close to the 1909 mapped position. Then, as today, Aialik was a tidewater, calving glacier that showed a large area of exposed bedrock along its southwest margin. Grant and Higgins state that the glacier may have retreated as much as 400 m in the decade prior to 1909. Aðalgeirsdóttir, Echelmeyer, and Harrison (1998) report that between the 1950s and middle 1990s Aialik Glacier, with a 1950s area of 118 km^2, had its terminus advance 540 m, but experienced no change in area. Its 1950–~1995 ice volume decreased by 2.6 km^3, its average elevation decreased by 11 m, and its mean annual mass balance was -0.2 m. On an annual basis, Aialik Glacier thinned by 0.25 m, had its volume decrease by 0.023 km^3, and lengthened by 13 m/yr (personal commun. March 2001, K.A. Echelmeyer, W.D. Harrison, V.B. Valentine, and S.I. Zirnheld, University of Alaska Fairbanks). About 300 m of the post 1950s retreat occurred between 1950 and 1964 (Field, 1975). Since the mid 1990s, the terminus has retreated several hundred meters. Aialik Glacier has a width at its face of 1.6 km, and an AAR of 0.88.

Pedersen Glacier

Pedersen Glacier has been retreating since prior to its first being mapped on July 22–24, 1909, by Grant and Higgins (1913). Its 1909 terminus position was 400–500 m behind its most recent post-Little Ice Age maximum position. Even then, part of the terminus was reached by high tide. Grant and Higgins speculated that the glacier may have been at its maximum position as recently as 15 years earlier (early 1890s). By 1950, the glacier retreated an additional 400 m to 1,200 m. A 600–800-m-wide tidal embayment fronted part of the glacier. By 1964, another 250 m of retreat occurred. As much as 1.5 km of retreat and the development of a large ice-marginal lake occurred during the last third of the 20th century. Through the start of the 2014, retreat and thinning were continuing.

Holgate Glacier

Holgate Glacier is a tidewater glacier at the head of Holgate Arm. Little Holgate Glacier, a former tributary, retreated from tidewater prior to 2001. During the first decade of the 20th century, just prior to being mapped on July 22–24, 1909, by Grant and Higgins (1913), the terminus of 8.5-km-long Holgate Glacier retreated about 1.5 km. When visited in 1909, the glacier terminus flowed on both sides of a bedrock outcrop that formerly had been a nunatak in the middle of the terminus. By 1950, the south side of the glacier retreated another 400 m while the north side showed no change (Field, 1975). Aðalgeirsdóttir, Echelmeyer, and Harrison (1998) report that between the 1950s and 1990s the glacier, with a 1950s area of 64.3 km^2, had its terminus retreat another 260 m and its area decrease by 0.25 km^2. During this ~40-yr period, Holgate's ice volume decreased by 1.3 km^3, its average elevation decreased by 16.3 m, and its mean annual mass balance was -0.3 m. Between the 1950s and middle 1990s, on an annual basis, Holgate Glacier thinned by 0.364 m, had its volume decrease by 0.023 km^3, and shortened by 6 m/yr (personal commun., March 2001, K.A. Echelmeyer, W.D. Harrison, V.B. Valentine, and S.I. Zirnheld, University of Alaska Fairbanks). Holgate Glacier has an accumulation area of 60 km^2 and an ablation area of 5 km^2, a width at its face of 0.6 km, and an AAR of 0.92.

Sheridan Glacier

Located ~ 2.5 km to the west of Sherman Glacier, Sheridan Glacier has a length of 24 km and an area of 101 km^2. Sheridan Glacier terminus is a small, retreating piedmont lobe with a width of more than 5 km. Since the last quarter of the 20th century, nearly all of the retreating and thinning glacier's margin was fronted by a single large ice-marginal lake.

In 1965, Tuthill and others (1968) examined a series of concentric recessional moraines and related deposits located as much as 2.5 km beyond the present margin of the glacier. Through analysis of these deposits, they were able to construct a late Pleistocene–Holocene history for Sheridan Glacier and adjacent Sherman Glacier. They

determined that, at the end of the Pleistocene Epoch, the two glaciers were joined and terminated a little more than 5 km south of the current terminus position of Sheridan Glacier. Subsequently, but at an unknown date, Sheridan Glacier retreated to a point north of its present margin. Sheridan Glacier remained in a retracted position until less than about 2,000 years ago, when it readvanced. Sheridan Glacier remained at this location until about AD 300, after which it underwent a series of fluctuations in position, culminating in an advance that produced a moraine in about AD 1700 (~315 years ago). This moraine is the outermost of the concentric recessional moraines that they examined. At least four younger moraines exist between the AD 1700 moraine and the present-day margin of Sheridan Glacier.

Tarr and Martin (1914) reported that when the glacier was visited by Seaton-Karr in 1886, a fresh moraine resulting from a recent advance or stillstand of the glacier was present. In 1910, Tarr and Martin (1914, p. 390) observed the glacier and noted, "The presence of thick mature forest up to the very edge of the bulb [bulb-shaped terminus] indicates that the glacier has not been more extensive for a score of years, perhaps for a century." When observed 21 years later in 1931, Wentworth and Ray (1936) described the margin as having retreated between 100 and 125 m and noted that the surface of Sheridan Glacier was showing signs of thinning produced by ablation. An average retreat rate for this interval would be about 5–6 m/yr.

Field (1975), on the basis of his own observations and on the analysis of aerial photographs collected by Bradford Washburn in 1938, the U.S. Army Air Force in 1941, and the USAF in 1950, concluded that "…the massive moraine nearest the present terminus was formed in the early or middle 1930s." In the approximately 30 years between the date of the formation of the moraine and the middle 1960s, Field (1975) reported that "…recession has varied from around 200 m on the ridges to perhaps 500 m in the lake basins." Hence, during this period, retreat rates averaged 7–17 m/yr. Without quantifying the amount of change, Field (1975) reported that, through 1971, the glacier "…showed considerable further lowering of the ice surface and some recession of the terminus since 1965 and 1968."

Field (1975) described the evolution of the ice-marginal lakes fronting Sheridan Glacier through 1971. He stated, "The lakes were only beginning to form by the recession of the terminus in 1931." Through examination of the USGS 1:63,300-scale Cordova C-4 topographic quadrangle map (1953) Field determined that, by 1950, five lakes had formed—one at the western end of the glacier, draining into the Glacier River; two 1-km-wide lakes along the front of the middle part of the terminus; and two small lakes along the eastern margin of the glacier. All had separate outlets. On the basis of his 1965 observations, Field (1975) noted that the five lakes still maintained their unique existence but that the level of one of the eastern lakes had dropped when an ice dam was removed. By 1971, the drainage of all of the lakes entered the two middle lakes, generally englacially, and all of Sheridan and Sherman glaciers' drainage flowed through the middle lake's outlet to the Gulf of Alaska. Field (1975) also reported that, through 1971, the glacier "showed considerable further lowering of the ice surface and some recession of the terminus since 1965 and 1968."

A comparison of 1950s map data of the glacier with data obtained during annual airborne profiling surveys in the middle 1990s indicates that Sheridan Glacier thinned by 0.725 m/yr and had a volume decrease of 0.073 km^3/yr (K.A. Echelmeyer, W.D. Harrison, V.B. Valentine, and S.I. Zirnheld, University of Alaska Fairbanks, written commun., March 2001).

In 2000, a significant amount of calving was occurring along the eastern margin of the glacier. Continued thinning of the glacier may have resulted in a floating ice tongue that was rapidly disarticulating.

Recent changes in the evolution of the ice-marginal lake system were studied by Bailey and others (2000). They found that, by 1981, the ice front in the center of the glacier had receded and allowed the two middle lakes and the western lake to combine. This merging was accompanied by about 10 m of downcutting of the outlet through the AD 1700 moraine. By August 22, 1979, the basins of the eastern lakes had filled with sediment, and they had completely disappeared. When I photographed the terminus area in October 1974, an isolated, small eastern lake still remained. Increased availability of sediment after 1964 from Sherman Glacier may have been a factor in the subsequent infilling of the basin. In 2013, the 4-km-long ice-marginal lake fronted all but the southwestern end of the terminus.

Unlike any other part of Sheridan Glacier, the southwesternmost margin is debris covered, possibly from a 1964 earthquake-generated landslide. This debris mantle has protected an ~500-m-wide segment of the terminus from retreat. Repeated visits by the author to this part of the glacier between 1974 and 2012 have documented that the rate of thinning of the debris-covered part is reduced and the rate of retreat is slower than that of the bare ice to the east. Before 1974, a small lake had formed at the western margin of the debris-covered ice. By 2002, it had a maximum length of ~600 m. A small advance occurred during the latter part of the first decade of 21st century. In 2013, the lake's maximum length was ~250 m.

CHAPTER 3.2

WHITTIER WATERFRONT OR PASSAGE CANAL

By Peter Haeussler[10]

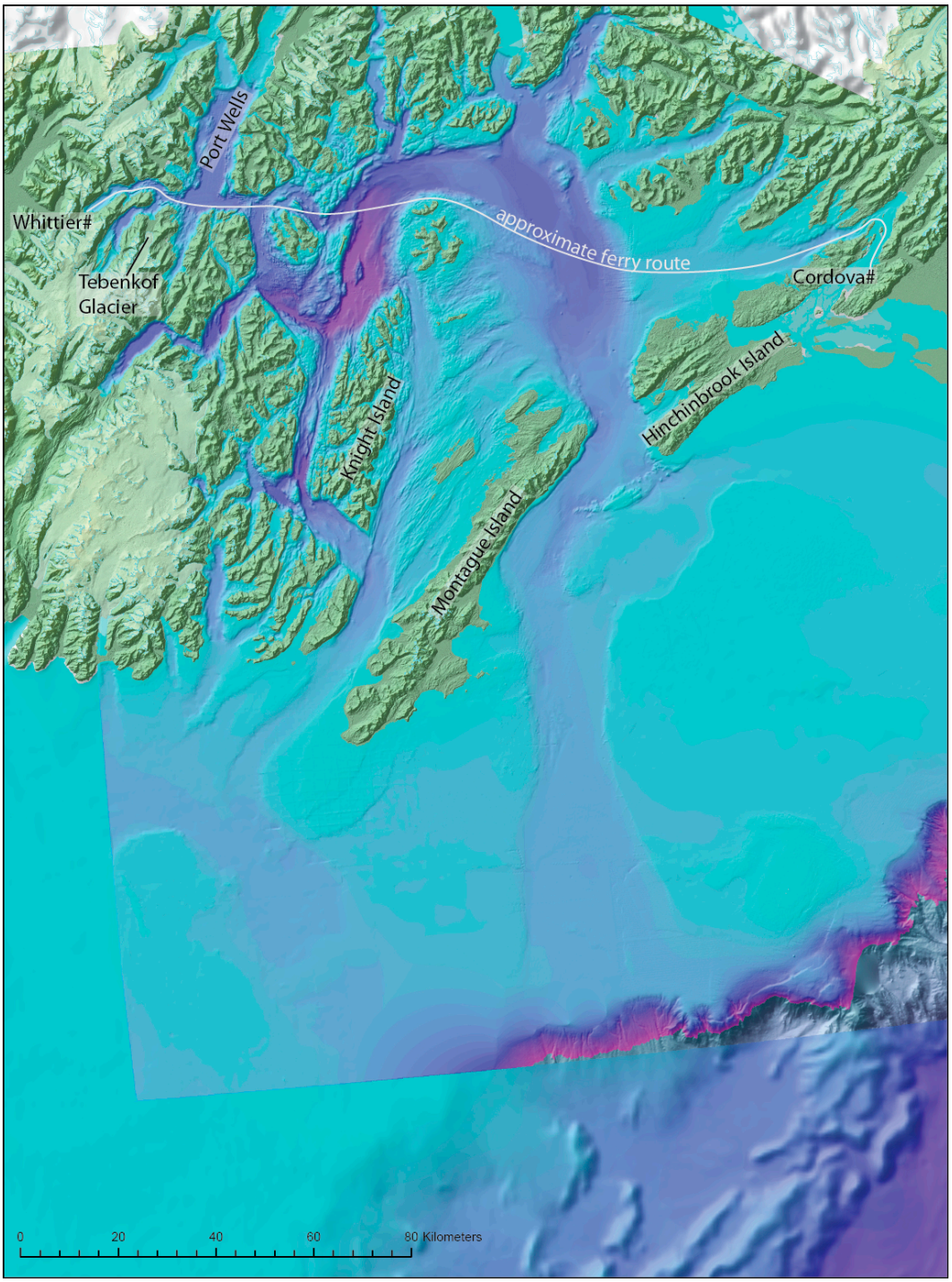

Figure 3.2.1. *Map showing the topography and bathymetry of the Prince William Sound region. The approximate ferry route is shown with the white line. The Alaska-Aleutian trench is at the lower right.*

[10] *Peter Haeussler, U.S. Geological Survey, 4210 University Drive, Anchorage, AK, U.S.A., 99508. pheuslr@usgs.gov*

The 1964 Alaska M_w 9.2 earthquake remains the second largest earthquake event ever recorded. In Alaska, 106 of 122 deaths from the earthquake were related to tsunamis, and 85 of these 106 deaths were associated with submarine landslide-generated tsunamis (fig. 3.2.2; NGDC tsunami database). Local submarine landslide-triggered tsunamis were the biggest single cause of deaths in this earthquake. This is in contrast to other great megathrust earthquakes, where most casualties come from the tectonic tsunami.

Two studies focused on submarine landsliding soon after the 1964 earthquake (Kachadoorian, 1965; Wilson and Tørum, 1972). Tsunami inundation maps were recently produced for this area, based on hypothetical source scenarios (Nicolsky *et al.*, 2011a), and Haeussler *et al.* (2013) utilized new multibeam and high-resolution sparker seismic data to produce a refined interpretation of the 1964 submarine landslide. The following is taken from Haeussler *et al.* (2013).

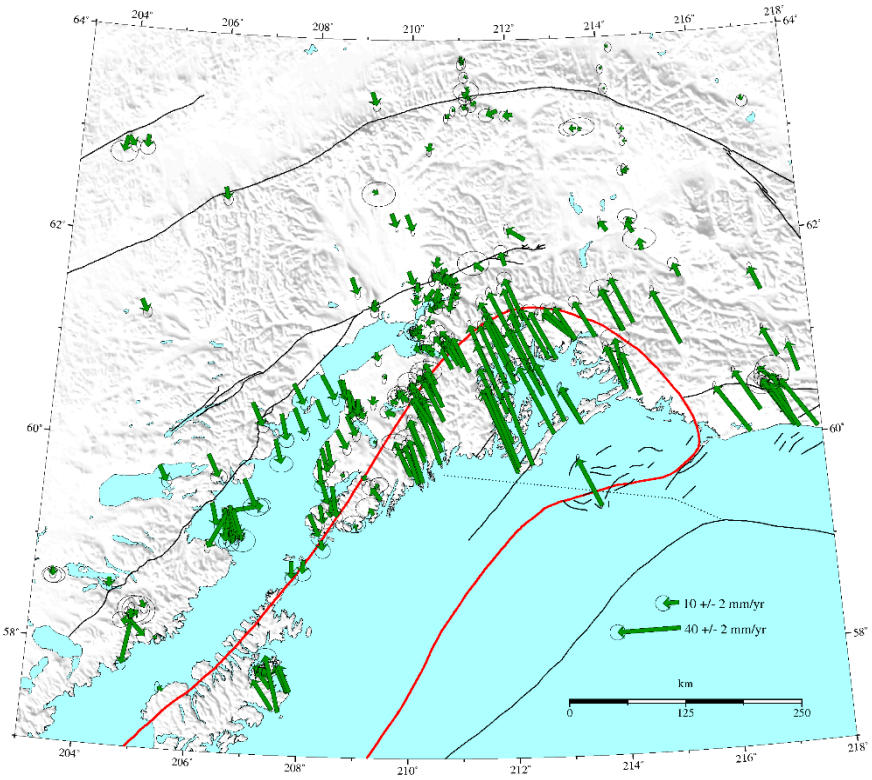

Figure 3.2.2. *Horizontal GPS velocities for south-central Alaska, shown in green, from Jeff Freymueller. Scale bar of GPS velocities is in the lower right. Major active faults are shown in black; outline of 1964 M9.2 earthquake aftershocks is shown in red.*

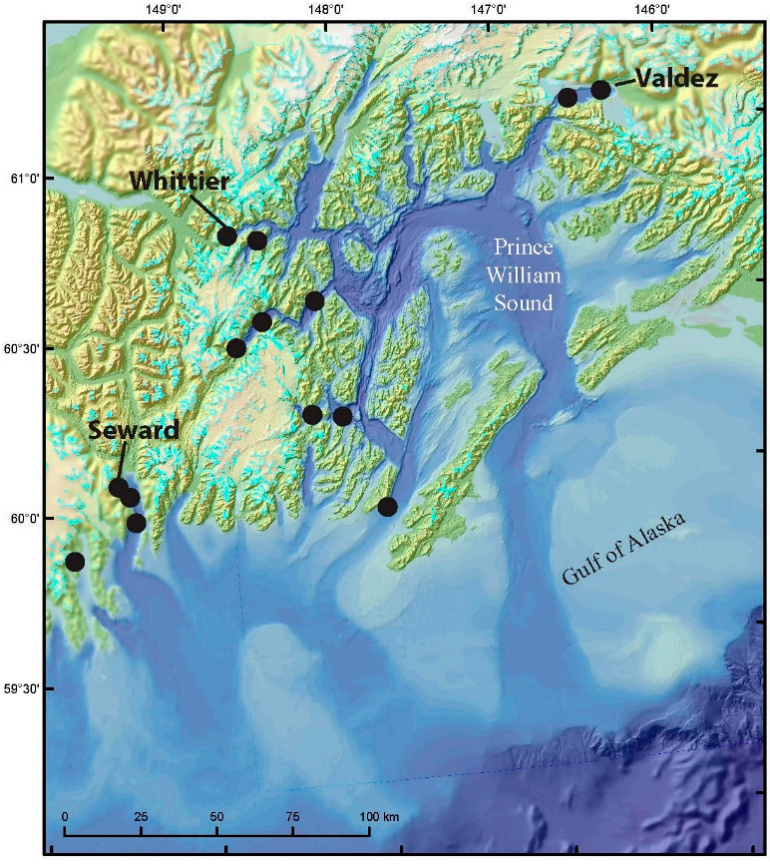

Whittier, Alaska, is a small (population 223) port town on the southern edge of Passage Canal, which is a fjord in western Prince William Sound (fig. 3.2.3). The town is built on the Whittier Creek alluvial fan at the edge of the fjord. Whittier was, and remains, an unusual community in that the majority of the residents live(d) in a 14-story building that lies about 450 m inland. Between this apartment building and the shoreline lies the industrial part of town with the port and harbor facilities, ferry dock, and railroad yard. The fjord ends about 2 km west of town, where two streams empty into Passage Canal and construct the fjord head delta.

There was about 4 minutes of strong, sustained, ground shaking in Whittier during the 1964

Figure 3.2.3. *Overview bathymetric and topographic map of the southern Alaska margin. Black circles show the locations we infer submarine landslides from data of Plafker et al. (1969) and our observations. Town names are listed with adjacent water body names in parentheses.*

earthquake. Plafker (1969) determined that Whittier and all of Passage Canal subsided about 1.6 m during the event.

At least three waves inundated Whittier soon after the earthquake (Kachadoorian, 1965). About a minute after shaking began, a large glassy wave formed in the middle of Passage Canal. This wave had a height of ~8 m above the sea level, but did not cause any damage. About a minute later, a muddy 12-m-high breaking wave inundated the port and railroad facilities. About 45 seconds later, a smaller third wave hit the town. The waves caused extensive destruction and 13 fatalities.

After the earthquake, Kachadoorian (1965) documented the tsunami run-up and changes in bathymetry along three profiles, and showed that failure of the fjord-head delta and the Whittier Creek fan generated the local tsunami.

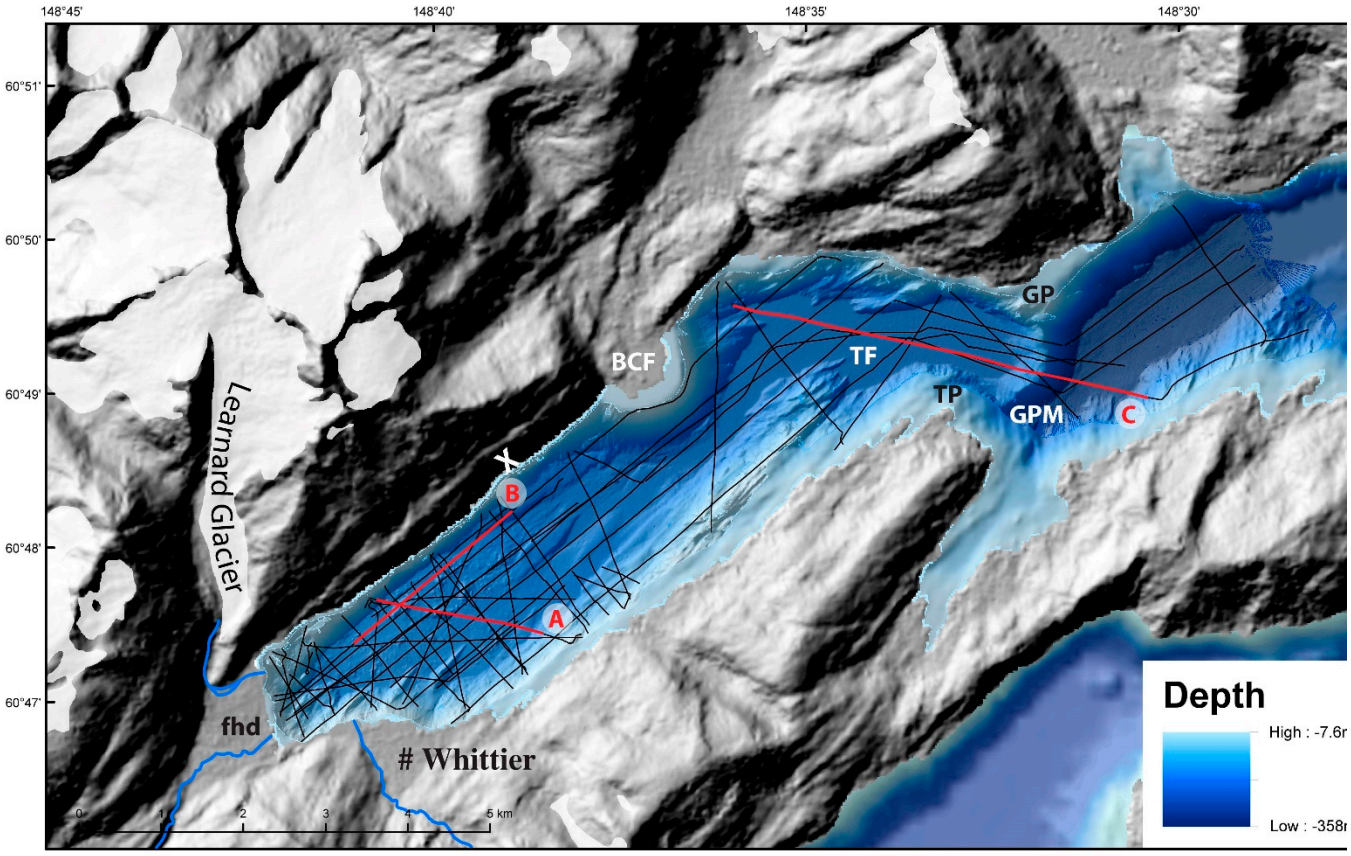

Figure 3.2.4. *Combined topography and bathymetry of the Passage Canal and Whittier area. Black lines are high-resolution seismic tracklines of Haeussler (2013). Tracklines in red, labeled A, B, and C, are shown in Figure 3.2.5. Location X is where Nicolsky et al. (2011b) found evidence for cracking in bedrock indicating rockfall potential. GP, Gradual Point; GPM, Gradual Point moraine; TP, Trinity Point; TF, Trinity flats; BCF, Billings Creek fan; fhd, fjord-head delta.*

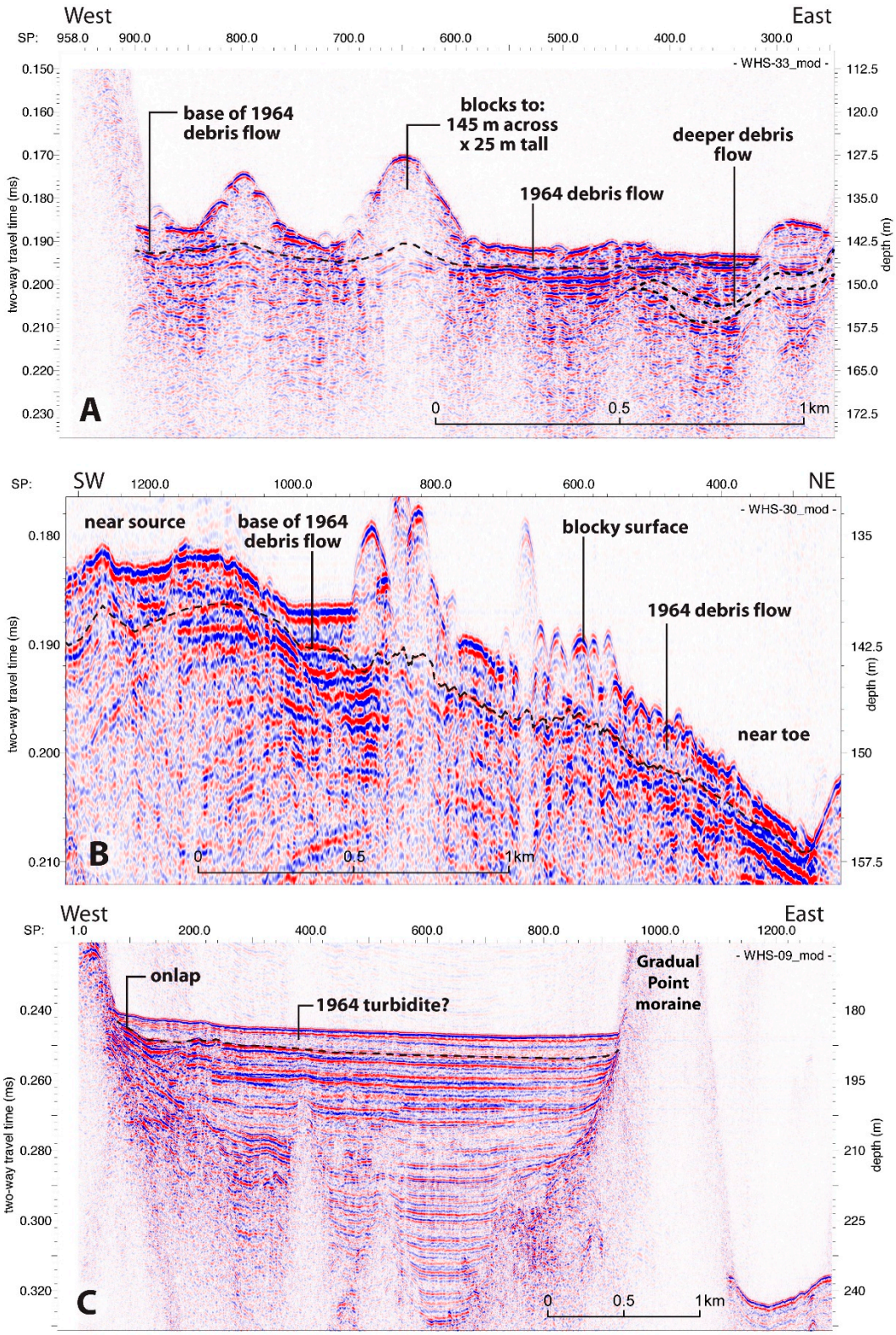

Figure 3.2.5. *Seismic reflection profiles showing features of the 1964 mass transfer deposit from Haeussler et al. (2013). Location of profiles shown on figure 3.2.4. Horizontal scale is shot points, vertical scale is two-way travel time in seconds. 0.01 sec TWT is approximately 8 m.* ***A.*** *Line (WHS-33) across the largest blocks in the area north of Whittier.* ***B.*** *Line (WHS-30) shows the main debris-flow deposit from near the source region on the left to the distal end of the debris flow to the right.* ***C.*** *Profile (WHS-09) across the Trinity flats and the Broad Point moraine that shows the nature of sedimentation beneath this basin. The uppermost ~4 m may be a turbidite generated in 1964. It onlaps older sediments at the west end of the profile. Older deposits may also contain turbidites.*

High-resolution seismic reflection data show the base of the 1964 submarine landslide deposit (figs. 3.2.4 and 3.2.5). The seismic data can be considered in two parts divided by the Billings Creek fan. At the west end of the fjord, the uppermost seismic-stratigraphic unit consists of a hummocky, acoustically transparent facies with low-amplitude internal reflections (figs. 3.2.5 A, B). This unit correlates with the geomorphic expression of a blocky debris flow, and we conclude this is the mass transfer deposit (MTD) triggered by the 1964 earthquake. This deposit is typically 2–8 m thick, assuming a velocity of 1,500 m/sec. Truncations of reflectors at the base of this unit indicate it was eroding as it flowed. Blocks within the deposit are up to 25 m tall and 145 m long. They have a velocity pull-up beneath, indicating they consist of relatively-high-velocity material, possibly till. We infer a volume of about 20 million m^3 based on mapping the deposit with the seismic reflection data.

Below the 1964 deposit, we observe reflectors that we interpret as mostly background fjord sedimentation (fig. 3.2.5). Blocks in the 1964 deposit make it difficult to better image the lower strata. Nonetheless, the reflectors usually parallel the bottom and pinch and swell slightly. There are acoustically transparent regions, but these do not have lateral continuity beyond a few hundred meters (fig. 3.2.5A). These likely represent sediments deposited in small debris flows off the fjord-head delta or Whittier Creek. We have not been able to confidently trace seismic-stratigraphic packages from line to line. We see no evidence for large-scale MTDs beneath the 1964 deposit.

East of the Billings Creek fan, beneath the Trinity flats, the uppermost deposit is possibly a turbidite from the 1964 earthquake (fig. 3.2.5C). The uppermost 0.005 secs TWT (~4 m) is a coherent seismic-stratigraphic unit with low amplitude and one or two weak internal reflectors. It locally shows onlap, and has a volume of about 14 million m^3. Given the large 1964 debris flow at the west end of the fjord, it is reasonable to expect that a turbidite developed and traveled farther eastward. The stratigraphic position, onlap, acoustic properties, and setting are consistent with a turbidite generated in 1964.

The bathymetry difference map shows redistribution of sediment during the 1964 earthquake (fig. 3.2.6). The primary features of the map are an increase in depth up to 80 m at the west end of the fjord and off Whittier, and the deposition of the block field and debris flow in the area north of Whittier. This conclusion is the same as that of Kachadoorian (1965), who did 2-D bathymetry differencing in this area and found broadly similar results. Based on differencing only the source regions, we calculate the volume of failed sediment was approximately 42 million m^3. This volume is greater than the calculated volume of the deposit from the seismic data (32 million m^3 [32 = 20 + 14 million m^3]), and moreover, we found evidence of erosion at the base of the debris flow, which indicates the deposit volume should be greater than the source region volume. This leads us to infer that there are errors in one of these two numbers, possibly related to incorrect mapping of flow margins or bathymetry on the older survey.

The new data provide a clear picture of the submarine landslide deposit generated in the 1964 earthquake. Simply, the fjord-head delta and the Whittier Creek delta failed, and the landslide material slid eastward up to 5 km. A large turbidite was likely generated and deposited farther eastward across the Trinity flats.

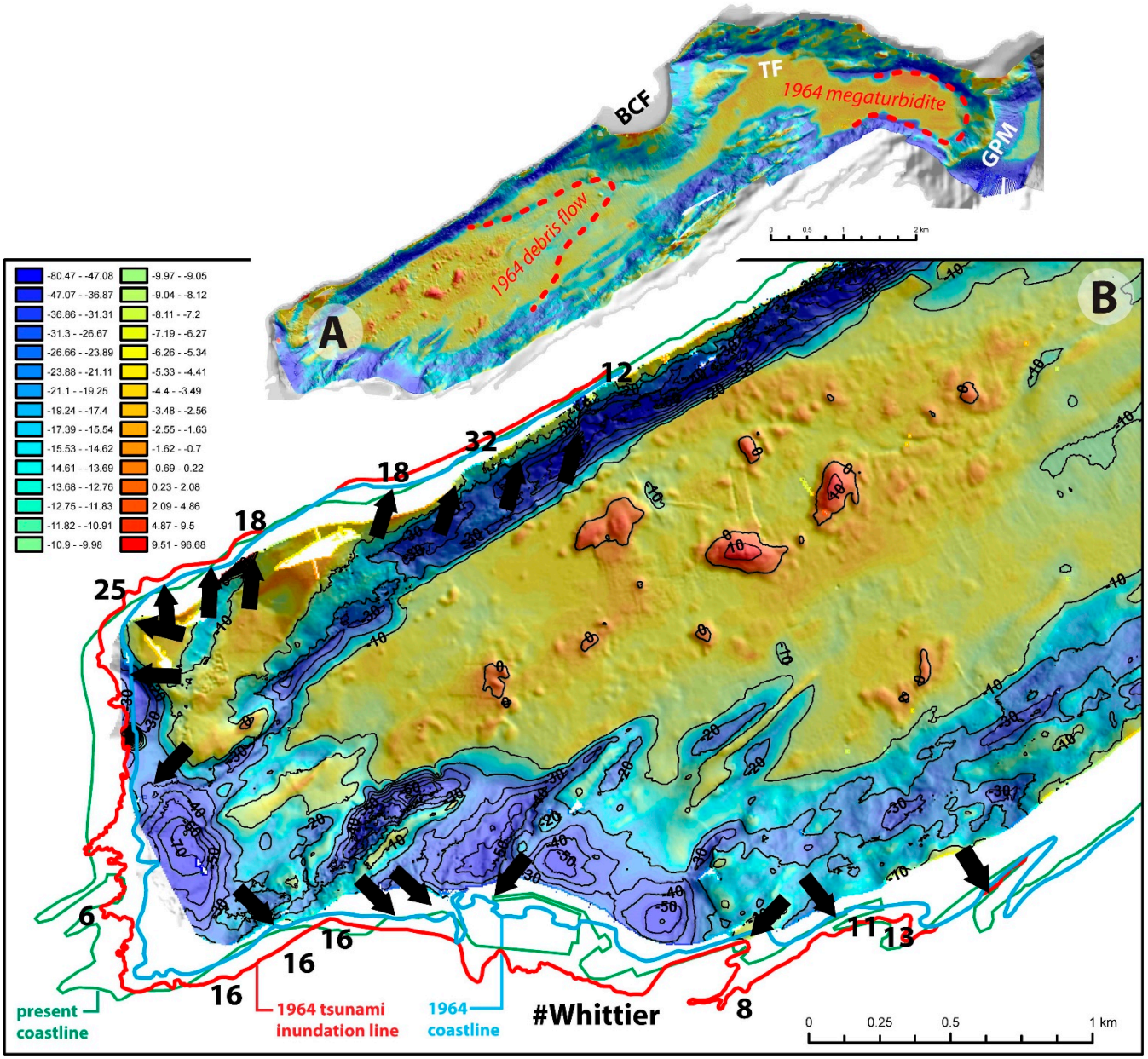

Figure 3.2.6. *Bathymetry difference, in meters, draped onto shaded-relief image of Passage Canal from Haeussler et al. (2013). Note zero depth change color is orange. Older bathymetric survey is from 1948, in comparison to multibeam survey of 2011. Cool colors indicate deeper values in 2012, warm colors indicate shallower depths in 2011.* ***A.*** *Overview map of entire area of multibeam survey. BCF, Billings Creek fan; TF, Trinity flats; GPM, Gradual Point moraine. Dashed red lines show the limits of the 1964 debris flow, and the 1964 megaturbidite deposit.* ***B.*** *Detail map of west end of Passage Canal near Whittier, which also shows the coastline and inundation line, tsunami runup directions (arrows) and heights, in meters (data from Kachadoorian, 1965).*

Tebenkof Glacier

To the south is usually a nice view of Tebenkof Glacier. Michail Tebenkov was trained in the Russian navy, joined the Russian American Company in 1825, and eventually became the director of the company (1845–1850). In this position, he was essentially the governor of Russian colonies in America.

Barclay *et al.* (2009) found a nice record of logs from glacially killed trees in the forefield of the Tebenkof Glacier. This record extends back almost 1,000 years before the present and nicely defines glacial expansions in this time period. This is the best record from central Prince William Sound of glacial advance and retreat for this time period. A plot of all the cross-dated trees clearly shows when trees were overrun during glacial advances (fig. 3.2.7). These dates can then be interpreted in terms of the location of the toe of the Tebenkof Glacier (fig. 3.2.8). Here is the abstract from their paper:

> *Tree-ring crossdates from glacially killed logs show that Tebenkof Glacier advanced into a forefield forest in the AD 710s and 720s. Recession from this First Millennium AD (FMA) advance occurred before the 950s, after which the ice margin readvanced in the 1280s to 1320s at the start of the Little Ice Age (LIA). A more extensive LIA advance was underway from the 1640s to 1670s, and the terminus stayed at or near its LIA maximum until the 1890s. These are the first absolute tree-ring crossdates for a FMA glacier advance in North America and support growing evidence from northwestern North America and Europe for a significant cool interval in the centuries around AD 500.*

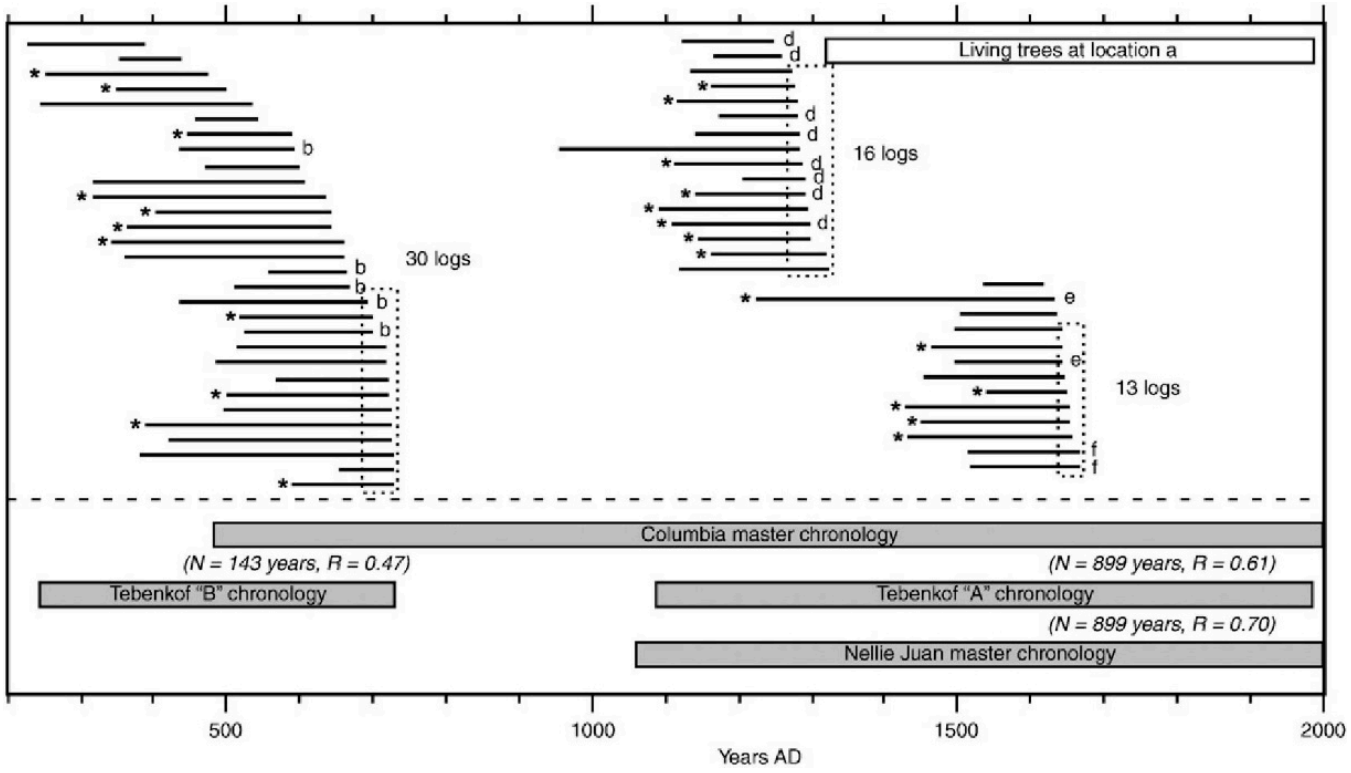

Figure 3.2.7. *Age spans of crossdated samples.* ***Upper panel:*** *Horizontal block shows the composite age span of living trees included in the Tebenkof "A" chronology, and horizontal lines show growth intervals of individual logs. Star symbols indicate samples that included pith, letter labels indicate sample locations b, d, e, or f for logs in situ or in original glacigenic deposits, and dotted boxes show inferred intervals when the ice margin was advancing and killing trees.* ***Lower panel****: Blocks represent age spans of the four tree-ring-width chronologies used in this study, and numbers in parentheses are years of overlap and correlation coefficients between the Tebenkof chronologies and the respective master chronologies. The Tebenkof chronologies are truncated when sample size is less than two trees and so are shorter than the total duration of forest growth shown by the individual log bars.*

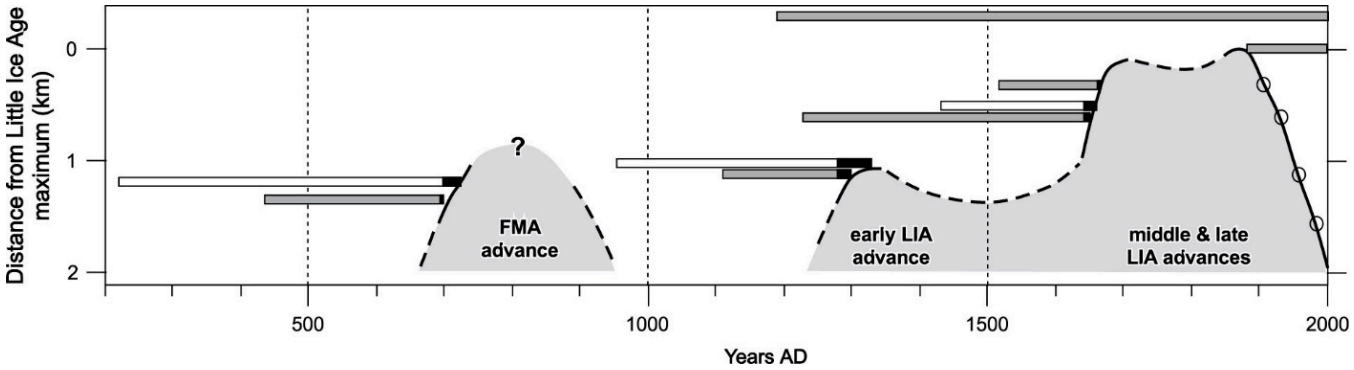

Figure 3.2.8. *Time-distance diagram for Tebenkof Glacier terminus. Horizontal blocks show durations of forest growth based on tree-ring crossdates: Grey blocks are for in situ logs and trees or logs in original glacigenic deposits, open blocks are for logs in modern stream channels or on the land surface, and black areas indicate inferred intervals when trees were being killed. Circles indicate ice-margin positions based on direct observations and letters are sample locations described in the text of Barclay et al. (2009).*

Port Wells

If the weather is good, there are gorgeous views to the north in Port Wells. For some reason, Port Wells becomes College Fiord where it narrows to the north. These glaciated peaks are the highest peaks in the Chugach Mountains with Mt. Marcus Baker at 13,176 ft (4,016 m) tall. It is perhaps the least impressive summit of all the peaks—it is just a snow cone—but it is the tallest mountain in an accretionary complex in the world. It was first climbed in 1938 by the famed Bradford Washburn, and his party also included Norman Dyhrenfurth, who in 1961 led the first American ascent of Mt. Everest. Anyway, the scenery is spectacular with the high peaks and the tidewater glaciers. Perhaps the first scientific exploration of this region was by the 1899 Harriman expedition, which was funded by a rich railroad magnate, whose doctor told him he needed a long summer vacation. Harriman decided a two-month trip from Seattle to Siberia would do the trick. He contacted the then head of the National Geographic Society and told him that he would pay for a scientific party to come along on the voyage, and some luminaries of the day accompanied him on the trip. Among these was the famed G.K. Gilbert, who documented aspects of these tidewater glaciers, as well as John Muir. A side effect of the Harriman expedition was that they named a number of peaks in the region after themselves, their peers, or their alma maters. Thus, there is Mt. Muir, Mt. Gilbert, Mt Gannett, Wellesley Glacier, Vassar Glacier, Bryn Mawr Glacier, Smith Glacier, Radcliffe Glacier, Harvard Glacier, Yale Glacier, and Amherst Glacier. Interestingly, the local native population did not name peaks after people.

Why are these mountains high? Recent thermochronology work by Arkle *et al.* (2013) shows that there is recent (<5 Ma) exhumation inside the bends of the major fault systems in northern Prince William Sound. Here is the abstract of the Arkle *et al.* (2013) paper:

> *The western Chugach Mountains and Prince William Sound are located in a syntaxial bend, which lies above flat-slab subduction of the Yakutat microplate and inboard of the Yakutat collision zone of southern Alaska. The syntaxis is characterized by arcuate fault systems and steep, high topography, which suggest focused uplift and exhumation of the accretionary prism. We examined the exhumation history with low-temperature thermochronometry of 42 samples collected across the region. These new apatite (U-Th)/He, apatite fission-track, zircon (U-Th)/He, and zircon fission-track ages, combined with ages from surrounding regions, show a bull's-eye pattern, with the youngest ages focused on the western Chugach syntaxis. The ages have ranges of ca. 10–4 Ma, ca. 35–11 Ma, ca. 33–25 Ma, and ca. 44–27 Ma, respectively. The youngest ages are located on the south (windward) side of the Chugach Mountains and just north of the Contact fault. Sequentially higher closure temperature systems are nested across Prince William Sound in the south, the Chugach Mountains, and the Talkeetna Mountains to the north. Computed exhumation rates typically are 0.2 mm/yr across Prince William Sound, increase abruptly to ~0.7 mm/yr across and adjacent to the Contact fault system, and decrease to ~0.4 mm/yr north of the core of the Chugach Mountains. The abrupt age and exhumation rate changes centered on the Contact fault system suggest that it may be a critical structural system*

for facilitating rock uplift. Our data are most consistent with Yakutat flat-slab subduction starting in the Oligocene, and since then ~11 km of rock uplift north of the Contact fault and ~4–5 km of rock uplift in Prince William Sound to the south. These data are consistent with a deformation model where the western Chugach core has approached long-term exhumational steady state, though exhumation rates have probably increased in the last ~5 m.y. We interpret that rock uplift in the overriding wedge has been driven dominantly by underplating, with long-term vertical displacement concentrated at the southern edge of the Chugach Mountains and centered on the Contact fault system. Though our data do not unequivocally differentiate between Pliocene tectonic- or climate-related causes for increased exhumation in the last ~5 m.y., we interpret the increased rates to be due to increased influx of underplated sediments that are derived from erosion in the Saint Elias orogen collision zone.

Here are a few figures from the paper that help to illustrate their findings and the interpreted processes.

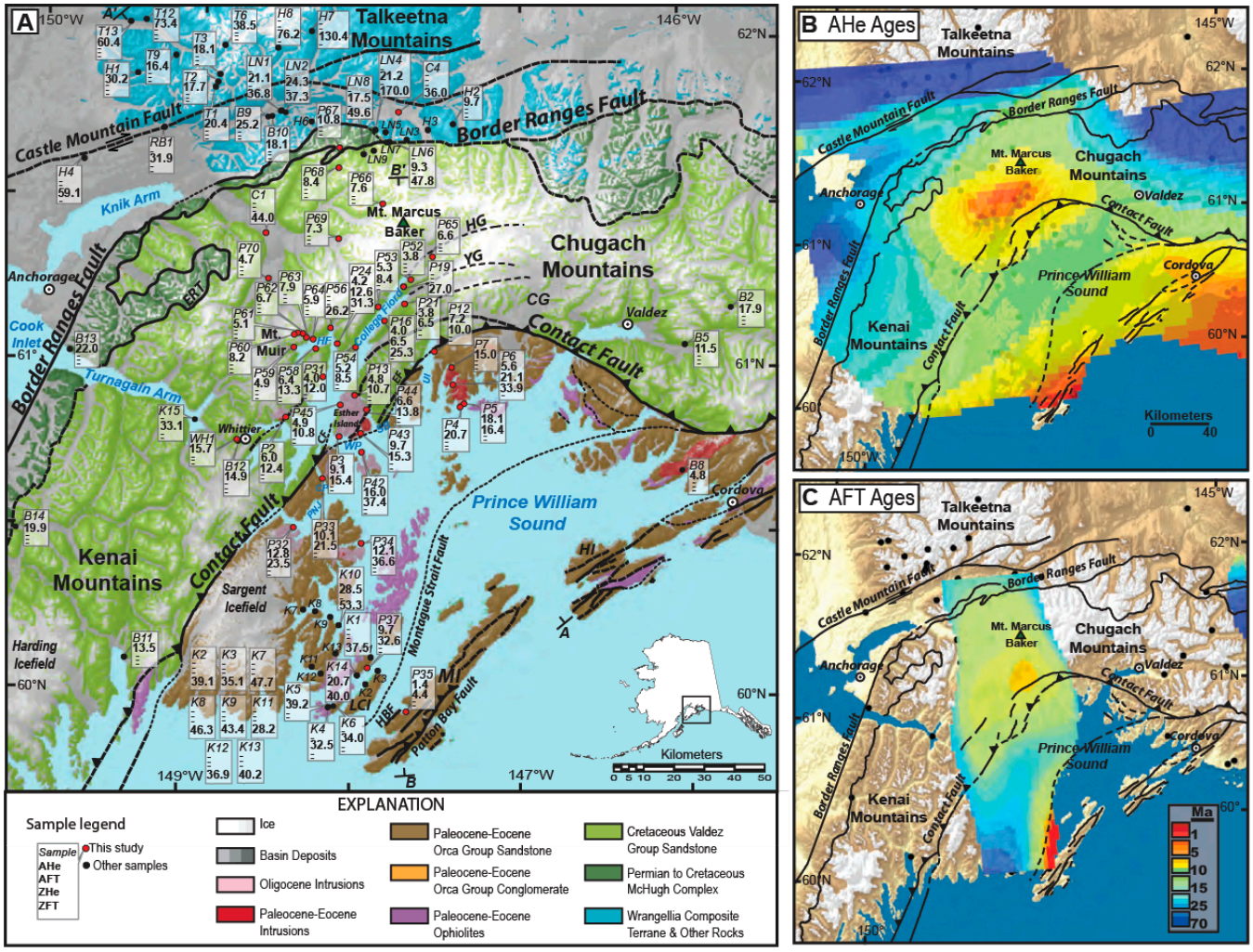

Figure 3.2.9. A. *Sample location map (from Arkle et al., 2013),* ***B.*** *Contoured apatite helium ages, and* ***C.*** *Contoured apatite fission-track ages with faults (solid lines), inferred faults (dashed lines), and major lithologic units (after Plafker et al., 1989; U.S. Geological Survey fault data repository). Large bold letters and markers in A indicate cross-section locations for their figures 3, 4, and 6. Age contour colors in B are same as in C. ERT–Eagle River thrust, CF–Culross fault, EF–Eagle fault, HBF–Hanning Bay fault, WP–Wells Passage ,CP–Culross Passage, SB–Squaw Bay, PNJ–Port Nellie Juan, UI–Unakwik Inlet, HF–Harriman Fiord, HG–Harvard Glacier, YG–Yale Glacier, CG–Columbia Glacier, HI–Hinchinbrook Island, LCI–Latouche Island, MI–Montague Island. The letters in the sample number blocks correspond to the following studies: P, C, and W–this study; K–Kveton (1989); LN–Little and Naeser (1989); RB–Parry et al. (2001); T–Hoffman and Armstrong (2006); B–Buscher et al. (2008); H–Hacker et al. (2011).*

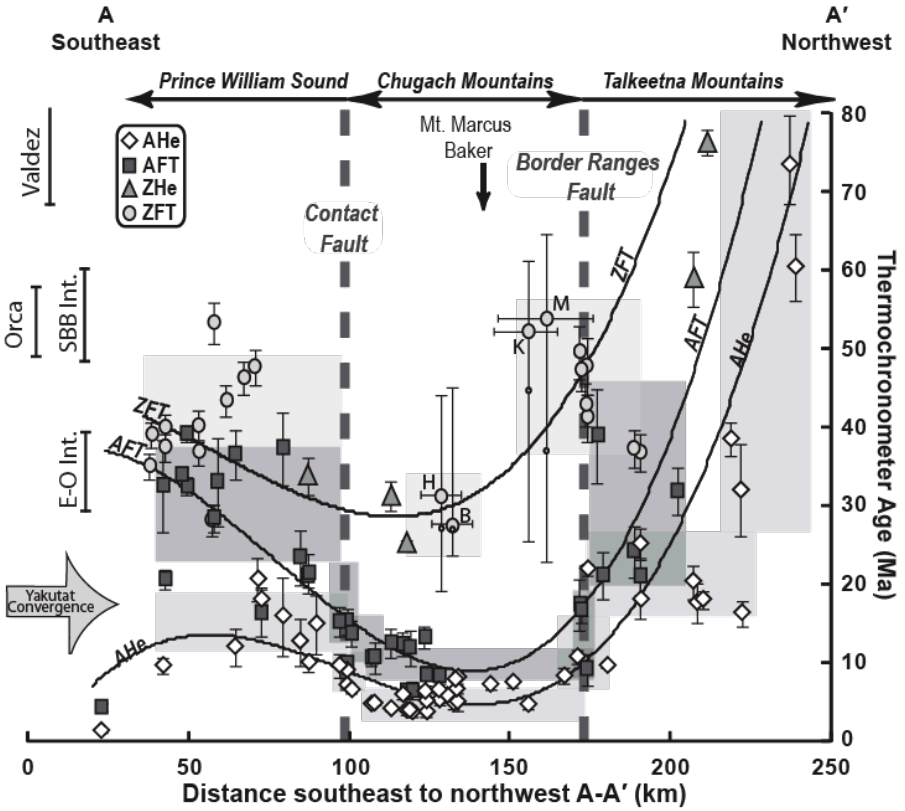

Figure 3.2.10. *Plot of thermochronology ages along a NW–SE trend (profile location shown in their fig. 2) parallel to the relative Yakutat convergence (convergence from left to right). Ages from a 100-km-wide swath are projected onto the profile along curved paths parallel to the structural grain. Age uncertainties are ±1σ. Shaded boxes approximately bound the average area of age-distance relations and are estimated in some areas. Curves are third-order polynomial fit lines used to show the nested pattern. The zircon fission-track (ZFT) ages in the Mount Marcus Baker area are detrital ages from modern glacial outwash deposits, and letter labels correspond to glacier names: H–Harvard; B–Barry; M–Matanuska; K–Knik. The width of the location error bar on the glacial samples corresponds to the distance along the transect crossed by the glacier. The small dot on the age error bar is the age of two youngest age peaks (see text). Age-location relationships show that sequentially higher temperature thermochronometers are nested across the entire width of the forearc. Vertical bars on left show approximate depositional ages for Valdez Group (Valdez) and Orca Group (Orca) and intrusion ages for Sanak–Baranof belt (SBB Int.) and Eocene–Oligocene (E–O Int.) intrusions. Figure from Arkle et al., 2013.*

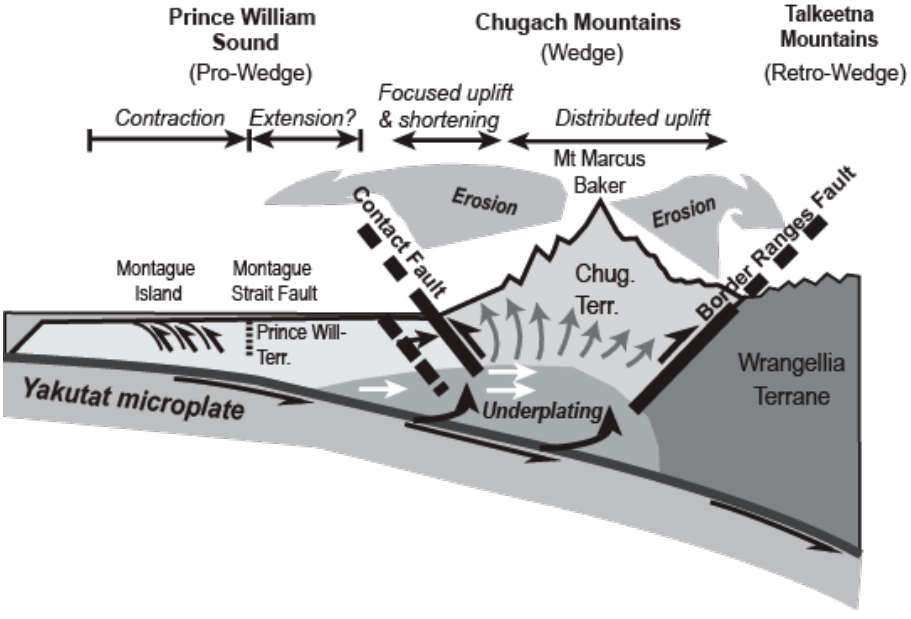

Figure 3.2.11. *Schematic model of rock uplift for the western Chugach Mountains and Prince William Sound. The Yakutat microplate subducts at shallow angle under Prince William Sound and the Chugach Mountains. Yakutat material is being underplated under the region. Underplating drives uplift of the Chugach Mountains between the Contact and Border Ranges faults, but exhumation may be focused along the southern edge of the wedge, as shown by the longer schematic arrows, adjacent to the Contact fault. Figure from Arkle et al., 2013.*

Middle of Prince William Sound

As we travel across the middle of Prince William Sound, it is interesting to consider that there is essentially 100 percent locking between the subducting plate and the overlying North American plate. This plot of GPS horizontal velocities illustrates this high degree of coupling beneath Prince William Sound, relatively low coupling at the southwest end of the Kenai Peninsula, and greater coupling near Kodiak. For additional details see Freymueller *et al.* (2008) and Suito and Freymueller (2009).

CHAPTER 4

CHAPTER 4.1

HARTNEY BAY AND THE WHITSHED PENINSULA

by Ed Garrett[11]

The Whitshed Peninsula divides the Copper River Delta to the east from Prince William Sound to the west. Point Whitshed lies approximately 15 km southwest of Cordova, with Orca Inlet and Hawkins Island to the north and west and Hinchinbrook Island to the southwest. Comparison of pre- and post-earthquake tides suggests coseismic uplift of approximately 2 m at Cordova in 1964 (Plafker, 1969). Our stops provide stimulus for discussion of the zonation of intertidal organisms and their use in reconstructing vertical coseismic deformation in coastal settings. Given favorable tides, our stop immediately to the north of Hartney Bay affords an opportunity to observe colonies of sessile intertidal organisms killed after uplift in 1964 raised them above the limits of tidal inundation (fig. 4.1.1). The tidal marshes of Hartney Bay provide an example of intertidal zonation of plants at both macroscopic and microscopic scales. Two lakes at the end of the peninsula, close to Point Whitshed, are the subject of ongoing research into vegetation history, Holocene climate and, of particular interest to this excursion, relative sea level and paleoseismology.

Hartney Bay

The rocky shorelines of Prince William Sound play host to a range of sessile intertidal organisms, including barnacles (principally *Balanus balanoides, B. glandula,* and *Chthamalus dalli*), which form a conspicuous band with a sharply defined upper growth limit. The duration of tidal inundation controls the elevation of the upper limit, with individuals attached above this "lethal limit" killed by prolonged exposure to air (Kaye, 1964). Consequently, tidal characteristics provide the dominant control on the height of the upper limit, which generally lies around mean high water. The barnacle line serves as a useful datum for estimating earthquake-induced land-level changes. When coseismically uplifted, barnacles are raised above the lethal limit, resulting in total colony mortality. Uplift can simply be quantified by measuring the difference in the elevation of the dead barnacle line and the post-earthquake, living barnacle line. The accuracy of such measurements is within 1 ft (0.3 m) and probably within 0.5 ft (0.15 m) in most places (Plafker, 1969). The approach was first used by Tarr and Martin (1912) after the 1899 Yakutat Bay earthquake and was subsequently used by George Plafker and others to quantify deformation in 1964 (Plafker, 1969; Haven, 1971). Our location at the northern end of Hartney Bay is one of a diminishing number of locations where the remains of pre-1964 earthquake intertidal communities can still be seen. Here, barnacles indicate uplift of between 1.5 and 2 m (fig. 4.1.2).

Southwest of our first stop lies Hartney Bay's broad expanse of tidal marsh and unvegetated tidal flat. The frequency and duration of tidal inundation provides an important control on vegetation, resulting in zonation of species across the marsh. Diatom assemblages from the surface sediments are similarly zoned, with characteristic species inhabiting tidal flat, vegetated marsh, and upper marsh environments (fig. 4.1.3). A transect of 22 surface samples from the site contributed to the Alaska diatom database, providing modern analogues used in the reconstruction of paleoseismic deformation from fossil diatom assemblages (see Chapter 1.3, Ocean View). A series of hand-driven cores at Hartney Bay has not revealed the minerogenic–organic couplets indicative of repeated coseismic uplift, as have been reported from Alaganik Slough to the east (Plafker *et al.,* 1992).

[11] *Ed Garrett, Department of Geography, Durham University, Lower Mountjoy, South Road, Durham, DH1 3LE, United Kingdom. Now at: Geological Survey of Belgium, Royal Belgian Institute for Natural Sciences, Jennerstraat 13, 1000 Brussels, Belgium. egarrett@naturalsciences.be*

Whitshed Lakes

Two freshwater lakes, Upper and Lower Whitshed, lie close to the distal end of the peninsula at elevations close to contemporary sea level. Diatom analysis suggests the sea has not inundated Upper Whitshed during the Holocene. By contrast, the biostratigraphy of Lower Whitshed indicates that a meter-thick inorganic mud unit reflects a period of brackish or marine sedimentation (fig. 4.1.4). Age modeling is currently in progress to constrain the timing of the marine phase; however, initial analyses suggest transgression occurred around AD 1700 and regression began in the late 19th or early 20th century. Aerial photographs indicate that the process of isolation was largely complete by the mid 20th century (fig. 4.1.1); however the highest tides continued to inundate Lower Whitshed until it was lifted clear of the tidal zone by coseismic uplift in 1964.

While tectonic deformation eventually isolated the lower basin, the advance of mountain glaciers during the Little Ice Age (LIA; see Chapter 3.1, Portage Valley: Little Ice Age moraines and current glacier retreat) may be responsible for the earlier transgression. Glacial isostatic adjustment modeling of the relative sea-level response to LIA ice loading suggests relative sea-level rises on the order of several decimeters at sites in Turnagain Arm (Barlow *et al.*, 2012). The closer proximity of the lakes at Point Whitshed to the Chugach Mountains may imply a greater magnitude of relative sea-level response, as reflected by the distribution of modeled rates of present-day uplift (fig. 4.1.5).

The two basins are of limited utility as paleoseismic recorders. Only Lower Whitshed records a change in environment in 1964 and neither basin reveals evidence for older earthquakes or tsunamis. The uninterrupted fresh water until at the base of the Lower Whitshed stratigraphy suggests relative sea-level rise over multiple earthquake deformation cycles, with the basin only close enough to sea level to record changes in salinity in the last few centuries.

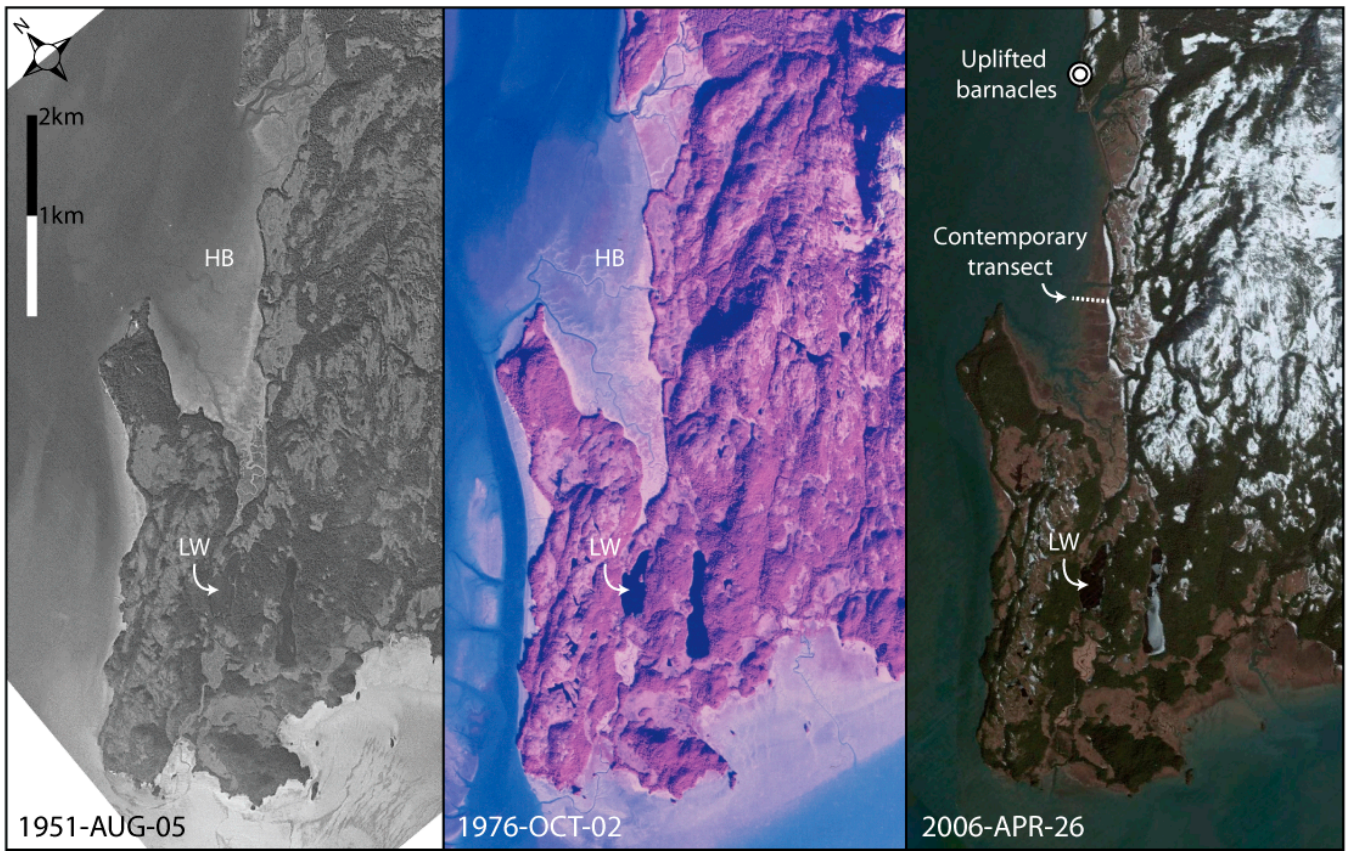

Figure 4.1.1. *Aerial photographs of Point Whitshed and Hartney Bay (HB), including the locations of barnacles uplifted in 1964, the contemporary diatom transect, and Lower Whitshed Lake (LW).*

Figure 4.1.2. *Ian Shennan points to the pre-earthquake barnacle line to the north of Hartney Bay. The contemporary barnacle line is approximately level with the top of Ian's Xtra Tufs.*

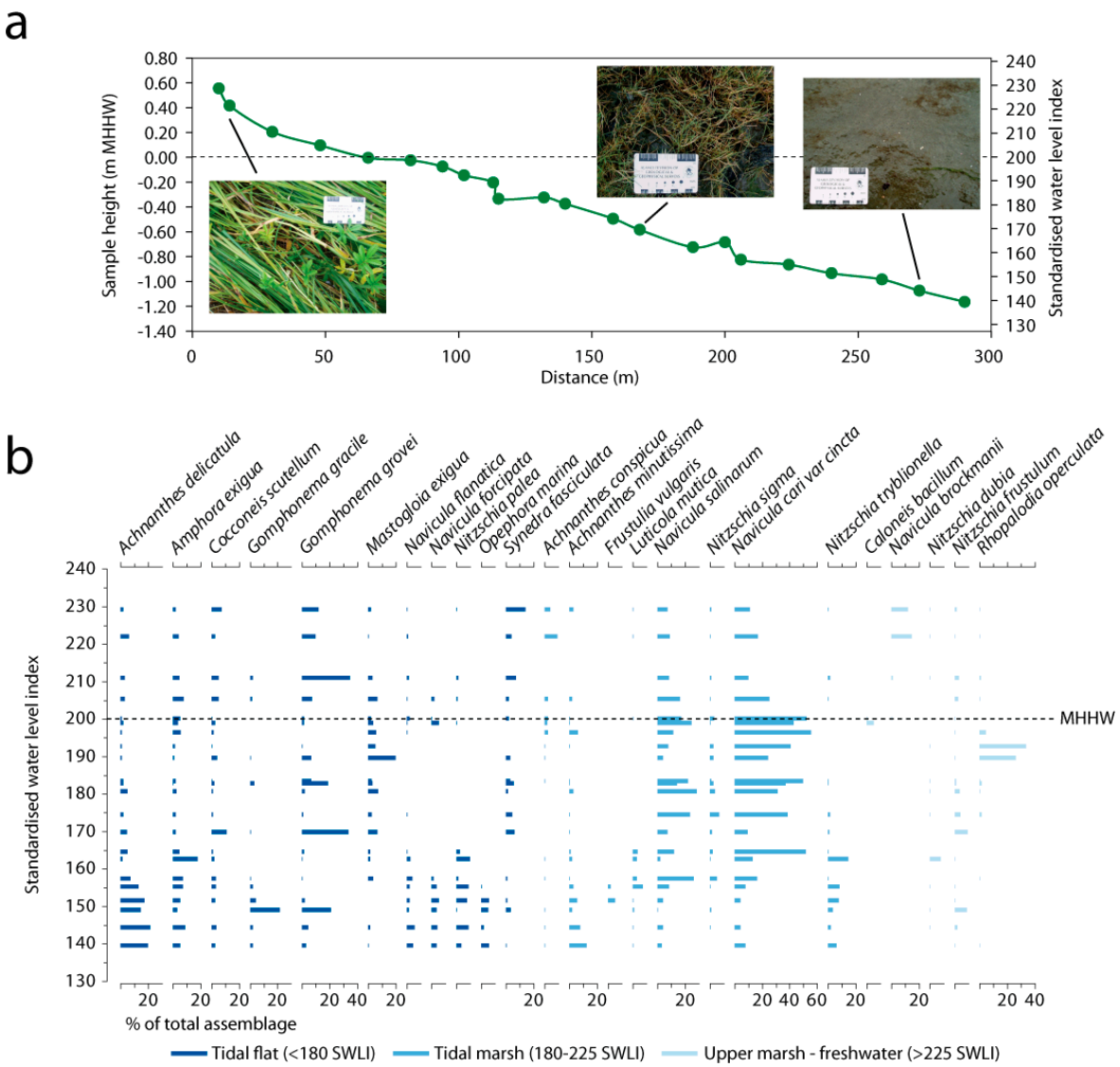

Figure 4.1.3. *Hartney Bay contemporary diatom assemblages (Shennan et al., 2007).* ***a.*** *Profile of the modern transect, with photos of selected sampling locations.* ***b.*** *Diatom species >5 percent, arranged by elevation and classified according to their optimum elevation in a training set incorporating samples from Cook Inlet, Kodiak, and Cordova.*

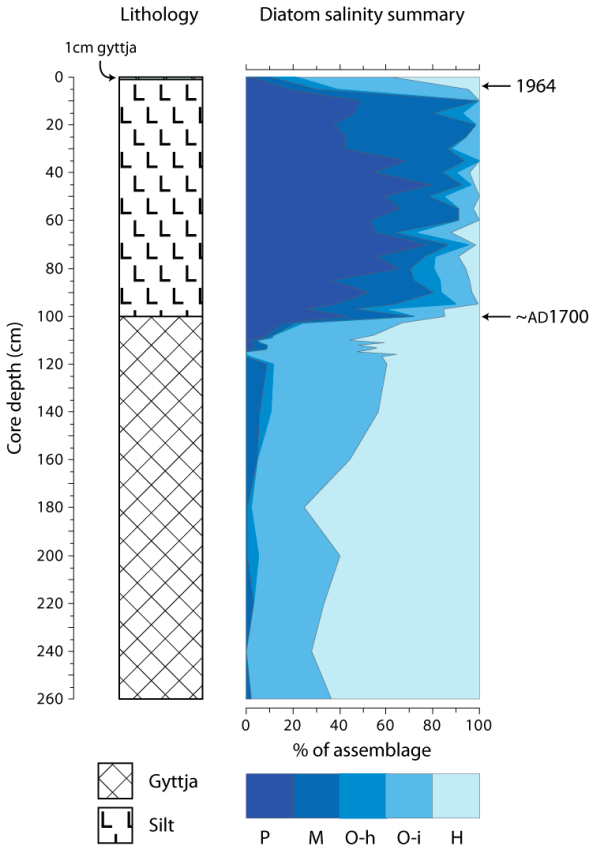

Figure 4.1.4. *Lower Whitshed core lithology and summary of diatom assemblages classified by salinity preference (Cool, 2013). P: Polyhalobous; M: Mesohalobous; O-h: Oligohalobian-halophile; O-i: Oligohalobian–indifferent; H: Halophobe.*

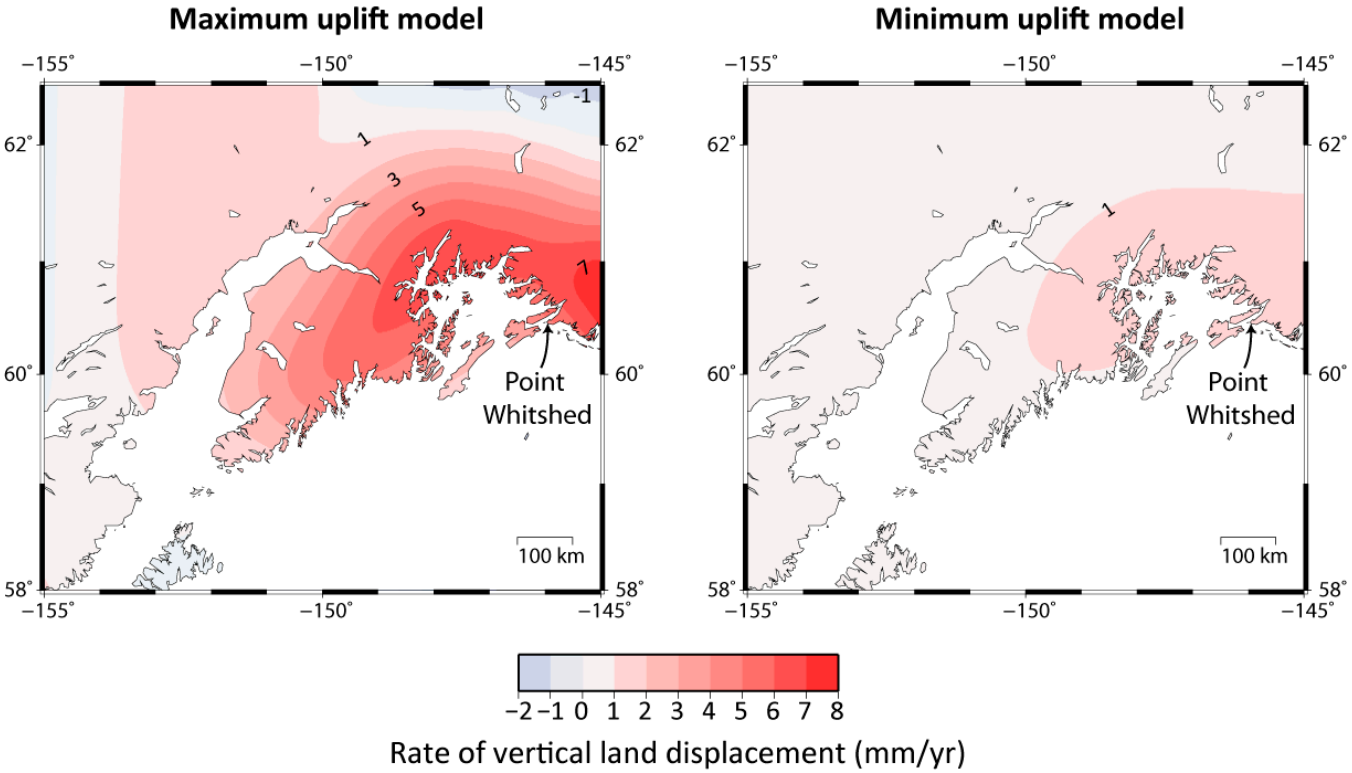

Figure 4.1.5. *Maximum and minimum modeled rates of present-day land uplift (mm/yr) due to LIA glacial isostatic adjustment (Barlow et al., 2012).*

CHAPTER 4.2

A UNIQUE 5,400-YEAR HISTORIC AND PALEOSEISMIC RECORD AT ALAGANIK SLOUGH ON THE COPPER RIVER DELTA: Great Megathrust Earthquakes in the Eastern Aleutian Subduction Zone

by George Plafker[12]

Alaganik Slough field trip itinerary

What makes Alaganik Slough unique for paleoseismic studies?

1. High sedimentation rate that maintains the delta surface close to extreme high tide where it can cycle from intertidal to supratidal environments with each great megathrust earthquake.
2. Possibly the only place on earth where meter-scale coseismic uplift occurs during great megathrust earthquakes but supratidal peat is found as deep as 11.5 m below present high tides because of an intertidal submergence rate that is at least twice the rate expected due to eustatic sea level rise alone.
3. The 1964 earthquake provides return interval vs magnitude data that allow calculation of uplift for the paleoseismic events in the same place—assuming that the present really is a key to the past. Allows calculation of return times for great events that involve regional tectonic uplift.
4. Miscellaneous: Easy to drill; easy access; abundant organics in all strata for radiocarbon dating and interpretation of paleoenvironments; virtually no bioturbation; varved clastic sediments that can help to estimate relative sedimentation rates; etc.

What will we see?

STOP #1 at Upper Alaganik River launch Ramp:

1. Classic flat delta topography and flora;
2. Supratidal and high intertidal marsh—and maybe animals;
3. Ongoing rapid changes to the delta marshes due to coseismic uplift in 1964 (fig. 4.2.2);
4. Riverbank exposures (mostly poor) that show the penultimate event horizon and possibly paleoseismic event 2 in riverbanks as we fly downstream 10 km in an airboat.

STOP # 2: At lower Alaganik River site: Spectacular river bank stratigraphic sequence exhibiting

- 1 or 2 (depending on tides) peat/mud pairs that document the two youngest paleoseismic events of the 1964 earthquake (figs. 4.2.5 and 4.2.66)—the 'Rosetta Stone' for understanding the paleoseismic implications of coseismic uplift in this unique tectonic environment.

Tectonic setting of the Copper River Delta

The Copper River Delta (CRD) is located just east of Cordova and Prince William Sound along the Gulf of Alaska coast and within the rupture zone of the great March 27, 1964, Alaska earthquake near the eastern end of the Aleutian arc (fig. 4.2.1). In this area the convergence rate between the Pacific and North American plates is about 5.5 cm/yr in a N18°W direction (Minster and Jordan 1978). The M 9.2 1964 Alaska earthquake was the greatest seismotectonic event of the 20th century in terms of the known surface area affected by crustal deformation. Because an extensive coastal area was affected, data on vertical crustal deformation, both up and down, are among the most complete ever obtained for a great earthquake (fig. 4.2.1). This field trip guide outlines research in progress directed toward determining the seismotectonic cycle in the Copper River Delta area of south-central Alaska in the 1964 area of regional coseismic uplift. A companion field trip to the Girdwood/Cook Inlet region by Ian Shennan and colleagues reviews ongoing and previous paleoseismic work at stops in areas where coseismic subsidence, rather than uplift, occurred during the 1964 earthquake (Shennan *et al.,* 2014, this guidebook).

[12] *George Plafker, Research Geologist Emeritus, U.S. Geological Survey, 345 Middlefield Road, Menlo Park, CA, U.S.A., 94025.* gplafker@usgs.gov

Vertical deformation in this region consisted of a broad asymmetric downwarp as large as 2 m on the landward side with uplift as large as 11.3 m on its seaward side (fig. 4.2.1). Also, triangulation data showed that the region between Anchorage and the Gulf of Alaska coast shifted seaward at least 20 m (fig. 4.2.1; inset). Movement on subordinate northwest-dipping reverse faults displaced the surface on Montague Island as much as 7.9 m dip-slip and the faults extended offshore to the southwest an unknown distance. A train of destructive sea waves (tsunami) was generated by sudden upheaval of the sea floor on the continental shelf along the zone of major uplift and subsidiary faulting.

Strandline and geodetic data revealed that vertical tectonic deformation during the 1964 Alaskan earthquake involved a segment of the eastern Aleutian Arc 800 km long with an area of more than 140,000 km²—about the size of Germany and slightly smaller than Japan.

1964 Alaska earthquake effects in the Copper River Delta region

With a 75 mile ocean front, the CRD is the largest delta on the west coast of North America (fig. 4.2.3). The CRD stratigraphic sequence near the eastern end of the Aleutian subduction zone records repeated coseismic uplift events separated by long periods of even larger interseismic submergence. The most recent uplift of about 2.2 m during the March 27, 1964, Alaska earthquake (M 9.2) resulted in abrupt conversion of intertidal mud flats into subaerial freshwater peat marshes in a belt 4 to 12 km wide along the coast (Thilenius, in press) (fig. 4.2.4).

Stratigraphy

The delta stratigraphy records at least eight, and possibly nine, pre-1964 sudden uplifts that are best interpreted as coseismic events (Plafker *et al.,* 1992; figs. 4.2.6–4.2.9). These uplift events were superimposed on long-term gradual interseismic subsidence and marine transgression. As a consequence, the upper 13.5 m of the stratigraphic sequence consists of multiple beds of freshwater peat 10–40 cm thick that have sharp basal contacts and upper contacts that grade upward into beds of mostly varved intertidal mud and silt to 2.3 m thick that mainly contain marine microfossils and the rooted remains of salt-tolerant sedge (fig. 4.2.4b). The deepest peat strata and corresponding silt or mud are at about 13 m below the delta surface.

Each peat and silt pair is interpreted to reflect a complete earthquake cycle consisting of an abrupt coseismic uplift above the highest tide level during which freshwater peat formed, followed by gradual resubmergence and burial beneath intertidal sediment (fig. 4.2.8). The combined thickness of the peat and silt layers between the last four pre-1964 events for which the best data are available require a minimum of 1 m of coseismic uplift. This suggests that the causative tectonic earthquakes were large and probably comparable in mechanism to the 1964 event.

Radiocarbon Data

The median calendar ages of nine coseismic events are dated from limiting Carbon-14 (^{14}C) ages at and immediately below the base of the corresponding peat layers at about 851; 1,423; 2,132; 2,567; 3,140; 3,447; 3,937; 4,593; and 5,594 calibrated years BP for nine paleoseismic events (fig. 4.2.9). For eight events, it is likely that events 2,132 and 2,567 calibrated years BP would be combined into an intermediate value (fig. 9). Average repeat times for the nine-event stratigraphic record average 700 or 800 years, depending on whether eight or nine pre-1964 uplift events are preserved.

Dating of plant fossils in the intertidal mud using Carbon-14 (^{14}C) methods indicates average interseismic submergence rates as high as 4.4 mm/yr with annual(?) mud varves that indicate accumulation rates of about 7 mm/yr. Net submergence averages ~2 mm/yr for the ~5,600 years during which 13.5 m of silt and peat accumulated. Late Holocene sediment thickness is as much as 250 m offshore from the Copper River Delta seaward margin (fig. 4.2.3). Assuming an average 1.5 mm/yr eustatic sea level rise and an average 1.5 m coseismic uplift for each of eight events, the combined tectonic and isostatic interseismic subsidence of the delta averaged ~2.6 mm/yr. This high rate of late Holocene interseismic subsidence and abundance of sediment make this sequence unique because the peat layers are sequentially buried and kept close enough to higher high tide levels so that the surface becomes supratidal during great megathrust earthquakes (figs. 4.2.7, 4.2.10, and 4.2.11).

Coseismic uplift and long-term submergence

The Copper River Delta area east of Cordova has an exceptionally complete record of multiple abrupt coseismic uplift events separated by gradual interseismic subsidence that exceeds the coseismic uplift, which was about 2.2 m in 1964. The Copper River Delta consists of at least 180 m of prograding Holocene sediment deposited by the Copper River and its distributaries (Reimnitz, 1966). The subaerial part of the delta has very low relief and is bordered by tide flats as much as 1.6 km wide that are separated from the open ocean by barrier sand islands. Freshwater peat-forming marsh (mostly sedge), brush (willow and alder), and conifer forest (spruce) cover the subaerial part of the delta, and salt-tolerant grasses of the *Carex/Potentilla* community occupy a broad area of the uppermost tidal flats. Because of the very low surface relief, a small amount of uplift causes large horizontal shifts in the position of the high tide strandline so that a wide coastal strip is abruptly converted from intertidal to supratidal marsh. Uplift of about 2.2 m in 1964 resulted in seaward shifts of the strandline of as much as 4–10 km, and the mudflats were entirely covered with vegetation within 10 years (Thilenius, in press; fig. 4.2.2). Our compacted peat accumulation rates based on C^{14} dates, averages about 10–12 mm per 100 years. Judging from the amount of supratidal vegetation accumulated on the present delta surface, we estimate that a peat soil layer 50 years old, or 5–6 mm thick, should be readily detectable in the stratigraphic record. Absence of any peat layers less than 10 cm thick implies that this segment of the megathrust is so tightly locked, possibly because of its size and subhorizontal configuration, that a 300 year return time is the minimum threshold for it to slip.

The stratigraphic section consists of thin (10–40 cm) beds of freshwater peat with sharp basal contacts that grade upward into thicker (1–3 m) beds of varved(?) intertidal mud and silt containing the rooted remains of salt-tolerant sedges (fig. 4.2.4a). Each peat-silt pair reflects a complete earthquake cycle consisting of an abrupt emergence (coseismic uplift) above the highest-tide level followed by gradual, though not necessarily uniform, submergence. The rate of submergence is the algebraic sum of tectonic and isostatic subsidence, sediment compaction, and eustatic sea level rise. In each cycle, peat accumulation begins some time after emergence and terminates upon gradual resubmergence into the intertidal zone; each uplift event occurred immediately after deposition of the uppermost horizon in each silt bed.

The abundant supply of glacial sediment carried by the Copper River and local glacier-fed rivers (Reimnitz, 1966; fig. 4.2.3) maintains the delta surface within about 1.5 m of the highest intertidal level where salt-tolerant sedge is able to survive. The sedge fossils, which occur throughout the silt beds, indicate that silt accumulation roughly keeps pace with submergence. Net submergence, reflected primarily by the thickness of the section, is 2.8 mm/yr over the past 1,450 years but varies from 2.2–5.9 mm/yr (figs. 4.2.10 and 4.2.11). Subtracting the assumed 1.5 mm/yr eustatic sea level rise yields a net subsidence rate of 1.3 mm/year over 1,450 years.

Summary

The Copper River Delta is situated ~15 km above the eastern Aleutian megathrust, which dips gently northward beneath the Alaska continental margin. Dip-slip displacement on the megathrust of more than 20 m generated the giant M 9.2 1964 Alaska earthquake and was accompanied by 2.2 ± 0.2 m of coseismic uplift at the CRD. As a result, a zone of intertidal mud flats to 12 km wide was abruptly raised above mean higher, high tide (MHHT) and has since been rapidly converted into supratidal freshwater peat marsh, ponds, and patchy forest since 1964. Study of slough bank exposures and drill cores to 12.3 m below the marsh surface show eight or nine probable pre-1964 layers of dominantly freshwater peat 8–35 cm thick. They commonly have sharp basal contacts and are overlain gradationally by beds of gray, mainly varved, intertidal mud 0.2–2.3 m thick that contain salt-tolerant plant fossils and diatoms. Each peat/mud pair, or “couplet”, is interpreted to be a complete earthquake cycle and the basal contact of the peat approximates the minimum age of the "event horizon." Based on ^{14}C dating of peat basal contacts, median ^{14}C ages in calendar years before present (cybp) are about: 850; 1,312; 2,220; 2,535; 3,122; 3,465; 3,995; 4,620; and 5,600. The 1964 Alaska earthquake, with M_w 9.2 and coseismic uplift of 2.2 m, followed an interseismic strain accumulation interval of ~850 years. Assuming that magnitude and uplift of the nine paleoseismic events scale roughly with their preceding interseismic intervals, the inferred magnitudes range from ~M_w 8.9–9.2+; uplift per event is from ~0.8–2.5 m and averages 1.6 m. We find no evidence of earthquake uplift events in the CRD stratigraphic record at the CRD smaller than M 8.9. The longest RI is 1,000 calendar years BP (E8), and

the shortest is 300 calendar years BP. The data suggest that energy release in this segment of the Aleutian megathrust occurs primarily during very large seismic events that have minimum recurrence intervals of at least 300 years.

Acknowledgments

Thanks to all the volunteers whose assistance made this study possible. Their names read like a "who's who" of western paleoseismology. They include: Ken LaJoie, Lou Gilpin, Gary Carver, Steven Ward, Peter Haeussler, Rich Koehler, Brian Sherrod, Rob Witter, Eileen Hemphill-Haly (diatoms), John Thilenius (botanist marine tidal plants), Dot Peteet (botanist and peat analysis), and Meyer Rubin (K-Ar dating). Special thanks go to U.S. Forest Service–Cordova Division personnel who kindly gave logistic support over the years with loans of vehicles, boats, housing, and especially their friendly and warm hospitality.

Figures

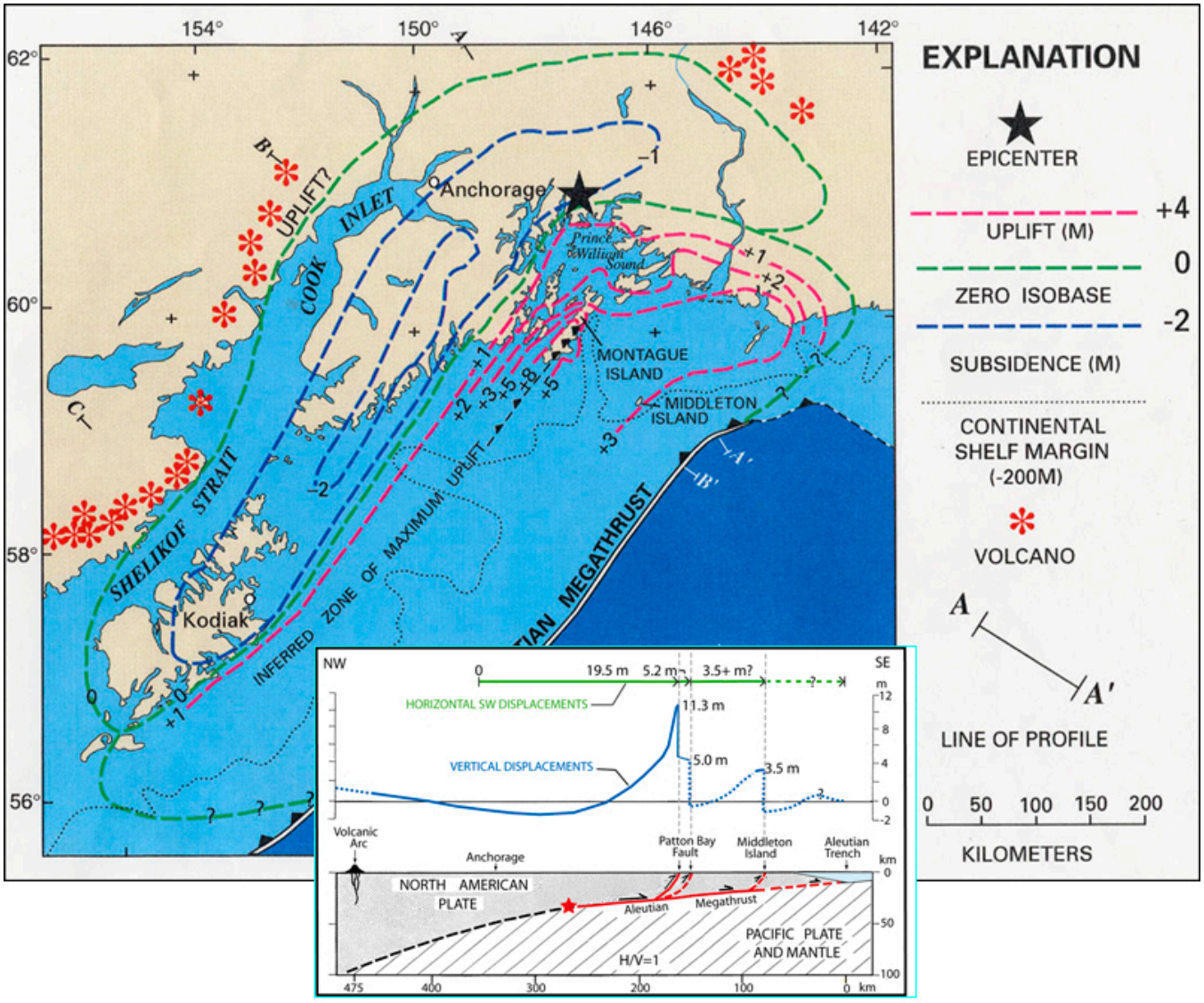

Figure 4.2.1. *Map and simplified section showing tectonic deformation that accompanied the 1964 Alaska earthquake. MAIN IMAGE: Map of land-level change, contoured in meters, dashed where approximate or inferred. INSET: Simplified structure section B–B' with known or inferred active faults in red; in middle, profile of known and inferred vertical coseismic displacements (blue); at top, horizonal SW coseismic displacement relative to Anchorage (Plafker, 1969).*

Figure 4.2.2. *Oblique aerial view showing part of delta. Low gradients, swampy surface, gray muddy distributaries, with Copper River rock flour. Area shown was entirely intertidal before 1964. Typical view of marshes and ponds on uplifted surface in which new peat is forming.*

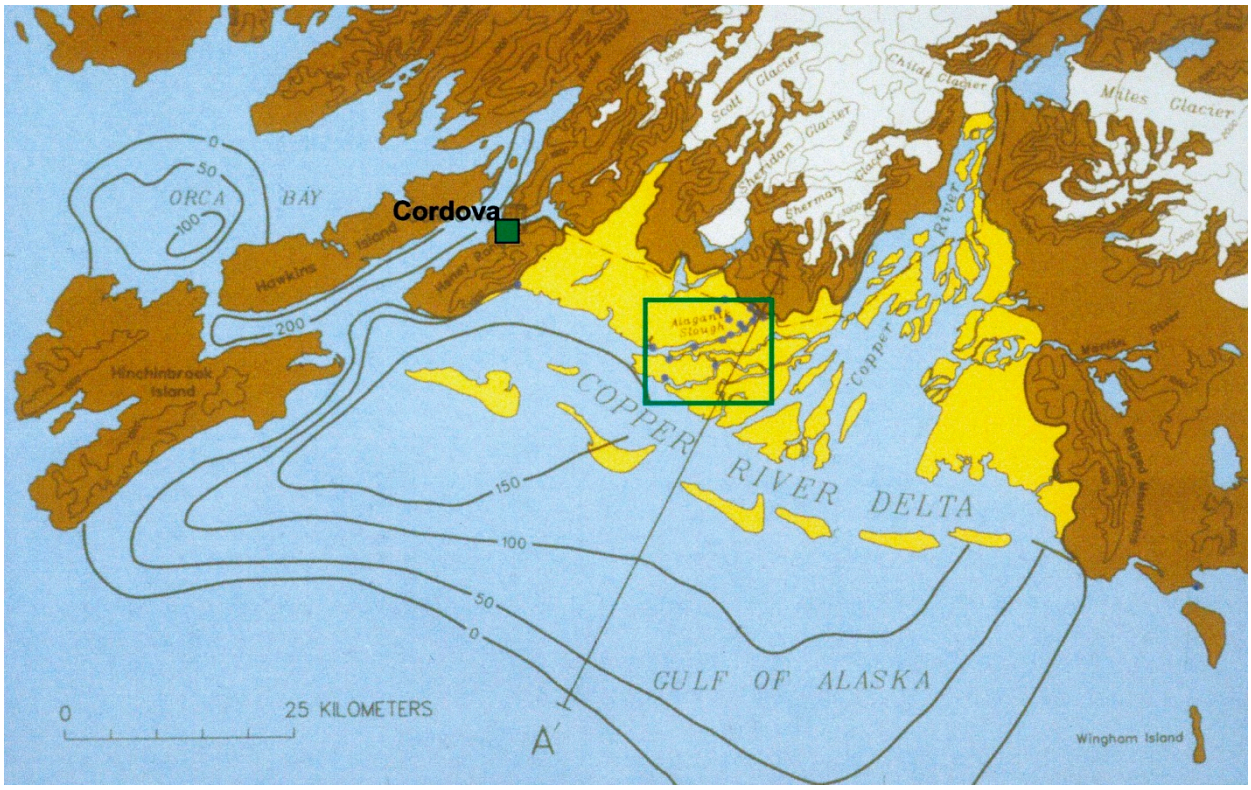

Figure 4.2.3. *Map of western Copper River Delta showing topography and sample sites. Isopachs are thickness of late Holocene sediment in meters.*

Figure 4.2.4. A. *Tree stumps rooted in peat exposed at low tide on the Copper River Delta. The stumps and the associated peat are remnants of a widespread forest flora on the delta that was submerged 2–3 m below highest tides by gradual tectonic subsidence prior to 1964 and buried by intertidal silt and mud deposited by distributaries of the Copper River.* ***B.*** *Varved intertidal silt containing abundant rooted sedge remains (mainly Carex). The continuous accumulation of lithologically uniform, varved, intertidal silt between peat layers suggests gradual and largely uninterrupted interseismic submergence of the Copper River Delta. Varve counts and radiocarbon ages of Carex remains suggest interseismic submergence rates of ca 2.2–5.9 mm/yr. Scale is 6 inches long.*

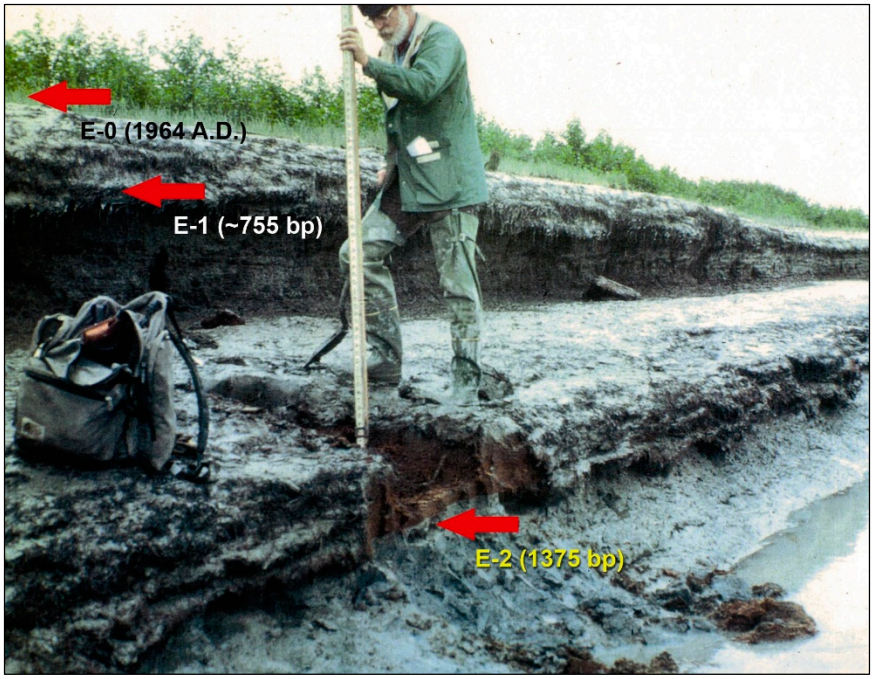

Figure 4.2.5. *Bank exposure in lower Alaganik Slough on the Copper River Delta showing resistant ledges formed by a lower bed of freshwater peat (E-2) 24 cm thick (foreground) and an upper bed of peat (E-1) to 51 cm thick that locally contains rooted stumps of brush and small trees (background). The 1964 event horizon (E-0) is at the brush line in the background. The peat beds have sharp contacts with underlying intertidal silt and sharp to locally gradational contacts with the overlying intertidal silt. The abrupt upward change from intertidal silt to subaerial peat is interpreted as due to coseismic uplift during paleoseismic events comparable in mechanism to the 1964 earthquake.*

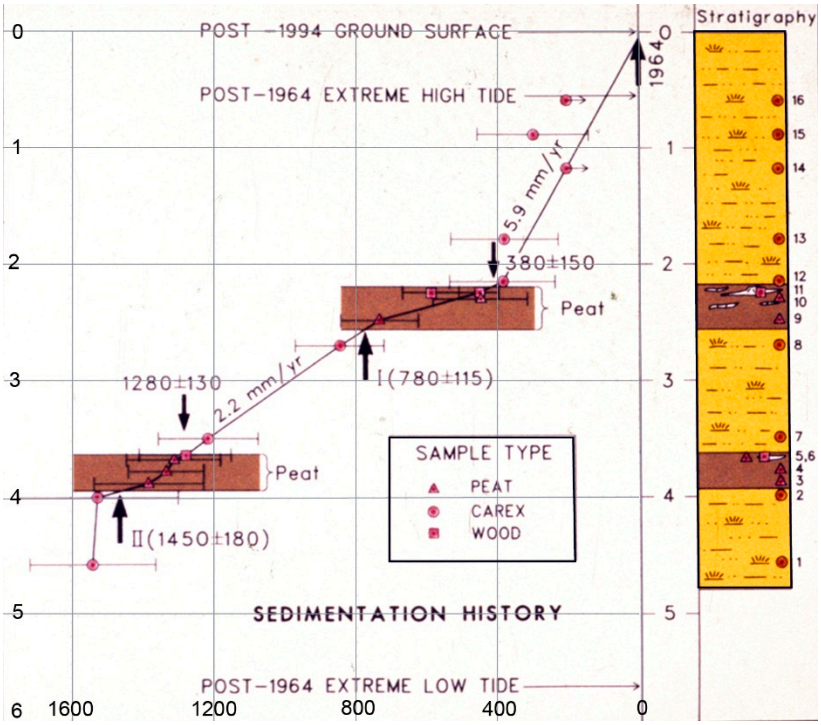

Figure 4.2.6. *Stratigraphy and sedimentation history of interbedded subaerial peat and intertidal silt at measured section in lower Alaganik Slough, Copper River Delta. Stratigraphy on right shows two pre-1964 peat-silt couplets and locations of dated ^{14}C samples. Left side shows age vs. depth (sedimentation rate) based on ^{14}C dated samples of peat (solid dots), wood (squares), and intertidal sedge in silt (open circles). Upward-pointing arrows indicate best ages for coseismic uplift that resulted in abrupt change from subaerial to intertidal deposition. The two coseismic uplift events at this site have calibrated ^{14}C ages of 780 and 1,450 yr BP. Downward-pointing arrows indicate the approximate time when the peat layer was drowned by gradual interseismic submergence; two equally plausible submergence times are shown for the upper layer.*

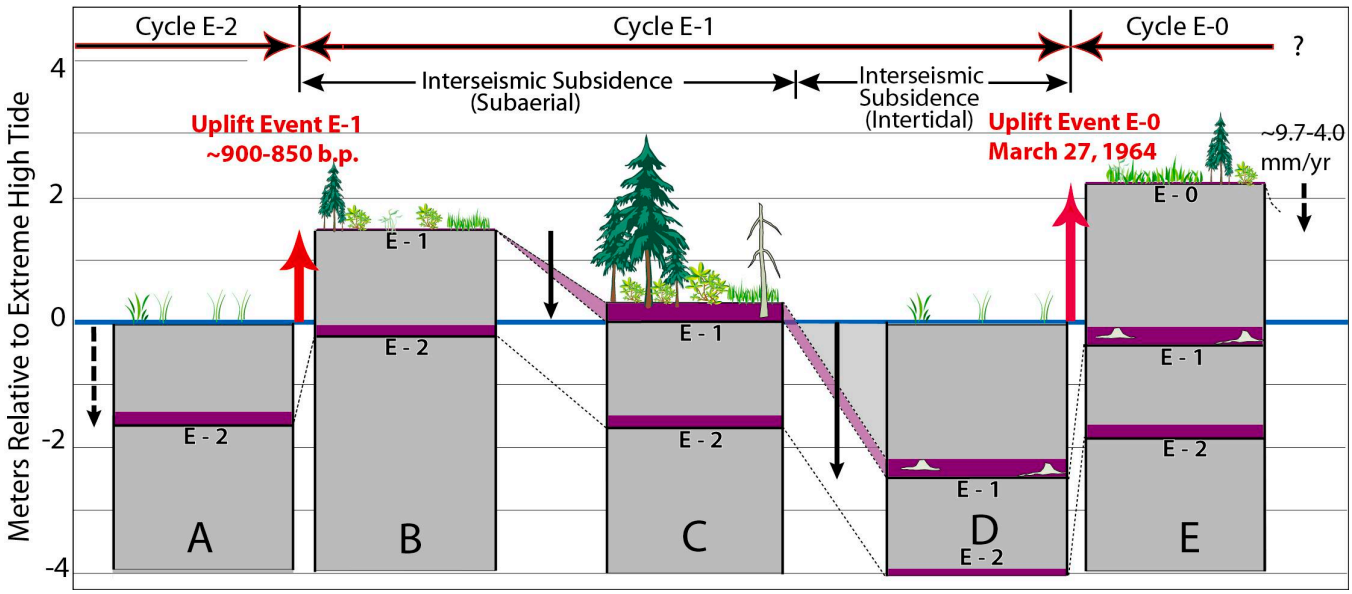

Figure 4.2.7. *Cartoon depicting a complete seismic cycle (E-1).* ***A.*** *Intertidal mud surface before E-1 uplift.* ***B.*** *E-1 surface after uplift.* ***B–C.*** *Accumulation of subaerial E-1 organic sediment. Submergence of E-1 surface below extreme high tide.* ***C–D.*** *Continued submergence of E-1 surface and deposition of 2 m of sediment.* ***E.*** *1964 2.2 m uplift and beginning of submergence.*

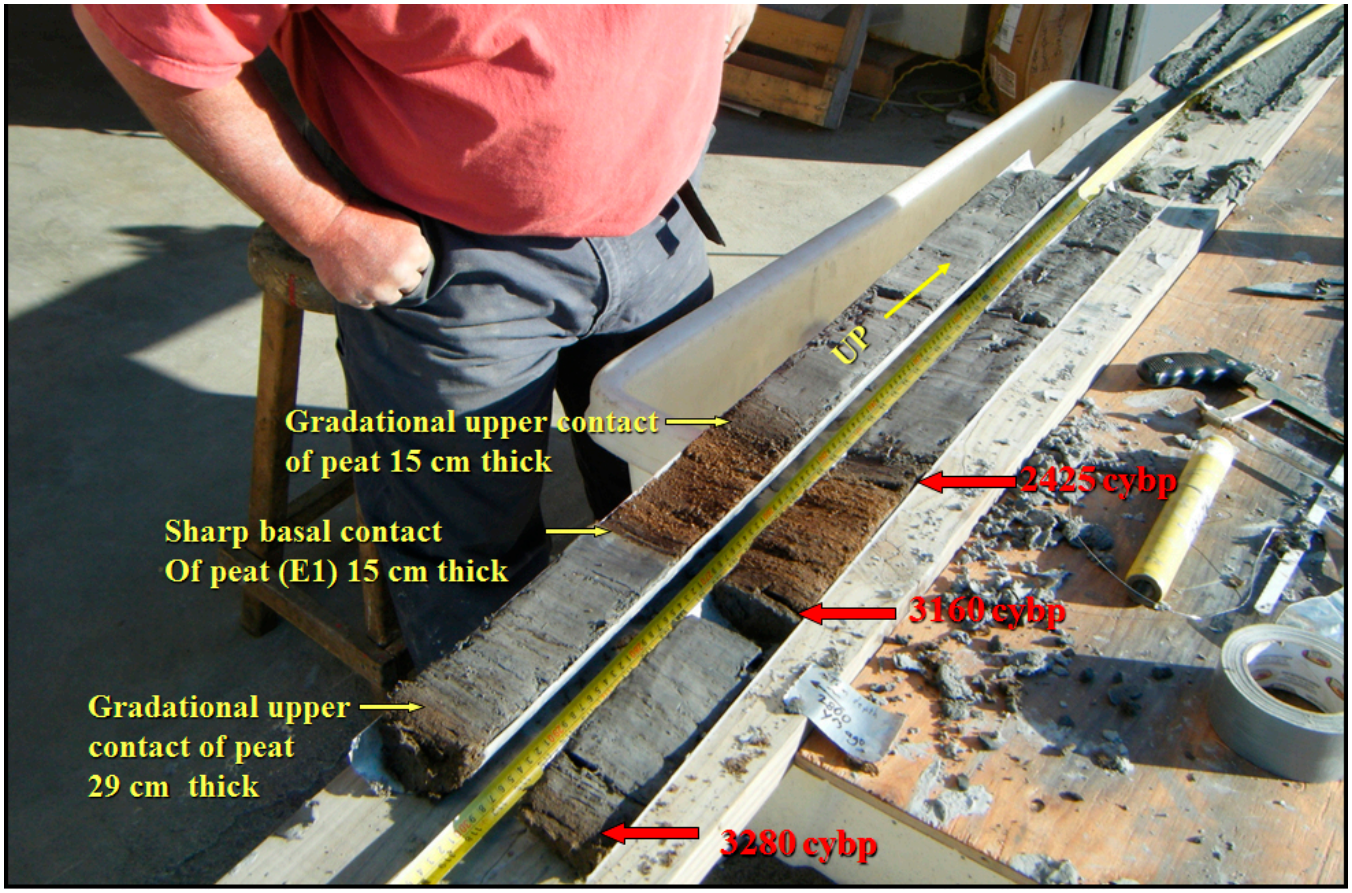

Figure 4.2.8. *Split core from 4.5 to 5.9 m depth showing typical pairs of intertidal silt (gray) and freshwater peat (brown). Note sharp lower contact and gradational upper contact. Up is to the right.*

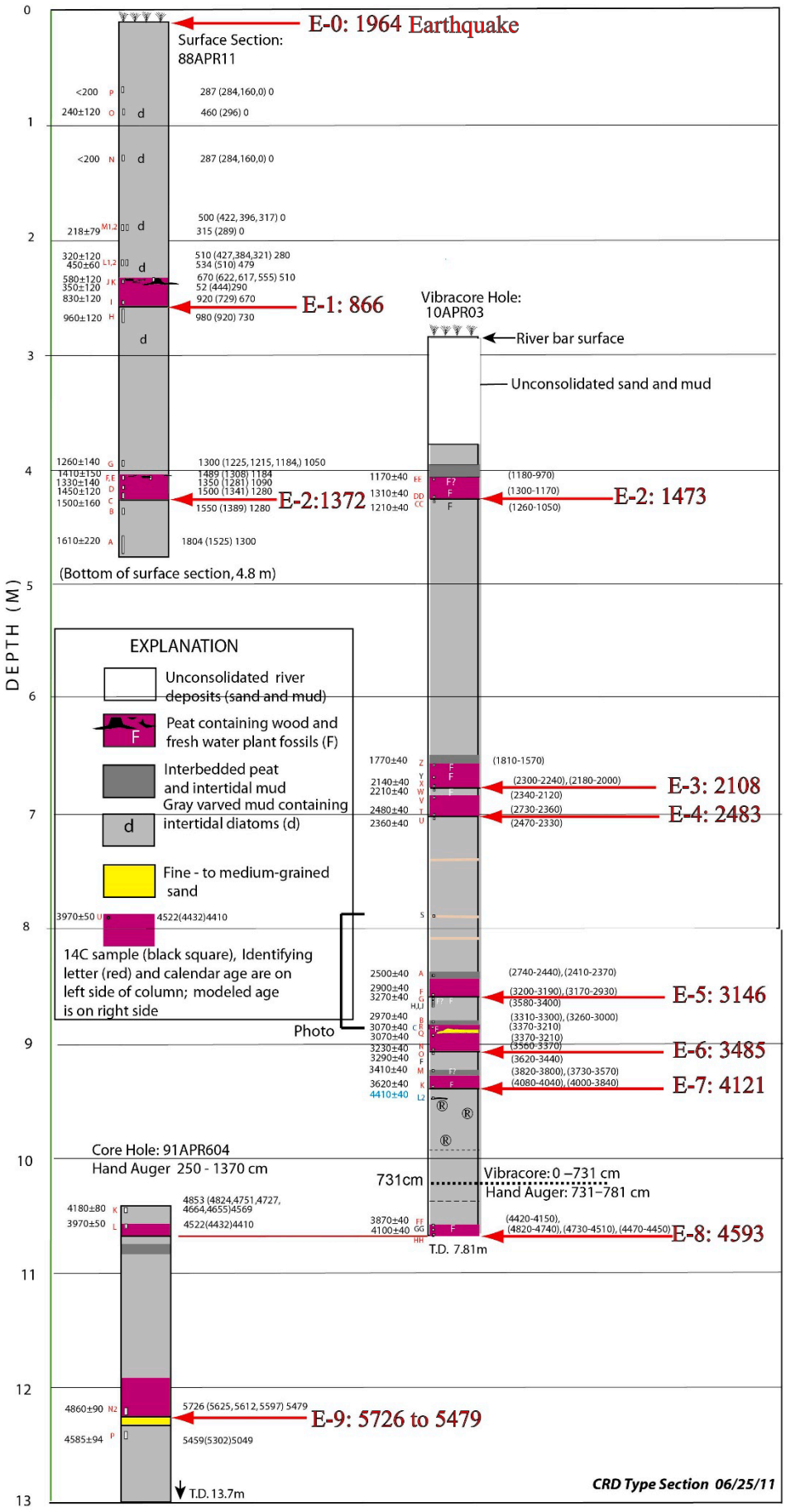

Figure 4.2.9. *Composite stratigraphic sections for the Alaganik Slough showing eight or nine peat layers interpreted as earthquake-generated uplift. Red arrows and numerals indicate locations of event horizons. Radiocarbon dated samples shown in red lettering.*

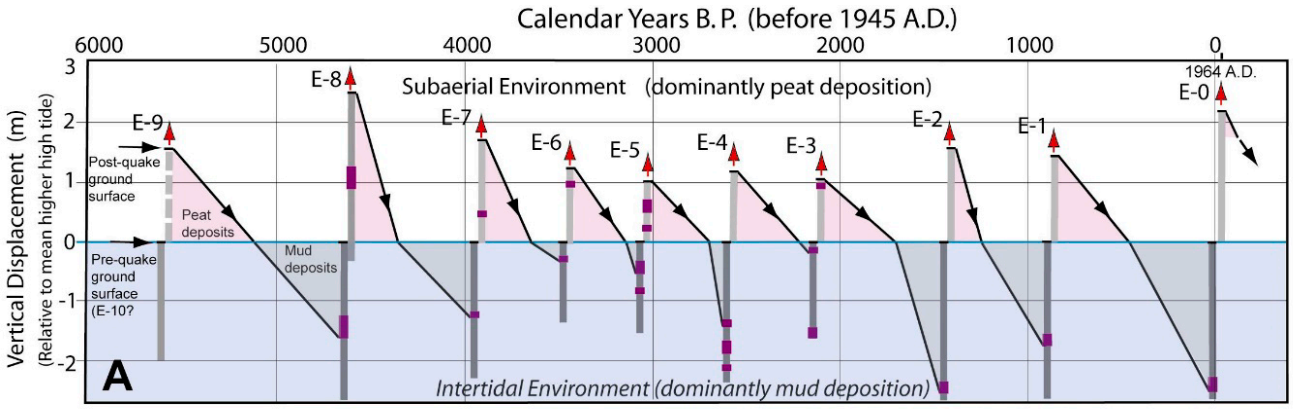

Figure 4.2.10. *Model of Copper River Delta seismic cycle to account for the stratigraphic section shown. The model assumes: (1) coseismic uplift comparable to the 1964 uplift of about 2 m and average linear 4.4 mm/yr interseismic subsidence comparable to the pre-1964 average long-term rate (dashed line), and (2) eustatic sea level rise of 1.0 mm/yr. The solid line shows the ground surface resulting from the combination of the tectonic displacements and sediment accumulation shown in the section.*

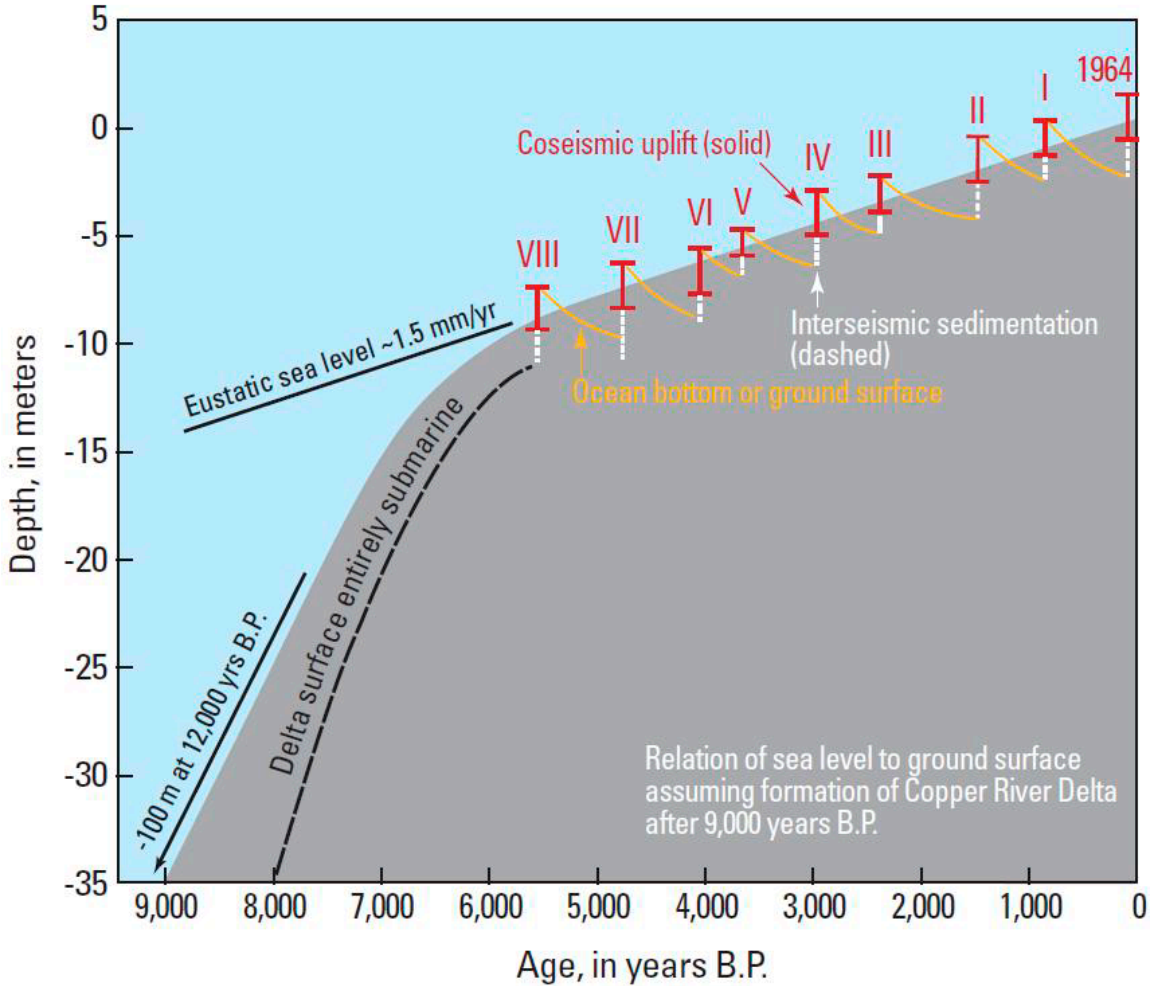

Figure 4.2.11. *Approximate relationship at Copper River Delta between sea level rise, the seismic cycle, and sedimentation assuming that the delta became subaerial after about 9,000 years b.p. Emergence = coseismic uplift + sedimentation. Submergence = interseismic subsidence + eustatic sea level rise + isostatic subsidence + sediment compaction.*

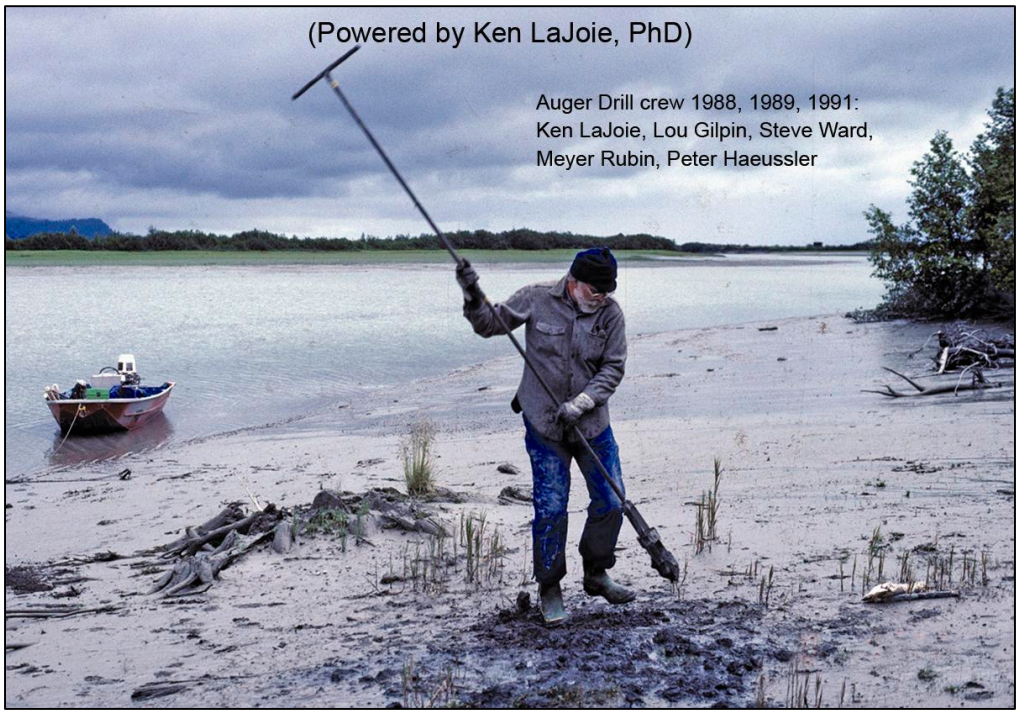

Figure 4.2.12. *Subsurface sampling methods showing USGS sophisticated 4" bucket auger powered by Ken. Note stumps in upper peat behind Ken.*

Figure 4.2.13*. Sampling with a 3.5" × 20' Vibracore to recover large undisturbed subsurface samples.*

CHAPTER 4.3

ST. ELIAS MOUNTAINS

by Eva Enkelmann[13]

The Copper River is the largest river system in southeastern Alaska, draining most of the Wrangell Mountains, the northeastern flanks of the Chugach Mountains, the Copper River Basin, and the northern flanks of the St. Elias Mountains (fig. 4.3.1). The Copper River incises the coastal mountain ranges, forming the geographic boundary between the Chugach Mountains (west) and the St. Elias Mountains (east), and creating a ~20-km-wide delta where the river enters the Gulf of Alaska. This is the easternmost stop of the field trip and allows a glance at the remote St. Elias Mountain Range that stretches 300 km, from the Copper River east to Yakutat Bay, constituting the highest coastal mountain range on Earth. The St. Elias Range is characterized by very rugged topography with >5,000 m peak elevation (Mt. Logan, 5,959 m; Mt. St. Elias, 5,489 m), up to ~5,000 m of local relief, and more than 50 percent of the surface is covered by glaciers and icefields including some of the largest glacial systems outside the polar regions (e.g. Bagley Ice Field, Bering Glacier, Seward–Malaspina Glacier). The southern flanks of the St. Elias Mountains receive high precipitation with rates of >3 m/yr, mostly as snow that feeds the large glacial systems (Royer, 1982).

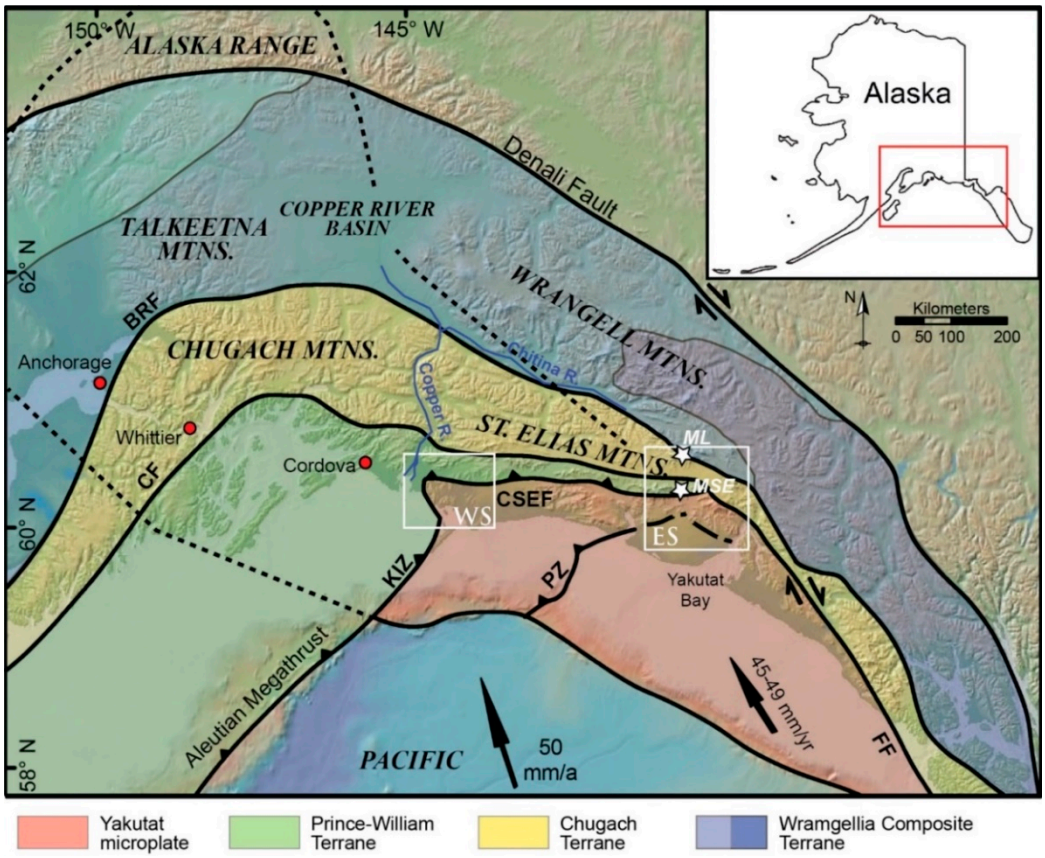

Figure 4.3.1. *Overview of the geology and main structures in southeastern Alaska. The different terranes are indicated in different colors. White boxes indicate the western (WS) and eastern (ES) syntaxis region of the Yakutat collision zone. Plate motion vectors are from Fletcher and Freymueller (2003). Dashed line indicates the flat-slab of the subducted Yakutat microplate. BRF: Border Range Fault, CF: Contact Fault, CSEF: Chugach–St. Elias Fault, FF: Fairweather Fault, KIZ: Kayak Island Zone, PZ: Pamplona Zone, ML: Mount Logan, MSE: Mount St. Elias.*

[13] *Eva Enkelmann, Department of Geology, University of Cincinnati, 500 Geology Physics Building, P.O. Box 210013, Cincinnati, OH, U.S.A., 45221. Eva.enkelmann@uc.edu*

The St. Elias Mountain Range

The St. Elias Range formed through the subduction/collision of the Yakutat microplate with the southern margin of North America, which itself is composed of several terranes that have been accreted throughout Mesozoic–Cenozoic time (fig. 4.3.1; Plafker *et al.*, 1994). Based on seismic velocity profiles the Yakutat microplate has been described as a wedge-shaped, oceanic plateau with crustal thickness of 15 km in the west (just east of the Copper River Delta) increasing to 30 km in the east at Yakutat Bay (Christeson *et al.*, 2010; Worthington *et al.*, 2012). The deformed and imbricated Cenozoic sedimentary cover sequence of the Yakutat microplate is > 10 km thick at its western end and tapers out toward Yakutat Bay, where basement rocks are exposed on land.

The Yakutat microplate is currently moving 45–49 mm/yr towards the NNW with respect to interior Alaska (fig. 4.3.1) (Fletcher and Freymueller, 1999). This high convergence rate is expressed by high seismicity between Prince William Sound and the Alaska panhandle, which has generated some of the largest earthquakes including the M 9.2 Prince William Sound earthquake in 1964 (e.g. Nishenko and Jacob, 1990; Plafker, 1969; Shennan *et al.*, 2009; Plafker and Thatcher, 2008). Active faulting causes the deformation and uplift of the Cenozoic sediments on the shelf and produced several islands (e.g. Kayak, Hinchinbrook, Montague) and bathymetric heights such as the Tarr Bank located south of the Copper River (fig. 4.3.1). Subduction of the Yakutat microplate started in the late Eocene–early Oligocene, causing the magmatism on the North American Plate to shut off, building topography, and causing rock exhumation in the region above the flat slab, and basin subsidence around the perimeter (fig. 4.3.1; Finzel *et al.*, 2011). The thick Yakutat slab has been imaged to reach 650 km inboard from the present-day collisional front to the Alaska Range (Ferris *et al.*, 2003) (fig. 4.3.1).

The mountain ridges visible across the Copper River Delta (looking E–SE) are the location of the western syntaxis where the suture zone between the colliding Yakutat microplate and North America, the Chugach–St. Elias Fault, bends 90° to connect with the Kayak Island Zone and the Aleutian megathrust (fig. 4.3.1). The western syntaxis region comprises rocks of the Orca Group (a Paleogene accretionary complex) that belong to the Prince William Terrane. East and south of the suture the rocks comprise Eocene to Pliocene sediments that were deposited on the Yakutat microplate as it moved northward along the dextral Queen-Charlotte–Fairweather transform, and which were later folded and imbricated within the developing accretionary wedge (e.g. Miller, 1971; Plafker *et al.*, 1994; McCalpin *et al.*, 2011). The Pamplona fault zone, located farther south, is the active deformational front and is continuous on land (east), coinciding with the eastern syntaxis and the location of the highest peaks in the region (fig. 4.3.1).

Mountain Building and Erosion

The high tectonic activity and heavy glaciation make the St. Elias Range a perfect natural example to study the interaction between tectonics, climate, and surface processes that together influence the geodynamic evolution of active orogens (e.g. Molnar and England, 1990; Beaumont *et al.*, 1992, 2001; Koons, 1995; Zeitler *et al.*, 2001). Most active mountain ranges have been extensively shaped throughout Quaternary glaciation, but have only remnants of glaciers and glacial landforms today. For that reason our understanding of coupling between glacial erosion and tectonic processes is mostly based on the study of the geomorphology of deglaciated landforms (Brocklehurst and Whipple, 2002, 2007; Champagnac *et al.*, 2009), and on conceptual (Whipple *et al.*, 1999), analytical (Tomkin and Roe, 2007), and numerical models (Tomkin and Braun, 2002; Tomkin, 2007; Herman and Braun, 2008; Yanites and Ehlers, 2012). The St. Elias Range provides the opportunity for direct field investigations of glacial erosion processes in an active orogen and testing glacial erosion models (e.g. Spotila *et al.*, 2004; Berger *et al.*, 2008; Enkelmann *et al.*, 2009, 2010; Spotila and Berger, 2010; Headley *et al.*, 2013).

Erosion through glaciers is the most efficient process for removal and redistribution of material and many studies have been conducted to quantify erosion in the St. Elias Mountain Range over various time scales. Based on the sediment accumulation in tidewater fjords it was suggested that short-term erosion rates ($<10^3$ years) in the St. Elias Mountains are the highest in the world with > 10 mm/yr (Hallet *et al.*, 1996). While the coarse-grained material is mostly trapped in the fjord along the coastline, large quantities of fine-grained sediments accumulate on the shelf. Taking into account the deposits in the fjords and on the shelf over centennial–Holocene time scales

the estimated sediment-accumulation rate exceeds 250 x 10^6 tons/yr (Jaeger *et al.*, 1998). With that, the coast of the St. Elias Range represents the largest source of sediments transported in the Pacific Ocean from North and South America (Jaeger *et al.*, 1998). The Bering Glacier, the Malaspina Glacier, and the Copper River make the largest contributions (fig. 4.3.2). The sediment load of the Copper River has been estimated to be 70 x 10^6 tons/yr, which makes it one of the 20 largest in the world (Milliman and Meade, 1983). More than 70 percent of the sediments are accumulated on the delta front and prodelta, and the remaining load is transported east, southeast, and west into Prince William Sound (Molina, 1989; Milliman *et al.*, 1996; Jaeger *et al.*, 1998).

To study erosion processes acting over longer time scales (> 10^6 years) numerous low-temperature thermochronometric methods have been used to quantify rates and their spatial variations. Figure 4.3.2 shows that erosion and rock exhumation is high (> 1–3 mm/yr) on the southern flanks of the St. Elias Range where precipitation rates are highest, whereas the northern flanks are much dryer, resulting in lower long-term erosion rates (< 0.3 mm/yr) and accordingly older cooling ages (e.g. Spotila *et al.*, 2004; Berger *et al.*, 2008; Berger and Spotila, 2008; Enkelmann *et al.*, 2010). However, the study of detrital material revealed that the most rapid and deep-seated exhumation of rocks occurs at the eastern syntaxis, in the high icefield region of Seward Glacier, coinciding with the highest topography and local relief (fig. 4.3.3). This pattern of exhumation has been found by the study of the sand-size glacial outwash material using zircon fission-track dating (Enkelmann *et al.*, 2008, 2009, 2010), which records the time of cooling below 250 ± 40°C (Brandon *et al.*, 1998). Exhumation of 8–10 km since 2–3 Ma have been estimated for the eastern syntaxis region and explained through the development of a positive feedback between localized strain concentration and efficient glacial erosion (Enkelmann *et al.*, 2009). The histograms in figure 4.3.3 summarize the zircon fission-track ages of the main drainages in the St. Elias and show that the youngest cooling ages occur in the Seward Glacier detritus. A small amount of this young cooling age population is also found in the Chitina River and gets transported into the Pacific through the Copper River (Enkelmann *et al.*, 2010). A recent study of the cobble-size clasts from the Malaspina Glacier combined zircon U-Th/He dating and petrographic analysis on thin sections (Grabowski *et al.*, 2013). The cooling age of the clasts provides information on the exhumation (cooling below 180 ± 20°C) and the lithology provides the provenance within the large Seward–Malaspina catchment (fig. 4.3.4). The histogram in figure 4.3.5 shows that different lithologies experienced very rapid cooling, suggesting that the area of rapid exhumation is large and involves most of the Seward Glacier (Grabowski *et al.*, 2013).

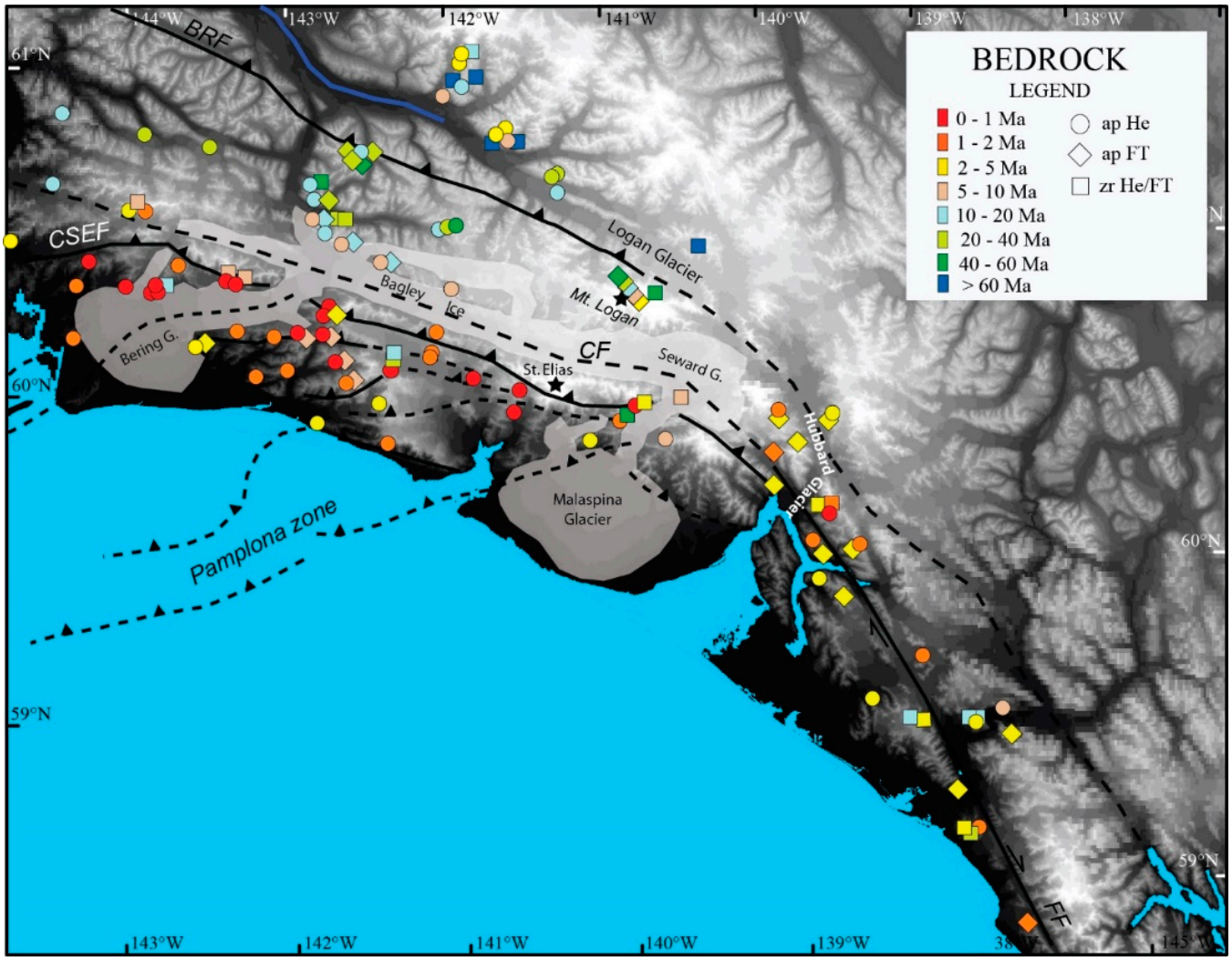

Figure 4.3.2. *Overview of all apatite and zircon U-Th/He and FT bedrock ages of O'Sullivan et al. (1995); O'Sullivan and Currie (1996); Spotila et al. (2004); Berger et al. (2008); Berger and Spotila (2008); Meigs et al. (2008); McAleer et al. (2009); Enkelmann et al. (2010).*

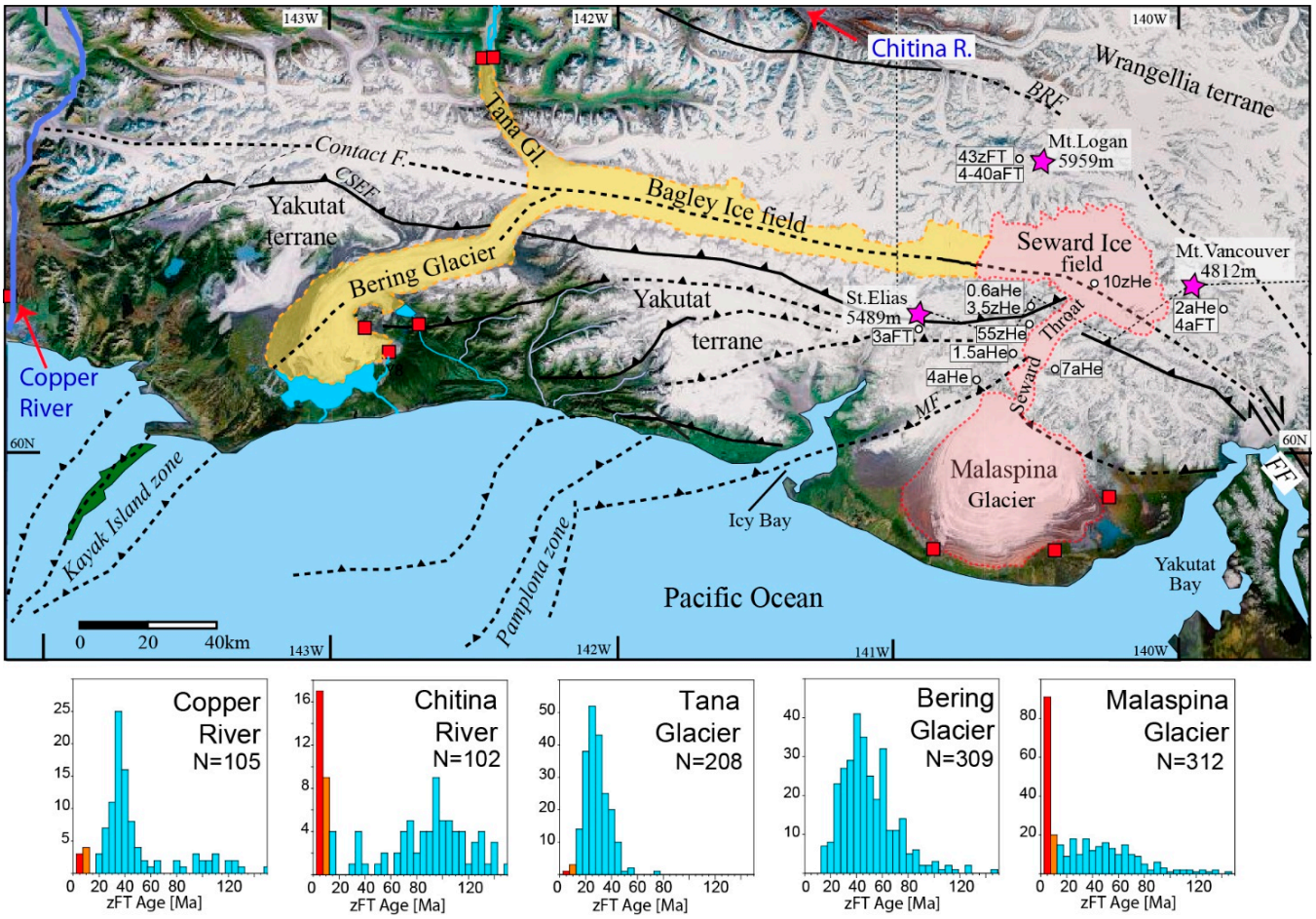

Figure 4.3.3. *Topography of the St. Elias Range and major glacial system (modified from Headley et al., 2013). Histograms show the single-grain zircon fission-track ages of large catchments. Cooling ages < 5 Ma and 5–10 Ma are indicated in red and orange, respectively. Cooling ages > 10 Ma are blue. N: number of single-grain ages. Data from Enkelmann et al. (2008, 2009, 2010). zHe and aHe: zircon and apatite U-Th/He ages of bedrock samples (data from O'Sullivan and Currie, 1996; Berger and Spotila, 2008; Enkelmann et al., 2010). CSEF: Chugach St. Elias fault; BRF: Border Ranges fault; FF: Fairweather fault; MF: Malaspina fault.*

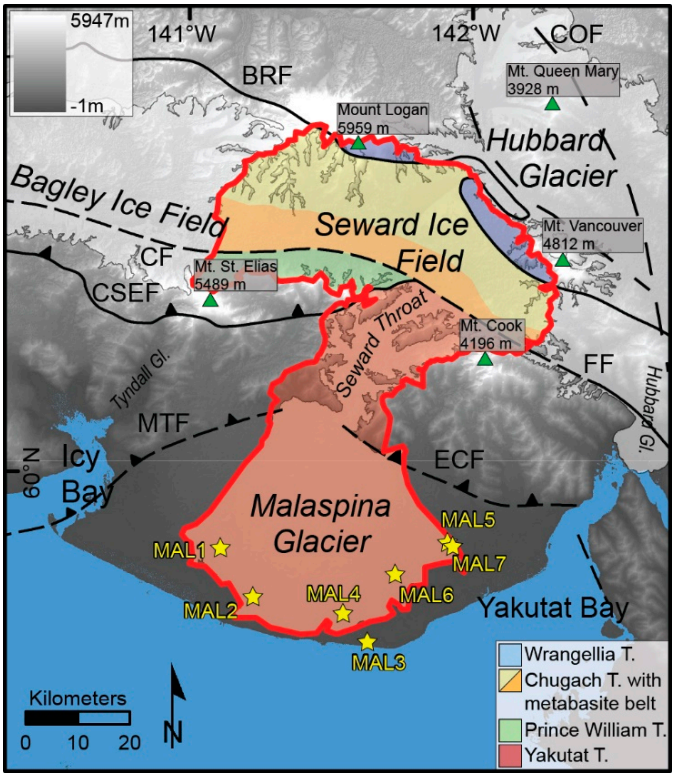

Figure 4.3.4. *ASTER GDEM of the eastern syntaxis region (figure from Grabowski et al., 2013). Color code highlights the terranes present within the Seward–Malaspina catchment (red line). Gray shaded areas show the ice cover of the major glacial systems covering the St. Elias syntaxis region. Red line marks the catchment area of the Seward–Malaspina Glacier. Stars mark the seven counting and sampling locations. BRF: Border Ranges fault; CF: Contact fault; CSEF: Chugach St. Elias fault; MTF: Malaspina thrust fault; ECF: Esker Creek fault; FF: Fairweather fault; COF: Totschunda connector fault.*

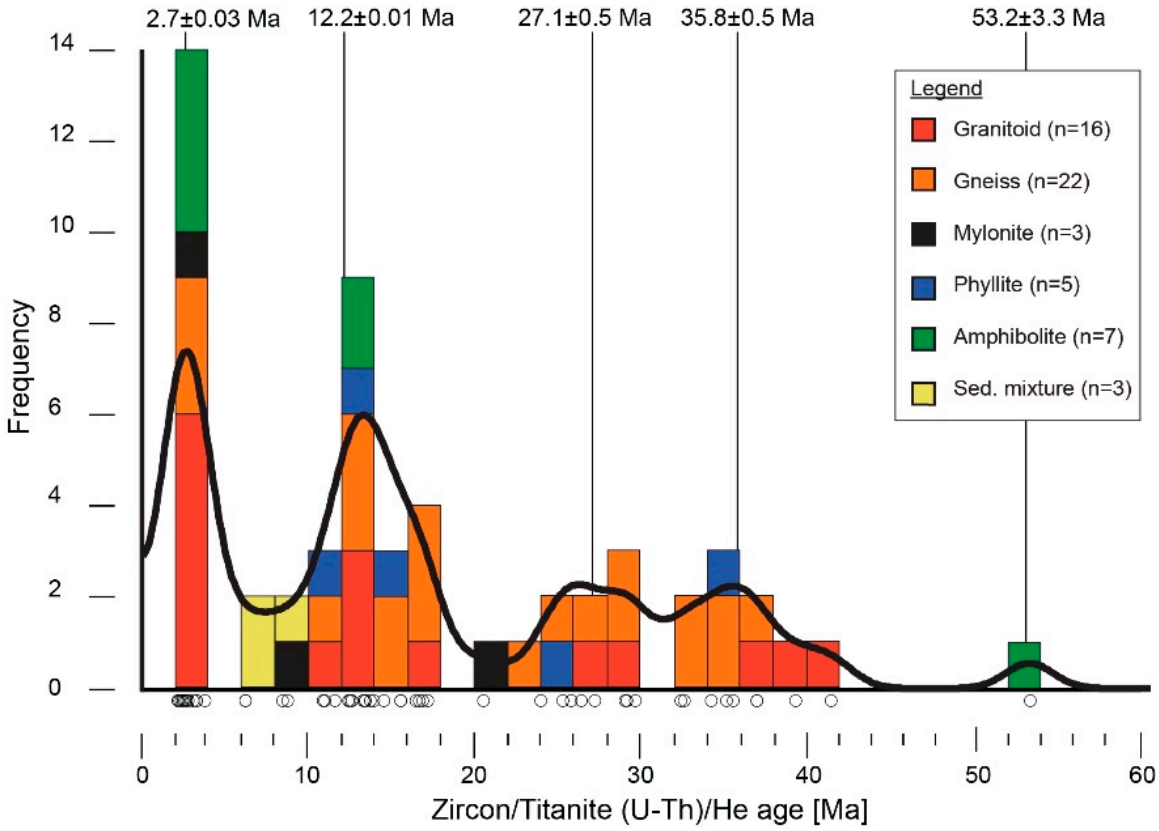

Figure 4.3.5. *Histogram (from Grabowski et al., 2013) of 56 zircon/titanite cobble ages (2 m yr bin size); the fractions of the different lithologies (color coded) are stacked on top of one another. The black line is a kernel density estimation. Peaks were calculated with the implied mixed population determination tool, which calculates the peak ages. Black circles display the data points, n=number of clast ages per lithology group.*

CHAPTER 5

CHAPTER 5.1

PORTAGE GARAGE AND AREA OF MAXIMUM COSEISMIC SUBMERGENCE

by Ian Shennan[14]

Portage lies along the axis of maximum coseismic subsidence in 1964. Following ~2.5 m subsidence, comprising 1.5 m tectonic subsidence and ~ 1.0 m due to ground shaking and consolidation of unconsolidated sediments, high sediment input rapidly buried and preserved the 1964 marsh surface, with much of the accommodation space infilled within the next 10 years (Atwater *et al.*, 2001; Ovenshine *et al.*, 1976). Rapid sedimentation over longer timescales, more than 90 m during the Holocene (Bartsch-Winkler *et al.*, 1983), means that records longer than a few hundred years require cores through thick, unconsolidated sediment sequences. As a result, studies of multiple earthquake cycles at Portage are limited to cores collected with motorized drilling rigs (Combellick, 1991, 1993; Combellick and Reger, 1994). Despite the early interest, it proved difficult to reliably correlate the Holocene paleoseismic record from Portage with those from other locations.

At this stop we will consider:

1. A new analysis of the 16 m core taken by Combellick in 1988
2. Old carbon in radiocarbon samples and implications for earthquake chronologies
3. The old garage site and post-1964 sedimentation and vegetation succession
4. The chronology of great earthquakes across sites visited during the excursion

Late Holocene earthquake record at Portage

In 1985, drilling at two sites in Turnagain Arm, one at Girdwood and one at Portage, confirmed the presence of multiple organic layers interbedded with tidal clastic deposits below the 1964 soil horizon (Combellick, 1991). The core was not continuous and the radiocarbon ages of the abrupt contacts correlated poorly with those from other sites in the region (Bartsch-Winkler and Schmoll, 1987). A second core at Portage, and another one at Girdwood, were commissioned in 1988, using a motorized drill rig capable of recovering a more continuous sequence (Combellick, 1991). These cores had excellent recovery and provided more than 16 m of undisturbed sediment at Portage. Fine laminations in many of the clastic horizons were very well preserved, suggesting intertidal sedimentation, and supported the original hypothesis of multiple cycles of coseismic subsidence and gradual interseismic recovery, superimposed upon glacio-isostatic relative sea-level change. But the radiocarbon chronologies from the 1988 cores at Girdwood and Portage failed to resolve the discrepancies between the sites, with no clear correlation of events or the number of events indicating coseismic submergence (Combellick, 1991, 1993; Combellick and Reger, 1994).

It was thought that the 1988 Portage core had been lost or destroyed, but it was found in 2008, repackaged and transferred to the Alaska Division of Geological & Geophysical Surveys' Geologic Materials Center for archiving. Initial analyses revealed the samples to be in good condition, and we undertook sampling for diatom and AMS radiocarbon dating. To preserve these important cores for future research we limited the number of samples and volume of sediment taken to address the key hypotheses relating to the identification of coseismic subsidence and the chronology of events (Shennan *et al.*, in press). This approach leaves the whole of the 16 m core available for future analyses.

We recorded six distinct organic layers in the archive core (fig. 5.1.1), each with a clear, abrupt, upper contact and directly comparable to those originally described. We could not identify a layer of disseminated fine organic

[14] *Ian Shennan, Department of Geography, Durham University, Lower Mountjoy, South Road, Durham, DH1 3LE, United Kingdom.* *Ian.shennan@durham.ac.uk*

material recorded in the original core at almost 16 m depth and saw only one, rather than two layers of sedge leaf and stem fragments in the upper 3 m.

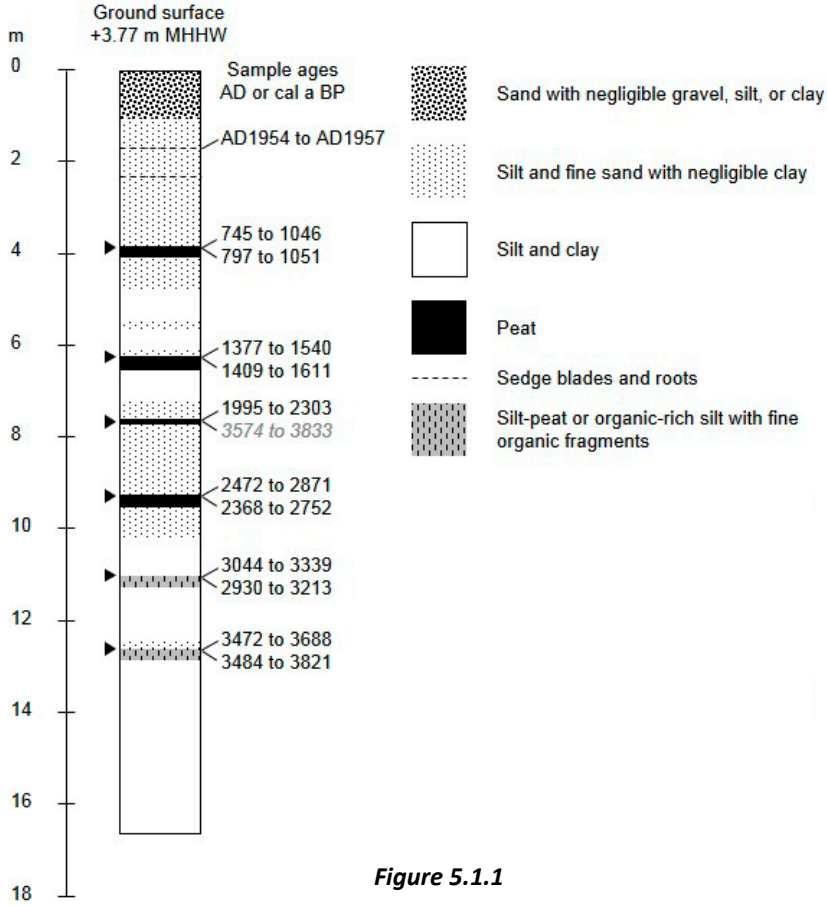

Figure 5.1.1

Submergence of the marshes in 1964 is indicated in the core by interlayered brown-gray silt and silty fine sand with disseminated fine organic material, probably sedge blades and roots. A sample of these gave a modern radiocarbon age, calibrated as AD 1954 to 1957. Other locations at Portage, including intertidal outcrops, record the submerged 1964 marsh surface as a 1–2 cm organic mud, with rooted plant remains (Atwater *et al.*, 2001; Combellick, 1991), rather than a thick peat horizon as seen at Girdwood, Bird Point, and Anchorage. Four of the six couplets show strong evidence of sudden submergence, with sharp peat-silt contacts, and estimates of vertical change in the range of 1.9 to 2.2 ± 0.9 m (95 percent limits) which together are consistent with rapid subsidence of high marsh or freshwater marsh to intertidal flat (see fig. 5.1.2 of the example from 924 cm). The lowest two couplets suggest slightly less submergence (Shennan *et al.*, in press).

Comparison of radiocarbon ages from bulk samples vs. AMS dating of macrofossils

By using AMS radiocarbon dating of plant macrofossils that we could pick with the aid of a microscope we now see a coherent chronology, with the exception of one sample. For the peat contact at 756 cm we obtained two very different ages. This illustrates the susceptibility of using single macrofossils, in this case a *Sphagnum* stem

Figure 5.1.2

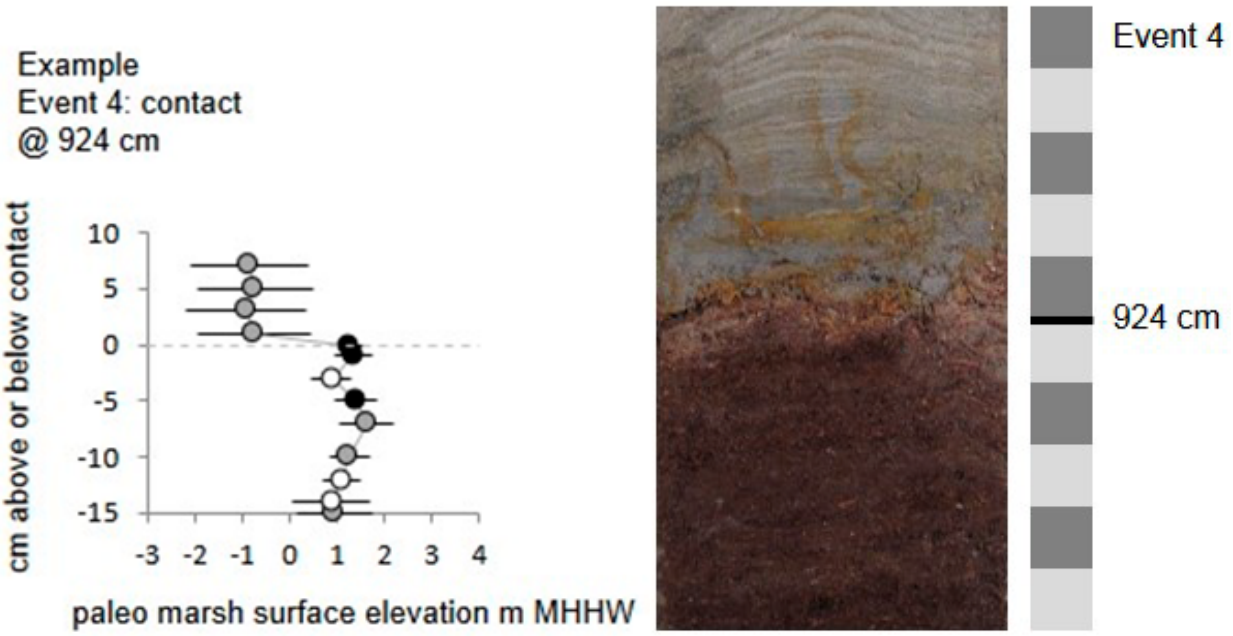

with leaves attached, as there is always chance that they may not be *in situ*. This is especially the case for a core sample rather than an outcrop. In this case all of the other samples form a coherent sequence in stratigraphic order and we suggest that the older sample at 756 cm, a very sharp contact with possible erosion, reflects a macrofossil eroded from an older peat layer. Therefore we do not consider this out of sequence sample further. The other samples resolve the difficulties faced by the original chronology based on bulk peat samples (Combellick, 1991), with the contacts at 756 and 924 cm having statistically different age ranges in contrast to the statistically identical bulk ages. Results from paired samples at sites around Cook Inlet show numerous significant discrepancies between ages obtained on bulk peat samples and ages from in situ plant macrofossils extracted from duplicate peat samples (fig. 5.1.3). We suggest that reworking and deposition of older organic material by winter ice seems possible (Hamilton *et al.*, 2005; Shennan *et al.*, 2008). This would particularly affect sediment accumulation at the vegetated marsh front where there is a concentration of transported ice blocks. Thus, bulk peat samples at the upper or lower contact of a marsh peat bed would be susceptible. We cannot say whether there is a significant effect on marshes not affected by winter ice. In addition, the river catchments of upper Cook Inlet include numerous coal-bearing rocks, which may be an additional source of old carbon. For all these reasons, we also caution against using the oldest ages reported by Combellick (1991), >10 ka BP, from Portage and Girdwood as either sea-level indicators or limiting ages for deglaciation.

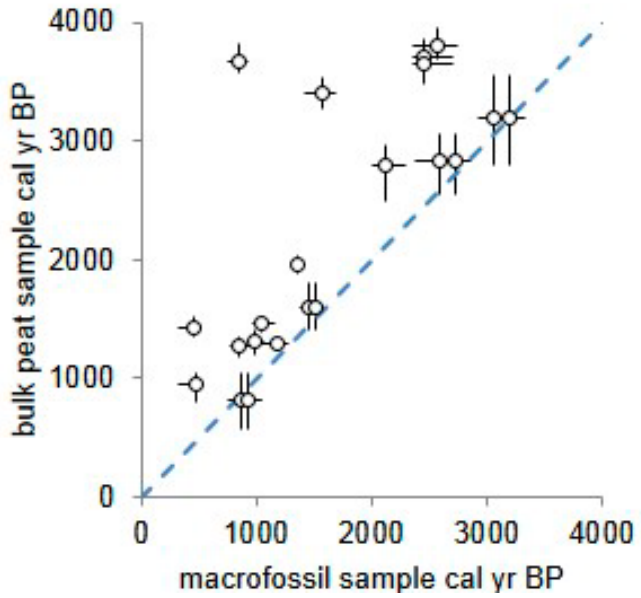

Figure 5.1.3

Portage garage

This is an iconic reminder of the 1964 earthquake and the rapid post-seismic changes in a dynamic marsh environment. Observations post 1964 indicate ~0.3 m land uplift by 1975 (Brown *et al.*, 1977) and 0.7 m by 1995–2000 (Freymueller *et al.*, 2008) and the photo mosaic (fig. 5.1.4) summarizes the colonization of the tidal flat by freshwater species.

The chronology of great earthquakes across the sites visited during the excursion

We can compare the new dates from Portage with a chronology derived from the analysis of all sites across the region (Shennan *et al.*, 2014) using a Bayesian modeling approach (Lienkaemper and Bronk Ramsey, 2009) of all radiocarbon ages that provide minimum or maximum ages to constrain events that may indicate coseismic subsidence or uplift. The probability density functions of the modeled ages reflect the better constraints on the more recent earthquakes (fig. 5.1.5). The oldest three events are recorded only at Copper River Delta (Carver and Plafker, 2008), with the younger ones dated at a minimum of two locations, one site indicating uplift and at least one indicating subsidence. When we overlay the ages obtained from the Portage core, which are not included in the regional model and therefore independent for this analysis, we see that they all fit within the joint probability ranges for earthquakes recorded elsewhere.

The differences in time between each earthquake are a suitable discussion topic for this final stop on the excursion.

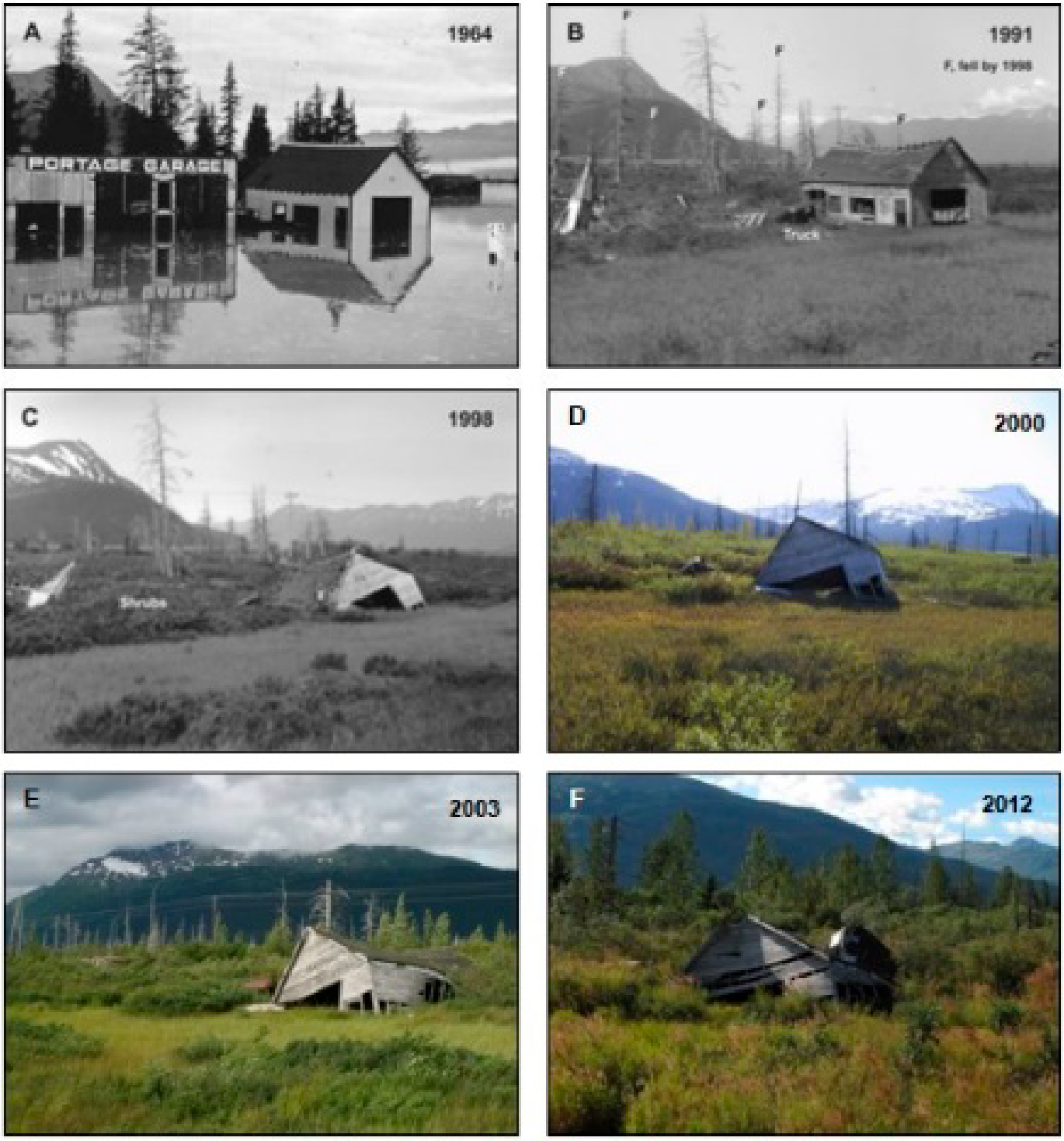

Figure 5.1.4. *Compiled from Atwater et al., 2001 (A–C), and photographs by I. Shennan (D–F).*

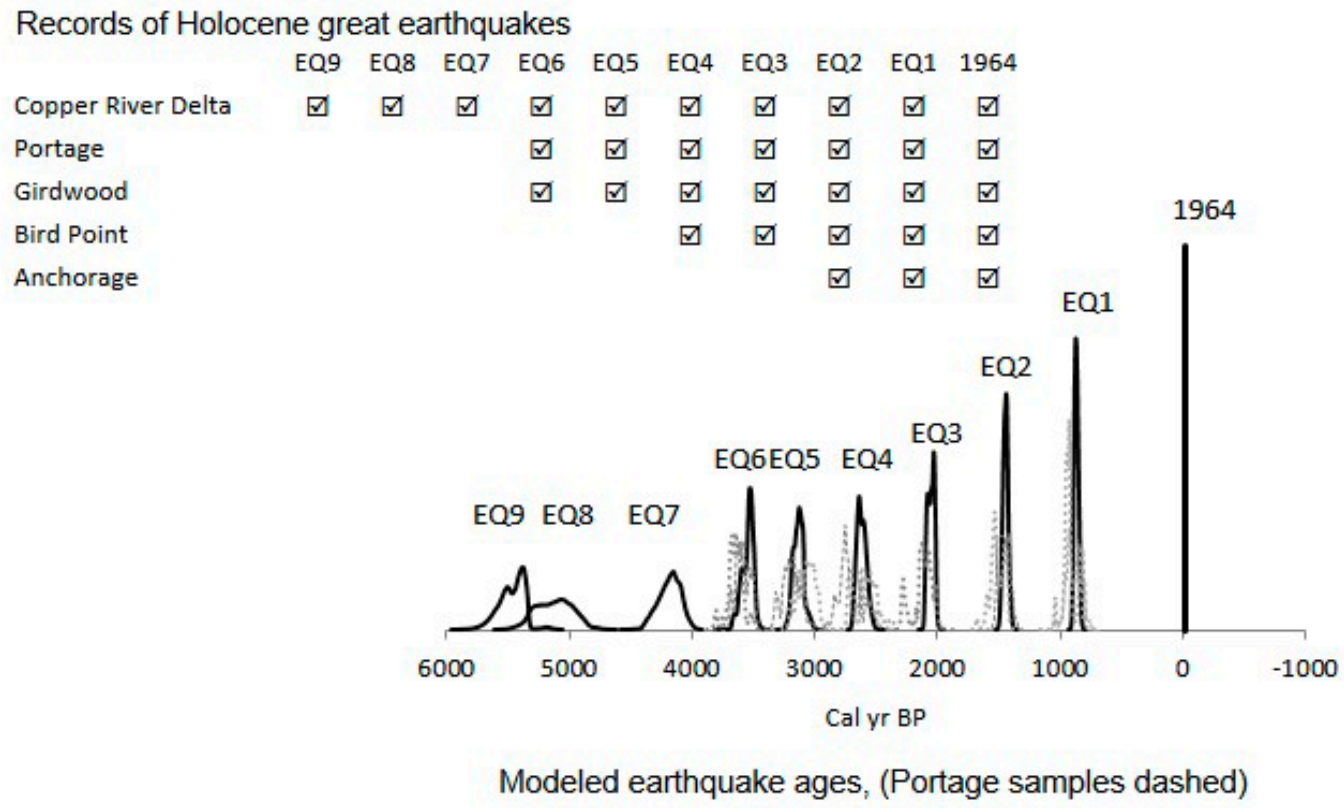
Records of Holocene great earthquakes
EQ9 EQ8 EQ7 EQ6 EQ5 EQ4 EQ3 EQ2 EQ1 1964
Copper River Delta
Portage
Girdwood
Bird Point
Anchorage
1964
EQ1
EQ2
EQ3
EQ6 EQ5 EQ4
EQ9 EQ8 EQ7
6000 5000 4000 3000 2000 1000 0 -1000
Cal yr BP
Modeled earthquake ages, (Portage samples dashed)

Figure 5.1.5

POSTERS AND PAPERS

POSTER AND PAPER PROGRAM

Time	Presenting author		Title
POSTERS (Full-day session: DAY 4 OR 5) – Presented below in Alphabetical Order			
4:00 pm	Natasha	Barlow	Salt marshes as Holocene tide gauges
4:00 pm	Lisa	Ely	Geological evidence of earthquakes and tsunamis in south-central Chile
4:00 pm	Ed	Garrett	Reconstructing palaeoseismic deformation: 1,000 years of earthquakes in south-central Chile
4:00 pm	Emma	Hocking	Recent and historical ruptures of the Chilean subduction zone: A latitudinal transect of earthquake deformation
4:00 pm	Wojciech	Jeglinski	Vistula Spit accretion as inferred from OSL dune datings and peatlands research
4:00 pm	Harvey	Kelsey	Paleoseismic investigations of subduction zone earthquakes on the southeastern coast of the Kenai Peninsula, Alaska
4:00 pm	Philipp	Kempf	A 4,000 year paleotsunami record from a coastal lake on the Valdivia segment, south-central Chile: A preliminary age-depth model and its implications
4:00 pm	Giuseppe	Mastronuzzi	Radiocarbon chronology of tsunami impacts on the Apulian Coast (southern Italy)
4:00 pm	Bruce	Molnia	Dynamics of the rapidly changing Gulf of Alaska coastal area
4:00 pm	Katrin	Monecke	Coastal changes in West Aceh, Indonesia, since the 2004 Indian Ocean tsunami
4:00 pm	Ann	Morey	A preliminary description of sediments from north Cascadia forearc lakes: Cryptic sequences contain evidence of a seismogenic influence
4:00 pm	Charles	Mueller	USGS 2007 Seismic Hazard Maps for Alaska
4:00 pm	Piotr	Przezdziecki	Remains of glaciofluvial deltas on Słupsk and Southern Middle Banks: New evidence for subaqual deglaciation of the Baltic Sea basin
4:00 pm	Helen	Roe	The late-glacial and Holocene relative sea-level history of the Seymour–Belize Inlet Complex, central mainland British Columbia, Canada
4:00 pm	Adam	Switzer	The three S's of tsunami sediments: Sediments, sources, and statistics
4:00 pm	Rob	Witter	Stable isotope values in coastal sediment estimate subsidence near Girdwood during the 1964 great Alaska earthquake

ORAL SESSIONS – Presented below in Order of Presentation			
Long-term uplift and exhumation (Full-day session: DAY 4 OR 5)			
9:00 am	Daniel	Melnick	Seismotectonic segmentation and relative sea-level change derived from Holocene and MIS-5 marine terraces in the 2010 Maule Chile earthquake (M 8.8) rupture zone
9:20 am	Theresa	Bardaji	Coseismic vs climatic effects in the record of relative sea-level changes: An example from last interglacials in SE Spain
9:40 am	Eva	Enkelmann	Neogene deformation at the Yakutat plate corner in southeast Alaska
11:00 am	Peter	Haeussler	Focused exhumation along megathrust splay faults in Prince William Sound, Alaska
11:20 am	Giuseppe	Mastronuzzi	Modeling of an uplifted coastal area: The case study of Taranto (Italy)
11:40 am	Koji	Okumura	Long-term enigmatic uplift of coastlines
Methods in reconstructing sea level change (Full-day session: DAY 4 OR 5)			
2:00 pm	Aron	Meltzner	Details of the mid-Holocene relative sea-level highstand at Belitung Island, Indonesia, on the Sunda Shelf, from coral microatolls
2:20 pm	Rob	Wesson	Uncertainties in field estimation of mean sea level
2:40 pm	Gösta	Hoffmann	The tsunami that was obscured by the birth of an island
Hazards (Half-day session: DAY 5 OR 6)			
8:30 am	Eric	Cannon	Characterizing site conditions for geotechnical engineering projects in Southeast Alaska
8:50 am	Javier	Lario	Implementing the coastal record in the INQUA ESI Scale—2007
9:10 am	Mark	Petersen	Update of the U.S. National Seismic Hazard Maps for Alaska
Segmentation of the Aleutian–Alaska megathrust (Half-day session: DAY 5 OR 6)			
10:30 am	Rich	Briggs	The 1938 M 8.2 Semidi Islands earthquake: A re-evaluation of 20th-century moment release along the Semidi Islands section of the Alaska–Aleutian megathrust
10:50 am	Simon	Englehart	A stratigraphic record of megathrust uplift and subsidence at Sitkinak Lagoon, Sitkinak Island, Alaska
11:10 am	Ian	Shennan	Paleoseismic investigations of subduction zone earthquakes on the southwestern coast of the Kenai Peninsula, Alaska
Evening speakers			
	Bruce	Molnia	Recent history and dynamics of Bering Glacier

Poster Abstracts

SALT MARSHES AS HOLOCENE TIDE GAUGES

Natasha Barlow

Sea Level Research Unit
Department of Geography
Durham University
South Road, Durham, DH1 3LE, UK
n.l.m.barlow@durham.ac.uk

Understanding Holocene relative sea-level changes requires geological records of past sea level in the absence of instrumental methods. Salt marsh sediments are one of the most reliable geological tide gauges, in both active and passive coastal margins. We outline the approach by which estuarine sediments and their associated microflora and fauna can be used to reconstruct the magnitude of past sea level change, in particular that associated with palaeoseismicity.

There are different pathways to quantitative reconstructions of relative sea level based on salt marsh sediments. We demonstrate that any reconstruction is in part a result of the environment from which the record is taken, the modern dataset used to calibrate the fossil changes, statistical assumptions behind calibrating microfossil assemblages and choices made by the researchers. Tidal range and sampled elevation range of the modern dataset also have a strong influence on model predictive ability. Model-specific errors may underrepresent total uncertainty that comes from field practices, sedimentary environment, palaeotidal changes and sediment compaction as well as statistical uncertainties.

Geological reconstructions of relative sea level change associated with past great subduction earthquakes have less uncertainty than records of gradual relative sea level change from passive coastal margins, as the magnitude of the reconstructed change is often much greater than the uncertainties of the reconstruction. This makes this a valuable method by which to understand the spatial and temporal patterns of palaeoseismicity.

GEOLOGICAL EVIDENCE OF EARTHQUAKES AND TSUNAMIS IN SOUTH-CENTRAL CHILE

Lisa L. Ely, ely@cwu.edu
Department of Geological Sciences
Central Washington University
Marco Cisternas, marco.cisternas@ucv.cl
Escuela de Ciencias del Mar
Pontificia Universidad Católica de Valparaíso Chile
Robert L. Wesson, rwesson@wispertel.net
U.S. Geological Survey
Denver, Colorado
Tina Dura, dura@sas.upenn.edu
Department of Earth and Environmental Science
University of Pennsylvania
Isabel Hong, hongji@geology.cwu.edu
Department of Geological Sciences
Central Washington University

Chile holds the longest historical record of earthquakes and tsunamis on the Pacific Coast of the Americas, extending back to AD 1570. Sparse historical settlement, however, has contributed to an incomplete understanding of the magnitude and aerial extent of past events. Our primary study site at Tirúa, Chile (38.3° S) contains sedimentary evidence of four large tsunamis and associated land-level changes in the last 500 years. The site lies within the region of overlap between the 1960 (M_w 9.5) and 2010 (M_w 8.8) Chilean earthquakes, and is thus positioned to selectively preserve deposits of the largest tsunamis from both northern and southern sources. Sand deposits from the 2010 tsunami extend 2 km up the Tirúa River. At least three buried sand layers exhibit characteristics analogous to those of the 2010 deposit, including the penultimate sand layer from the 1960 tsunami and two older deposits most likely from historical tsunamis in AD 1751 and 1575. A similar chronology of deposits was found at nearby Quidico, Chile, supporting the interpretation of a regional tsunami origin. Both sites contain older deposits that could predate the historical record. The stratigraphy of the organic soils and inorganic laminated silts between the tsunami sand layers at Tirúa indicate that this area has experienced varying coseismic land-level changes. Tirúa uplifted ≥ 50 cm during the 2010 earthquake and subsided slightly during the 1960 earthquake. The geological evidence can help differentiate both the relative magnitudes of historical tsunamis and seismic land-level changes associated with subduction-zone ruptures at this critical intersection of known great earthquake sources.

RECONSTRUCTING PALAEOSEISMIC DEFORMATION: 1,000 YEARS OF EARTHQUAKES IN SOUTH CENTRAL CHILE

Ed Garrett[1]*, Ian Shennan[1], Sarah Woodroffe[1]

[1]Sea Level Research Unit, Department of Geography, Durham University
*edmund.garrett@durham.ac.uk

The 1960 Chilean earthquake (M_w 9.5) caused land surface deformation along 1,000 km of the south central Chilean coast. At Chucalen, northern Isla de Chiloé, subsidence is recorded in the lithostratigraphy and biostratigraphy, with organic peats overlain by minerogenic sediments and changes in diatom assemblages indicating an abrupt increase in marine influence. At this site and others in south central Chile, our diatom-based transfer function model gives estimates of coseismic deformation that agree with independent estimates of land-level change, confirming the potential for this approach to be used to quantify coseismic deformation for previous great earthquakes.

In addition to the 1960 earthquake and tsunami, the stratigraphy at Chucalen records three earlier ruptures. The sequence includes the historically recorded 1575 earthquake, but there is no evidence for earthquakes documented in 1737 and 1837, limiting the northward extent of these ruptures. We constrain the timing of two prehistoric earthquakes to AD 1270–1410 and AD 1050–1200 and infer subsidence during each event of a similar magnitude to 1960. The timing of earthquakes recorded at Chucalen closely matches the chronology at Maullín, 45 km to the northeast (Cisternas *et al.*, 2005). The transfer function approach also allows reconstructions of interseismic deformation and suggests that emergence seen before the 1960 earthquake was not matched by emergence before 1575.

The occurrence of organic marsh soils below their contemporary elevation of formation implies relative sea-level rise over the course of the Chucalen record. This rise is contrary to falling relative sea levels implied by glacial isostatic adjustment models, long-term tectonic uplift and field data from the adjacent mainland. The causes of this discrepancy are unclear and remain an area for further study.

Cisternas, M., Atwater, B.F., Torrejon, F., Sawai, Y., Machuca, G., Lagos, M., Eipert, A., Youlton, C., Salgado, I., Kamataki, T., Shishikura, M., Rajendran, C.P., Malik, J.K., Rizal, Y., Husni, M., 2005, Predecessors of the giant 1960 Chile earthquake: Nature, v. 437, p. 404–407.

RECENT AND HISTORICAL RUPTURES OF THE CHILEAN SUBDUCTION ZONE: A LATITUDINAL TRANSECT OF EARTHQUAKE DEFORMATION

Emma P. Hocking[1], Ed Garrett[1,2]

[1]Northumbria University, Department of Geography, Newcastle-upon-Tyne, UK
[2]Durham University, Department of Geography, Durham, UK

The 1960 Chile earthquake ruptured a 1,000-km-long segment of the interface between the Nazca and South American plates. Historical records describe three further south-central Chilean earthquakes in 1837, 1737 and 1575; however the magnitude and slip distribution of these events is largely unknown.

Here we present the first results from recent palaeoseismic investigations in south-central Chile, assessing vertical deformation associated with two of the most recent ruptures of the Valdivia seismic segment and the lateral extent of the associated tsunami deposits. We present data from a north–south transect of sites between Valdivia and Isla de Chiloé, including Chaihuin, Pucatrihue, Llico and Chucalen, where sediments record evidence of the 1960 and up to three earlier events. We quantify vertical deformation using a diatom transfer function based on an expanded modern training set, with the aim of determining whether the magnitude of deformation is similar for each event at these sites. We also seek to reconstruct interseismic deformation between these events and postseismic deformation following the 1960 earthquake.

VISTULA SPIT ACCRETION AS INFERRED FROM OSL DUNE DATINGS AND PEATLANDS RESEARCH

Wojciech Jegliński*, Grażyna Miotk-Szpiganowicz*, Szymon Uścinowicz*, Andrzej Bluszcz, Grzegorz Adamiec****

* Polish Geological Institute—National Research Institute, Branch of Marine Geology, Kościerska 5 st. 80-328, Gdańsk, Poland, szymon.uscinowicz@pgi.gov.pl

** Silesian University of Technology, Institute of Physics, Krzywoustego 2 st. 44-100 Gliwice, Poland

Vistula Spit is one of the largest barriers on the southern Baltic coast. It is ~100 km long, 700–1,800 m wide, with a well-developed system of dunes. Traditionally, three phases of dune formation were distinguished, however, age of the dunes is still debatable. Older research revealed the ^{14}C age of basal peat, located at 14–9 m bsl, between 8,870 and 7,275 cal. y. BP and age of marine shells in barrier sands between 6,131 and 1,994 cal. y. BP.

Recently the age of dunes was investigated by OSL datings of 12 samples taken mainly from excavations located at the foot of the windward slopes of dunes. Two peat profiles from peatland formed in depressions between dune ridges were also investigated by ^{14}C dating and palynological analyses.

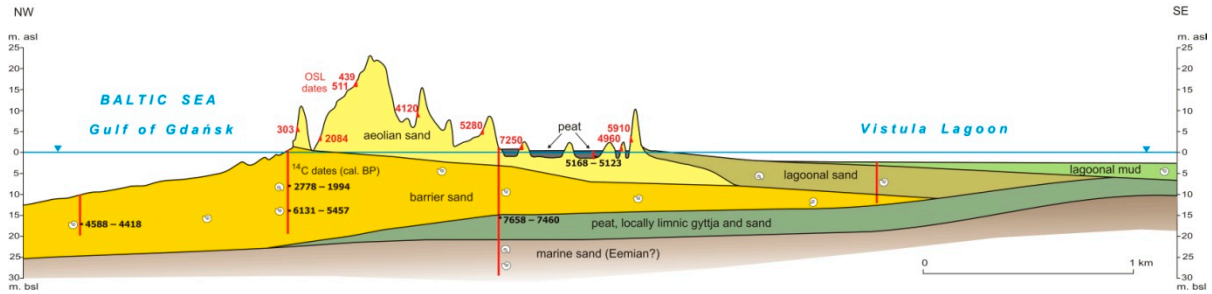

Figure 1. Geological cross-section across Vistula Spit

The oldest dunes, so-called brown, are situated on the banks of the Vistula Lagoon age 7,250 to 4,960 years (Fig. 1). The sequence of OSL dates indicate that the next ridge of dunes, so-called yellow dunes, were formed 5,280 to 2,084 years ago, and the highest of them rising up to 20–49.5 m asl, were created 4,120–2,084 y. BP. Only the topmost parts of the ridge were active about 500–400 y. BP. The youngest ridge of coastal dunes, so called white, were formed ~300 y. PB. The oldest ^{14}C date from the floor of coastal peatland is 5,168–5,123 cal. y. BP and correlates well with age of dune stabilization. The latest results move backwards in time to the creation and stabilization of the system of dune ridges and document the continuous, rather than periodic (phase), process of accretion of the Vistula Spit related to decreasing rate of sea level rise.

PALEOSEISMIC INVESTIGATIONS OF SUBDUCTION ZONE EARTHQUAKES ON THE SOUTHEASTERN COAST OF THE KENAI PENINSULA, ALASKA

H.M. Kelsey[1], R.C. Witter[2], R. Briggs[3], S. Engelhart[4], A.R. Nelson[3], P. Haeussler[2]

[1]Department of Geology, Humboldt State University, Arcata CA
[2]U.S. Geological Survey, Anchorage, AK
[3]U.S. Geological Survey, Golden, CO
[4]Geosciences, University of Rhode Island, Kingston RI

Rupture extents for prehistoric subduction zone earthquakes on the Alaska margin are poorly documented. For example, the 1964 great Alaska earthquake ruptured the subduction zone from Prince William Sound westward to the southwest end of Kodiak Island, but an outstanding question is whether or not earlier subduction earthquakes ruptured a shorter segment in the Kodiak region with the eastern margin located in the Kenai Peninsula. To address the question, we investigated several embayments on the Pacific (southeastern) coast of the Kenai Peninsula to reconstruct the late Holocene paleoseismic history. Constraints to constructing a paleoseismic history on the outer Kenai coast include recent deglaciation of embayments that limits a stratigraphic record to approximately the last 1 to 3 thousand years and the high wave-energy environment that results in frequent closure of embayments by barrier bars. Recognizing these constraints, two approaches have proved productive in investigating paleoseismic history on the outer Kenai coast. One involves understanding how beach ridges can be formed and modified by coseismic subsidence and documenting timing and number of late Holocene prehistoric earthquakes based on beach ridge genesis and evolution. The other approach, which is the more conventional paleoseismic approach for subduction zones, is investigating stratigraphic evidence for coseismic subsidence in peaty and muddy sediment within embayments. We illustrate these two approaches using two coastal sites in Aialik Bay within Kenai Fjords National Park—a strandplain complex at Verdant Cove and a drowned embayment at Quicksand Cove. Both sites record two prehistoric subduction zone earthquakes prior to the historically known 1964 great Alaska earthquake.

A 4,000 YEAR PALEOTSUNAMI RECORD FROM A COASTAL LAKE ON THE VALDIVIA SEGMENT, SOUTH-CENTRAL CHILE: A PRELIMINARY AGE-DEPTH MODEL AND ITS IMPLICATIONS

Kempf, Philipp[1], philipp.kempf@ugent.be
Moernaut, Jasper[2], jasper.moernaut@erdw.ethz.ch
Vandoorne, Willem[1], willem.vandoorne@ugent.be
Van Daele, Maarten[1], maarten.vandaele@ugent.be
Pino, Mario[3], mpino@uach.cl
Urrutia, Roberto[4], rurrutia@udec.cl
De Batist, Marc[1], marc.debatist@ugent.be

[1]Renard Centre of Marine Geology, Ghent University, Krijgslaan 281 S8, 9000 Ghent, Belgium
[2]Geologisches Institut, ETH Zürich, Switzerland
[3]Instituto de Geociencias, Universidad Austral de Valdivia, Chile
[4]Centro EULA, Universidad de Concepción, Chile

Long and continuous sedimentary records of tsunami deposits are few. They can be recovered by coring coastal lakes, e.g. Bradley Lake, Cascadia (Kelsey *et al.*, 2005). The necessity of long and continuous records arises due to the centennial- to millennial-scale recurrence times of great tsunamigenic earthquakes. Lago Huelde on Chiloé (42.5°S), Chile, is a coastal lake located in the middle of the Valdivia segment, which is known for producing the strongest ever instrumentally recorded earthquake in 1960 AD (M_W 9.5). Also, large earthquakes are historically recorded for 1575 AD, 1737 AD (no report of a tsunami) and 1837 AD on this segment (Lomnitz, 1970, 2004). We present a new paleotsunami record from Lago Huelde, which extends over the last 4,000 years and includes 16 event deposits (EDs). This long and continuous sedimentary record was radiocarbon dated with 22 (four outliers) samples. The resulting age-depth model was calculated using BACON, a new bayesian statistics tool. The implications of this age-depth model are discussed in this contribution.

RADIOCARBON CHRONOLOGY OF TSUNAMI IMPACTS ON THE APULIAN COAST (SOUTHERN ITALY)

G. Mastronuzzi[1], **P.M. De Martini**[2], **P. Sansò**[3], **L.Calcagnile**[4], **M.D'Elia**[4], **G. Quarta**[4], **A. Smedile**[2]

[1] Dipartimento di Scienze della Terra e Geoambientali, Università degli Studi "Aldo Moro", Bari, Italy giuseppeantonio.mastronuzzi@uniba.it
[2] Istituto Nazionale di Geofisica e Vulcanologia, Roma, Italy paolomarco.demartini@ingv.it, alessandra.smedile@ingv.it
[3] DISTEBA, Università del Salento, Lecce, Italypaolo.sanso@unisalento.it
[4] CEDAD—Dipartimento di Ingegneria dell'Innovazione, Università del Salento, Lecce, Italy lucio.calcagnile@unisalento.it, marisa.delia@unisalento.it, gianluca.quarta@unisalento.it

In historical times, the southern coasts of Italy were hit by several tsunamis, causing casualties on a large scale. Recent surveys performed along the coasts of Apulia have evidenced the presence of morphological and sedimentological imprints of the impact of catastrophic waves. Often the availability of a good set of dated samples is not enough for a correct interpretation of these phenomena in terms of space and time. Historical catalogues of past earthquakes and tsunamis can help in identifying the correlation between geomorphic forms, calibrated ages and events. All available geochronological data derived from fine/coarse sediment and megaboulder accumulation are considered as geological evidence of the impact of tsunami. These have been divided in groups according to their location and traced in diagrams according to their calibrated radiocarbon ages together with the associated statistical uncertainties (1σ and 2σ). The issues related to the calibration of the radiocarbon ages of marine samples are discussed together with the presented results, which have been obtained by using the CALIB 6.01 software and the last data on marine reservoir correction factor available for the Mediterranean.

Historical catalogues have been consulted and linked to the available data sets.

Taking into account all available ages, geomorphological landforms, and other geochronological data, it is possible to recognize and discriminate only tsunamis documented also by historical sources and with a good time gap in between. If radiocarbon ages of tsunami impact could be one of the evidences to prove such events, more "clues" are necessary to identify "the guilty", and geomorphological observations and comparisons between different chronological methods have to be considered fundamental. In substance, ^{14}C ages are circumstantial evidences and not a final verdict.

DYNAMICS OF THE RAPIDLY CHANGING GULF OF ALASKA COASTAL AREA

Bruce F. Molnia

U.S. Geological Survey
12201 Sunrise Valley Drive
Reston, VA 20192
bmolnia@usgs.gov

The nearly 1,000-km-long Gulf of Alaska coastal segment that includes Glacier Bay National Park, Wrangell–St. Elias National Park, Bering Glacier, Prince William Sound, and Kenai Fjords National Park, is one of the most active and unique coastlines on Earth. It is subject to high-intensity coastal processes and natural hazards, and has changed rapidly, repeatedly, and radically on a variety of time scales, ranging from decadal to millennial.

Located adjacent to the North American Plate–Pacific Plate boundary, this coastal segment is subject to active tectonic and isostatic uplift. Maximum post-Little Ice Age isostatic uplift rates are ~4 cm/yr. At many locations, crustal warping associated with large-magnitude earthquakes has produced significant instantaneous uplift and subsidence, with maximum magnitudes approaching 15 m.

Glaciers exist on all of the mountain ranges adjacent to this coastline. About half of the large, currently advancing glaciers in Alaska are located within this coastal segment. Many now have, or recently had, tidewater termini. At times, ~20 percent of the shoreline of this coastal area has been made up of glacier ice.

Natural hazards affecting this coastline include: Intense storms, storm surge, rapid coastal erosion, extreme seismicity, faulting, instantaneous uplifts, submarine and terrestrial mass wasting, giant waves and tsunamis, glacier advance and retreat, rapid sedimentation, and glacier outburst flooding. At least four bays have evolved through large-scale, asynchronous glacier retreats. Icy Bay, the most recent to form, is the product of ~ 50 km of 20th century glacial retreat. Several other bays have filled with sediment. All large bays are shoaling rapidly and have sedimentation rates of >1 m/yr. Maximum rates may exceed 10 m/yr.

Bering Glacier is the largest surging temperate glacier on Earth. Recent geophysical investigations suggest that its ongoing retreat may produce a fifth large bay.

COASTAL CHANGES IN WEST ACEH, INDONESIA, SINCE THE 2004 INDIAN OCEAN TSUNAMI

Katrin Monecke[1], **Caroline K. Templeton**[1], **Willi Finger**[2], **Brian McAdoo**[3], **Ella Meilianda**[4], **Joep E.A. Storms**[5], **Dirk-Jan R. Walstra**[6]

[1] Wellesley College, Wellesley, Massachusetts, USA, kmonecke@wellesley.edu
[2] Swiss Agency for Development and Cooperation, Zurich, Switzerland, willi.finger@bluewin.ch
[3] Yale-NUS College, Singapore, brian.mcadoo@yale-nus.edu.sg
[4] Tsunami Disaster Research and Mitigation Center, Banda Aceh, Indonesia, ella.meilianda@tdmrc.org
[5] Delft University of Technology, Delft, The Netherlands, J.E.A.Storms@tudelft.nl
[6] Deltares, Delft, The Netherlands, DirkJan.Walstra@deltares.nl

The western Acehnese coastline in northern Sumatra, Indonesia, receded on average 134 m due to subsidence and tsunami inundation in the course of the December 26, 2004 Sumatra–Andaman earthquake and tsunami. Here, we investigate the regrowth of the coast since 2004 through field surveys, spatial imagery analysis, and numerical modeling. Three automatic level surveys were conducted in 2009, 2012, and 2013 over a beach ridge plain 15 km north of the city of Meulaboh in West Aceh. The surveys followed a transect from the coast up to 1.8 km inland. An 18.8-km-long stretch of the same coastline was analyzed by digitizing the shoreline on satellite and aerial images taken between 2002 and 2013 and by computing the shoreline change rates using the Digital Shoreline Analysis System (DSAS) developed by the U.S. Geological Survey. Following the initial erosion during the December 26, 2004, event, the coast prograded rapidly and a new wide beach ridge formed. However, the coastline never fully recovered and in 2011 was still an average of 52.7 m from its pre-2004 position. The topographic surveys show that the top of the newly formed beach ridge stands out 80 cm higher than older beach ridges farther inland, probably a response to the higher relative sea level induced by co-seismic subsidence in 2004. While topographic surveys and satellite images indicate coastal progradation until 2011, most recent data show a renewed retreat of the coastline of up to 40 m since 2011. To understand the complex interaction of land level changes, sediment supply, and hydrodynamic parameters, we have applied the coastal model UNIBEST-TC developed by Delft University of Technology to the Aceh coastal system to get further insight into the mechanisms of beach ridge formation and modifications by earthquakes and tsunamis.

A PRELIMINARY DESCRIPTION OF SEDIMENTS FROM NORTH CASCADIA FOREARC LAKES: CRYPTIC SEQUENCES CONTAIN EVIDENCE OF A SEISMOGENIC INFLUENCE

Ann E. Morey, Chris Goldfinger, and Steve Galer

College of Earth, Ocean and Atmospheric Sciences
Oregon State University, Corvallis, OR
morey@coas.oregonstate.edu

Here we describe the characteristics of lake sediments we recently acquired along a transect from just west of the Olympic Peninsula to the Cascade foothills at the latitude of Seattle, Washington. Density (from computed tomography and gamma-ray attenuation) and magnetic susceptibility data and imagery for the kettle lake cores were compared to each other and to the physical properties from cores containing a record of Cascadia offshore seismoturbidites. Preliminary correlations show strong similarities over the past ~8,000 years when anchoring the records in time with a tephra layer we interpret to be the Mazama tephra (MA) based on published data from nearby lakes. Why do the lake and offshore sedimentary records correlate? There are no graded turbidite deposits visible in the cores, only very subtle differences in texture and color associated with the correlative layers (other than the Mazama tephra). We are in the process of describing and analyzing the sediment from these cores in an attempt to understand why these sedimentary records from such different depositional environments have similar patterns in their physical properties through time.

We present our first results from multiple cores from two kettle lakes, Leland Lake and Tarboo Lake. These lakes are depressions in permeable glacial till that formed when blocks of glacial ice melted, and lake levels during modern times are primarily an expression of the water table. Tarboo Lake (0.09 km^2, 17.7 m deep, and 195 m MSL) is perched relative to local terrain with little overland flow, whereas Leland Lake (0.41 km^2, 6.1 m deep, and 58 m MSL) is fed by local streams, including a couple of seasonal streams to the west sourced from the foothills of the Olympic Mountains. Sediment properties of these cores are similar, however the average sedimentation rate at Tarboo Lake is about half that of Leland Lake, likely a reflection of the much smaller watershed at this site. Smear slides show that in general the sediment is dominated by diatoms and very fine organic matter, with a smaller percentage of clastics. Layers that correlate to the offshore seismoturbidite record are slightly stiffer and lighter in color than sediment above and below, and contain a higher percentage of clastics. The percentage of clastics in both the denser layers and the background sediment is highest near the base of the cores, and decreases through time to the top of the core. This may be a result of the depletion of clastics in the watershed, much of which is likely to have resulted from sedimentation within a proglacial lake that formed in this area during the latest Pleistocene as the Puget Lobe retreated. Periodic thin layers of vivianite (a blue hydrous Fe [II] phosphate mineral) are observed in Leland Lake cores and are associated with the denser layers. Overturn in deep lakes has been identified as a possible mechanism that could result in the formation of vivianite, however this is not a possible mechanism in Leland Lake, which is likely wind-mixed throughout the year because it is so shallow. Would strong shaking entrain sediment into the water column, causing flocculation, stripping the water column of primary producers? We will explore this and other possibilities as we continue to learn about the sedimentary history and the influence of great earthquakes in these unique lake settings.

USGS 2007 SEISMIC HAZARD MAPS FOR ALASKA

Charles S. Mueller (U.S. Geological Survey, cmueller@usgs.gov)
Robert L. Wesson (U.S. Geological Survey, rwesson@usgs.gov)
Oliver S. Boyd (U.S. Geological Survey, olboyd@usgs.gov)
Charles G. Bufe (U.S. Geological Survey, cbufe@usgs.gov)
Arthur D. Frankel (U.S. Geological Survey, afrankel@usgs.gov)
Mark D. Petersen (U.S. Geological Survey, mpetersen@usgs.gov)

The U.S. Geological Survey (USGS) has made seismic hazard maps for Alaska in 1985, 1999, and 2007 (Wesson and others, USGS Open-File Report 2007-1043), with each update incorporating advances in data and methodology. The maps show probabilistic, time-independent ground motions for various structural periods and probability levels. The probabilistic methodology computes rates of ground shaking considering all capable seismic sources with their magnitude and rate distributions. Specific fault sources can be modeled if slip-rate or recurrence information is available. Otherwise, historical earthquake catalogs are used to develop seismicity source models. In seismically active regions like Alaska, shaking levels and their uncertainties are usually predicted empirically.

For the 2007 Alaska maps modeled seismic sources included the Alaska–Aleutian megathrust fault, a few crustal faults, and several seismicity sources. The megathrust was modeled as a segmented dipping plane, with segment boundaries largely controlled by the slip patches of past great earthquakes. Unique source models for each segment reflected regional differences in seismicity and strain accumulation. Segment recurrence models were developed from seismic history and statistics, rather than plate rates and moment balancing. Modeled crustal faults included the Fairweather–Queen Charlotte system, the Denali–Totschunda system, the Castle Mountain fault, crustal faults on Kodiak Island, and the Transition fault. Recurrence rates were estimated from geologic and paleoseismic data. Seismicity source models were developed from earthquake catalogs and statistics for crustal earthquakes and Benioff-zone earthquakes.

Updated source models for the next Alaska maps will incorporate new thinking on megathrust segmentation, recurrence, and geometry; new fault characterizations; new geodetic data; and updated seismicity catalogs. Some of the 2007 ground-motion relations are obsolete, and the next maps will implement recently-developed equations for crustal and subduction earthquakes. In particular, new subduction interface relations incorporate major datasets from recent great earthquakes in Japan and Chile.

REMAINS OF GLACIOFLUVIAL DELTAS ON SŁUPSK AND SOUTHERN MIDDLE BANKS: NEW EVIDENCE FOR SUBAQUAL DEGLACIATION OF THE BALTIC SEA BASIN

Piotr Przezdziecki[1], Szymon Uścinowicz[1], Kazimierz Szefler[2]

[1] Polish Geological Institute
National Research Institute
Branch of Marine Geology
Kościerska 5 st. 80-328
Gdańsk, Poland
e-mail: szymon.uscinowicz@pgi.gov.pl
[2] Maritime Institute
Dlugi Targ 41/42, 80-830
Gdańsk, Poland

Timeframe and manner of ice sheet decay in the southern Baltic is still debatable. This is due to the fact that little is known about ice-marginal landforms on the seabed, and patterns of ice sheet retreat were reconstructed so far only on the basis of spatial correlation of ice-marginal landforms on adjacent land across the sea. Application of the OSL method to dating glaciofluvial deltas and ice-marginal lake sediments creates new possibilities for understanding the course of deglaciation of the Baltic area.

Three partly eroded, glaciofluvial deltas on Słupsk Bank and the large, complex system of deltas on Southern Middle Bank were investigated by seismo-acoustic (boomer) profiling (191 km) and vibrocoring. Remains of glaciofluvial deltas from Słupsk Bank have a dimensions ~1 × 1.5 km, average bed inclination ~4–5°, and directions of progradation from N to E and from E to W (fig. 1). Deltas from the Southern Middle Bank are larger and the inclinations of beds indicate directions of progradation from N to S and from NW to SE.

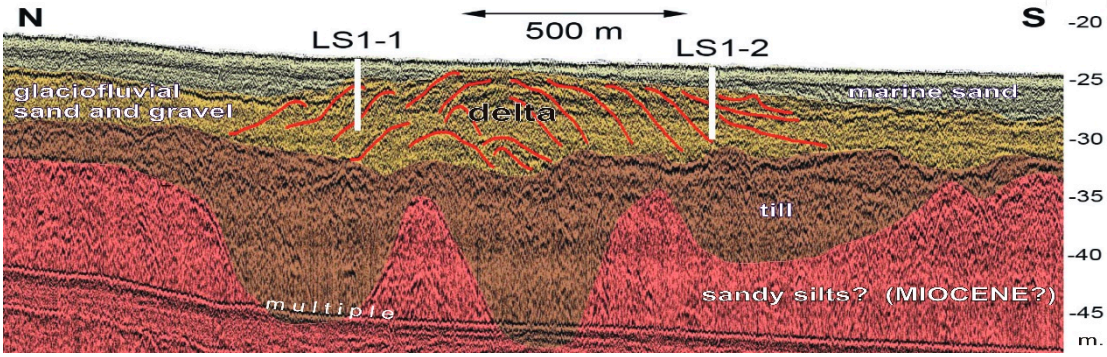

Fig. 1. Seismo-acoustic, interpreted profile across glaciofluvial delta on Słupsk Bank

Occurrence of glaciofluvial deltas and De Geer moraines in the shallows of the southern Baltic, as well as vast areas of ice-dammed lake sediments indicate that deglaciation of the southern Baltic took place in subaqual conditions. Datings of 60 samples of glaciofluvial and ice-dammed lakes sediments by the OSL method is in progress. Authors hope that results will allow for time–space correlation of ice-marginal landforms of Słupsk and Southern Middle Banks with ice-marginal zones on adjacent lands.

THE LATE-GLACIAL AND HOLOCENE RELATIVE SEA-LEVEL HISTORY OF THE SEYMOUR–BELIZE INLET COMPLEX, CENTRAL MAINLAND BRITISH COLUMBIA, CANADA

Helen M. Roe[1], **Christine T. Doherty**[1], **R. Timothy Patterson**[2], and **Glenn A. Milne**[3]

[1] School of Geography, Archaeology and Palaeoecology, Queen's University Belfast, Belfast, BT7 1NN, United Kingdom; h.roe@qub.ac.uk
[2] Department of Earth Sciences, College of Natural Sciences, Carleton University, Ottawa, Ontario, K1S 5B6, Canada; Tim.Patterson@carleton.ca
[3] Department of Earth Sciences, University of Ottawa, Ontario, K1N 6N5 Canada; gamilne@uottawa.ca

The infills of three low-lying (<5 m elevation) isolation basins in the remote Seymour–Belize Inlet Complex of central mainland British Columbia provide new insights into the post-glacial relative sea-level (RSL) history and a preliminary basis for testing model predictions of RSL change. The basins were flooded by the sea in late-glacial times and were subsequently isolated at ~11,820 ^{14}C yr BP in response to rapid glacio-isostatic rebound. A subsequent RSL rise during the early Holocene (~8,000 ^{14}C yr BP) breached the 2.13 m sill of the lowest basin (Woods Lake), but the two more elevated basins (sill elevations of ~3.6 m) remained isolated. At ~2,400 ^{14}C yr BP, RSL stood at 1.49 ± 0.34 m above present MTL. Falling RSLs in the late Holocene led to the final emergence of the Woods Lake basin by 1,604 ± 36 ^{14}C yr BP. Model predictions generated using the ICE-5G model partnered with a small number of different Earth viscosity models generally show poor agreement with the observational data, indicating that the ice model and/or Earth models considered can be improved upon. The best data-model fits were achieved with relatively low values of upper mantle viscosity (5×10^{19} Pas), which is consistent with previous modeling results from the region. The RSL data align more closely with observational records from the southeast of the region (eastern Vancouver Island, central Strait of Georgia), than the immediate north (Bella Bella–Bella Coola, and Prince Rupert–Kitimat) and areas to the northwest (Queen Charlotte Sound, Hecate Strait), underlining the complexity of the regional response to glacio-isostatic recovery.

THE THREE S's OF TSUNAMI SEDIMENTS: SEDIMENTS, SOURCES AND STATISTICS

Switzer, A.D.[1,2], **Gouramanis, C.**[1], **Dat, P.T.**[1,2], **Jankaew, K.**[3], **Srinivasalu, S.**[4], **Anandasabari, K.**[4], **Rubin, C.M.**[1,2], **Jones, B.G.**[5], **Carr, P.F.**[5] and **Kartik, G.R.**[1]

[1] Earth Observatory of Singapore, Singapore, Singapore
[2] Division of Earth Sciences, Nanyang Technological University, Singapore, Singapore
[3] Chulalongkorn University, Bangkok, Thailand
[4] Department of Geology, Anna University, Chennai, India
[5] University of Wollongong, NSW, Australia

To demarcate overwash deposits in the geological record, a number of criteria have been assembled from storm and tsunami deposits from coastlines of markedly different geomorphologies, sedimentary characteristics, and sediment sources. Here we report on two studies. In the first we compare the deposits of the 26/12/2004 Indian Ocean Tsunami (IOT) from a well-known site at Phra Thong Island and the 31/12/2011 Cyclone Thane (CT), from a site in southeast India. The IOT scoured and deposited sands on intertidal sediments and was overlain by re-worked aeolian sands, which were capped by the CT sediments. The samples were examined for grain size, loss on ignition, sediment shape, microfauna, and heavy minerals. We then applied ANOVAs, principal component analysis (PCA) and discriminant function analysis (DFA) to the sediment characteristics of each deposit. Each test showed no significant difference between the four deposit types. In a second study, X-Ray Diffraction (XRD) and X-Ray Fluorescence (XRF) were applied to determine the sediment provenance of the tsunami deposits preserved on Phra Thong Island, Thailand. Benthic marine sediment samples from offshore Phra Thong Island, samples from the onshore modern beach, and samples of the IOT and the most recent palaeo-tsunami deposit were analyzed. The XRD results indicate that quartz dominates all of the sediment samples with more than 90–95 wt%, whereas the XRF data provided additional information on 22 useful trace elements. We then employed cluster and DFA to investigate the differences between the sample groups. The XRF results indicate that the onshore beach deposits are clearly different from the statistically similar offshore, IOT, and palaeo-tsunami deposits. This shows that the main source of non-quartz material in the IOT deposit comes from offshore marine sources and that the trace-element composition of the sediments is a good indicator for tsunami provenance studies.

STABLE ISOTOPE VALUES IN COASTAL SEDIMENT ESTIMATE SUBSIDENCE NEAR GIRDWOOD DURING THE 1964 GREAT ALASKA EARTHQUAKE

Adrian Manley Bender[1,2] (adrianmbender@gmail.com)
Robert Carleton Witter[1] (rwitter@usgs.gov)
Matthew Rogers[3] (mcrogers@uaa.alaska.edu)
Casey P Saenger[4] (caseysaenger@gmail.com)

[1] USGS Alaska Science Center, Anchorage, AK, USA
[2] Department of Geology, Western Washington University, Bellingham, WA, USA
[3] ENRI Stable Isotope Lab, University of Alaska, Anchorage, Anchorage, AK, USA
[4] Geological Sciences, University of Alaska, Anchorage, Anchorage, AK, USA

During the M_w 9.2 1964 great Alaska earthquake, Turnagain Arm near Girdwood, Alaska, subsided 1.5–1.8 m based on pre- and post-earthquake leveling. The coseismic subsidence in 1964 caused equivalent sudden relative sea-level (RSL) rise that is stratigraphically preserved as sharp mud-over-peat contacts where intertidal silt buried former marshes. Changes in intertidal microfossil assemblages across these contacts have been used to accurately estimate subsidence in 1964 by applying quantitative microfossil transfer functions to reconstruct corresponding RSL rise. Here we report independent estimates of subsidence in 1964 by using stable C and N isotope values from intertidal sediment to assess RSL change caused by the earthquake.

Isotopic analyses of modern sediment samples along a 60-m-long transect at Bird Point, 11 km west of Girdwood, indicate a decrease in $\delta^{13}C$ (4.64‰) and $\delta^{15}N$ (3.97‰) over the ~2.5 m change in elevation between tide flat and upland. Along the same transect we sampled mud and peat across the 1964 contact in 11 sediment cores. Both $\delta^{13}C$ and $\delta^{15}N$ show positive shifts (≤4‰) across the contact from peat to mud.

To assess RSL change across the 1964 contact we calculated paleo-elevations for $\delta^{13}C$ and $\delta^{15}N$ in sediment above and below the contact using linear regressions of modern sediment isotope values against sample elevation. By subtracting the average paleo-elevations of mud from peat we estimate 1.5 ± 0.7m of RSL rise across the 1964 contact at Bird Point. This estimate compares well with the 1.5–1.8 m of subsidence measured after the earthquake, and suggests that this method may provide reasonable estimates of vertical displacements of the coast caused by pre-1964 earthquakes at this site and others. To continue developing this method, we plan to test it against known 1964 earthquake vertical displacement at other sites, and against microfossil transfer function subsidence estimates across deeper Bird Point contacts.

Oral Abstracts

SEISMOTECTONIC SEGMENTATION AND RELATIVE SEA-LEVEL CHANGE DERIVED FROM HOLOCENE AND MIS-5 MARINE TERRACES IN THE 2010 MAULE CHILE EARTHQUAKE (M8.8) RUPTURE ZONE

Julius Jara-Muñoz, University of Potsdam, Germany, jara@geo.uni-potsdam.de
Daniel Melnick*, University of Potsdam, Germany, melnick@geo.uni-potsdam.de
Dominik Brill, University of Cologne, Germany, brilld@uni-koeln.de
Manfred R. Strecker, University of Potsdam, Germany, strecker@geo.uni-potsdam.de

**Presenting author*

Comparing permanent deformation patterns, such as coastal terraces, with deformation transients during the earthquake cycle may provide insight into the segmentation of earthquake-rupture processes, the long-term characteristics of seismotectonic segmentation, and help mitigate seismic hazards. Permanent deformation can be estimated from marine terraces, which record relative sea-level change resulting from a mixture of eustatic and tectonic processes. Separating both signals is challenging, particularly for the Holocene, when the amplitude of the eustatic component might be of several meters with strong spatial variability. We studied marine terraces along the 2010 Maule Chile earthquake (M 8.8) rupture to gain insight into the nature of eustatic sea-level changes and seismotectonic segmentation processes in the forearc. Precise elevations of Holocene and MIS-5 marine terraces were obtained using high-resolution topography from airborne LiDAR and 2-m contour maps, virtually with continuous coverage along the coastline. OSL ages constrain MIS-5 levels and ^{14}C ages suggest a mid-Holocene highstand at ~4.5 cal ka BP in the Maule region. MIS-5 terraces are sharply offset across discrete crustal-scale faults and have been deformed in areas of broad warping with wavelengths of ~100 km, likely reflecting deeper processes within the interplate zone. Broad warping occurs at the southern and northern sectors of the rupture, where uplift rates reach 1.8 mm/yr. Holocene markers follow the warping pattern, and the eustatic component can be isolated by subtracting the uplift rate from MIS-5 terraces, assuming a constant rate at millennial timescales. In turn, the central rupture zone is characterized by low rates of permanent uplift. Based on the similarities between seismic-cycle deformation and historical earthquake ruptures, we propose that the southern sector of the Maule rupture constitutes a stable, discrete seismotectonic boundary, whereas the northern sector defines a rather diffuse boundary that may inhibit propagation of only some earthquakes.

COSEISMIC VS CLIMATIC EFFECTS IN THE RECORD OF RELATIVE SEA-LEVEL CHANGES: AN EXAMPLE FROM LAST INTERGLACIALS IN SE SPAIN

Bardají, T.[1], **Cabero, A.**[2], **Lario, J.**[2]; **Zazo, C.**[3], **Silva, P.G.**[4], **Goy, J.L.**[5], **Dabrio, C.J.**[6]

[1] U.D. Geología. Universidad de Alcalá. 28871-Alcalá de Henares (Madrid), España. Corresponding author teresa.bardaji@uah.es
[2] Facultad de Ciencias, UNED. 28040-Madrid, España acabero@ccia.uned.es; Javier.lario@ccia.uned.es
[3] Dpto. Geología, Museo Nacional CC. Naturales, CSIC. 28006-Madrid, España. mcnzc65@mncn.csic.es
[4] Dpto. Geología, Universidad de Salamanca, EPTS de Avila. 05003-Ávila, España. pgsilva@usal.es
[5] Dpto. Geología, Facultad de Ciencias; Universidad de Salamanca. 37008-Salamanca, España. joselgoy@usal.es
[6] Dpto. Estratigrafía, Facultad de CC. Geológicas, UCM. 28040-Madrid, España. dabrio@geo.ucm.es

Abstract

Trying to decipher how palaeoseismic activity has influenced the altitudinal disposition of interglacial deposits is one of the main challenges that must be achieved in order to quantify relative sea-level changes between consecutive highstands. Likewise, identifying palaeoseismic features in an area with low instrumental seismic activity can implement the seismic record, contributing to better seismic hazard knowledge. In this sense, Cope basin (SE Spain) becomes a reference basin to undertake this kind of analysis, first, by the excellent outcrop conditions, and second, because the sea-level record is undoubtedly conditioned here by both effects: Climatically driven changes and local and regional seismotectonics.

This basin is located in the inner part of the tectonically active structure of the Aguilas Arc (Eastern Betics) and holds one of the most complete and better exposed sequences of Quaternary marine terraces in SE Spain. The chronology of the whole sequence has been achieved by means of palaeomagnetism (upper Matuyama–Brunhes transition), faunal content (*Strombus bubonius*, MIS7–MIS5 in Iberian Peninsula), and sedimentary facies (Oolithic sediments, characteristic of MIS5e). Several Quaternary faults cross the basin, promoting the development of structural blocks with differential uplift and, hence, different present-day altitude of marine terraces, particularly MIS7–MIS5 units. The topographic survey carried out across the basin evidences that tectonics has been active both before and after the last Interglacial.

The studied sequence shows three different highstands: Two littoral sedimentary units separated by terrestrial deposits that are affected by liquefaction (palaeoseismic activity), and the whole sequence being later cut by a palaeocliff and a wave-cut bench. This wave-cut bench is related to a later lower sea level that could have been promoted either by a climatically driven lower sea level or by a coseismic uplift. The comparative altitudinal analysis of the three maximum transgressive heights allows discriminating between these two possibilities. However, later earthquakes may have been responsible for the liquefaction and slumping-like structures observed in the intermediate terrestrial unit that flows onto the younger wave-cut bench.

Acknowledgments: Spanish Projects**:** CGL2012-33430, CGL2012-37581-CO2-01 and ACI-2009-1037. It is a contribution of the Spanish Working Group of IGCP Project 588.

NEOGENE DEFORMATION AT THE YAKUTAT PLATE CORNER IN SOUTHEAST ALASKA

Eva Enkelmann

University of Cincinnati

A sequence of M > 8 earthquakes occurred in September 1899 in Yakutat Bay (Southeast Alaska) resulting in coseismic rock uplift of up to 14 m. The earthquakes were located within the Yakutat microplate, a thick oceanic plateau that is moving northwestward at 48 mm/yr relative to North America. A structurally complex set of faults developed in the Yakutat Bay region, where deformation changes from transform motion along the northwest-trending Fairweather Fault into the west-trending thrust belt that connects with the Aleutian megathrust system. A zone of regional upwarp occurred in the area between the Fairweather, the Boundary, and the Yakutat faults, which is superimposed by very high uplift of a block located on the west side of Yakutat Bay that is bounded by the Esker Creek and the Bancas Point faults towards the south and east, respectively. The deformation model of the 1899 earthquakes and subsequent seismic events that occurred along the Yakutat plate boundary reveal a complex strain pattern at the plate corner including significant surface uplift occurring at the northernmost splays of the Fairweather transform system as it transients into a convergence-dominated region. Unknown so far is how this current deformation pattern at the plate corner compares with to deformation accumulated over geological time scales (> 10^5 years). Apatite and zircon U-Th/He thermochronometry was used to investigate the pattern, amount, and rates of rock exhumation in Yakutat Bay. Extremely young apatite ages of 0.2–0.5 Ma occur in the hanging wall of the Esker Creek fault and the Chaix Hill fault, and give evidence for rapid thrusting over geologic times. Apatite ages are also young (~0.8–1 Ma) at the hanging wall of the Bancas Point fault at the west side of Disenchantment Bay and become older toward east, matching the deformation occurring in 1899.

FOCUSED EXHUMATION ALONG MEGATHRUST SPLAY FAULTS IN PRINCE WILLIAM SOUND, ALASKA

P.J. Haeussler[1], **P.A. Armstrong**[2], **L.M. Liberty**[3], **K. Ferguson**[2], **S.P. Finn**[3], **J.C. Arkle**[2], **T.P. Pratt**[4]

[1] U.S. Geological Survey, Anchorage, AK, USA
[2] California State University, Fullerton, CA, USA
[3] CGISS, Boise State University, Boise, ID, USA
[4] U.S. Geological Survey, Reston, VA, USA

Megathrust splay faults are a common feature of accretionary prisms and can be important for generating tsunamis during some subduction zone earthquakes. Here we provide new evidence from Alaska that megathrust splay faults have been conduits for focused exhumation for the last 5 Ma. Published and new low-temperature thermochronology data indicate little to no permanent rock uplift over tens of thousands of earthquake cycles in most of central Prince William Sound. However, in southern Prince William Sound on Montague Island, apatite (U-Th)/He ages are as young as 1.1 Ma, indicating focused and rapid rock uplift. Montague Island lies in the hanging wall of the Patton Bay megathrust splay fault system, which ruptured during the 1964 M 9.2 earthquake and produced ~9 m of vertical uplift. Recent geochronology and thermochronology studies show rapid exhumation for the last 5 Ma in a pattern similar to the uplift in the 1964 earthquake. The region of older exhumation correlates with rocks that are older and thermally mature and constitute a mechanically strong backstop. The region of rapid exhumation consists of much younger, thermally immature rocks, which we infer are mechanically weak. The region of rapid exhumation is separated from the region of slow exhumation by the newly identified Montague Strait fault. New high-resolution bathymetry, seismic reflection profiles, and an earthquake show this feature as a 75-km-long high-angle active normal fault. There are numerous smaller active normal(?) faults in the region between the Montague Strait fault and the splay faults. We interpret this hanging wall extension as developing between the rapidly uplifting sliver of younger and weaker rocks on Montague Island from the essentially fixed region to the north. Deep seismic reflection profiles show the splay faults root into the subduction megathrust where there is probable underplating. Thus the exhumation and extension in the hanging wall are likely driven by underplating along the megathrust décollement, thickening in the overriding plate and a change in rheology at the Montague Strait fault to form a structural backstop. A comparison with other megathrust splay faults around the world shows they have significant variability in their characteristics, and there is not a simple model for megathrust splay faults.

MODELING OF AN UPLIFTED COASTAL AREA: THE CASE STUDY OF TARANTO (ITALY)

Domenico Capolongo, Emanuele Giachetta, Giuseppe Mastronuzzi*

Dipartimento di Scienze della Terra e Geoambientali
Università degli Studi di Bari "Aldo Moro"
Via E. Orabona, 4 - Bari , Italy
domenico.capolongo@uniba.it
emanuele.giachetta@uniroma3.it
giuseppeantonio.mastronuzzi@uniba.it

The Gulf of Taranto (southern Italy) is comprised between the Apennines fold-and-thrust belt to the West and the Apulian foreland to the East. Its coastal landscape is characterized by a staircase of marine terraces, gently tilted to the east; MIS 5.5 marine deposits have been recognized between about 200 m in the area of Messina Strait and 6 m in the southernmost part of Apulia. They are incised by a fluvial network as the result of the superimposition of the deep fluvial erosion driven by the dramatic climatic and eustatic sea level changes connected to the glacial cycles, heavily conditioned by the tectonic uplift of the entire area.

The Holocene final transgression filled of marine/alluvial sediments the previous incised valleys, building an extent coastal plain where the sedimentary budget was enough. In the Taranto area a deep inlet has still the features of a rias.

We investigate the evolution of the coastal landscape in the Taranto, which is considered one of the most significant in the Mediterranean basin in the definition of the general features of the MIS 5.5. In particular the long-term landscape evolution of the area has been reconstructed using a numerical model, SIGNUM. The numerical model originally includes and interpolate geomorphic process like hillslope diffusion, channel incision, and uplift coupled to a wave-cut platform down-wearing and cliff retreat model. The simulated processes have been just improved and optimized applying local data of sea-level history, uplift rates, measured cliff retreat rates, wave base, and speed deriving from different surveys recently performed in this area. Results help to constrain the long-term landscape evolution and the complex history of the Gulf of Taranto.

LONG-TERM ENIGMATIC UPLIFT OF COASTLINES

Koji Okumura

Hiroshima University
kojiok@hiroshima-u.ac.jp

Pleistocene and Holocene marine terraces and sediments are invaluable indicators of crustal movements in coastal areas. Seismological, geodetical, and geological modeling and observation usually agree with each other. However, when we try to apply the modeling to existing marine terraces there are a lot of difficulties. We do not know how marine terraces are deformed. In the southern part of the 2011 Tohoku earthquake source area, long-term coastal uplift is evident by Pleistocene terraces, but the M 9 earthquake submerged the entire coastline. There is no rebound. Before the 2011 earthquake only subsidence we observed. Nothing favors ~50 m uplift of MIS 5e terraces. Large slip in deeper interface is expected but never observed. Similar discrepancy occurs in Hokkaido along the western end of Kuril subduction zone. Both coseismic and interseismic subsidence continued. A paroxysmal large earthquake and post-earthquake deeper slip in 17 century A.D. is reported. During 1946 Nankai earthquake, the famous northward tilt of two peninsulas was interpreted from leveling. However, the uplift pattern may be interpreted as NS anticlinal uplift of the two peninsulas. Offshore geologic structures formed by oblique subduction are concordant with the anticlinal deformation. Detailed studies of the Pleistocene and Holocene terraces indicate the role of intraplate structures. Through 1993 Japan Sea earthquake and other submarine large earthquakes, we learned the cumulative deformations are formed by combination of deformations by different sources. An earthquake shows one pattern of deformation, but in most cases we do not know the others. Resolving composite uplift history is an important task. For most coastal terraces, we do not have a reasonable tectonic model even if there are possible causative faults. And in case there is no geologic structure to push the coast up, still there develop Pleistocene marine terraces. We need better understanding how the coastlines are deformed.

DETAILS OF THE MID-HOLOCENE RELATIVE SEA-LEVEL HIGHSTAND AT BELITUNG ISLAND, INDONESIA, ON THE SUNDA SHELF, FROM CORAL MICROATOLLS

Aron J. Meltzner
Earth Observatory of Singapore, Nanyang Technological University, Singapore
meltzner@ntu.edu.sg
Adam D. Switzer
Earth Observatory of Singapore, Nanyang Technological University, Singapore
aswitzer@ntu.edu.sg
Benjamin P. Horton
Department of Marine and Coastal Sciences, Rutgers University, New Brunswick, NJ
bphorton@marine.rutgers.edu
Chung-Che Wu
Department of Geosciences, National Taiwan University, Taipei, Taiwan ROC
r94224112@ntu.edu.tw
Hong-Wei Chiang
Earth Observatory of Singapore, Nanyang Technological University, Singapore
hwchiang@ntu.edu.sg
Chuan-Chou Shen
Department of Geosciences, National Taiwan University, Taipei, Taiwan ROC
river@ntu.edu.tw
Shou-Yeh Gong
Department of Geology, National Museum of Natural Science, Taichung, Taiwan ROC
gng@mail.nmns.edu.tw
Bambang W. Suwargadi
Research Center for Geotechnology, Indonesian Institute of Sciences, Bandung, Indonesia
bambang.suwargadi@gmail.com
Danny Hilman Natawidjaja
Research Center for Geotechnology, Indonesian Institute of Sciences, Bandung, Indonesia
danny.hilman@gmail.com
Andrea J. Ritch
Division of Geological and Planetary Sciences, California Institute of Technology, Pasadena, CA
aritch@caltech.edu

Details of relative sea level (RSL) since the mid-Holocene in Southeast Asia are poorly determined. We have developed a mid-Holocene RSL record from Belitung Island, Indonesia, on the Sunda Shelf, based primarily on coral microatolls. Microatolls' upward growth is limited by aerial exposure and hence they track low water to within a few centimeters, providing a high-resolution record of former RSL, except in cases where the microatolls' elevation is biased upward by moating. On northwestern Belitung, we slabbed 14 fossil and 2 modern microatolls (each yielding a series of sea-level index points) and slabbed or cored 14 additional fossil corals (each yielding a minimum sea-level marker). Preliminary U-Th and ^{14}C dates suggest RSL rose rapidly to a highstand of +1.9 m at ~6.7 ka; RSL may have fallen to +1.3 m quickly thereafter, but was back up at around +1.7 m by ~6.5 ka. We are investigating whether these apparent fluctuations could have been caused by moating, but similar observations at a site on southeastern Belitung, 80 km away, suggest these fluctuations reflect real changes in regional RSL.

UNCERTAINTIES IN FIELD ESTIMATION OF MEAN SEA LEVEL

Robert L. Wesson, rwesson@wispertel.net
Evergreen, Colorado, USA
Marco Cisternas, marco.cisternas@ucv.cl
Escuela de Ciencias del Mar, Pontificia Universidad Católica de Valparaíso, Chile
Lisa L. Ely, ely@cwu.edu
Department of Geological Sciences, Central Washington University, USA
Daniel Melnick, daniel.melnick@geo.uni-potsdam.de
Institut für Erd- und Umweltwissenschaften, Universität Potsdam, Potsdam, Germany
Richard Briggs, rbriggs@usgs.gov
U.S. Geological Survey, Denver, Colorado, USA
Edmund Garrett, edmund.garrett@durham.ac.uk
Department of Geography, Durham University, Durham, UK

One objective of field studies of Holocene coastal stratigraphy and apparent relative sea level changes associated with earthquakes is to determine the extent to which tectonic uplift or subsidence is recorded. A common requirement is to estimate modern mean sea level (MSL) or other tidal datum at a field site tens to hundreds of kilometers from the nearest permanent tide gauge. Common practice is to measure the relative elevation of water level frequently over a period of hours, or to record level changes with a pressure or other temporary tide gauge over periods of hours to days. These measurements are then compared with either the records of the closest tide gauge or a tidal model to estimate MSL or other tidal datum for the field site. We show how the uncertainties in the resulting estimates can be deduced from a statistical bootstrapping technique in which we use resampled tide gauge measurements and a tidal model to estimate MSL. The uncertainties depend on the length of time over which the water level is measured, the tidal range, wave conditions, weather, and seasonal variations, among other factors. We show examples from a site in a riverine estuary at Tirua, Chile; a modestly protected bay site at Isla Santa María off the coast of Chile; and sites in Alaska and Oregon, USA. On the coast of south-central Chile, for example, we show that tidal measurements over periods of hours to days during relatively calm summer conditions, and comparison to the TPXO tidal model, lead to estimates of mean sea level with a standard error of ±0.07 m. Our field measurements employ an inexpensive, portable, easy-to-deploy, acoustic tide gauge which will also be described.

THE TSUNAMI THAT WAS OBSCURED BY THE BIRTH OF AN ISLAND

Gösta Hoffmann[1,2], **Sultan Al-Yahyai**[3], **Mareike Kociok**[1,2], **Christoph Grützner**[2]

[1] German University of Technology, Department of Applied Geosciences, PO Box 1816, PC 130 Muscat, Sultanate of Oman, goesta.hoffmann@gutech.edu.om
[2] Institute of Neotectonics and Natural Hazards, RWTH Aachen University, Lochnerstr. 4-20, 52056 Aachen, Germany
[3] Public Authority for Civil Aviation (PACA), National Meteorological Service, PO Box 1, PC 111 Muscat, Sultanate of Oman, s.alyahyai@met.gov.om

The historical record of tsunami events within the Northern Indian Ocean (NIO) is fragmentary. Large tsunamigenic earthquakes are known to be generated in the Makran Subduction Zone, the area that forms the boundary of Arabian and Eurasian plates. Submarine sliding is reported along the Owen Fracture Zone (OFZ), demarking the boundary between the Arabian and Indian plates. The tsunami hazard potential within the NIO is enigmatic. Here we present the first instrumentally recorded tsunami wave within the NIO. This event is a secondary effect of a 7.7 magnitude earthquake that struck southern Pakistan on 24 September 2013. The tsunami wave went almost unnoticed as (a) the wave height was low, (b) it occurred at low tide, and (c) all media attention was drawn to the emergence of a new island. Our analysis is based on sea-level oscillations recorded at various tide-gauge stations along the coastlines of Oman, Pakistan, and Iran, as well as eyewitness accounts of the event in Oman. Our results indicate that the wave was in the range of 1 m and less in height. It was first recorded along the eastern coast of Oman and propagated towards the west. We conclude that the wave must have been triggered by a submarine slide either on the Makran margin or at the OFZ. Large submarine slope failures within the NIO may be more frequent than postulated.

CHARACTERIZING SITE CONDITIONS FOR GEOTECHNICAL ENGINEERING PROJECTS IN SOUTHEAST ALASKA

Eric Cannon

Golder Associates Inc.
Anchorage, Alaska
ecannon@golder.com

Southeast Alaska is a dynamic environment that provides many challenges to geotechnical engineering projects due to numerous active processes from geological, hydrological, and glacial systems. In addition, working in the field is often demanding due to the remote nature of projects and often variable weather conditions. An important component in the development of these projects—roads, marine facilities, airports, powerlines, and dams, for example—is the site characterization of the project. While the site characterization may have project-specific requirements, in general, key elements include selecting and optimizing project sites or alignments, identifying geological hazards, locating and proving out material sources, and identifying water resources. The foundation of the complex natural environment in Southeast Alaska is the bedrock geology, consisting of a number of northwest-trending geologic terranes that have been accreted to the North American continent throughout the Mesozoic and Cenozoic. Extensive Pleistocene glaciations, significant glacial retreat, and current glacio-isostatic uplift have contributed to landform development in Southeast Alaska. Modern icefields are found at higher elevations in the coastal mountains. The tectonic setting is dominated by two Quaternary, right-lateral, strike-slip faults—the Queen Charlotte–Fairweather fault offshore to the west, and the Chatham Strait fault, an extension of the Denali fault system. Several volcanoes are present in the southern region. Tsunami hazards result from distant earthquakes or from locally-triggered events, for example landslides or rockfalls. This presentation includes an overview of the geology, tectonics, and glacial history of Southeast Alaska, and focuses on providing examples of site conditions and active processes in the region that influence geotechnical engineering projects. Examples include mass movements on steep glacial fjord walls, deposition of glacial and post-glacial sediments, development of temperate rainforest vegetation and muskeg, tectonic and volcanic hazards, and glacial processes.

IMPLEMENTING THE COASTAL RECORD IN THE INQUA ESI SCALE—2007

Lario, J.[1], **Bardají, T.**[2], **Cabero, A.**[1], **Silva, P.G.**[3], **Zazo, C.**[4], **Goy, J.L.**[5]

[1] Facultad de Ciencias, UNED. 28040-Madrid, España
acabero@ccia.uned.es; Javier.lario@ccia.uned.es
[2] U.D. Geología. Universidad de Alcalá. 28871-Alcalá de Henares (Madrid), España. Corresponding author teresa.bardaji@uah.es
[3] Dpto. Geología, Museo Nacional CC. Naturales, CSIC. 28006-Madrid, España. mcnzc65@mncn.csic.es
[4] Dpto. Geología, Universidad de Salamanca, EPTS de Avila. 05003-Ávila, España. pgsilva@usal.es
[5] Dpto. Geología, Facultad de Ciencias; Universidad de Salamanca. 37008-Salamanca, España. joselgoy@usal.es

Seismic Intensity scales are based on the effects of earthquakes on man, man-made structures, and on natural environment. However, the effects on the environment usually have been minimized because they were considered to be inaccurate features. The growth of palaeoseismology as an independent discipline led to the development of the ESI-2007 Intensity Scale, based on the effects of earthquakes on the environment, and ratified by INQUA during its XVII Congress (Cairns, Australia, 2007). This scale can be used alone or jointly with other intensity scales, but it becomes especially useful for seismic intensity higher than X, when damage-based scales get saturated and environmental effects are still diagnostic.

The ESI scale comprises twelve intensity degrees and it considers primary and secondary effects, depending on whether they are caused directly by earthquake energy reaching the surface, or they are induced by ground-shaking. However, the effects on coastal settings are not properly and specifically considered. This work aims to take a first step in including the coastal record in this scale by gathering all the available information on the effects of earthquakes in this environment.

Two features have primarily been considered: Coastal uplift/subsidence and geological record of tsunamis.

Coastal uplift/subsidence is a primary effect evidenced by, for example, displaced notches or wave-cut platforms. The ESI scale presents different uplift/subsidence values for every intensity degree; we just propose to compare the existing data on coastal features to refine the scale.

Tsunamis are only considered in the ESI scale by the height of the waves, and not by their geological or sedimentary record. Data from present-day tsunamis (authors' own work and others' published data) are used as a first approach to the implementation of this record in the ESI scale. However, the joint effort of an international working group is desirable in order to properly match effects and intensity degrees.

Acknowledgments: Spanish Projects: CGL2012-33430, CGL2012-37581-CO2-01 and ACI-2009-1037. It is a contribution of the Spanish Working Group of IGCP Project 588.

UPDATE OF THE U.S. NATIONAL SEISMIC HAZARD MAPS FOR ALASKA

Mark D. Petersen, Charles S. Mueller

U.S. Geological Survey
mpetersen@usgs.gov, cmueller@usgs.gov

The U.S. Geological Survey (USGS) developed the National Seismic Hazard Map for Alaska in 2007 based on the latest information available on earthquake sources and ground shaking (Wesson *et al.*, 2007). These probabilistic seismic hazard maps are applied in building design provisions for seismic shaking, insurance rate structures, earthquake risk analyses, and many other public policy applications. The maps represent our assessment of the best-available seismic-hazard information at the time of the update. USGS updates the maps regularly to account for new data, models, and methods, as our understanding of earthquake ground shaking advances. During the past few years we have updated the National Seismic Hazard Maps for the conterminous United States based on new seismological and geological data. To develop this update, we held a series of regional workshops to gather new information. Final models were reviewed by a Steering Committee composed of experts in hazard estimation.

The new models and methodology applied in the 2014 National Seismic Hazard Maps for the 48 States are also applicable for updating the Alaska hazard maps. For example, the 2007 maps applied crustal and subduction earthquake ground motion models that have been updated over the past few years. In addition, geodetic data and geologic data were both used to update the fault slip rates across the western United States. These slip rates are used to determine the activity rates of faults in the model. New geodetic data and geologic data for Alaska could also provide the basis for a new seismic source model. New estimates of maximum magnitude and alternative smoothing methods provide a basis for updating the seismicity-based source model that controls the hazard in regions where no faulting is characterized. All of these advances should be considered in developing a new seismic hazard model for Alaska.

THE 1938 M 8.2 SEMIDI ISLANDS EARTHQUAKE: A RE-EVALUATION OF 20TH-CENTURY MOMENT RELEASE ALONG THE SEMIDI ISLANDS SECTION OF THE ALASKA-ALEUTIAN MEGATHRUST

Richard W. Briggs, rbriggs@usgs.gov
Geologic Hazards Science Center, U.S. Geological Survey, Golden, CO
William D. Barnhart, wbarnhart@usgs.gov
Geologic Hazards Science Center, U.S. Geological Survey, Golden, CO
Simon E. Engelhart, engelhart@mail.uri.edu
Dept. of Geosciences, University of Rhode Island, Providence, RI
Alan R. Nelson, anelson@usgs.gov
Geologic Hazards Science Center, U.S. Geological Survey, Golden, CO
Robert C. Witter, rwitter@usgs.gov
Alaska Science Center, U.S. Geological Survey, Anchorage, AK
Richard D. Koehler, richard.koehler@alaska.gov
State of Alaska, Division of Geological and Geophysical Surveys, Fairbanks, AK
Peter J. Haeussler, pheuslr@usgs.gov
Alaska Science Center, U.S. Geological Survey, Anchorage, AK
Guy Gelfenbaum, ggelfenbaum@usgs.gov
Pacific Coastal and Marine Science Center, U.S. Geological Survey, Santa Cruz, CA
Tina Dura, dura@sas.upenn.edu
Dept. of Earth and Environmental Science, University of Pennsylvania, Philadelphia, PA

Moment release by great subduction earthquakes is often represented by rupture areas projected into map view along the plate boundary. For the Alaska–Aleutian megathrust, this type of depiction implies 20th-century moment release has been substantial along the entire subduction zone due to great earthquakes between 1938 and 1965. To better characterize potential seismic hazard and long-term rupture behavior of the Alaska–Aleutian megathrust, we revisit the distribution and extent of slip during the 1938 rupture along the ~330 km Semidi Islands section between Kodiak Island and the Shumagin Islands. We summarize previous work on the source of the 1938 rupture and find that (1) significant slip (> 1 m) is limited to ~100 km of the ~330 km Semidi Islands section; and (2) the depth of significant slip along the subduction interface is unclear. No significant tsunami (> 8 cm) or land-level change from the 1938 rupture was reported; our ongoing work suggests geologic evidence of tsunami inundation in 1938 may be recorded on Chirikof Island, but not on Sitkinak Island. To further evaluate the character of moment release by the 1938 rupture, we performed a series of forward elastic models using a subduction interface geometry along the Semidi Islands section defined by Slab 1.0 (Hayes *et al.*, 2012). We find that ruptures up to M 8.2 associated with decimeter-scale coseismic land-level changes are permitted in the vicinity of Chirikof Island, and that a number of reasonable hypothetical M 8.2 ruptures can be modeled that rupture only a small portion of the Semidi Islands section. We propose that for purposes of seismic hazard analyses, substantial moment release has not occurred along most of the Semidi Islands section since the July 1788 rupture that likely extended from the eastern edge of the Shumagin Islands to at least Three Saints Bay on Kodiak Island.

A STRATIGRAPHIC RECORD OF MEGATHRUST UPLIFT AND SUBSIDENCE AT SITKINAK LAGOON, SITKINAK ISLAND, ALASKA

Simon E. Engelhart[1], **Tina Dura**[2], **Richard W. Briggs**[3], **Alan R. Nelson**[3], **Andrew C. Kemp**[4], **Peter J. Haeussler**[5], **D. Reide Corbett**[6], **Stephen J. Angster**[3], **Lee-Ann Bradley**[3]

[1] Dept. of Geosciences, University of Rhode Island, Kingston, RI, USA
[2] Dept. of Earth and Environmental Science, University of Pennsylvania, Philadelphia, PA, USA
[3] U.S. Geological Survey, Geologic Hazards Science Center, Golden, CO, USA
[4] Dept. of Earth and Ocean Sciences, Tufts University, Medford, MA, USA
[5] U.S. Geological Survey, Alaska Science Center, Anchorage, AK, USA
[6] Dept. of Geological Sciences and Coastal Processes Program, East Carolina University, Greenville, NC, USA

The Alaska–Aleutian subduction zone is the source of frequent great earthquakes and accompanying destructive tsunamis, as demonstrated by a series of M 8–9 ruptures during the 20th century, which has ruptured almost the entire convergent plate boundary. However, very little is known about great earthquake and tsunami prehistory west of central Kodiak Island (154.3°W). Here, we report new stratigraphic evidence of land-level change and tsunami inundation along the Alaska–Aleutian megathrust. Cores and tidal outcrops fringing the lagoon of Sitkinak Island (154.15°W), 25 km southwest of Kodiak Island, reveal five sharp lithologic contacts that record both coseismic uplift and subsidence in the past ~1,000 years. Radiocarbon dates, ^{137}Cs profiles, CT X-ray tomography scans, and changes in diatom/foraminiferal assemblages suggest sudden uplift prior to 290–0, 650–500, and 1,050–780 cal yr BP, and sudden subsidence in AD 1964 and after 800–670 cal yr BP. A sand bed traced 1.5 km inland and bracketed with ^{14}C, ^{137}Cs, and ^{210}Pb ages was most likely deposited by a tsunami described by Russian colonists on other islands in AD 1788 immediately following sudden contemporaneous uplift of similar age. The mixed uplift and subsidence record suggests that Sitkinak Island sits above the non-persistent southwestern boundary of the AD 1964 M_w 9.2 megathrust rupture. We are reconstructing amounts of subsidence/uplift associated with each earthquake by applying a regional diatom transfer function to fossil diatom data from cores. The precise estimates of vertical displacement on Sitkinak will help us estimate past magnitudes, more accurately define the limits of past megathrust ruptures, and improve seismic hazard maps in Alaska.

PALEOSEISMIC INVESTIGATIONS OF SUBDUCTION ZONE EARTHQUAKES ON THE SOUTHWESTERN COAST OF THE KENAI PENINSULA, ALASKA

Ian Shennan, Natasha Barlow, and Ed Garrett

Sea Level Research Unit
Department of Geography
Durham University
South Road, Durham, DH1 3LE, UK
ian.shennan@durham.ac.uk

Investigations of Holocene sediment sequences at Kenai, Kasilof, Homer, Peterson Bay, and Sadie Cove show highly contrasting records that also differ from those found in Turnagain Arm and on Kodiak Island. We use the evidence from all of these sites to consider the following questions:

1. Can we quantify geologic estimates of land-level changes from great Holocene plate boundary earthquakes and complete earthquake cycles across the Kenai Peninsula–Kachemak Bay region?
2. Is there evidence of late Holocene earthquake-generated or volcano-generated tsunami?
3. How do spatial patterns of estimated land-level changes for different Holocene plate boundary earthquakes vary between Kodiak Island and western Yakataga?
4. Are great earthquake ruptures in south-central Alaska controlled by persistent segment boundaries or do the rupture areas overlap?

RECENT HISTORY AND DYNAMICS OF BERING GLACIER

Bruce F. Molnia

U.S. Geological Survey
12201 Sunrise Valley Drive
Reston, VA 20192
bmolnia@usgs.gov

Bering Glacier is the largest glacier in continental North America with an area of ~5,000 km^2. This is ~1.5 times larger than the state of Rhode Island. The entire glacier lies within 100 km of the Gulf of Alaska. Bering Glacier alone accounts for > 6 percent of the glacier-covered area of Alaska and may contain ~ 15–20 percent of Alaska's glacier ice and as much as 10,000 km^3 of water.

Bering is also the largest surging glacier on Earth, having surged at least six times during the 20th and early 21st centuries. With a length of 191 km, Bering Glacier is the longest glacier in continental North America. During a typical Bering Glacier surge, ice is rapidly transferred from the glacier's accumulation area to the ~900 km^2 piedmont lobe. As a result, the piedmont lobe rapidly thickens and expands. During the 1993–1995 surge, the piedmont lobe thickened more than 100 m and advanced a maximum of > 10 km. With maximum elevation of less than 575 m, the piedmont lobe lies completely within the area of ablation. Consequently, following a surge, it rapidly thins and retreats. Initially, retreat is dominated by active calving and melting. However, as the glacier margin thins and begins to float, passive calving becomes the dominant process.

Complementary geophysical studies reveal that Bering Glacier's piedmont lobe occupies a deeply scoured basin that is a terrestrial continuation of the Gulf of Alaska's Bering Trough. Offshore, the trough's maximum depth to bedrock is ~ 500 m. In parts of Vitus Lake, the ice-marginal lake located adjacent to the terminus of the eastern margin of Bering Glacier, the depth to the bedrock floor of the basin exceeds 350 m. Prior to the latest surge, this 20-km-long, ice-marginal lake had an area of ~150 km^2.

ACKNOWLEDGMENTS

We thank all chapter authors for putting together all the information in this guide and leading field trip stops. We are incredibly grateful to Paula Davis and Joni Robinson at the Division of Geological & Geophysical Surveys for all their hard work assembling the field guide. Joy Troyer at the Seismological Society of America provided fantastic administrative support. We thank Orca Lodge staff for all their work supporting our stay in Cordova.

Chapters by Shennan *et al.* are supported by the U.S. Geological Survey, Department of the Interior, earthquake hazards projects (awards 06HQGR0033, G09AP00105, and G10AP00075; see note below), and the UK NERC Radiocarbon Facility (grants #935.0901 and #1339.1008). The Alaska Division of Geological & Geophysical Surveys provided Shennan *et al.* access to Portage core at its Geologic Materials Center, and generously provided funds for AMS radiocarbon dating. Garrett *et al.* kindly thank Darrell Kaufman for the samples from Whitshed Lake, and Hannah Cool for her work on the core.

NOTE: The views and conclusions contained in this document are those of the authors and should not be interpreted as necessarily representing the official policies, either expressed or implied, of the U.S. Government.

COLLECTED REFERENCES

Aðalgeirsdóttir, G., Echelmeyer, K.A., and Harrison, W.D., 1998, Elevation and volume changes on the Harding Icefield, Alaska: Journal of Glaciology, v. 44, no. 148, p. 570–582.

Arendt, A.A., Echelmeyer, K.A., Harrison, W.D., Lingle, C.S., and Valentine, V.B., 2002, Rapid wastage of Alaska glaciers and their contribution to rising sea level: Science, v. 297, no. 5580, p. 382–386. Table S1 at http://www.sciencemag.org/cgi/content/full/297/5580/382/DC1.

Arendt, A.A., Bolch, T., Cogley, J.G., Gardner, A., Hagen, J.-O., Hock, R., Kaser, G., Pfeffer, W.T., Moholdt, G., Paul, F., Radić, V., Andreassen, L., Bajracharya, S., Beedle, M., Berthier, E., Bhambri, R., Bliss, A., Brown, I., Burgess, E., Burgess, D., Cawkwell, F., Chinn, T., Copland, L., Davies, B., Dolgova, E., Filbert, K., Forester, R., Fountain, A., Frey, H., Giffen, B., Glasser, N., Gurney, S., Hagg, W., Hall, D., Haritashya, U.K., Hartmann, G., Helm, C., Herreid, S., Howat, I., Kapustin, G., Khromova, T., Kienholz, C., Koenig, M., Kohler, J., Kriegel, D., Kutuzov, S., Lavrentiev, I., LeBris, R., Lund, J., Manley, W., Mayer, C., Li, X., Menounos, B., Mercer, A., Moelg, N., Mool, P., Nosenko, G., Negrete, A., Nuth, C., Pettersson, R., Racoviteanu, A., Ranzi, R., Rastner, P., Rau, F., Rich, J., Rott, H., Schneider, C., Seliverstov, Y., Sharp, M., Sigurðsson, O., Stokes, C., Wheate, R., Winsvold, S., Wolken, G., Wyatt, F., and Zheltyhina, F., 2012, Randolph Glacier inventory [v. 3.2]—A dataset of global glacier outlines: Boulder, CO, Global Land Ice Measurements from Space, digital media.

Atwater, B.F., 1987, Evidence for great Holocene earthquakes along the outer coast of Washington state: Science, v. 236, p. 942–944.

Atwater, B.F., Yamaguchi, D.K., Bondevik, S., Barnhardt, W.A., Amidon, L.J., Benson, B.E., Skjerdal, G., Shulene, J.A., and Nanayama, F., 2001, Rapid resetting of an estuarine recorder of the 1964 Alaska earthquake: Geological Society of America Bulletin, v. 113, p. 1,193–1,204.

Bailey, Palmer, Fleisher, P.J., Mankoff, Evan, and Senglaub, Michael, 2000, An evolving ice-contact proglacial lake, Sheridan Glacier, Alaska [abs.]: Geological Society of America, Abstracts with Programs, v. 32, no. 7, p. 117.

Barclay, D.J., Calkin, P.E., and Wiles, G.C., 1999, A 1,119-year tree-ring-width chronology from western Prince William Sound, southern Alaska: The Holocene, v. 9, no. 1, p.79–84.

Barlow, N.L.M., Shennan, Ian, and Long, A.J., 2012, Relative sea-level response to Little Ice Age ice mass change in south central Alaska—Reconciling model predictions and geological evidence: Earth and Planetary Science Letters, v. 315-316, p. 62–75.

Barnes, F.F., 1943, Geology of the Portage Pass area, Alaska: U.S. Geological Survey Bulletin 926D, p. 211–235, with map.

Barnhardt, W.A., and Kayen, R.E., 2000, Radar structure of earthquake-induced, coastal landslides in Anchorage, Alaska: Environmental Geosciences, v. 7, p. 38–45.

Bartsch-Winkler, S., and Ovenshine, A.T., 1984, Macrotidal subarctic environment of Turnagain and Knik Arms, upper Cook Inlet, Alaska—Sedimentology of the intertidal zone: Journal of Sedimentary Petrology, v. 54, p. 1,221–1,238.

Bartsch-Winkler, Susan, and Schmoll, H.R., 1987, Earthquake-caused sedimentary couplets in the upper Cook Inlet region, *in* Hamilton, T.D., and Galloway, J.P., ed., Geologic studies in Alaska by the U.S. Geological Survey during 1986: U.S. Geological Survey Circular 998, p. 92–95.

Bartsch-Winkler, S., Ovenshine, A.T., and Kachadoorian, R., 1983, Holocene history of the estuarine area surrounding Portage, Alaska, as recorded in a 93 m core: Canadian Journal of Earth Sciences, v. 20, p. 802–820.

Beaumont, C., Fullsack, P., and Hamilton, J., 1992, Erosional control of active compressional orogens*, in* McClay, K.R. ed., Thrust Tectonics: New York, Chapman & Hall, p. 1–18.

Beaumont, C., Jamieson, R.A., Nguyen, M.H., and Lee, B., 2001, Himalayan tectonics explained by extrusion of a low-viscosity crustal channel coupled to focused surface denudation: Nature, v. 414, no. 6865, p. 738–742. doi:10.1038/414738a

Berger, A.L., and Spotila, J.A., 2008, Denudation and deformation in a glaciated orogenic wedge—The St. Elias orogen, Alaska: Geology, v. 36, p. 523–526.

Berger, A.L., Spotila, J.A., Chapman, J., Pavlis, T.L., Enkelmann, E., Ruppert, N.A. and Buscher, J.T., 2008, Architecture, kinematics, and exhumation of a convergent orogenic wedge—A thermochronological investigation of tectonic-climatic interactions within the central St. Elias Orogen, Alaska: Earth and Planetary Science Letters, v. 270, p. 13–24.

Brandon, M.T., Roden-Tice, M.K., and Garver, J.I., 1998, Late Cenozoic exhumation of the Cascadia accretionary wedge in the Olympic Mountains, northwest Washington state: Geological Society of America Bulletin, v. 110, p. 985–1,009.

Brocklehurst, S.H., and Whipple, K.X., 2002, Glacial erosion and relief production in the Eastern Sierra Nevada, California: Geomorphology, v. 42, no. 1-2, p. 1–24. doi:10.1016/S0169-555X(01)00069-1

Brocklehurst, S.H., and Whipple, K.X., 2007, Response of glacial landscapes to spatial variations in rock uplift rate: Journal of Geophysical Research, v. 112, no. F2, p. 1–18. doi:10.1029/2006JF000667

Brown, L.D., Reilinger, R.E., Holdahl, S.R., and Balazs, E.I., 1977, Postseismic crustal uplift near Anchorage, Alaska: Journal of Geophysical Research, v. 83, p. 3,369–3,378.

Bruhn, R.L., Pavlis, T.L., Plafker, George, and Serpa, L., 2004, Deformation during terrane accretion in the Saint Elias orogen, Alaska: Geological Society of America Bulletin, v. 116, p. 771–787. doi:10.1130/B25182.1

Carver, Gary, and Plafker, George, 2008, Paleoseismicity and Neotectonics of the Aleutian subduction zone—An overview, *in* Freymueller, J.T., Haeussler, P.J., Wesson, R., and Ekström, G., eds., Active tectonics and seismic potential of Alaska: American Geophysical Union Geophysical Monograph Series, v. 179, p. 43–63.

Champagnac, J.D., Schlunegger, F., Norton, K., von Blanckenburg, F., Abbühl, L.M., and Schwab, M., 2009, Erosion-driven uplift of the modern Central Alps: Tectonophysics, v. 474, no. 1-2, p. 236–249. doi:10.1016/j.tecto.2009.02.024

Christensen, D.H., and Beck, S.L., 1994, The rupture process and tectonic implications of the great 1964 Prince William Sound earthquake: Pure and Applied Geophysics, v. 142, p. 29–53.

Christeson, G.L., Gulick, S.P.S., van Avendock, H.J.A., Worthington, L.L., Reece, R.S., and Pavlis, T.L., 2010, The Yakutat terrane—Dramatic change in crustal thickness across the Transition fault, Alaska: Geology, v. 38, p. 895–898. doi:10.1130/G31170.1

Combellick, R.A., 1991, Paleoseismicity of the Cook Inlet region, Alaska—Evidence from peat stratigraphy in Turnagain and Knik Arms: Alaska Division of Geological & Geophysical Surveys Professional Report 112, 52 p. doi:10.14509/2303

Combellick, R.A., 1993, The penultimate great earthquake in southcentral Alaska—Evidence from a buried forest near Girdwood, *in* Solie, D.N., and Tannian, Fran, eds., Short Notes on Alaskan Geology 1993: Alaska Division of Geological & Geophysical Surveys Professional Report 113B, p. 7–15. doi:10.14509/2306

Combellick, R.A., 1994, Investigation of peat stratigraphy in tidal marshes along Cook Inlet, Alaska, to determine the frequency of 1964-style great earthquakes in the Anchorage region: Alaska Division of Geological & Geophysical Surveys Report of Investigation 94-7, 24 p. doi:10.14509/2493

Combellick, R.A., and Reger, R.D., 1994, Sedimentological and radiocarbon-age data for tidal marshes along eastern and upper Cook Inlet, Alaska: Alaska Division of Geological & Geophysical Surveys Report of Investigation 94-6, 60 p. doi:10.14509/2492

Cool, H., 2013, Holocene relative sea-level change and local influence of late Holocene great earthquakes derived from stratigraphic and microfossil evidence in Whitshed, near Cordova, Alaska: United Kingdom, Durham University undergraduate dissertation.

Crossen, K.J., 2007, Portage Glacier and Portage Pass, Alaska—Little Ice Age dynamics and the chronology of glacial retreat: Polar Geography, v. 30, no. 3-4, p. 107–138.

Enkelmann, E., Garver, J.I., and Pavlis, T.L., 2008, Rapid exhumation of ice-covered rocks of the Chugach–St. Elias orogen, Southeast Alaska: Geology, v. 36, p. 915–918. doi:10.1130/G2252A.1

Enkelmann, E., Zeitler, P.K., Garver, J.I., Pavlis, T.L., and Hooks, B.P., 2010, The thermochronological record of tectonic and surface process interaction at the Yakutat–North American collision zone in Southeast Alaska: American Journal of Science, v. 310, p. 231–260. doi:10.2475/04.2010.01

Enkelmann, E., Zeitler, P.K., Pavlis, T.L., Garver, J.I., and Ridgway, K.D., 2009, Intense localized rock uplift and erosion in the St Elias orogen of Alaska: Nature Geoscience, v. 2,. P. 360–363. doi:10.1038/ngeo502

Ferris, A., Abers, G.A., Christensen, D.H., and Veenstra, E., 2003, High resolution image of the subducted Pacific(?) plate beneath central Alaska, 50–150 km depth: Earth and Planetary Science Letters, v. 214, p. 575–588. doi:10.1016/S0012-821X(03)00403-5

Field, W.O., ed., 1975, Mountain glaciers of the Northern Hemisphere: Hanover, New Hampshire, U.S. Army Corps of Engineers, Cold Regions Research and Engineering Laboratory, 2 vols., v. 1, 698 p., v. 2, 932 p. Includes atlas containing index maps of each glacierized region.

Finzel, E.S., Trop, J.M., Ridgway, K.D., and Enkelmann, E., 2011, Upper plate proxies for flat-slab subduction processes in southern Alaska: Earth and Planetary Science Letters, v. 303, p. 348–360. doi:10.1016/j.epsl.2011.01.014

Fletcher, H.J., and Freymueller, J.T., 1999, New GPS constraints on the motion of the Yakutat Block: Geophysical Research Letters, v. 26, no. 19, p. 3,029–3,032. doi:10.1029/1999GL005346

Fletcher, H.J., and Freymueller, J.T., 2003, New constraints on the motion of the Fairweather fault, Alaska, from GPS observations: Geophysical Research Letters, v. 30, p. 1,139. doi:10.1029/2002GL016476

Freymueller, J.T., Woodard, H., Cohen, S.C., Cross, R., Elliott, J., Larsen, C.F., Hreinsdottir, S., and Zweck, C., 2008, Active deformation processes in Alaska, based on 15 years of GPS measurements, *in* Freymueller, J.T., Haeussler, P.J., Wesson, R., and Ekström, G., eds., Active tectonics and seismic potential of Alaska: Washington, D.C., American Geophysical Union Geophysical Monograph, v. 179, p. 1–42. doi:10.1029/179GM02

Gibson, J.R., 1976, Imperial Russia in frontier America: New York, Oxford University Press.

Grabowski, D.M., Enkelmann, Eva, and Ehlers, T.A., 2013, Spatial extent of rapid denudation in the glaciated St. Elias syntaxis region, SE Alaska: Journal of Geophysical Research—Earth Surface, v. 118, no. 3, p. 1,921–1,938. doi:10.1002/jgrf.20136

Grant, U.S., and Higgins, D.F., 1913, Coastal glaciers of Prince William Sound and Kenai Peninsula, Alaska: U.S. Geological Survey Bulletin 526, 75 p., 2 plates.

Greb, S.F., and Archer, A.W., 2007, Soft-sediment deformation produced by tides in a meizoseismic area, Turnagain Arm, Alaska: Geology, v. 35, p. 435–438.

Grinsted, A., 2013, An estimate of global glacier volume: The Cryosphere, v. 7, p. 141–151. doi:10.5194/tc-7-141-2013

Hallet, B., Hunter, L., and Bogen, J., 1996, Rates of erosion and sediment evacuation by glaciers—A review of field data and their implications: Global Planetary Change, v. 12, p. 213–235.

Hamilton, S.L., and Shennan, Ian, 2005a, Late Holocene relative sea-level changes and the earthquake deformation cycle around upper Cook Inlet, Alaska: Quaternary Science Reviews, v. 24, p. 1,479–1,498.

Hamilton, S.L., and Shennan, Ian, 2005b, Late Holocene great earthquakes and relative sea-level change at Kenai, southern Alaska: Journal of Quaternary Science, v. 20, p. 95–111.

Hamilton, S.L., Shennan, Ian, Combellick, R.A., Mulholland, John, and Noble, Cate, 2005, Evidence for two great earthquakes at Anchorage, Alaska, and implications for multiple great earthquakes through the Holocene: Quaternary Science Reviews, v. 24, no. 18-19, p. 2,050–2,068.

Hansen, W.R., 1965, Effects of the earthquake of March 27, 1964, at Anchorage, Alaska: U.S. Geological Survey Professional Paper 542A, p. A1–A68.

Harding-Lawson Associates, 1979, Geotechnical hazards assessment study, Municipality of Anchorage: Harding-Lawson Associates Job No. 5502,009.08.

Haven, S.B., 1971, Effects of land-level changes on intertidal invertebrates, with discussion of post-earthquake ecological succession, *in* The Great Alaska earthquake of 1964: Biology, National Academy of Sciences publication 1604, p. 82–128.

Headley, R., Enkelmann, E., and Hallet, B., 2013, Examination of the interplay between glacial processes and exhumation in the Saint Elias Mountains, Alaska: Geosphere, v. 9, p. 229–241. doi:10.1130/GES00810.1

Herman, Frederic, and Braun, Jean, 2008, Evolution of the glacial landscape of the Southern Alps of New Zealand—Insights from a glacial erosion model: Journal of Geophysical Research, v. 113, no. F2, p. 9. doi:10.1029/2007JF000807

Jaeger, J.M., Nittrouer, C.A., Scott, N.D., and Milliman, J.D., 1998, Sediment accumulation along a glacially impacted mountainous coastline— Northeast Gulf of Alaska: Basin Research, v. 10, p. 155–173.

Jibson, R.W., and Michael, J.A., 2009, Maps showing seismic landslide hazards in Anchorage, Alaska: U.S. Geological Survey Scientific Investigations Map 3077, scale 1:25,000, 11 p. http://pubs.usgs.gov/sim/3077

Karlstrom, T.N.V., 1964, Quaternary geology of the Kenai lowland and the glacial history of the Cook Inlet region, Alaska: U.S. Geological Survey Professional Paper 443, p. 1–69.

Kaye, C.A., 1964, The upper limit of barnacles as an index of sea-level change on the New England coast during the past 100 years: Journal of Geology, v. 75, p. 580–600.

Kelsey, H.M., Witter, R.C., Briggs, R.W., Engelhart, S.E., Nelson, A.R., and Haeussler, P.J., 2013, Paleoseismic investigations of subduction zone earthquakes on the southeastern coast of the Kenai Peninsula, Alaska: American Geophysical Union Fall Meeting, abstract no. EP13A-0818.

Kerr, P.F., and Drew, I.M., 1968, Quick-clay slides in the U.S.A: Engineering Geology, v. 2, p. 215–238.

Koons, P.O., 1995, Modeling the topographic evolution of collisional belts: Annual Review of Earth and Planetary Sciences, v. 23, no. 1, p. 375–408, doi:10.1146/annurev.ea.23.050195.002111

Lampright, R.L., 2008, Gold placer deposits near Anchorage, Alaska, 2nd ed: Nederland, CO, Iron Fire Publications.

Larsen, C.F.; Motyka, R.J.; Freymueller, J.T.; Echelmeyer, K.A.; and Ivins, E.R., 2005, Rapid viscoelastic uplift in Southeast Alaska caused by post-Little Ice Age glacial retreat: Earth and Planetary Science Letters (EPSL), v. 237, p. 548–560.

Lienkaemper, J.J., and Bronk Ramsey, C., 2009, OxCal, Versatile tool for developing paleoearthquake chronologies—A primer: Seismological Research Letters, v. 80, p. 431–434.

Mann, D.H., and Crowell, A.L., 1996, A large earthquake occurring 700–800 years ago in Aialik Bay, southern coastal Alaska: Canadian Journal of Earth Sciences, v. 33, no. 1, p. 117–126.

McAleer, R.J., Spotila, J.A., Enkelmann, Eva, and Berger, A.L., 2009, Exhumation along the Fairweather fault, southeastern Alaska, based on low temperature thermochronometry: Tectonics, v. 28, no. 1, 17 p. doi:10.1029/2007TC002240

McCalpin, J.P., Bruhn, R.L., Pavlis, T.L., Gutierrez, F., Guerrero, J., and Lucka, P., 2011, Antislope scarps, gravitational spreading, and tectonic faulting in the western Yakutat microplate, south coastal Alaska: Geosphere, v. 7, no. 5, p. 1,143–1,158.

Meier, M.F., 1984, Contributions of small glaciers to global sea level: Science, v. 226, no. 4681, p. 1,418–1,421.

Meier, M.F., and Dyurgerov, M.B., 2002, Sea level changes—How Alaska affects the world: Science, v. 297, no. 5580, p. 350–351.

Meier, M.F., and Post, Austin, 1962, Recent variations in mass net budgets of glaciers in western North America, *in* Symposium of Obergurgl, Variations in the regime of existing glaciers: International Association of Hydrological Sciences-Association Internationale des Sciences Hydrologiques (IAHS-AISH), Publication No. 58, p. 63–77.

Meigs, A.J., Johnston, S., Garver, J., and Spotila, J., 2008, Crustal-scale structural architecture, shortening, and exhumation of an active, eroding orogenic wedge (Chugach/St. Elias Range, southern Alaska): Tectonics, v. 27, TC4003, 26 p.

Mendenhall, W.C., 1900, A reconnaissance from Resurrection Bay to the Tanana River, Alaska, in 1898: U.S. Geological Survey Annual Report 20, Part 7, p. 265–340.

Miller, D.J., 1971, Geologic map of the Yakataga district, Gulf of Alaska Tertiary province, Alaska: U.S. Geological Survey Map I-610, scale 1:125,000.

Milliman, J.D., and Meade, R.H., 1983, World-wide delivery of river sediment to the oceans: Journal of Geology, v. 91, no. 1, p. 1–21.

Milliman, J.D., Stocks, D., Jaeger, J.M., and Nittrouer, C.A., 1996, Prince William Sound, Alaska—Distal depocenter for Copper River sediment: EOS Transactions, v. 77, OS202.

Minster, J.B., and Jordan, T.H., 1978, Present-day plate motions: Journal of Geophysical Research, v. 83, p. 5,331-5,354.

Molnar, Peter, and England, P.C., 1990, Late Cenozoic uplift of mountain ranges and global climate change—Chicken or egg?: Nature, v. 346, no. 6,279, p. 29–34. doi:10.1038/346029a0

Molnia, B.F., 1989, Subarctic glacial marine sedimentation, NE Gulf of Alaska, *in* Anderson, J.N., and Molnia, B.F., eds., Glacial marine sedimentation—A short course: American Geophysical Union, Short Course in Geology 9, p. 59–106.

Molnia, B.F., 2001, Glaciers of Alaska: Anchorage, Alaska Geographic, v. 28, no. 2, 112 p.

Molnia, B.F., 2007, Late nineteenth to early twenty-first century behavior of Alaskan glaciers as indicators of regional climate change: Global and Planetary Change—Special Issue on Climate Change Impacts on Mountain Glaciers and Permafrost, v. 56, p. 23–56.

Molnia, B.F., 2008, Glaciers of Alaska, with sections on Columbia and Hubbard tidewater glaciers by Krimmel, R.M.; The 1986 and 2002 temporary closures of Russell Fiord by the Hubbard Glacier by Molnia, B.F., Trabant, D.C,. March, R.S., and Krimmel, R.M.; and Geospatial inventory and analysis of glaciers: a case study for the eastern Alaska Range by Manley, W.F., *in* Williams, R.S., Jr., and Ferrigno, J.G., eds., Satellite Image Atlas of Glaciers of the World: U.S. Geological Survey Professional Paper 1386-K, 525 p.

Molnia, B.F., and Post, Austin, 1995, Holocene history of Bering Glacier, Alaska—A prelude to the 1993–1994 surge: Physical Geography, v. 16, no. 2, p. 87–117.

Naske, C.-M., and Slotnick, H.E., 1987, Alaska—A history of the 49th State: Norman, OK, University of Oklahoma Press.

National Oceanic and Atmospheric Administration (NOAA). http://www.co-ops.nos.noaa.gov

Nelson, A.R., Shennan, Ian, and Long, A.J., 1996, Identifying coseismic subsidence in tidal-wetland stratigraphic sequences at the Cascadia subduction zone of western North America: Journal of Geophysical Research, v. 101, p. 6,115–6,135.

Nishenko, S.P., and Jacob, K.H., 1990, Seismic potential of the Queen Charlotte–Alaska–Aleutian seismic zone: Journal of Geophysical Research, v. 95, no. B3, p. 2,511–2,532.

O'Sullivan, P.B., and Currie, L.D., 1996, Thermotectonic history of Mt. Logan, Yukon Territory, Canada—Implications of multiple episodes of middle to late Cenozoic denudation: Earth and Planetary Science Letters, v. 144, p. 251–261.

O'Sullivan, P.B., Plafker, George, and Murphy, J.M., 1995, Apatite fission-track thermotectonic history of crystalline rocks in the northern Saint Elias Mountains, Alaska, *in* Dumoulin, J.A., and Gray, J.E., eds., Geological studies in Alaska by the United States Geological Survey, 1995: United States Geological Survey Professional Paper 1574, p. 283–294.

Ovenshine, A.T., Lawson, D.E., and Bartsch-Winkler, S.R., 1976, The placer river silt—Intertidal sedimentation caused by the Alaska earthquake of March 27, 1964: U.S. Geological Survey Journal of Research, v. 4, p. 151–162.

Perry, S.E., Garver, J.I., and Ridgway, K.D., 2009, Transport of the Yakutat terrane, southern Alaska—Evidence from sediment petrology and detrital zircon fission-track and U/Pb double dating: The Journal of Geology, v. 117, p. 156–173.

Plafker, George, 1969, Tectonics of the March 27, 1964, Alaska earthquake: U.S. Geological Survey Professional Paper 543-I, 74 p.

Plafker, George, 1972, The Alaskan earthquake of 1964 and Chilean earthquake of 1960—Implications for arc tectonics: Journal of Geophysical Research, v. 77, no. 5, p. 901–925.

Plafker, George, 1987, Application of marine-terrace data to paleoseismic studies, *in* Crone, A.J. and Omdahl, E.M., eds., Proceedings of conference XXXIX—Directions in Paleoseismology: U. S. Geological Survey Open-File Report 87-673, p. 146–156.

Plafker, George, and Berg, H.C., 1994, Overview of the geology and tectonic evolution of Alaska, *in* Plafker, George, and Berg, H.C., edEs., The Geology of Alaska: Boulder, CO, Geological Society of America.

Plafker, George, and Thatcher, Wayne, 2008, Geological and geophysical evaluation of the mechanisms of the Great 1899 Yakutat Bay earthquakes, *in* Freymueller, J.T., Haeussler, P.J., Wesson, R.L., and Ekström, G., eds., Active tectonics and seismic potential of Alaska: Geophysical Monograph Series, v. 179, p. 215–236. doi:10.1029/179GM12

Plafker, George, Kachadoorian, R., Eckel, E.B. and Mayo, L.R., 1969, Effects of the earthquake of March 27, 1964, on various communities: U.S. Geological Survey Professional Paper, 543-G, 50 p.

Plafker, George, Lajoie, K.R., and Rubin, M., 1992, Determining recurrence intervals of great subduction zone earthquakes in southern Alaska by radiocarbon dating, *in* Taylor, R.E., Long, A., and Kra, R.S., eds., Radiocarbon after Four Decades—An Interdisciplinary Perspective: New York, Springer-Verlag, p. 436–453.

Plafker, George, Moore, J.C., and Winkler, G.R., 1994, Geology of the southern Alaska margin, *in* Plafker, George, and Berg, H.C., eds., The Geology of Alaska: Boulder, CO, Geological Society of America, The Geology of North America, p. 389–449.

Plafker, George, Naeser, C.W., Zimmermann, R.A., Lull, J.S., and Hudson, Travis, 1992, Cenozoic uplift history of the Mount McKinley area in the central Alaska Range based on fission-track dating, *in* Bradley, D.C., and Dusel-Bacon, Cynthia, eds., Geologic studies in Alaska by the U.S. Geological Survey, 1991: U.S. Geological Survey Bulletin 2041, p. 202–212.

Post, Austin, and Meier, M.F., 1980, A preliminary inventory of Alaskan glaciers, *in* World Glacier Inventory Workshop Proceedings, 17–22 September 1987, Reideralp, Switzerland: International Association of Hydrological Sciences (IAHS) Publication No. 126, p. 45–47.

Reger, R.D., Combellick, R.A., and Brigham-Grette, J., 1995, Update of latest Wisconsin events in the upper Cook Inlet region, southcentral Alaska, *in* Combellick, R.A., and Tannian, F., eds., Short Notes on Alaska Geology: Alaska Division of Geological & Geophysical Surveys Professional Report 117, p. 33–45. doi:10.14509/2320

Reimnitz, Erk, 1966, Late Quaternary history and sedimentation of the Copper River Delta and vicinity: San Diege, California University—San Diego, unpublished PhD thesis, 160 p.

Royer, T.C., 1982, Coastal fresh water discharge in the northeast Pacific: Journal of Geophysical Research, v. 87, p. 2,017–2,021.

Sauber, Jeanne, and Molnia, B.F., 2000, Glacial fluctuations and the rate of deformation in south-central coastal Alaska [abs.]: EOS Transactions, American Geophysical Union, v. 81, no. 48, Fall Meeting Supplement, p. F325.

Sauber, Jeanne, and Molnia, B.F., 2004, Glacier ice mass fluctuations and fault instability in tectonically active southern Alaska: Journal of Global and Planetary Change, v. 42, no. 1-4, p. 279–293.

Sauber, Jeanne, Plafker, George, Molnia, B.F., and Bryant, M.A., 2000, Crustal deformation associated with glacial fluctuations in the eastern Chugach Mountains, Alaska: Journal of Geophysical Research, v. 105, no. B4, p. 8,055–8,077.

Schmoll, H.R., and Dobrovolny, Ernest, 1972, Generalized geologic map of Anchorage and vicinity, Alaska: U.S. Geological Survey Miscellaneous Geological Investigations Map I-787A.

Seed, H.B., and Wilson, S.D., 1967, The Turnagain Heights landslide, Anchorage, Alaska: Journal of the Soil Mechanics and Foundations Division, American Society of Civil Engineers, v. 93, p. 325–353.

Shannon and Wilson, Inc., 1964, Report on Anchorage area soil studies, Alaska, to the U.S. Army Engineer District, Anchorage, Alaska: Seattle, Shannon and Wilson, Inc., 109 p.

Shennan, Ian, and Hamilton, S., 2006, Coseismic and pre-seismic subsidence associated with great earthquakes in Alaska: Quaternary Science Reviews, v. 25, p. 1–8.

Shennan, Ian, Barlow, N.L.M., and Combellick, R.A., 2008, Paleoseismological records of multiple great earthquakes in south-central Alaska—A 4,000-year record at Girdwood, *in* Freymueller, J.T., Haeussler, P.J., Wesson, R., and Ekström, G., eds., Active tectonics and seismic potential of Alaska: American Geophysical Union, Geophysical Monograph Series, v. 179, p. 185–199.

Shennan, Ian, Bruhn, R., and Plafker, George, 2009, Multi-segment earthquakes and tsunami potential of the Aleution mega-thrust. Quaternary Science Reviews, v. 28, p. 7–13.

Shennan, Ian, Long, A., and Barlow, N., 2007, Recurrent Holocene paleoseismicity and associated land/sea-level changes in south-central Alaska: U.S. Geological Survey Report, Award 06HQGR0033.

Shennan, Ian, Barlow, N.L.M., Combellick, R.A., Pierre, K., and Stuart-Taylor, O., in press (2014), Late Holocene paleoseismology of a site in the region of maximum submergence during the 1964 M_w9.2 Alaska earthquake: Journal of Quaternary Science.

Shennan, Ian, Bruhn, R., Barlow, N.L.M., Good, K., and Hocking, E., 2014, Late Holocene great earthquakes in the eastern part of the Aleutian megathrust: Quaternary Science Reviews, v. 84, p. 86–97. doi:10.1016/j.quascirev.2013.11.010

Shennan, Ian, Scott, D.B., Rutherford, M.M., and Zong, Y., 1999, Microfossil analysis of sediments representing the 1964 earthquake, exposed at Girdwood Flats, Alaska, USA: Quaternary International, v. 60, p. 55–73.

Shulski, M., and Wendler, G., 2007, The Climate of Alaska: Anchorage, AK, University of Alaska Press.

Spotila, J.A., and Berger, A.L., 2010, Exhumation at orogenic indentor corners under long-term glacial conditions—Example of the St. Elias orogen, southern Alaska: Tectonophysics, v. 490, no. 3-4, p. 241–256. doi:10.1016/j.tecto.2010.05.015

Spotila, J.A., Buscher, J.T., Meigs, A.J., and Reiners, P.W., 2004, Long-term glacial erosion of active mountain belts—Example of the Chugach St. Elias Range, Alaska: Geology, v. 32, p. 501–504. doi:10.1130/G20343.1

Stuiver, M., and Reimer, P.J., 1986, A computer program for radiocarbon age calculation: Radiocarbon, v. 28, no. 2B, p. 1,022–1,030.

Suito, Hisashi, and Freymueller, J.T., 2009, A viscoelastic and afterslip postseismic deformation model for the 1964 Alaska earthquake: Journal of Geophysical Research, v. 114, no. B11, p. 404–426. doi:10.1029/2008JB005954

Tarr, R.S., and Martin, Lawrence, 1914, Alaskan glacier studies of the National Geographic Society in the Yakutat Bay, Prince William Sound and lower Copper River regions: Washington, D.C., National Geographic Society, 498 p.

Tarr, R.S., Martin, Lawrence, and Gilbert, G.K., 1912, The earthquakes at Yakutat Bay, Alaska, in September, 1899; with a preface by G. K. Gilbert: U.S. Geological Survey Professional Paper 69, 135 p., 3 sheets, scale 1:5,000,000.

Tomkin, J.H., 2007, Coupling glacial erosion and tectonics at active orogens—A numerical modeling study: Journal of Geophysical Research, v. 112, p. F02015. doi:10.1029/2005JF000332

Tomkin, J.H., and Braun, J., 2002, The influence of alpine glaciation on the relief of tectonically active mountain belts: American Journal of Science, v. 302, p. 169–190.

Tomkin, J.H., and Roe, G.H., 2007, Climate and tectonic controls on glaciated critical-taper orogens: Earth and Planetary Science Letters, v. 262, no. 3-4, p. 385–397. doi:10.1016/j.epsl.2007.07.040

Tuthill, S.J., Field, W.O., and Clayton, Lee, 1968, Post-earthquake studies at Sherman and Sheridan glaciers, *in* The great Alaska earthquake of 1964, v. 1, Hydrology, Part A: National Academy of Sciences, Publication 1603, p. 318–328.

Updike, R.G., Olsen, H.W., Schmoll, H.R., Kharaka, Y.K., and Stokoe, K.H., 1988, Geologic and geotechnical conditions adjacent to the Turnagain Heights landslide, Anchorage, Alaska: U.S. Geological Survey Bulletin 1817, 40 p.

Viens, R.J., 1995, Dynamics and mass balance of temperate tidewater calving glaciers of southern Alaska: Seattle, University of Washington, M.S. dissertation, 149 p.

Viereck, L.A., 1967, Botanical dating of recent glacial activity in western North America, *in* Wright, H.E., Jr., and Osburn, W.H., eds., Arctic and Alpine Environment: Indiana University Press, p. 189–204.

Wentworth, C.K., and Ray, L.L., 1936, Studies of certain Alaskan glaciers in 1931: Geological Society of America Bulletin, v. 47, no. 6, p. 879–933.

Whipple, K., Kirby, E., and Brocklehurst, S., 1999, Geomorphic limits to climatically induced increases in topographic relief: Nature, v. 401, p. 39-43.

Wiles, G.C., Barclay, D.J., and Calkin, P.C., 1999, Tree-ring dated "Little Ice Age" histories of maritime glaciers from western Prince William Sound, Alaska: The Holocene, v. 9, no. 2, p. 163–173.

Wilson, F.H., and Hults, C.P., comps., 2012, Geology of the Prince William Sound and Kenai Peninsula region, Alaska: U.S. Geological Survey Scientific Investigations Map 3110, pamphlet 38 p., scale 1:350,000. http://pubs.usgs.gov/sim/3110/

Worthington, L.L., van Avendonk, H.J.A., Gulick, S.P.S., Christeson, G.L., and Pavlis, T.L., 2012, Crustal structure of the Yakutat terrane and the evolution of subduction and collision in southern Alaska: Journal of Geophysical Research, v. 117, B01102. doi:10.1029/2011JB008493

Yanites, B.J., and Ehlers, T.A., Global climate and tectonic controls on the denudation of glaciated mountains: Earth and Planetary Science Letters, v. 325-326, p. 63–75.

Zeitler, P.K., Meltzer, A.S., Koons, P.O., Craw, D., Hallet, B., Chamberlain, C.P., Kidd, W.S.F., Park, S., Seeber, L., Bishop, M.L., and Shroder, J., 2001, Erosion, Himalayan geodynamics, and the geology of metamorphism: GSA Today, v. 11, p. 4–8.

Zong, Y., Shennan, Ian, Combellick, R.A., Hamilton, S.L., and Rutherford M.M., 2003, Microfossil evidence for land movements associated with the AD 1964 Alaska earthquake: Holocene, v. 13, p. 7–20.